Signatures of topological superconductivity

Dissertation

zur Erlangung des Grades
eines Doktors der Naturwissenschaften (Dr. rer. nat.)

am Fachbereich Physik
der Freien Universität Berlin

vorgelegt von

Yang Peng

Berlin, März 2017

Gutachter

Erstgutachter: Prof. Felix von Oppen, PhD (Freie Universität Berlin)
Zweitgutachter: Prof. Dr. Piet W. Brouwer (Freie Universität Berlin)
Drittgutachter: Prof. B. Andrei Bernevig, PhD (Princeton University)
Tag der Disputation: 19.07.2017

Selbstständigkeitserklärung

Hiermit versichere ich, dass ich in meiner Dissertation alle Hilfsmittel und Hilfen angegeben habe, und auf dieser Grundlage die Arbeit selbstständig verfasst habe. Diese Arbeit habe ich nicht schon einmal in einem früheren Promotionsverfahren eingereicht.

Berlin, März 2017

Contents

List of publications

This cumulative dissertation is based on the following first-author publications with the author's contribution indicated.

- [1] Yang Peng, Falko Pientka, Leonid I. Glazman, Felix von Oppen, *Strong localization of Majorana end states in chains of magnetic adatoms*, Phys. Rev. Lett. **114**, 106801, 2015
  The author is the main contributor of this publication, in particular he performed the numerical and analytical calculations.
- [2] Yang Peng, Falko Pientka, Yuval Vinkler-Aviv, Leonid I. Glazman, Felix von Oppen, *Robust Majorana conductance peaks for a superconducting lead*, Phys. Rev. Lett. **115**, 266804, 2015
  The author is the main contributor of this publication, he performed most of the numerical and analytical calculations.
- [3] Yang Peng, Falko Pientka, Erez Berg, Yuval Oreg, Felix von Oppen, *Signatures of topological Josephson junctions*, Phys. Rev. B, **94**, 085409, 2016 (Editors' Suggestion)
  The author is the main contributor of this publication, he performed the numerical and analytical calculations, and had a leading role in the writing of the manuscript.
- [4] Yang Peng, Yuval Vinkler-Aviv, Piet W. Brouwer, Leonid I. Glazman, Felix von Oppen, *Parity anomaly and spin transmutation in quantum spin Hall Josephson junctions*, Phys. Rev. Lett. 117, 267001, 2016
  The author is the main contributor of this publication, he performed the numerical and analytical calculations.

Publications, that have been completed in parallel to this thesis:

- [5] Michael Ruby, Falko Pientka, Yang Peng, Felix von Oppen, Benjamin W. Heinrich, Katharina J. Franke, *Tunneling processes into localized subgap states in superconductors*, Phys. Rev. Lett. **115**, 087001, 2015
- [6] Falko Pientka, Yang Peng, Felix von Oppen, *Topological superconducting phase and Majorana bound states in Shiba chains*, Phys. Scr. **T164**, 014008, 2015
- [7] Michael Ruby, Falko Pientka, Yang Peng, Felix von Oppen, Benjamin W. Heinrich, Katharina J. Franke, *End states and subgap structure in proximity-coupled chains of magnetic adatoms*, Phys. Rev. Lett. **115**, 197204, 2015
- [8] Niko Säkkinen, Yang Peng, Heiko Appel, Robert van Leeuwen, *Many-body Green's function theory for electron-phonon interactions: The Kadanoff-Baym approach to*

spectral properties of the Holstein dimer, J. Chem. Phys. **143**, 234102, 2015

- [9] Niko Säkkinen, Yang Peng, Heiko Appel, Robert van Leeuwen, *Many-body Green's function theory for electron-phonon interactions: Ground state properties of the Holstein dimer*, J. Chem. Phys. **143**, 234101, 2015
- [10] Michael Ruby, Yang Peng, Felix von Oppen, Benjamin W. Heinrich, Katharina J. Franke, *Orbital Picture of Yu-Shiba-Rusinov Multiplets*, Phys. Rev. Lett. **117**, 186801, 2016
- [11] Felix von Oppen, Yang Peng, Falko Pientka, *Topological superconducting phases in one dimension* in C. Chamon et al. (Ed.) Lecture Notes of the Les Houches Summer School: Topological Aspects of Condensed Matter Physics, Oxford University Press, 2017
- [12] Yang Peng, Yimu Bao, Felix von Oppen, *Boundary Green functions of topological insulators and superconductors*, Phys. Rev. B **95**,235143, 2017
- [13] Michael Ruby, Benjamin W. Heinrich, Yang Peng, Felix von Oppen, Katharina J. Franke, *Exploring a proximity-coupled Co chain on Pb (110) as a possible Majorana platform*, Nano Lett. *17*(7), pp 4473–4477, 2017
- [14] Benedikt Friess, Yang Peng, Bernd Rosenow, Felix von Oppen, Vladimir Umansky, Klaus von Klitzing, Jurgen H. Smet, *Negative permittivity in bubble and stripe phases*, Nature Physics, 2017

Abstract

The prediction and experimental discovery of topological insulators brought the importance of topology in condensed matter physics into the limelight. Topology hence acts as a new dimension along which more and more new states of matter start to emerge. One of these topological states of matter, namely topological superconductors, comes into the focus because of their gapless excitations. These gapless excitations, especially in one dimensional topological superconductors, are Majorana zero modes localized at the ends of the superconductor and exhibit exotic nonabelian statistics, which can be potentially applied to fault-tolerant quantum computation. Given their highly interesting physical properties and potential applications to quantum computation, both theorists and experimentalists spend great efforts to realize topological supercondoctors and to detect Majoranas.

In two projects within this thesis, we investigate the properties of Majorana zero modes in realistic materials which are absent in simple theoretical models. We find that the superconducting proximity effect, an essential ingredient in all existing platforms for topological superconductors, plays a significant role in determining the localization property of the Majoranas. Strong proximity coupling between the normal system and the superconducting substrate can lead to strongly localized Majoranas, which can explain the observation in a recent experiment. Motivated by experiments in Molenkamp's group, we also look at realistic quantum spin Hall Josephson junctions, in which charge puddles acting as magnetic impurities are coupled to the helical edge states. We find that with this setup, the junction generically realizes an exotic 8π periodic Josephson effect, which is absent in a pristine Josephson junction.

In another two projects, we propose more pronounced signatures of Majoranas that are accessible with current experimental techniques. The first one is a transport measurement, which uses superconducting rather than normal-metal leads to probe the Majoranas. We predict a universal conductance as a signature, which is more robust at finite temperatures. These predictions have already been partially checked by several experiments. The second signature is based on Josephson junctions. Rather than directly measuring the current-phase relation, which is able to distinguish a topological junction from a conventional one only if fermion parity is conserved, we propose to detect topological Josephson junctions via switching probability measurements. This provides robust signatures of topological Josephson junctions without the requirement for a conserved fermion parity. Since this type of measurement has already been realized for conventional Josephson junctions, experiments on topological Josephson junctions are likely to be performed in the near future.

Zusammenfassung

Durch die Prognose und experimentelle Entdeckung topologischer Isolatoren ist die Rolle der Topologie in der Festkörperphysik in den Vordergrund gerückt. So wirkt Topologie wie eine neue Dimension, aus welcher fortwährend neue Materialzustände entspringen. Ein solcher Zustand, welcher aufgrund seiner bandlückenlosen Anregungen auffällt, ist der topologische Supraleiter. In eindimensionalen topologischen Supraleitern sind diese Anregungen Majorana-Nullmoden, welche an den Enden des Supraleiters lokalisiert sind und über eine nichtabelsche Vertauschungsstatistik verfügen. Diese Eigenschaften können für fehlertolerantes Quantenrechnen verwendet werden. Aufgrund dieser hochgradig interessanten Eigenschaften und deren Anwendung in Bezug auf Quantenrechner gibt es große Bemühungen in der theoretischen Physik sowie Experimentalphysik, topologische Supraleiter zu realisieren und Majoranas zu messen.

In zwei Projekten dieser Doktorarbeit untersuchen wir die Eigenschaften von Majorana-Nullmoden in realistischen Materialien, welche in vereinfachten theoretischen Modellen fehlen. Wir stellen fest, dass der Proximity-Effekt der Supraleitung, welcher für alle existierenden topologischen Supraleiter von höchster Bedeutung ist, eine entscheidende Rolle für die Lokalisierungseigenschaften von Majoranas spielt. Starke Proximity-Kopplung zwischen dem normalleitenden System und dem supraleitenden Substrat kann zu einer starken Lokalisierung von Majoranas führen, was eine Erklärung für kürzlich gemessene Phänomene liefert. In Anlehung an Experimente, welche in Molenkamps Gruppe durchgeführt wurden, untersuchen wir zudem realistische Quanten-Spin-Hall Josephson-Kontakte, in welchen Ladungsansammlungen sich wie magentische Störstellen verhalten und an die helikalen Randzustände koppeln. In solchen Konfigurationen finden wir einen exotischen 8π-periodischen Josephson-Effekt, welcher in einem störstellenfreien Josephson-Kontakt nicht vorhanden ist.

In zwei anderen Projekten schlagen wir ausschlaggebendere Majorana-Signaturen vor, welche mithilfe heutiger experimenteller Techniken messbar sind. Die erste Signatur ist eine Transportmessung, welche supraleitende Kontakte anstelle normalleitender Kontakte nutzt um Majoranas zu untersuchen. Wir prognostizieren einen universellen elektrischen Leitwert, welcher robust ist bei endlichen Temperaturen. Diese Voraussagen wurden bereits teilweise in Experimenten überprüft. Die zweite Signatur beruht auf Josephson-Kontakten. Anstatt die Strom-Phasen-Beziehung direkt zu messen, durch welche man einen topologischen von einem herkömmlichen Kontakt nur unter Voraussetzung von Fermionenparitätserhaltung unterscheiden kann, schlagen wir vor, topologische Josephson-Kontakte durch Messungen der Umschaltwahrscheinlichkeit zu detektieren. Dies liefert robuste Signaturen für topologische Josephson-Kontakte ohne Fermionenparitätserhaltung vorauszusetzen. Da solche Messungen bereits für herkömmliche Josephson-Kontakte durchgeführt wurden, ist es wahrscheinlich, dass solche Experimente in naher Zukunft auch für topologische Josephson-Kontakte realisiert werden.

1 Introduction

It is known for a long time that free-fermion Hamiltonians, which are quadratic in fermionic operators, have few interesting features in the sense that they are exactly solvable. Particularly, electronic band theory is extremely successful in describing the properties of this kind of system with translational invariance. When the band structure is gapless at the chemical potential, the system is a metal. While if the system aquires a band gap it is an insulator (or a BCS superconductor for Bogoliubov–de Gennes (BdG) Hamiltonians).

For many decades, it seemed that the classification of crystals into metals and insulators was complete. It was believed that all insulators have very low electric and thermal conductivity, and are essentially the same type of material. This began to change after the the discovery of the quantum Hall effect in 1980 [15].

The quantum Hall effect is realized in a two-dimensional electron gas subject to a strong magnetic field perpendicular to the sample. The bulk is gapped and insulating because of the formation of Landau levels. However, the system is different from a conventional atomic insulator since the quantum Hall sample has a precisely quantized Hall conductance of $\sigma_{xy} = ne^2/h$ [16] with integer n. Although the bulk is insulating, the quantum Hall insulator has gapless chiral edge modes which are perfectly conducting [17]. The number of these edge modes exactly equals the quantized value n. It was shown by Thouless, Kohmoto, Nightingale and den Nijs [18] that the integer n is a topological quantity known as a Chern number, answering the question why the quantization is so precise.

Soon after the discovery of the quantum Hall effect which requires a large magnetic field, Haldane proposed a theoretical model [19] — the celebrated Haldane model — which realizes quantum Hall physics in the absence of external magnetic fields. This model describes a system of electrons hopping on a honeycomb lattice, with complex nearest neighbor hopping amplitude. Because of this, the electrons on the two sublattices feel opposite magnetic flux and the net flux per plaquet is zero. This intrinsic quantum Hall effect is now termed quantum anomalous Hall effect [20] which is generally realized in 2D systems known as Chern insulators. The Haldane model was the first model of a Chern insulator. Although proposed almost 30 years ago, the Haldane model has no experimental realizations in solid state systems up to now. It was only recently realized experimentally with ultra cold atoms [21]. In solid state devices, the quantum anomalous Hall effect is recently observed in Ref. [22].

Since Chern insulators have finite Hall conductance, they must break time-reversal symmetry. We can build a corresponding time-reversal invariant system, called quantum spin Hall insulator [23, 24, 25] by stacking two Chern insulators made of spin-up and spin-down electrons with Hall conductances (Chern number) of opposite signs. By time-reversal symmetry, the quantum spin Hall insulator does not have a non-zero Hall conductance. However, it differs from a conventional atomic insulator in that it has a non-zero spin-Hall conductance. Moreover, it has helical edge modes, which consist of two gapless chiral modes for spin up and down electrons propagating in opposite directions. The existence of helical edge modes and non-zero spin Hall conductance in a quantum spin Hall insulator is not described by a $\mathbb{Z}$ Chern number, but are related to a $\mathbb{Z}_2$ topological invariant of the bulk [23]. A quantum spin Hall insulator was realized experimentally in 2007 [26], even before the realization of the Chern insulator.

Besides Chern and quantum spin Hall insulators in 2D, there exist further free-fermion systems in various dimensions which have insulating bulk yet differ from atomic insulators by a topological invariant defined from their bulk electronic structure. These types of systems are called *topological insulators* [27, 28] in general. Moreover, we can consider superconducting pairing of BCS type, and view the BdG Hamiltonian [29, 30] as a free-fermion Hamiltonian by introducing the Nambu-spinor representation [31]. Similar to topological insulators, there are gapped superconducting systems which are different from conventional BCS superconductors in terms of topological invariants. These are known as *topological superconductors* [28].

Quite generally, the nontrivial topological invariants defined from the bulk band structure of topological insulators or superconductors faithfully reflect the existence of gapless excitations located at the boundary of the systems. This is known as the bulk-boundary correspondence [32, 33, 34]. In topological insulators these gapless boundary modes are fermionic, while in topological superconductors, the gapless modes are known as *Majorana* modes [35], as will be addressed in more detail later.

The existence of topological insulators and superconductors depends not only on the dimension that the system lives in, but also on the symmetry class of the free-fermion Hamiltonian. Here, symmetry refers to non-spatial symmetries of the Hamiltonian, namely time-reversal, paticle-hole and chiral symmetries. We require that the Hamiltonian be irreducible in the sense that it cannot be further block-diagonalized according to other symmetries [36]. With these requirements, there are in total ten symmetry classes [37]. One can associate topological invariants with each symmetry class and dimension, and obtain a table that classifies all possible topological insulators and superconductors, see Table 1.1 [38, 36, 34].

1.1 Symmetries

A second-quantized free-fermion Hamiltonians (including BdG Hamiltonian after introducing the Nambu representation) defined on a d-dimensional lattice can generally be written as

$$H = \sum_{I,J} \Psi_I^\dagger \mathcal{H}_{IJ} \Psi_J \tag{1.1}$$

where I, J label the lattice coordinates in each direction, i.e. $I = (i_1, \ldots, i_d)$. Ψ_J ($\Psi_I^\dagger$) is the fermionic annihilation (creation) operator at site J (I) of the lattice, which is in general a column (row) vector with m components, denoted as $\Psi_J = (\Psi_{J,1}^T, \ldots, \Psi_{J,m}^T)^T$ ($\Psi_I^\dagger = (\Psi_{I,1}^\dagger, \ldots, \Psi_{I,m}^\dagger)$). Thus, the first quantized Hamiltonian $\mathcal{H}_{IJ}$ is a $m \times m$ matrix.

Class	$\hat{\mathcal{T}}$	$\hat{\mathcal{C}}$	$\hat{\mathcal{S}}$	0	1	2	3	4	5	6	7
A	0	0	0	$\mathbb{Z}$	0	$\mathbb{Z}$	0	$\mathbb{Z}$	0	$\mathbb{Z}$	0
AIII	0	0	1	0	$\mathbb{Z}$	0	$\mathbb{Z}$	0	$\mathbb{Z}$	0	$\mathbb{Z}$
AI	+	0	0	$\mathbb{Z}$	0	0	0	$2\mathbb{Z}$	0	$\mathbb{Z}_2$	$\mathbb{Z}_2$
BDI	+	+	1	$\mathbb{Z}_2$	$\mathbb{Z}$	0	0	0	$2\mathbb{Z}$	0	$\mathbb{Z}_2$
D	0	+	0	$\mathbb{Z}_2$	$\mathbb{Z}_2$	$\mathbb{Z}$	0	0	0	$2\mathbb{Z}$	0
DIII	-	+	1	0	$\mathbb{Z}_2$	$\mathbb{Z}_2$	$\mathbb{Z}$	0	0	0	$2\mathbb{Z}$
AII	-	0	0	$2\mathbb{Z}$	0	$\mathbb{Z}_2$	$\mathbb{Z}_2$	$\mathbb{Z}$	0	0	0
CII	-	-	1	0	$2\mathbb{Z}$	0	$\mathbb{Z}_2$	$\mathbb{Z}_2$	$\mathbb{Z}$	0	0
C	0	-	0	0	0	$2\mathbb{Z}$	0	$\mathbb{Z}_2$	$\mathbb{Z}_2$	$\mathbb{Z}$	0
CI	+	-	1	0	0	0	$2\mathbb{Z}$	0	$\mathbb{Z}_2$	$\mathbb{Z}_2$	$\mathbb{Z}$

Table 1.1: Periodic table of topological insulators and superconductors in $d = 0, \ldots, 7$ dimensions. The first column denotes the ten symmetry classes of fermionic Hamiltonians, characterized by the absence or presence of time-reversal ($\hat{\mathcal{T}}$), particle-hole ($\hat{\mathcal{C}}$), and chiral symmetries ($\hat{\mathcal{S}}$) of different types denoted by 0, ± or 1. Classes which support only trivial phases are denoted by "0", while classes with nontrivial topological classifications are indicated by the type of their topological invariant ($\mathbb{Z}, 2\mathbb{Z}, \mathbb{Z}_2$).

In the following, we first introduce the non-spatial symmetries that define the ten symmetry classes.

1.1.1 Time-Reversal Symmetry

Time-reversal symmetry requires the existence of an antiunitary operator $\hat{\mathcal{T}} = \mathcal{U}_T \hat{\mathcal{K}}$ such that

$$[\hat{\mathcal{T}}, \mathcal{H}_{IJ}] = 0, \quad \forall I, J, \tag{1.2}$$

where the square brackets denote the commutator, $\mathcal{U}_T$ is an $m \times m$ unitary matrix and $\hat{\mathcal{K}}$ is the complex conjugation operator such that $\hat{\mathcal{K}} i = -i \hat{\mathcal{K}}$. If we apply time-reversal twice, we obtain

$$[\mathcal{U}_T \mathcal{U}_T^*, \mathcal{H}_{IJ}] = 0, \quad \forall I, J, \tag{1.3}$$

and we have that $\mathcal{U}_T \mathcal{U}_T^* = \exp(i\alpha) \mathbb{1}_m$ is a multiple of the identity matrix by Schur's lemma. Moreover, because of the unitarity of $\mathcal{U}_T$, we find $\exp(i\alpha) = \pm 1$ which leads to two types of time-reversal symmetry

$$\mathcal{U}_T \mathcal{U}_T^* = \pm \mathbb{1}_m. \tag{1.4}$$

or $\hat{\mathcal{T}}^2 = \pm 1$.

1.1.2 Particle-Hole Symmetry

Particle-hole symmetry requires the existence of an antiunitary operator $\hat{\mathcal{C}} = \mathcal{U}_C \hat{\mathcal{K}}$ such that

$$\{\hat{\mathcal{C}}, \mathcal{H}_{IJ}\} = 0, \quad \forall I, J, \tag{1.5}$$

where the braces denote the anticommutator and $\mathcal{U}_C$ is a $m \times m$ unitary matrix. As for time-reversal symmetry, we find that there are two types of particle-hole symmetries given by

$$\mathcal{U}_C \mathcal{U}_C^* = \pm \mathbb{I}_m. \tag{1.6}$$

or $\hat{\mathcal{C}}^2 = \pm 1$.

1.1.3 Chiral Symmetry

Chiral symmetry requires the existence of a unitary operator $\hat{\mathcal{S}} = \mathcal{U}_S$ represented by an $m \times m$ unitary matrix $\mathcal{U}_S$, such that

$$\{\hat{\mathcal{S}}, \mathcal{H}_{IJ}\} = 0, \quad \forall I, J. \tag{1.7}$$

Applying chiral symmetry twice we find that $\mathcal{U}_S^2 = \exp(i\alpha)\mathbb{I}_M$. Redefining $\mathcal{U}_S \to \mathcal{U}_S \exp(-i\alpha/2)$, we have

$$\mathcal{U}_S^2 = \mathbb{I}_m, \tag{1.8}$$

namely $\mathcal{U}_S = \mathcal{U}_S^\dagger$. Note that Hamiltonians which are both time-reversal and particle-hole symmetric, automatically obey chiral symmetry with $\mathcal{U}_S = \mathcal{U}_T \mathcal{U}_C^*$. If either time-reversal or particle-hole symmetry is absent, chiral symmetry is absent. However, chiral symmetry can exist when both time-reversal and particle-hole symmetry are absent.

The absence or presence of time-reversal ($\hat{\mathcal{T}}$), particle-hole ($\hat{\mathcal{C}}$) and chiral symmetries ($\hat{\mathcal{S}}$) of different types according to Eq. (1.4), (1.6) and (1.8), lead to the ten symmetry classes which are summarized in the first two columns of Table 1.1.

1.2 Periodic Table

In a given spatial dimension and symmetry class, topological insulators and superconductors are characterized by a topological invariant which takes values in $\mathbb{Z}$, $\mathbb{Z}_2$, or $2\mathbb{Z}$. As one varies parameters of the Hamiltonian, the topological invariant remains constant as long as the bulk gap does not close and the symmetry of the system does not change. Since both symmetry and topology play a significant role in characterizing phases, topological insulators and superconductors are generally known as symmetry-protected topological phases [39].

One key property of Table 1.1 is that the topological invariants exhibit a periodicity of 2 or 8 as a function of spatial dimension [38, 36, 34], which is closely related to *Bott periodicity* in K-theory in mathematics [40, 41]. We follow the approach described in Ref. [34] to briefly sketch the derivation of this periodic table by making use of homotopy groups of classifying spaces of symmetry allowed Dirac mass terms and Clifford algebras.

Since topological invariants only change if the system crosses a topological phase transition, i.e., when the bulk gap vanishes and reopens, the topological nature of the system is fully contained in the low-energy effective Hamiltonian near the topological phase transition. The latter is a Dirac Hamiltonian in d dimensions vanishing at k_0 in momentum space right at the transition plus a small mass term $m\Gamma_0$,

$$\mathcal{H}(\mathrm{k}) = \mathrm{k} \cdot \mathbf{\Gamma} + m\Gamma_0, \tag{1.9}$$

where $\mathrm{k} = (k_1, \ldots, k_d)$ is the momentum measured from k_0, and $\Gamma = (\Gamma_1, \ldots, \Gamma_d)$ together with Γ_0 are Dirac matrices, which satisfy the Clifford algebra $\left\{\Gamma_\mu, \Gamma_\nu\right\} = 2\delta_{\mu,\nu}$ with $\mu, \nu = 0, \ldots, d$. Because Γ_0 anticommutes with all Dirac matrices contained in the kinetic energy, it gives rise to an energy gap.

If some of the symmetries defined in the previous section are present, Γ_0 must transform in the same way as defined in Eq. (1.2), (1.5) and (1.7). The different topological phases correspond to different types of masses. Let us make this statement more precise by considering Hamiltonians in class A as an example. Since no other symmetry exists in class A, the massless Dirac Hamiltonian has a complex Clifford algebra Cl_d consisting of d generators, which all come from the Dirac matrices appearing in the kinetic part of the Hamiltonian. Here "complex" means that the generators are represented by complex matrices. When a mass term is introduced, the Clifford algebra is extended by one more generator to Cl_{d+1}, since the mass term anticommutes with the kinetic part. Topologically different phases correspond to different extensions of the Clifford algebra $Cl_d \longrightarrow Cl_{d+1}$. Let us define the *classifying space*, denoted by C_d, as the set of all allowed Γ_0. The types of extentions are given by the path-connected components of this classifying space, referred to as the zeroth homotopy group $\pi_0(C_d)$.

In one dimension, a low-energy Hamiltonian in class A can be written as

$$\mathcal{H}(k) = k_x \sigma_3 \otimes \mathbb{I}_N + M, \tag{1.10}$$

where the mass term fulfills $\{\sigma_3 \otimes \mathbb{I}_N, M\} = 0$. Note that in order to discuss general phases, we are allowed to enlarge the matrix dimension of the Hamiltonian by a tensor product with the $N \times N$ identity matrix $\mathbb{I}_N$ for large enough N. The general solution for M is

$$M = \begin{pmatrix} 0 & U^\dagger \\ U & 0 \end{pmatrix}, \quad U \in U(N). \tag{1.11}$$

In this case, the extension problem is $Cl_1 \longrightarrow Cl_2$ with classifying space

$$C_1 = \lim_{N\to\infty} U(N). \tag{1.12}$$

Since the unitary group is path-connected and $\pi_0(U(N)) = 0$ for fixed N, we have $\pi_0(C_1) = 0$. This implies that all masses can be continuously deformed into each other [34].

In two dimension, the low-energy Hamiltonian in class A can be written as

$$\mathcal{H}(\mathrm{k}) = k_x \sigma_1 \otimes \mathbb{I}_N + k_y \sigma_2 \otimes \mathbb{I}_N + M. \tag{1.13}$$

As for the case in one dimension, the mass M needs to anticommute with the kinetic terms. Thus, M should have the form $M = \sigma_3 \otimes A$ where A is a $N \times N$ hermitian matrix. Since A can be diagonalized via a unitary transformation, the Hamiltonian can be regarded as N decoupled copies of Dirac insulators with the different masses given by the eigenvalues. The magnitude of the masses does not matter for the classification, so that the matrix A can be written as

$$A = U \,\mathrm{diag}\,(\mathbb{I}_n, -\mathbb{I}_{N-n})\, U^\dagger, \quad U \in U(N). \tag{1.14}$$

Then, with n positive and $N-n$ negative eigenvalues we find that $A \in U(N)/[U(n)\times U(N-n)]$ for fixed n. To derive the classifying space, we need to include all possible values of n. Hence, we find that the extension problem $C_2 \longrightarrow C_3$ has the classifying space

$$C_2 = \lim_{N\to\infty} \bigcup_{n=0}^{N} \frac{U(N)}{U(n)\times U(N-n)} = BU \times \mathbb{Z}, \tag{1.15}$$

	Classifying space	Extension	$\pi_0(\cdot)$	Symmetry classes
$\mathcal{C}_0$	$BU \times \mathbb{Z}$	$Cl_0 \to Cl_1$	$\mathbb{Z}$	A
$\mathcal{C}_1$	$U(N)$	$Cl_1 \to Cl_2$	0	AIII
$\mathcal{R}_0$	$BO \times \mathbb{Z}$	$Cl_{p,p} \to Cl_{p,p+1}$	$\mathbb{Z}$	AI
$\mathcal{R}_1$	$O(N)$	$Cl_{p,p+1} \to Cl_{p,p+2}$	$\mathbb{Z}_2$	BDI
$\mathcal{R}_2$	$O(2N)/U(N)$	$Cl_{p,p+2} \to Cl_{p,p+3}$	$\mathbb{Z}_2$	D
$\mathcal{R}_3$	$U(N)/Sp(N)$	$Cl_{p,p+3} \to Cl_{p,p+4}$	0	DIII
$\mathcal{R}_4$	$BSp \times \mathbb{Z}$	$Cl_{p,p+4} \to Cl_{p,p+5}$	$\mathbb{Z}$	AII
$\mathcal{R}_5$	$Sp(N)$	$Cl_{p,p+5} \to Cl_{p,p+6}$	0	CII
$\mathcal{R}_6$	$Sp(N)/U(N)$	$Cl_{p,p+6} \to Cl_{p,p+7}$	0	C
$\mathcal{R}_7$	$U(N)/O(N)$	$Cl_{p,p+7} \to Cl_{p,p+8}$	0	CI

Table 1.2: Classifying space for complex and real symmetry classes in 0 dimension [34].

where BU is the classifying space for the unitary group. Since $\pi_0(\mathcal{C}_2) = \mathbb{Z}$, we have that the gapped phases in class A in two dimensions are classfied by $\mathbb{Z}$, as shown in Table 1.1.

In fact, we can continue our analysis to arbitrary dimensions for class A Hamiltonians, by considering the extension $Cl_d \to Cl_{d+1}$ with classifying space $\mathcal{C}_d$. Because of $Cl_{n+2} \simeq Cl_n \otimes \mathbb{C}(2)$, where $\mathbb{C}(2)$ is the algebra of 2×2 complex matrices which does not affect the extension problem, the classifying spaces appear with a period of two,

$$\mathcal{C}_{n+2} \simeq \mathcal{C}_n, \tag{1.16}$$

which is known as *complex Bott periodicity*. The name originates from the fact that class A together with class AIII are complex symmetry classes without antiunitary symmetry.

Now let us perform the analysis of the Hamiltonians in class AIII. Because of chiral symmetry, there exists a unitary matrix $\mathcal{U}_s$ with $\{\mathcal{H}, \mathcal{U}_s\} = 0$. We can think of $\mathcal{U}_s$ as another Clifford generator in addition to the gamma matrices in the kinetic term. Hence, for d-dimensional Hamiltonians in class AIII, we need to consider the extension problem $Cl_{d+1} \to Cl_{d+2}$, with classifying space $\mathcal{C}_{d+1} \simeq \mathcal{C}_{d-1}$. We have that the topological classification in class AIII is the same as that in class A, up to a shift by one dimension, as can be seen in Table 1.1.

Apart from classes A and AIII, the remaining eight classes are real symmetry classes, where there exists at least one antiunitary symmetry. In this case, we need to consider the extension of real Clifford algebras $Cl_{p,q} \to Cl_{p,q+1}$ instead of complex ones, and denote the classifying space as $\mathcal{R}_{q-p}$. Deriving expressions for $\mathcal{R}_{q-p}$ is beyond the scope of this thesis. We only list the classifying spaces for real as well as complex symmetry classes in zero dimension in Table 1.2. Using the property $Cl_{p+8,q} \simeq Cl_{p,q+8} \simeq Cl_{p,q} \otimes \mathbb{R}(16)$ of real Clifford algebras, where $\mathbb{R}(16)$ denotes the algebra of 16×16 real matrices, we have the *real Bott periodicity*

$$\mathcal{R}_{q+8} \simeq \mathcal{R}_q. \tag{1.17}$$

1.3 Topological Superconductors and Majorana Modes

After this brief introduction to noninteracting symmetry-protected topological phases, we now turn our attention to a specific class of systems, known as *topological superconductors*. Topological superconductors host gapless excitations at the edge, protected by the nontrival topology of their bulk band structures. Specifically in one dimension, the excitations located at the ends of the wire have zero energy and are quite remarkable as they turn out to be *Majorana zero modes* or in short *Majoranas*. These Majoranas are neither fermions nor bosons but obey nonabelian quantum statistics when braided around one another [42, 43]. This nonabelian statistics is not only interesting physically, but may also be useful for quantum computation. Due to their zero-energy nature, Majoranas give rise to degenerate ground states, which can be used as qubits and to store quantum information in a nonlocal fashion. For a system of Majorana qubits, gate operations can then be effected via braiding. Hence, decoherence by local perturbations is highly suppressed. This leads to the amazing concept of topological quantum computation [44, 45].

In the following, we first explain why Majoranas appear naturally as excitations in superconductors.

1.3.1 Majorana Bound States

At the mean field level (BCS theory), superconductors can be described by a second-quantized BCS Hamiltonian. When doubling the degrees of freedom, the Hamiltonian defined in d dimensions can be written as

$$H = \int d^d x \Psi^\dagger \mathcal{H} \Psi. \tag{1.18}$$

Here Ψ is a Nambu spinor composed of field operators with the x dependence left implicit, and $\mathcal{H}$ is the first-quantized Bogoliubov–de Gennes (BdG) Hamiltonian. Because of the doubling of degrees of freedom, the Nambu spinor is constrained by an antiunitary operator $\hat{C}$ with $\Psi = \hat{C}\Psi$. Due to this constraint, the BdG Hamiltonian acquires a particle-hole symmetry $\{\hat{C}, \mathcal{H}\} = 0$ [11].

Let $\Phi_n(\mathrm{x})$ be a vector-valued wave function, which is an eigenstate of $\mathcal{H}$ with energy E_n,

$$\mathcal{H}\Phi_n(\mathrm{x}) = E_n \Phi(\mathrm{x}). \tag{1.19}$$

Then $\Phi_{-n}(\mathrm{x}) = \hat{C}\Phi_n(\mathrm{x})$ is another eigenstate of $\mathcal{H}$ with energy $E_{-n} = -E_n$. Hence, all finite-energy eigenvalues of $\mathcal{H}$ appear in pairs of $\pm E_n$. However, an isolated zero-energy state $\Phi_0(\mathrm{x})$ can exist if the state transforms into itself under particle-hole symmetry, i.e., $\Phi_0(\mathrm{x}) = \hat{C}\Phi_0(\mathrm{x})$. This state is known as a Majorana zero mode, where the name originates from Majorana fermions in high energy physics which are their own antiparticle. Since for a superconductor, the bulk is gapped by superconducting pairing, Majoranas only appear at the boundary of the system, and their wave function decays into the bulk.

In the language of second quantization, the BCS Hamiltonian can be diagonalized as

$$H = \sum_n E_n \gamma_n^\dagger \gamma_n \tag{1.20}$$

by introducing Bogoliubov quasiparticle operator

$$\gamma_n = \int d^d x \Phi_n^\dagger(\mathrm{x})\Psi(\mathrm{x}) \tag{1.21}$$

associated with the eigenstates $\Phi_n(x)$ of energy E_n. By particle-hole symmetry, we have the relation

$$\gamma_{-n}^\dagger = \int d^d x \Psi^\dagger(\mathrm{x})\Phi_{-n}(\mathrm{x}) = \int d^d x \left[\hat{C}\Psi(\mathrm{x})\right]^\dagger \left[\hat{C}\Phi_n(\mathrm{x})\right] = \int d^d x \Psi^\dagger(\mathrm{x})\Phi_n(\mathrm{x}) = \gamma_n. \tag{1.22}$$

For an isolated state with $E_0 = 0$, we conclude that the Bogoliubov operator fulfills $\gamma_0 = \gamma_0^\dagger$, i.e., that it is a Majorana operator and indeed its own antiparticle.

We will now provide a few simple models which host Majoranas.

1.3.2 Kitaev Chain

The simplest system hosting Majorana bound states is the Kitaev chain [43], a lattice realization of a spinless p-wave superconductor in one dimension. Consider a chain of N sites with the Hamiltonian

$$H = -t \sum_{j=1}^{N-1} \left(c_{j+1}^\dagger c_j + c_j^\dagger c_{j+1} \right) + \Delta \sum_{j=1}^{N-1} \left(c_{j+1} c_j + c_j^\dagger c_{j+1}^\dagger \right) - \mu \sum_{j=1}^{N} c_j^\dagger c_j, \tag{1.23}$$

where c_j ($c_j^\dagger$) is the electron annihilation (creation) operator of site j, t is the hopping amplitude from site to site, Δ is the pairing potential between neighboring sites (p-wave type) which is taken to be real for simplicity, and μ is the chemical potential.

First consider the situation when $\Delta = t$ and $\mu = 0$. Let us write the fermionic operators c_j as

$$c_j = \frac{1}{2}\left(\gamma_{Aj} + i\gamma_{Bj}\right), \tag{1.24}$$

in terms of two hermitian Majorana operators γ_{Aj} and γ_{Bj}. The Hamiltonian can then be rewritten as

$$H = -it \sum_{j=1}^{N-1} \gamma_{Aj}\gamma_{B,j+1}. \tag{1.25}$$

Introducing new fermionic operators through

$$d_j = \frac{1}{2}\left(\gamma_{Aj} - i\gamma_{B,j+1}\right) \tag{1.26}$$

with $j = 1, \ldots, N-1$, the original Hamiltonian becomes diagonal,

$$H = 2t \sum_{j=1}^{N-1} \left(d_j^\dagger d_j - \frac{1}{2} \right). \tag{1.27}$$

We see that the d_j correspond to the Bogoliubov quasiparticles. There is still one fermionic operator missing. We can define it by using the two remaining Majorana operators localized at the two ends of the chain,

$$d_0 = \frac{1}{2}\left(\gamma_{AN} - i\gamma_{B1}\right). \tag{1.28}$$

This fermionic operator does not appear in the Hamiltonian and thus corresponds to zero-energy states, implying a twofold degeneracy of the many-body spectrum. If $|n\rangle$ is an arbitrary many-body eigenstate of the system of fixed fermion number parity, then either $d_0^\dagger |n\rangle$ or $d_0 |n\rangle$ will vanish and the other state constitutes a second eigenstate of the system with the same energy. In particular, the ground state is degenerate which is essential for performing quantum computation.

Up to now, we only showed for specific points in parameter space ($t = \Delta$ and $\mu = 0$) that we have a topological superconductor with Majorana zero modes. To obtain the full phase diagram, we compute the bulk properties of the model with periodic boundary conditions, $c_1 = c_{N+1}$. Expanding c_j as

$$c_j = \frac{1}{\sqrt{N}} \sum_{j=1}^{N} e^{ikj} a_k, \tag{1.29}$$

H can be written as

$$H = \sum_k \xi_k a_k^\dagger a_k + \Delta \sum_k \left[e^{ik} a_k a_{-k} + e^{-ik} a_{-k}^\dagger a_k^\dagger \right] \tag{1.30}$$

with $\xi_k = -2t \cos k - \mu$. If we introduce the Nambu spinor $\Psi_k^\dagger = (a_k^\dagger, a_{-k})$, the Hamiltonian can be written as (up to an additional constant)

$$H = \sum_{k>0} \Psi_k^\dagger h_k \Psi_k, \tag{1.31}$$

with

$$h_k = \xi_k \tau_z - 2\Delta \sin k \tau_y, \tag{1.32}$$

where $\tau_{x,y,z}$ are Pauli matrices in Nambu space. The summation is restricted to positive k to avoid double counting when introducing the Nambu spinor. We thus obtain the bulk dispersion

$$E_k = \pm\sqrt{\xi_k^2 + 4\Delta^2 \sin^2 k}. \tag{1.33}$$

From the dipersion, we see that the bulk gap vanishes only at $k = 0$ with $\mu = -2t$ or $k = \pi$ with $\mu = 2t$. Hence, the phase boundary is given by $\mu = \pm 2t$. When $\Delta = 0$, the system is gapped for $|\mu| > 2|t|$, which corresponds to the trivial phase. This trivial phase extends to arbitrary Δ. The topological phase containing the special points discussed above extends for $|\mu| < 2|t|$.

The Kitaev chain falls into symmetry class BDI, since there exists a unitary operator τ_x which commutes with the Hamiltonian in Eq. (1.32). This chiral symmetry allows us to rewrite the Hamiltonian in a basis in which it becomes block off-diagonalized

$$h_k = \xi_k \tau_x - 2\Delta \sin k \tau_y = \begin{pmatrix} 0 & \xi_k + 2i\Delta \sin k \\ \xi_k - 2i\Delta \sin k & 0 \end{pmatrix}. \tag{1.34}$$

In 1D, the topological invariant for class BDI is given by an integer winding number $w \in \mathbb{Z}$, which can be computed as

$$w = \int_0^{2\pi} dk \frac{d}{dk} \ln(-2t \cos k - \mu + 2i\Delta \sin k). \tag{1.35}$$

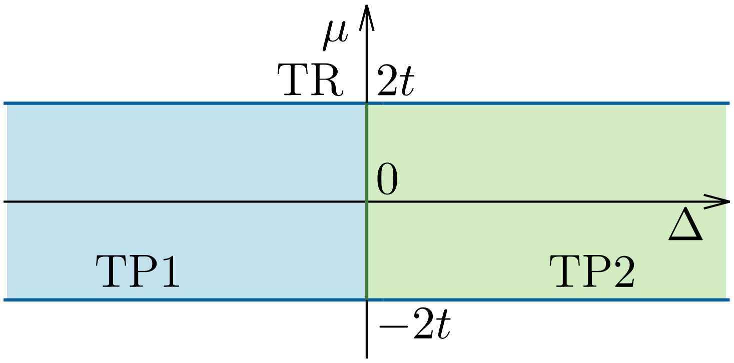

Figure 1.1: Phase diagram of the Kitaev chain as function of p-wave pairing strength Δ and chemical potential μ (assuming positive hopping amplitude t). There are topological superconducting phases when the chemical potential is within the band of the normal-state Hamiltonian, while the system is topologically trivial when the chemical potential is outside the band.

We observe that for $|\mu| > 2t$, the phase of $(-2t\cos k - \mu + 2i\Delta \sin k)$ does not wind, and we have a trivial phase with $w = 0$. For $|\mu| < 2t$, the phase winds once, with opposite winding numbers for $\Delta > 0$ and $\Delta < 0$, corresponding to two topological phases. The boundary between these two phases is located at $\Delta = 0$. The phase diagram of the Kitaev chain is shown in Figure 1.1.

It is worth mentioning that for a homogeneous system, the Hamiltonians with $\pm\Delta$ are related to each other via a unitary transformation. Nevertheless, a domain wall between Δ and $-\Delta$ segments is associated with a gap closing. In this sense, systems with $\pm\Delta$ correspond to distinct phases.

1.3.3 Spinless p-wave Superconductor in 1D

A continuum model of a spinless p-wave superconductor in 1D, is given by the BdG Hamiltonian [11, 46]

$$H = \sum_{p>0} \Psi_p^\dagger \mathcal{H}_p \Psi_p$$

$$\mathcal{H}_p = \xi_p \tau_z + \Delta p \tau_x, \quad \xi_p = \frac{p^2}{2m} - \mu, \quad \Delta \in \mathbb{R}, \tag{1.36}$$

where p, m, μ, and Δ are the momentum, mass, chemical potential, and pairing potential of the electrons, and $\Psi_p^\dagger$ is the Nambu spinor. As in the analysis of the Kitaev chain, we have topological phases when $\mu > 0$, and a trivial phase when $\mu < 0$ [11]. This model also belongs to class BDI, because $\{\tau_y, \mathcal{H}_p\} = 0$. Nevertheless, generically this chiral symmetry would be absent. For example, when the pairing potential becomes complex (and spatially dependent), $\Delta = |\Delta|\, e^{-i\theta}$, the Hamiltonian falls into class D. The topological invariant reduces from integer winding numbers to a $\mathbb{Z}_2$ index.

1.3.4 Spinless $p + ip$ Superconductors in 2D

If we extend the previous one-dimensional model to two dimensions, we obtain a spinless $p + ip$ superconductor in symmetry class D, with Hamiltonian

$$H = \int d^2 r \Psi^\dagger(\mathrm{r}) \mathcal{H}(\mathrm{r}) \Psi(\mathrm{r})$$

$$\mathcal{H}(\mathrm{r}) = \begin{pmatrix} \frac{\hat{p}^2}{2m} - \mu(\mathrm{r}) & \frac{1}{2}\{\Delta(r), \partial_x + i\partial_y\} \\ -\frac{1}{2}\{\Delta^*(r), \partial_x - i\partial_y\} & \mu(\mathrm{r}) - \frac{\hat{p}^2}{2m} \end{pmatrix}, \tag{1.37}$$

where $\Psi(\mathrm{r})^\dagger = (\psi(\mathrm{r})^\dagger, \psi(\mathrm{r}))$ is the Nambu spinor consisting of electron operators. Similar to the previous 1D case, we have a topological phase for $\mu > 0$ and a trivial phase for $\mu < 0$.

Let us first consider such a system on an infinite plane with constant pairing potential $\Delta(\mathrm{r}) = \Delta \in \mathbb{R}$ and chemical potential $\mu(\mathrm{r}) = \mu(x)$. Consider a domain wall in $\mu(x)$, with $\mu < 0$ for $x < 0$ and $\mu > 0$ for $x > 0$, parallel to the y-direction. Since the momentum along the y-direction is a good quantum number, in the limit $m \to \infty$ we can write the Hamiltonian parametrized by x and p_y as

$$\mathcal{H}(x, p_y) = \begin{pmatrix} -\mu(x) & \Delta(\partial_x - p_y) \\ -\Delta(\partial_x + p_y) & \mu(x) \end{pmatrix}. \tag{1.38}$$

We see that at each p_y, the Hamiltonian is a 1D Dirac Hamiltonian with a domain wall at $x = 0$. From the work of Jackiw and Rebbi [47], we know that there will be a bound state localized at the domain wall in such 1D models.

In our situation, we actually have a gapless mode localized at the domain wall propagating along the y-direction, whose dispersion and wave function are

$$E(p_y) = -\Delta p_y, \tag{1.39}$$

and

$$\Phi_{p_y}(x, y) = e^{ip_y y} \exp\left(-\frac{1}{\Delta}\int^x \mu(x')dx'\right)|\phi_0\rangle \tag{1.40}$$

with $\phi_0 = (1, 1)^T/\sqrt{2}$. The existence of the gapless mode, known as a *chiral Majorana mode*, located at the boundary is a general property of a topological superconductor in two dimensions.

Now we change to a different geometry: Consider a disk of radius R, which has $\mu < 0$ surrounded by a region with $\mu > 0$ for $r > R$. Moreover, consider a vortex with vanishing Δ at $\mathrm{r} = 0$ whose size is assumed to be very small. Outside the vortex, Δ is taken to be constant. We expect a zero mode localized at the domain wall $r = R$, which is shown in the following.

In polar coordinates,

$$\partial_x + i\partial_y = e^{i\theta}(\partial_r + \frac{i}{r}\partial_\theta), \tag{1.41}$$

so that the BdG Hamiltonian in the large-mass limit becomes

$$\mathcal{H}(r) = \begin{pmatrix} -\mu & \Delta e^{i\theta}(\partial_r + \frac{i}{r}\partial_\theta) \\ -\Delta e^{-i\theta}(\partial_r - \frac{i}{r}\partial_\theta) & \mu \end{pmatrix}. \tag{1.42}$$

Solving for $\mathcal{H}(r,\theta)\Phi(r,\theta) = 0$, we find a zero-energy Majorana wave function

$$\Phi(r,\theta) = \frac{i}{\mathcal{N}\sqrt{r}} \exp\left(-\int^{r} dr' \frac{\mu(r')}{\Delta}\right) \begin{pmatrix} -e^{i\theta/2} \\ e^{-i\theta/2}, \end{pmatrix} = if(r) \begin{pmatrix} -e^{i\theta/2} \\ e^{-i\theta/2} \end{pmatrix}, \tag{1.43}$$

where $\mathcal{N} \in \mathbb{R}$ is a normalization factor. This state indeed corresponds to a Majorana since its operator

$$\gamma(\mathrm{r}) = \int rdrif(r) \left[-e^{i\theta/2}\psi(\mathrm{r}) + e^{-i\theta/2}\psi(\mathrm{r})^{\dagger}\right], \tag{1.44}$$

fulfills $\gamma = \gamma^{\dagger}$. Note that the Bogoliubov quasiparticle operators obey anti-periodic boundary conditions,

$$\gamma(r,\theta + 2\pi) = -\gamma(r,\theta), \tag{1.45}$$

corresponding to π-flux insertion at the vortex.

1.4 Braiding Majoranas

Majorana operators differ from normal (Dirac) fermionic operators due to their hermitian constraint. In fact, two Majoranas γ_1, γ_2 can represent a Dirac fermion f via

$$f = \frac{\gamma_1 + i\gamma_2}{2}. \tag{1.46}$$

If the two zero-energy Majoranas are infinitely far apart, the system has two degenerate states given by $|0\rangle$ with $f\,|0\rangle = 0$ and $f^{\dagger}\,|0\rangle$. When they come close to each other, their interaction is proportional to $i\gamma_1\gamma_2 = 2f^{\dagger}f - 1$, which splits the degeneracy. The system can go into either of the two states which differ by fermion number parity. Hence, to characterize a quantum state of two Majoranas, another quantum number – the *fusion channel* of the two Majoranas – needs to be introduced. In the following, we will first derive the anyonic properties of Majoranas in the framework of category theory, based on simple fusion rules, without referring to explicit Majorana operators or Hamiltonians. At the end of this section (in Sec. 1.4.4), in order to gain some physical intuition, we will further show that the Majorana operators indeed realize all properties derived from category theory.

1.4.1 Fusion Rules

To investigate the properties of Majoranas, we introduce the language of topological quantum field theory, in particular category theory [45, 46]. Within this framework, the possibility of having two fusion channels for two Majoranas can be reformulated as

$$\sigma \times \sigma = 1 + \psi, \tag{1.47}$$

where σ denotes the Majorana, 1 denotes the vacuum without fermions, and ψ denotes the state with one extra fermion. Here the × and + have the meaning of direct product and direct sum of Hilbert spaces, as used when adding angular momenta. For example, from

$$\frac{1}{2} \times \frac{1}{2} = 0 + 1, \tag{1.48}$$

we know that two spin-1/2 particles can form singlet (0) and triplet (1) subspaces. Moreover, it is worthwhile to mention that it is the nonuniqueness of the fusion product that produces the non-abelian anyonic nature of the Majoranas. In addition to Eq. (1.47), we have

$$1 \times \sigma = \sigma, \quad 1 \times \psi = \psi, \quad \sigma \times \psi = \sigma, \quad \psi \times \psi = 1. \tag{1.49}$$

These fusion rules define a *fusion category.*

A general fusion rule can be written in the following form

$$a \times b = b \times a = \sum_c N_{ab}^c c, \tag{1.50}$$

where the $N_{ab}^c \in \mathrm{Z}_+$ (positive integers) can be regarded as the dimension of the Hilbert space V_{ab}^c with particles a, b, and c at the punctures of a 3-punctured sphere. Note that if one of the particles is the trivial particle 1, then that puncture can be removed.

As mentioned previously, fusion or × can be understood as a direct-product operation, which should be symmetric with respect to the two inputs. Since the order of fusion does not matter in defining fusion rules, we can fuse multiple particles by sequentially fusing two particles in any order. From another point of view, this corresponds to the fact that any n-punctured sphere is homeomorphic to surfaces constructed from glueing 3-punctured spheres at the punctures.

Now let us consider fusing n Majoranas. We have the Hilbert space $V_{\sigma\ldots\sigma}^1$ of an n-punctured sphere with one Majorana at each puncture. This Hilbert space is constructed as

$$V_{\sigma\ldots\sigma}^1 = \bigoplus_{c_i} V_{\sigma\sigma}^{c_1} V_{\sigma c_1}^{c_2} \ldots V_{\sigma c_{n-3}}^{\sigma}, \tag{1.51}$$

where we have used the fact that the last fusion must produce σ in order to fuse with σ to produce 1.

The ground-state degeneracy, which is the dimension of this Hilbert space is given by

$$\dim\left(V_{\sigma\ldots\sigma}^1\right) = \sum_{c_i} N_{\sigma\sigma}^{c_1} N_{\sigma c_1}^{c_2} \ldots N_{\sigma c_{n-3}}^{\sigma} = \sum_{c_i} (N_\sigma)_{\sigma c_1} (N_\sigma)_{c_1 c_2} \ldots (N_\sigma)_{c_{n-3}\sigma} . \tag{1.52}$$

In the second equality, we regard $N_{\sigma c_i}^{c_j}$ as a matrix element $(N_\sigma)_{c_i c_j}$ of a matrix N_σ. Denote the largest eigenvalue of N_σ as d_σ. For large n, we have the dimension $\dim\left(V_{\sigma\ldots\sigma}^1\right) \sim d_\sigma^{n-2}$. We call d_σ the *quantum dimension* of the Majorana, which is the asymptotic degeneracy per particle of a collection of Majoranas.

In the basis $(1, \sigma, \psi)$, we have

$$N_\sigma = \begin{pmatrix} 0 & 1 & 0 \\ 1 & 0 & 1 \\ 0 & 1 & 0 \end{pmatrix} \tag{1.53}$$

and the quantum dimension $d_\sigma = \sqrt{2}$. Hence, for a system of $2M$ Majoranas with M large, the ground state degeneracy of the system is 2^{M-1}.

In general, the quantum dimension of different particles fulfills

$$d_a d_b = \sum_c N_{ab}^c d_c, \tag{1.54}$$

which is consistent with the fusion rule in Eq. (1.50). It is also convenient to introduce the *total quantum dimension*

$$\mathcal{D} = \sum_c \sqrt{d_c^2}, \tag{1.55}$$

where c runs over all particle types of a given model. For systems of Majoranas, we have $\mathcal{D} = 2$.

1.4.2 Exchange properties

To explore the exchange properties of anyons, we introduce the phase factor R_c^{ab} to characterize the effect of exchanging a and b in the fusion process. Diagrammatically, R_c^{ab} can be defined via

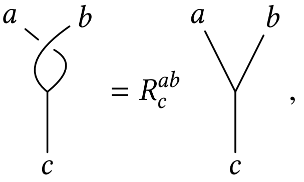

(1.56)

where the exchange of a and b is realized in a clockwise manner.

To write down an equation obeyed by R^c_{ab}, we first need to use that fusion of n particles can be implemented sequentially by fusing pairs in any order. Define $\left(F_d^{abc}\right)_j^i$ as the factor between fusing three particles in different orders via

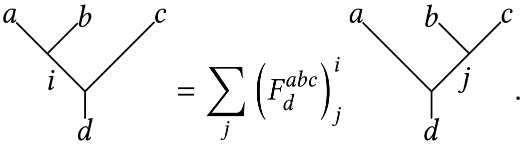

(1.57)

The quantities $(F_d^{abc})_j^i$ fulfill a consistency relation known as the *pentagon identity*

$$\left(F_5^{a34}\right)_c^b \left(F_5^{12c}\right)_d^a = \sum_e \left(F_b^{123}\right)_e^a \left(F_5^{1e4}\right)_d^b \left(F_d^{234}\right)_c^e . \tag{1.58}$$

Diagrammatically, this identity comes from the equivalence between fusing along the upper and the lower paths of the pentagon

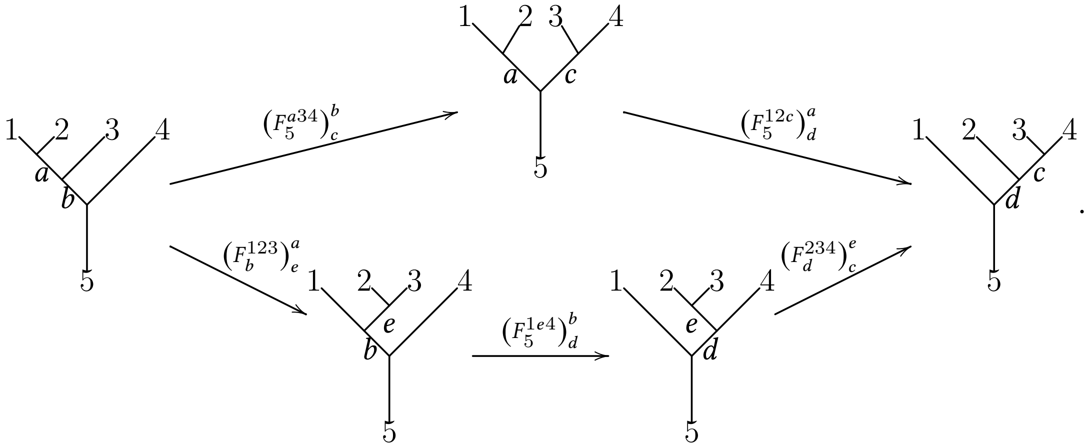

(1.59)

By the same spirit, we require the operation implemented along the upper and lower paths of the following hexagon to be the same,

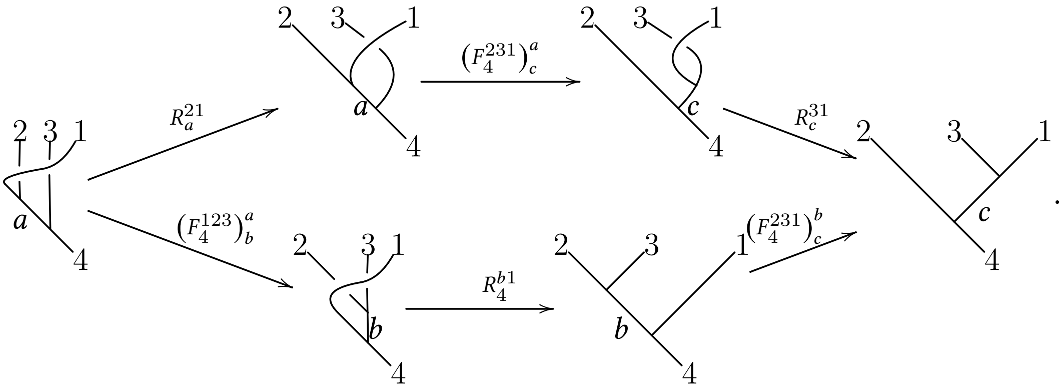

. (1.60)

This gives rise to the *hexagon identity*

$$R^{21}_a \left(F^{231}_4\right)^a_c R^{31}_c = \sum_b \left(F^{123}_4\right)^a_b R^{b1}_4 \left(F^{231}_4\right)^b_c \tag{1.61}$$

satisfied by R^{ab}_c.

1.4.3 F and R for Majoranas

With the above general definitions, we can now compute F and R for a system of Majoranas. From the fusion rules and Eq. (1.53) we know that

$$N^1_{\sigma\sigma} = N^\psi_{\sigma\sigma} = N^\sigma_{\sigma 1} = N^\sigma_{\sigma\psi} = 1. \tag{1.62}$$

Moreover, we have that F^{123}_4 is a one dimensional matrix except when $1, 2, 3, 4$ are all σ. In that case, we have $i, j = 1, \psi$, and $F^{\sigma\sigma\sigma}_\sigma$ is a 2×2 matrix. All one dimensional matrices can take arbitrary complex phases, corresponding to gauge degrees of freedom. We fix these phases to be 1.

To solve the pentagon identity, we first set $1, 2, 3, 4$ to be σ and 5 to be 1 in Eq. (1.58) and the corresponding diagram. Then $b = d = \sigma$, and a, c can be 1 or ψ. For $a = c = 1$, the pentagon identity becomes

$$\left(F^{1\sigma\sigma}_1\right)^\sigma_1 \left(F^{\sigma\sigma 1}_1\right)^1_\sigma = \sum_{e=1,\psi} \left(F^{\sigma\sigma\sigma}_\sigma\right)^1_e \left(F^{\sigma e\sigma}_1\right)^\sigma_\sigma \left(F^{\sigma\sigma\sigma}_\sigma\right)^e_1 . \tag{1.63}$$

Setting $(F^{\sigma\sigma 1}_1)^1_\sigma = (F^{1\sigma\sigma}_1)^\sigma_1 = (F^{\sigma 1\sigma})^\sigma_\sigma = (F^{\sigma\psi\sigma})^\sigma_\sigma = 1$, we have

$$1 = \left[(F^{\sigma\sigma\sigma}_\sigma)^1_1\right]^2 + (F^{\sigma\sigma\sigma}_\sigma)^1_\psi (F^{\sigma\sigma\sigma}_\sigma)^\psi_1. \tag{1.64}$$

Now consider $a = 1$, $c = \psi$. We have

$$\left(F^{1\sigma\sigma}_1\right)^\sigma_\psi \left(F^{\sigma\sigma\psi}_1\right)^1_\sigma = \sum_e \left(F^{\sigma\sigma\sigma}_\sigma\right)^1_e \left(F^{\sigma e\sigma}_1\right)^\sigma_\sigma \left(F^{\sigma\sigma\sigma}_\sigma\right)^e_\psi . \tag{1.65}$$

The left hand side of the obove equation is zero because $\left(F_1^{\sigma\sigma\psi}\right)_\sigma^1 = 0$. We thus have

$$\left(F_\sigma^{\sigma\sigma\sigma}\right)_1^1 = -\left(F_\sigma^{\sigma\sigma\sigma}\right)_\psi^\psi . \tag{1.66}$$

Finally, when $a = c = \psi$ we have

$$1 = \left[(F_\sigma^{\sigma\sigma\sigma})_\psi^\psi\right]^2 + (F_\sigma^{\sigma\sigma\sigma})_1^\psi (F_\sigma^{\sigma\sigma\sigma})_\psi^1 . \tag{1.67}$$

Now we take 1 to be ψ while $2, 3, 4$ and 5 to be σ. We require $a = d = \sigma$, and b, c take values $1, \psi$. For $b = c = 1$, the pentagon identity becomes

$$\left(F_\sigma^{\sigma\sigma\sigma}\right)_1^1 \left(F_\sigma^{\psi\sigma 1}\right)_\sigma^\sigma = \sum_{e=1,\psi} \left(F_1^{\psi\sigma\sigma}\right)_e^\sigma \left(F_\sigma^{\psi e\sigma}\right)_\sigma^1 \left(F_\sigma^{\sigma\sigma\sigma}\right)_1^e = \left(F_1^{\psi\sigma\sigma}\right)_\psi^\sigma \left(F_\sigma^{\psi\psi\sigma}\right)_\sigma^1 \left(F_\sigma^{\sigma\sigma\sigma}\right)_1^\psi \tag{1.68}$$

where in the second equality we used $\left(F_1^{\psi\sigma\sigma}\right)_1^\sigma = 0$. Fixing the gauge, we have

$$\left(F_\sigma^{\sigma\sigma\sigma}\right)_1^1 = \left(F_\sigma^{\sigma\sigma\sigma}\right)_1^\psi . \tag{1.69}$$

For $b = 1$ and $c = \psi$, we have

$$\left(F_\sigma^{\sigma\sigma\sigma}\right)_\psi^1 \left(F_\sigma^{\psi\sigma\psi}\right)_\sigma^\sigma = \sum_e \left(F_1^{\psi\sigma\sigma}\right)_e^\sigma \left(F_\sigma^{\psi e\sigma}\right)_\sigma^1 \left(F_\sigma^{\sigma\sigma\sigma}\right)_\psi^e = \left(F_1^{\psi\sigma\sigma}\right)_\psi^\sigma \left(F_\sigma^{\psi\psi\sigma}\right)_\sigma^1 \left(F_\sigma^{\sigma\sigma\sigma}\right)_\psi^\psi . \tag{1.70}$$

We need to choose $\left(F_\sigma^{\psi\sigma\psi}\right)_\sigma^\sigma = -1$ such that the matrix $F_\sigma^{\sigma\sigma\sigma}$ is unitary. We thus get

$$\left(F_\sigma^{\sigma\sigma\sigma}\right)_\psi^1 = -\left(F_\sigma^{\sigma\sigma\sigma}\right)_\psi^\psi . \tag{1.71}$$

With all relations derived, we obtain

$$F_\sigma^{\sigma\sigma\sigma} = \pm\frac{1}{\sqrt{2}}\begin{pmatrix} 1 & 1 \\ 1 & -1 \end{pmatrix} \tag{1.72}$$

in the basis $(1, \psi)$. The choice of ± is called *Frobenius-Schur indicator* χ_σ, which is ±1 for particles which are their own antiparticles. The Frobenius-Schur indicator for systems of Majoranas is +1 [48].

After solving the pentagon equation, we now turn to the hexagon equation to determine R. We take $1, 2, 3, 4$ to be all σ, and a, c have to take values $1, \psi$. First consider $a = c = 1$. Eq. (1.61) becomes

$$R_1^{\sigma\sigma} \left(F_\sigma^{\sigma\sigma\sigma}\right)_1^1 R_1^{\sigma\sigma} = \sum_{b=1,\psi} \left(F_\sigma^{\sigma\sigma\sigma}\right)_b^1 R_\sigma^{b\sigma} \left(F_\sigma^{\sigma\sigma\sigma}\right)_1^b , \tag{1.73}$$

which reduces to

$$\left(R_1^{\sigma\sigma}\right)^2 = \frac{1}{\sqrt{2}}\left(R_\sigma^{1\sigma} + R_\sigma^{\psi\sigma}\right). \tag{1.74}$$

For $a = 1$, $c = \psi$ we get

$$R_1^{\sigma\sigma}\left(F_\sigma^{\sigma\sigma\sigma}\right)_\psi^1 R_\psi^{\sigma\sigma} = \sum_{b=1,\psi}\left(F_\sigma^{\sigma\sigma\sigma}\right)_b^1 R_\sigma^{b\sigma}\left(F_\sigma^{\sigma\sigma\sigma}\right)_\psi^b, \tag{1.75}$$

which reduces to

$$R_1^{\sigma\sigma}R_\psi^{\sigma\sigma} = \frac{1}{\sqrt{2}}\left(R_\sigma^{1\sigma} - R_\sigma^{\psi\sigma}\right). \tag{1.76}$$

This can also be obtained from taking $a = \psi$, $c = 1$.

Finally, for $a = c = \psi$, we have

$$R_\psi^{\sigma\sigma}\left(F_\sigma^{\sigma\sigma\sigma}\right)_\psi^\psi R_\psi^{\sigma\sigma} = \sum_{b=1,\psi}\left(F_\sigma^{\sigma\sigma\sigma}\right)_b^\psi R_\sigma^{b\sigma}\left(F_\sigma^{\sigma\sigma\sigma}\right)_\psi^b, \tag{1.77}$$

which reduces to

$$\left(R_\psi^{\sigma\sigma}\right)^2 = -\frac{1}{\sqrt{2}}\left(R_\sigma^{1\sigma} + R_\sigma^{\psi\sigma}\right). \tag{1.78}$$

From Eq. (1.74) and (1.78), we have

$$R_1^{\sigma\sigma} = \pm iR_\psi^{\sigma\sigma}. \tag{1.79}$$

The ± corresponds to a gauge degree of freedom, and we will choose the lower sign in the following. Using Eq. (1.76), and $R_\sigma^{1\sigma} = 1$, we have

$$R_\psi^{\sigma\sigma} = \exp\left(i\frac{3\pi}{8}\right), \quad R_1^{\sigma\sigma} = \exp\left(-i\frac{\pi}{8}\right), \quad R_\sigma^{\psi\sigma} = R_\sigma^{\sigma\psi} = -i. \tag{1.80}$$

With F and R for Majoranas, we can finally look at the effect of braiding Majoranas. Consider a system of four Majoranas, which form a two-dimensional Hilbert space (a qubit). For simplicity, we initialize our system in a state $|\sigma, \sigma \longrightarrow 1\rangle \otimes |\sigma, \sigma \longrightarrow 1\rangle$ (for fixed fermion number parity), or diagrammatically as

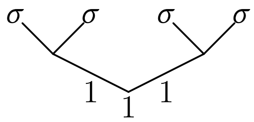

$=$

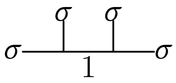

(1.81)

Let us braid the middle two Majoranas around one another. We have

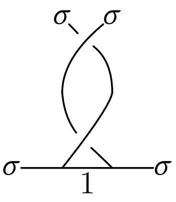

$= \sum_{c=1,\psi}\left(F_\sigma^{\sigma\sigma\sigma}\right)_c^1$

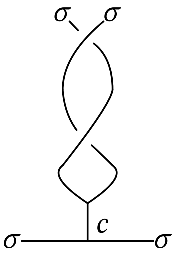

$= \sum_{c=1,\psi}\left(F_\sigma^{\sigma\sigma\sigma}\right)_c^1\left(R_c^{\sigma\sigma}\right)^2$

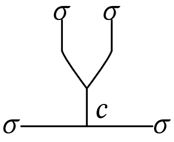

$= \sum_{d=1,\psi} B_{1d}$

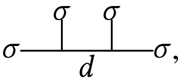

, (1.82)

where we introduced the *braiding matrix*

$$B_{ij} = \sum_{k=1,\psi} \left(F^{\sigma\sigma\sigma}_{\sigma}\right)^i_k \left(R^{\sigma\sigma}_k\right)^2 \left[\left(F^{\sigma\sigma\sigma}_{\sigma}\right)^{-1}\right]^k_j, \quad i,j = 1,\psi, \tag{1.83}$$

or in matrix form

$$B = F^{\sigma\sigma\sigma}_{\sigma}(R^{\sigma\sigma})^2 \left(F^{\sigma\sigma\sigma}_{\sigma}\right)^{-1}, \tag{1.84}$$

with the matrix

$$R^{\sigma\sigma} = \mathrm{diag}\left(R^{\sigma\sigma}_1, R^{\sigma\sigma}_{\psi}\right) = e^{-i\pi/8}\begin{pmatrix} 1 & 0 \\ 0 & i \end{pmatrix}. \tag{1.85}$$

and $F^{\sigma\sigma\sigma}_{\sigma}$ derived in Eq. (1.72) (with + sign). From straightforward calculation, we find

$$B = e^{-i\pi/4}\begin{pmatrix} 0 & 1 \\ 1 & 0 \end{pmatrix}. \tag{1.86}$$

Hence, braiding transforms the two states $|0\rangle = |\sigma,\sigma \rightarrow 1\rangle \otimes |\sigma,\sigma \rightarrow 1\rangle$ and $|1\rangle = |\sigma,\sigma \rightarrow \psi\rangle \otimes |\sigma,\sigma \rightarrow \psi\rangle$ into each other up to a phase. Furthermore, using a similar approach it can be shown that the states $|\sigma,\sigma \rightarrow \psi\rangle\otimes|\sigma,\sigma \rightarrow 1\rangle$ and $|\sigma,\sigma \rightarrow 1\rangle\otimes|\sigma,\sigma \rightarrow \psi\rangle$, which also form a two-dimensional Hilbert space, transform into each other under braiding.

1.4.4 Realization by Majorana Operators

At the end of this section, we will show that the Majorana operators $\{\gamma_i\}, i = 1, 2, \ldots,$ with $\{\gamma_i, \gamma_j\} = 2\delta_{ij}$ and $\gamma_i = \gamma_i^\dagger$, give rise to a concrete realization of the anyonic properties derived above.

For simplicity, let us consider four Majoranas $\gamma_1, \gamma_2, \gamma_3$, and γ_4 localized at four different spatial points. Since two Majoranas can form a Dirac fermion, we can introduce two Dirac fermions as

$$z_1 = (\gamma_1 + i\gamma_2)/2, \quad z_2 = (\gamma_3 + i\gamma_4)/2, \tag{1.87}$$

or as

$$w_1 = (\gamma_1 + i\gamma_3)/2, \quad w_2 = (\gamma_2 + i\gamma_4)/2. \tag{1.88}$$

Since fermion number parity (the evenness/oddness of the total number of fermions) is always conserved, the system is restricted to a sector with fixed fermion number parity. In general for $2M$ Majoranas, the actual Hilbert space with a fixed fermion parity has dimension 2^{M-1}, indicating that the quantum dimension of Majoranas is $\sqrt{2}$.

Let us denote the physical state as $|ij\rangle_z = |i\rangle_{z_1} \otimes |j\rangle_{z_2}$, where i, j denote the occupation number of fermion modes z_1, z_2 respectively. Moreover, we restrict ourselves to the even-parity sector whose basis vectors can be chosen as $|00\rangle_{z/w}$ and $|11\rangle_{z/w}$.

Since $w_1^\dagger w_1 = (1 + i\gamma_1\gamma_3)/2$, we have

$$\left(2w_1^\dagger w_1 - 1\right)|00\rangle_z = i\gamma_1\gamma_3\,|00\rangle_z = i(z_1^\dagger + z_1)(z_2^\dagger + z_2)\,|00\rangle_z = iz_1^\dagger z_2^\dagger\,|00\rangle_z = |11\rangle_z\,, \tag{1.89}$$

where the last equality is regarded as a definition for $|11\rangle_z$ with a particular gauge choice.

Notice that $w_1^\dagger w_1$ is a projector onto state $|11\rangle_w$. Then we have

$$\frac{1}{\sqrt{2}}\left(|00\rangle_z + |11\rangle_z\right) = \sqrt{2} w_1^\dagger w_1 \, |00\rangle_z = |11\rangle_w \, . \tag{1.90}$$

Moreover, $w_1 w_1^\dagger$ is a projector onto state $|00\rangle_w$, so that

$$|00\rangle_w = \sqrt{2} w_1 w_1^\dagger \, |00\rangle_z = \sqrt{2}(1 - w_1^\dagger w_1) \, |00\rangle_z = \frac{1}{\sqrt{2}}\left(|00\rangle_z - |11\rangle_z\right) . \tag{1.91}$$

It is more enlightening to write this as a matrix

$$\begin{pmatrix} |00\rangle_z \\ |11\rangle_z \end{pmatrix} = F_\sigma^{\sigma\sigma\sigma} \begin{pmatrix} |11\rangle_w \\ |00\rangle_w \end{pmatrix}, \quad F_\sigma^{\sigma\sigma\sigma} = \frac{1}{\sqrt{2}} \begin{pmatrix} 1 & 1 \\ 1 & -1 \end{pmatrix}, \tag{1.92}$$

in which the transformation is exactly the one that we derived from the pentagon equations in Eq. (1.72). This is not a surprise because grouping Majoranas into different Dirac fermions actually implements the fusion process as

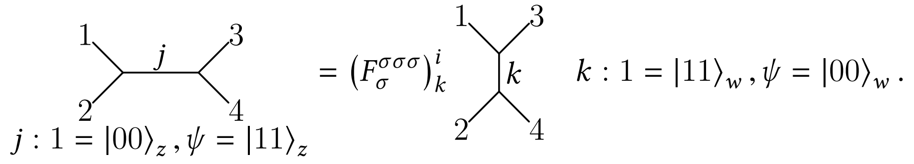

$$= \left(F_\sigma^{\sigma\sigma\sigma}\right)^i_k \qquad k : 1 = |11\rangle_w \, , \psi = |00\rangle_w \, . \tag{1.93}$$

Now let's turn to the exchange properties. If we exchange two Majoranas in a counterclockwise manner, the unitary operator $\mathcal{U}$ representing this process should fulfill

$$\mathcal{U}\gamma_i\mathcal{U}^\dagger \propto \gamma_j, \quad \mathcal{U}\gamma_j\mathcal{U}^\dagger \propto \gamma_i. \tag{1.94}$$

Since $\mathcal{U}$ acts on Majoranas i and j, generally it can be written as

$$\mathcal{U} = a + b\gamma_i + c\gamma_j + d\gamma_i\gamma_j, \quad a, b, c, d \in \mathbb{C}. \tag{1.95}$$

From unitarity $\mathcal{U}\mathcal{U}^\dagger = 1$, we have

$$\begin{aligned} aa^* + bb^* + cc^* + dd^* &= 1, & ab^* + ba^* + cd^* + dc^* &= 0, \\ ac^* - bd^* + ca^* - db^* &= 0, & -ad^* + bc^* - cb^* + da^* &= 0. \end{aligned} \tag{1.96}$$

From $\mathcal{U}\gamma_i\mathcal{U}^\dagger \propto \gamma_j$, we have

$$\begin{aligned} aa^* + bb^* - cc^* - dd^* &= 0, & ab^* + ba^* - cd^* - dc^* &= 0, \\ -ac^* + bd^* + ca^* - db^* &= 0, & ad^* - bc^* - cb^* + da^* &= \text{phase}. \end{aligned} \tag{1.97}$$

From $\mathcal{U}\gamma_j\mathcal{U}^\dagger \propto \gamma_i$, we have

$$\begin{aligned} aa^* - bb^* + cc^* - dd^* &= 0, & -ab^* + ba^* - cd^* + dc^* &= 0, \\ ac^* + bd^* + ca^* + db^* &= 0, & ad^* + bc^* + cb^* + da^* &= \text{phase}. \end{aligned} \tag{1.98}$$

These relations can be reduced into

$$\begin{gathered} |a|^2 + |b|^2 = |c|^2 + |d|^2 = |a|^2 + |c|^2 = |b|^2 + |d|^2 = \frac{1}{2}, \\ ab^* + ba^* = cd^* + dc^* = ba^* + dc^* = ab^* + cd^* = 0, \\ ac^* + ca^* = bd^* + ca^* = ac^* + db^* = bd^* + db^* = 0, \\ |b|^2 = |c|^2 \, , \quad |a|^2 = |d|^2 \, , \quad ab^* = dc^*, \quad ac^* = bd^*, \\ iab^*, icd^*, iac^*, ibd^* \in \mathbb{R} \quad \Rightarrow \quad b = c, a = d. \end{gathered} \tag{1.99}$$

From Eq. (1.97) we have

$$2(|a|^2 - |b|^2) = \text{phase}. \tag{1.100}$$

We thus require either $a = d = 0$, $b = c = e^{i\phi}/\sqrt{2}$ or $b = c = 0$, $a = d = e^{i\theta}/\sqrt{2}$, which gives rise to two unitary operators

$$\mathcal{U}' = \frac{e^{-i\theta}}{\sqrt{2}} \left(\gamma_i + \gamma_j\right), \quad \mathcal{U} = \frac{e^{-i\phi}}{\sqrt{2}} \left(1 + \gamma_i \gamma_j\right). \tag{1.101}$$

$\mathcal{U}'$ only produces abelian braiding since $\mathcal{U}'^2 = e^{-2i\phi}$, whereas braiding with $\mathcal{U}$ is non-abelian since $\mathcal{U}^2 = e^{-2i\theta}\gamma_i\gamma_j$.

One can actually show that $\mathcal{U}$ indeed describes the exchange of two Majoranas based on the concrete real-space Majorana operators in Eq. (1.44). We see that if the phase of the superconducting order parameter is increased by 2π, the Hamiltonian is invariant (see Eq. (1.42)), while $\gamma(\mathrm{r}) \to -\gamma(\mathrm{r})$. Following the arguement by Ivanov [42], one can introduce branch cuts in real space from the Majoranas to the left boundary of the system. Away from these cuts, the phase is single valued whereas it jumps by 2π when crossing a cut. Exchanging one Majorana with another makes one of the Majoranas (γ_i) cross the cut of the other (γ_j) but not vice versa. We thus have $\gamma_i \to -\gamma_j$, $\gamma_j \to \gamma_i$ under the exchange operation. This is the same as the effect of $\mathcal{U}$ up to a phase.

We illustrate the action of $\mathcal{U}$ on a system of four Majoranas. Exchanging γ_1 and γ_3 twice corresponds to a unitary operation

$$\mathcal{U}^2 = e^{-2i\theta}\gamma_1\gamma_3 = e^{-2i\theta}\left(z_1^\dagger z_2^\dagger + z_1^\dagger z_2 + z_1 z_2^\dagger + z_1 z_2\right), \tag{1.102}$$

which exchanges the states $|00\rangle_z$ and $|11\rangle_z$ up to a phase. (We assume the system is in the even-parity sector.) This operation looks very similar to the braiding operator derived from category theory in Eq. (1.86). We will show that they are essentially the same by determining the phase angle θ.

If we exchange any two Majoranas (as a Dirac fermion) around another Dirac fermion, we get a -1 factor because of fermion statistics. Hence, if we braid (exchange twice) a single Majorana around one Dirac fermion, we get a -1 factor. Let γ_1 first braid around γ_2, γ_3, corresponding to the operation $e^{-4i\theta}\gamma_1\gamma_3\gamma_1\gamma_2 = e^{-4i\theta}\gamma_2\gamma_3$. Then let us fuse γ_2, γ_3, whose outcome can be vacuum or a Dirac fermion. Finally, braid γ_1 around this outcome in the opposite direction. If we introduce fermionic operator $\alpha = (\gamma_2 + i\gamma_3)/2$, then this operation can be written as $1 - 2\alpha^\dagger\alpha = i\gamma_3\gamma_2$, which gives 1 if the fermionic mode is empty and -1 if the fermionic mode is occupided. Since the phase factor should be equal the identity after these three steps, we have the equation

$$e^{-4i\theta}\gamma_2\gamma_3 i\gamma_3\gamma_2 = 1, \tag{1.103}$$

which leads to $\theta = \pi/8$. Thus, the operator $\mathcal{U}^2$ is essentially the same as B in Eq. (1.86). The phase angle θ is known as the *topological spin* of Majoranas [48, 46].

1.4.5 Topological Quantum Computation

From the discussion above, we saw that a qubit can be obtained from four Majoranas, and a σ_x operation on the qubit is implemented via braiding one Majorana around the other. The advantage of building qubits from Majoranas is that quantum information can be stored nonlocally, and is thus insensitive to local perturbations. Moreover, braiding Majoranas does not depend on the geometry of the paths spanned by the Majoranas, but only on their topology. This gives rise to the concept of *topological quantum computation* [44, 45], which greatly motivates the endeavour to investigate topological superconductors and Majoranas.

Practically, at least $4M$ Majoranas are required to construct M logical qubits. Adiabatically braiding Majoranas can produce some gate operations. However, braiding Majoranas in terms of F, R matrices cannot span the whole SU(2) group, required for universal quantum computation. In spite of this, quantum computation with Majoranas is still worth pursuing since at least some of the gate operations are topologically protected. Moreover, it has been shown that the addition of a phase gate implemented by dynamical operations is able to realize universal quantum computation [49, 50].

1.5 Experimental Realization

In order to realize topological quantum computation, realizing topological superconductors and Majoranas is the first step. Although Sec. 1.3 introduced several theoretical models which host Majoranas, these models are difficult to realize in the laboratory. This is mainly because in reality electrons do have spin, and most superconductors have s-wave rather than p-wave pairing. Moreover, for 1D superconductor, the order parameter strongly fluctuates which invalidates the applicability of BCS mean field theory.

After the breakthrough made by Fu and Kane [51, 52], it became clear that topological superconductor can be realized experimentally if we combine the following three ingredients [11]:

- proximity coupling to an s-wave superconductor
- spin-polarization
- spin-orbit coupling.

Rather than searching for a topological superconductor directly, we can employ a lower dimensional (1D or 2D) normal system and couple it to a conventional s-wave superconductor. Since the s-wave superconductor used for proximity-induced superconductivity is always two or three dimensional, the resulting p-wave order parameter does not strongly fluctuate and BCS mean field theory can be safely applied. For strong spin-polarization, the spin-up and spin-down electrons are essentially decoupled. If the Fermi surface of the system crosses only one of the spin-split bands, the system behaves similar to a spinless system. Finally, with spin-orbit coupling, electron spin is not a good quantum number, and the proximity induced pairing is not fully between electrons of opposite spin. Thus, a p-wave pairing potential is generated and we obtain a p-wave superconductor.

In fact, the way of putting these three pieces together is quite flexible. For example, the spin polarization can come either from an external magnetic field or from intrinsic magnetic order. Another ingredient, spin-orbit coupling, can either come from the bulk superconductor or the lower dimensional normal system.

In the following, we will briefly review three platforms for hosting Majoranas, which have been or are likely to be realized experimentally.

1.5.1 Quantum Spin Hall Insulator Edge

The first proposed physical platform for a 1D topological superconductor is based on the edge of a quantum spin Hall insulator, proximity coupled to an s-wave superconductor as proposed by Fu and Kane [52]. Let us assume that the Fermi energy lies within the gap of the quantum spin Hall insulator, so that only the helical edge states are electronically active. If we focus on a single edge, which is well separated from other edges, the spin is fully and oppositely polarized for the two propagation directions. To gap out these modes, one can either introduce superconducting pairing from an s-wave superconductor or an external magnetic field perpendicular to the direction of the spin polarization. We will show that Majorana zero modes appear at domain walls between these two gapped regions.

The first-quantized BdG Hamiltonian for the proximity-coupled quantum spin Hall insulator edge at zero chemical potential (for simplicity) can be written as

$$\mathcal{H} = v_F p \sigma_x \tau_z - B\sigma_z + \Delta\tau_x, \quad B, \Delta \in \mathbb{R}, \tag{1.104}$$

with σ_i, τ_j denoting Pauli matrices in spin and Nambu space, respectively. The Nambu basis is $(\psi_\uparrow, \psi_\downarrow, \psi_\downarrow^\dagger, -\psi_\uparrow^\dagger)$.

If we apply a unitary transformation $\mathcal{H} \to U\mathcal{H}U^\dagger$, with $U = \exp(-i\pi\tau_y/4)$, we have

$$\mathcal{H} = v_F p \sigma_x \tau_x - B\sigma_z - \Delta\tau_z, \tag{1.105}$$

which decouples into two 2×2 Hamiltonian as $\mathcal{H} = \mathcal{H}_1 \oplus \mathcal{H}_2$ with

$$\mathcal{H}_1 = -(B + \Delta)\rho_{1,z} + v_F p \rho_{1,x} \tag{1.106}$$

$$\mathcal{H}_2 = (B - \Delta)\rho_{2,z} + v_F p \rho_{2,x}. \tag{1.107}$$

Here $\rho_{a,j}$ $(a = 1, 2, j = x, y, z)$ are the Pauli matrices in the effective two dimensional space for $\mathcal{H}_1$ and $\mathcal{H}_2$.

We notice that $\mathcal{H}_1$ and $\mathcal{H}_2$ are essentially the same as the Hamiltonian in Eq. (1.36) for a spinless p-wave superconductor with a very large electron mass $m \to \infty$, chemical potential $(\Delta \pm B)$, and pairing amplitude v_F. If we consider a domain wall between two regions with $|B| > |\Delta|$ and $|B| < |\Delta|$, then either $(\Delta + B)$ or $(\Delta - B)$ changes sign at the domain wall. From our knowledge of spinless p-wave superconductor, we conclude that a Majorana zero mode is created at this domain wall.

Before ending this part of the discussion, it is worth mentioning two points. First, a 2D topological superconductor can also be constructed along these lines. Instead of using the edge of a quantum spin Hall insulator, a 2D topological insulator, one can use the surface of a 3D topological insulator with a single protected Dirac cone, proximity coupled to an s-wave superconductor. At the interface, we obtain a 2D topological superconductor. Second, in engineering 1D topological superconductors using quantum spin Hall insulator edges, we only used the helical property of the edge, rather than any other topological property of the insulator. This is indeed true and one can use a semiconductor quantum wire with intrinsic Rashba spin-orbit coupling to achieve the same goal, as will be shown in the following.

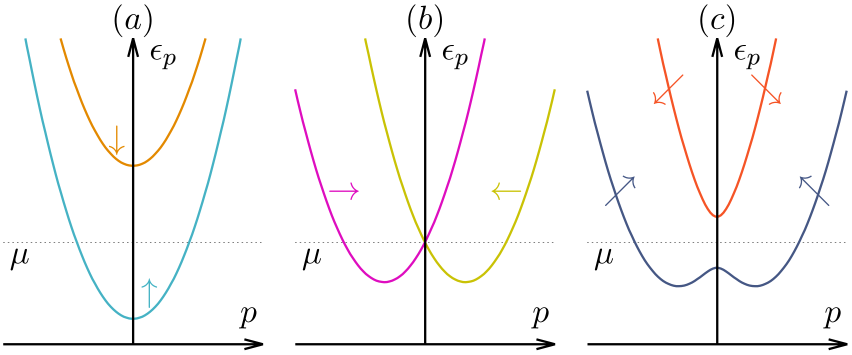

Figure 1.2: Normal-state dispersions of the quantum wire in (a) the Kitaev limit, (b) the topological insulator limit without Zeeman field, and (c) the topological insulator limit with Zeeman field.

1.5.2 Quantum Wires

Instead of using edges of quantum spin Hall insulators, one can build topological superconductors out of semiconductor quantum wires with strong spin-orbit coupling [53, 54], e.g., InAs or InSb wires. Strong spin-orbit coupling and an applied magnetic field essentially turn the wire into a helical liquid when appropriately tuning the Fermi energy. Proximity coupling to an s-wave superconductor realizes a 1D topological superconductor with Majorana zero modes at its ends.

Let us consider a single-channel quantum wire with Rashba spin-orbit coupling of strength u, an external magnetic field B, proxmity coupling to an s-wave superconductor which induces a pairing potential Δ. The first quantized Hamiltonian of this system can be written as

$$\mathcal{H} = \left(\frac{p^2}{2m} + up\sigma_x - \mu\right)\tau_z - B\sigma_z + \Delta\tau_x \tag{1.108}$$

where σ_i, τ_j denote Pauli matrices in spin and Nambu space and m is the electron mass. Instead of presenting results for generic parameters, we will focus on two limiting cases: the Kitaev limit when magnetic field is much larger than spin-orbit coupling ($B \gg mu^2$), and the topological insulator limit when spin-orbit coupling is much larger than magnetic field ($mu^2 \gg B$). For the normal state, the dispersions for the Hamiltonian in the two limits are shown in Figure 1.2. We assume weak pairing $\Delta \ll mu^2, B$.

Kitaev Limit

Let us first look at the situation where $B \gg mu^2$. In this case, we can first neglect spin-orbit coupling and superconducting pairing, and obtain two spin-polarized bands with dispersions

$$\epsilon_\pm(p) = \frac{p^2}{2m} \pm B, \tag{1.109}$$

as shown in Figure 1.2(a). The chemical potential μ can be tuned such that it crosses one of the spin-polarized bands, say the spin-up band. The eigenvectors for spin up electrons and holes can be written as

$$|e\rangle = (1,0,0,0)^T, \quad |h\rangle = (0,0,0,1)^T \tag{1.110}$$

in the Nambu basis $(\psi_\uparrow, \psi_\downarrow, \psi_\downarrow^\dagger, -\psi_\uparrow^\dagger)$. We can see that there is no superconducting correlation between these two states since $\langle e| \Delta\tau_x |h\rangle = 0$.

Now we include spin-orbit coupling as a perturbation. Using first-order perturbation theory, the spin is slightly tilted and the eigenvectors become

$$|e\rangle = \frac{1}{\sqrt{1+u^2p^2/4B^2}}(1, -up/2B, 0, 0)^T, \quad |h\rangle = \frac{1}{\sqrt{1+u^2p^2/4B^2}}(0, 0, -up/2B, 1)^T. \tag{1.111}$$

This generates a p-wave pairing potential through the matrix elements

$$\langle e| \Delta\tau_x |h\rangle = \langle h| \Delta\tau_x |e\rangle = -\frac{up}{B}\Delta. \tag{1.112}$$

Projecting onto the two-dimensional subspace spanned by $|e\rangle$ and $|h\rangle$, we find the effective Hamiltonian

$$\mathcal{H}_{\text{effective}} = \left(\frac{p^2}{2m} - (\mu - B)\right)\rho_z - \frac{up}{B}\Delta\tau_x. \tag{1.113}$$

Hence, we recover the Hamiltonian for a 1D spinless p-wave superconductor with pairing strength $\Delta u/B$.

Topological Insulator Limit

Now let us look at the other limit where $mu^2 \gg B$. Moreover, we choose $\mu = 0$ for simplicity. Without magnetic field and superconductivity, the dispersion consists of horizontally split parabolas as shown in Figure 1.2(b). We see that the bands cross the Fermi surface for the three momenta $p \simeq 0, \pm p_F$ with $p_F = mu$.

Since spin-orbit coupling is large, the low-energy physics near $p = 0$ is decoupled from the low-energy physics near $p = \pm p_F$, and thus we can look at these two regions in momentum space separately.

If we linearize the spectra around $p = 0$, include superconductivity, and apply a magnetic field perpendicular to the direction of the spin-orbit coupling, we obtain the Hamiltonian

$$\mathcal{H}_{p=0} = up\sigma_x\tau_z - B\sigma_z + \Delta\tau_x, \tag{1.114}$$

which has the same form as the one for the 2D topological insulator edge. Depending on the strength of Δ and B, two different types of gaps can open around $p = 0$.

Moreover, a superconducting gap opens at $p = \pm p_F$ which essentially gives rise to a separate 1D p-wave superconductor. Because of the $\mathbb{Z}_2$ nature of Majoranas (for class D in 1D), the total Hamiltonian is a topological superconductor only when $\mathcal{H}_{p=0}$ is trivial. Hence, we need the gap around $p = 0$ to be due to the magnetic field B to realize the topological phase.

We conclude that in the topological insulator limit, the phase diagram for the quantum wire is the reverse of the phase diagram for a 2D topological insulator.

1.5.3 Magnetic Adatom Chains

Another platform for realizing Majoranas is based on magnetic adatoms on s-wave superconductors [55, 56]. This platform has the advantage that one can use scanning tunneling microscopy (STM) to manipulate the adatoms and to detect the Majoranas [57, 7].

For a single magnetic impurity in an s-wave superconductor, a subgap bound state with full spin-polarization, known as a Shiba state [58, 59], is formed. If we have a chain of magnetic adatoms on top of an s-wave superconductor, the low-energy physics can be described by a chain of Shiba states, which form a 1D subgap band. Each Shiba state overlaps with its neighbors just like ordinary atomic states. If the chain is ferromagnetically ordered (which is possible since the interaction is long-range and there is an underlying substrate to stablize the order), we obtain a spin-polarized band just as in the other two platforms.

If the superconductor has strong spin-orbit coupling, as it does for Pb [57, 7], then we have all ingredients for creating a topological superconductor and Majoranas should appear at the ends of the chain.

We will look at this platform in great detail in Chapter 2.

1.6 Open Problems and Outline of the Thesis

Over the last few years, the field of topological superconductors and Majoranas was advancing very rapidly, both theoretically and experimentally. Several experiments have claimed to observe Majoranas in quantum wires [60, 61, 62, 63] and in magnetic adatom chains [57, 7, 64, 65].

Despite these promising results, there remained and remains doubt in interpreting the experimental data as signatures of Majoranas. For example, the localization length of the end states observed in Ref. [57] was far too small compared to a simple theoretical estimation based on Majoranas. To solve this puzzle, the proximity effect needs to be treated more carefully, beyond just introducing the pairing potential into the Hamiltonian by hand as we did in the last section. This problem will be properly treated in Chapter 2 of this thesis.

To detect Majoranas, most experiments took the approach of quantum transport, by measuring conductance at a given voltage bias. It was shown theoretically that tunneling from a normal metal lead into a Majorana mode gives rise to a prominent zero-bias conductance peak, with a quantized value $2e^2/h$ [66, 67]. However, this result is valid only at zero temperature. At finite temperature, two issues appear [11]. First, temperature broadening of the distribution function limits the energy resolution. Second, the zero-bias Majorana peak is also broadened by inelastic quasiparticle excitations. Presumably for these reasons, Majorana experiments consistently show non-quantized peaks. To solve this issue, we propose to use a superconducting lead to probe the Majorana zero mode. One advantage of this setup is that the gap exponentially suppresses finite-temperature broadening. The signatures of probing Majoranas with superconducting leads will be worked out in Chapter 3.

It is worth mentioning that in parallel to the above two projects, there are several related works done in collaboration with the experimentalists in the group of K. Franke, which are also part of the PhD research. In Ref. [5], we studied the tunneling processes from a superconducting STM tip into subgap states in superconductors. In Ref. [7], we investigated the end states in a magnetic adatom chain made of Fe on a Pb superconductor. In Ref. [10], we looked at the subgap states created by a magnetic adatom on a superconductor and analyzed its spatial pattern.

Another celebrated signature of topological superconductivity is the 4π-periodic fractional Josephson effect [43]. However, experimental observation of the fractional Josephson effect requires the local fermion parity to be conserved. In practice, this condition is difficult to fulfill, since various quasiparticle poisoning processes lead to changes of the fermion parity. Hence, experiments need to be done in a sufficiently short time to avoid fermion parity switching. On the other hand, the phase difference across the two superconductors needs to be changed slowly enough to avoid nonadiabatic transitions. It is this conflict that makes this simple effect difficult to observe in the laboratory. In Chapter 4, I will propose a way of detecting the topological Josephson effect without the restriction of fermion parity conservation.

More recently, there are experiments [68, 69] on quantum spin Hall Josephson junctions without external magnetic field, where evidence for a 4π-periodic Josephson effect is found. However, this 4π-periodic Josephson is only expected by basic theory when a magnetic field is introduced between the two superconducting regions, as discussed in Sec. 1.5.1. This puzzle motivates the research reported in Chapter 5. We provide a way to generate a yet more exotic 8π-periodic Josephson effect in a time-reversal invariant quantum spin Hall Josephson junction, which can be interpreted as a result of coupling $\mathbb{Z}_4$ parafermions, and which may appear in experiment as a 4π-periodic Josephson effect.

Finally, conclusions will be presented in Chapter 6.

2 Strong Localization of Majorana End States in Chains of Magnetic Adatoms

Recently, Yazdani's lab in Princeton realized an intriguing Majorana platform by placing a ferromagnetically aligned Fe adatom chain on top of a superconducting Pb substrate [57]. The STM measurements, providing both energetic and spatial resolution, showed zero-energy bound states at the ends of the chain which were identified as Majoranas. It was initially a major puzzle why the localization length of these bound states was shorter than the coherence length of Pb by two orders of magnitude, although the latter was expected to be a rough estimate of the Majorana localization length. To unravel this puzzle, I looked at the superconducting proximity effect more closely, and showed that one can indeed have strongly localized Majoranas in proximity coupled systems. My key insight was that for strong coupling between normal and superconducting system, the coherence length of proximity-induced superconductivity can differ dramatically from the coherence length of the proximity-providing superconductor, which is the result of a strong velocity renormalization. The strong localization of the Majoranas may be useful in future quantum computation as braiding requires the distance between Majoranas to be larger than their localization lengths.

Strong Localization of Majorana End States in Chains of Magnetic Adatoms

Yang Peng,[1] Falko Pientka,[1] Leonid I. Glazman,[2] and Felix von Oppen[1]
[1]*Dahlem Center for Complex Quantum Systems and Fachbereich Physik, Freie Universität Berlin, 14195 Berlin, Germany*
[2]*Department of Physics, Yale University, New Haven, Connecticut 06520, USA*

(Received 10 December 2014; published 9 March 2015)

A recent experiment [Nadj-Perge *et al*, Science 346, 602 (2014)] gives possible evidence for Majorana bound states in chains of magnetic adatoms placed on a superconductor. While many features of the observed end states are naturally interpreted in terms of Majorana states, their strong localization remained puzzling. We consider a linear chain of Anderson impurities on a superconductor as a minimal model and treat it largely analytically within mean-field theory. We explore the phase diagram, the subgap excitation spectrum, and the Majorana wave functions. Owing to a strong velocity renormalization, the latter are localized on a scale which is parametrically small compared to the coherence length of the host superconductor.

DOI: 10.1103/PhysRevLett.114.106801 PACS numbers: 73.63.Nm, 74.20.-z, 75.70.Tj, 75.75.-c

Introduction.—There is currently great interest in Majorana bound states in condensed-matter systems which realize non-Abelian quantum statistics [1,2] and which may have applications in topological quantum information processing [3]. Several platforms allow one to engineer topological superconducting phases supporting Majorana bound states, based on proximity coupling to s-wave superconductors (SCs). These include topological insulators [4,5], semiconductor quantum wires [6–8], and chains of magnetic adatoms [9–14] (see also Refs. [15–17]). All of these proposals are being actively pursued in the laboratory [18–26].

A recent experiment [26] exhibits signatures of Majorana bound states in chains of Fe atoms placed on a Pb surface. The experiment suggests that the Fe chain orders ferromagnetically. The subgap spectrum is probed by scanning tunneling spectroscopy with both spatial and spectral resolution, which shows zero-energy states near the ends of the chains. It is tempting to interpret these as Majorana bound states [26,27], as the system combines the three essential ingredients: (i) Proximity-induced superconductivity, (ii) a finite Zeeman splitting due to the exchange field of the ferromagnetic Fe chains, and (iii) Rashba spin-orbit (SO) coupling (presumably from the surface of the Pb substrate).

However, the observed localization of the end states on the scale of a few adatom sites is puzzling [28,29]. The Majorana localization length is typically estimated as $\xi_M = \hbar v_F/\Delta_{\rm top}$, while the coherence length ξ_0 of the proximity-providing SC is given by $\xi_0 = \hbar v_F/\Delta$. Here, we assume comparable Fermi velocities v_F in the one-dimensional electron system ("wire") and the host SC. At the same time, the induced topological gap $\Delta_{\rm top}$ is smaller than the host gap Δ. Thus, one may expect $\xi_M \gtrsim \xi_0$. This contrasts with the observation that the localization length of the end states is orders of magnitude smaller than the coherence length of Pb. Here we address this puzzle by modeling the adatoms as a chain of Anderson impurities hybridized with a SC and show that it predicts Majorana localization lengths which are parametrically smaller than ξ_0 over wide regions of parameter space.

The physics underlying the topological phase in chains of magnetic adatoms has been discussed using two approaches. One approach [9,10,30–33] starts with the subgap Shiba states [34–37] induced by the individual magnetic adatoms. The adatom is described as a classical magnetic moment which is exchange coupled to the electrons in the substrate, but otherwise electronically inert. Such Shiba chains exhibit topological superconducting phases and hence Majorana end states. An alternative approach [26,27] starts with exchange-split adatom states. While they are far from the Fermi energy for individual adatoms, hopping between the adatoms of the chain broadens these states into bands. For sufficiently strong hopping, these bands cross the Fermi energy and effectively realize a one-dimensional spin-polarized electron system. In this band limit, topological superconductivity is induced by proximity, in combination with SO coupling for ferromagnetic chains or helical magnetic order along the chain. As an additional benefit, our model unifies both of these approaches.

Heuristic considerations.—We start by discussing conventional proximity coupling of a free-electron wire to a bulk s-wave SC. The wire electrons are described by their Green function $G(k,E) = [E - v_F k\tau_z - \Sigma(k,E)]^{-1}$, where τ_i denote Pauli matrices in particle-hole space. The self-energy Σ accounts for the coupling to the SC and takes the familiar form [38,39]

$$\Sigma(k,E) = -\Gamma \frac{E + \Delta\tau_x}{\sqrt{\Delta^2 - E^2}}. \tag{1}$$

Here, Γ measures the strength of hybridization between wire and SC. Far above the gap, $E \gg \Delta$, the SC behaves as a normal metal and the escape of electrons into the bulk SC is described by $\Sigma \simeq i\Gamma$. For subgap energies, electrons enter the SC only virtually and Σ becomes real.

0031-9007/15/114(10)/106801(5)

For definiteness, consider energies far below the bulk gap, $E \ll \Delta$. Then, we can approximate $\Sigma \simeq -(\Gamma/\Delta)E - \Gamma\tau_x$, and $G(k,E) \simeq Z[E - Zv_F k\tau_z - Z\Gamma\tau_x]^{-1}$ with a renormalized quasiparticle weight $Z = [1 + \Gamma/\Delta]^{-1}$, which describes the shift of the electrons' spectral weight from the wire into the SC. The quasiparticle weight ensures [1] that the induced s-wave gap (described by the pairing term $\propto \tau_x$) interpolates between the hybridization strength Γ at weak hybridization, $\Gamma \ll \Delta$, and the host gap Δ at strong hybridization, $\Gamma \gg \Delta$. It also renormalizes the Fermi velocity $v_F \to \tilde{v}_F = Zv_F$ which controls the coherence length of the induced superconductivity in the wire. Physically, the fraction of time an excitation spends in the wire is suppressed by Z, which reduces the effective velocity to Zv_F.

In adatom chains, the SO coupling in the SC allows for an induced p-wave pairing while the strong on-site repulsion and resulting spin polarization suppress s-wave correlations. Thus, the induced gap $\Delta_{\mathrm{top}} = \alpha\Delta$ is now p wave and controlled by the (dimensionless) SO strength α. At the same time, it is natural to assume that the hybridization Γ modifies *single-particle* properties as before and the renormalization of v_F remains operative. This predicts a Majorana localization length

$$\xi_M = \hbar\tilde{v}_F/\Delta_{\mathrm{top}} = Z\hbar v_F/\Delta_{\mathrm{top}}. \tag{2}$$

For Fe adatoms in Pb, the hybridization is controlled by atomic scales so that $\Gamma \sim 1$ eV [26]. When compared to the host gap $\Delta \sim 10$ K, we find $Z \sim 10^{-3}$. This can dramatically suppress ξ_M relative to the host coherence length $\xi_0 \sim \hbar v_F/\Delta$ ($\simeq$100 nm for Pb). In fact, $\xi_M \sim \xi_0(\Delta/\Gamma)(\Delta/\Delta_{\mathrm{top}})$, so that for $\alpha = \Delta_{\mathrm{top}}/\Delta \sim 0.1$, the Majorana localization length ξ_M becomes of the order of the spacing between adatoms, as observed in Ref. [26].

Model.—We now show that these heuristic arguments are borne out in a microsopic model. We model the system as a linear chain of Anderson impurities placed in an s-wave SC. Each adatom hosts a spin-degenerate level of energy ϵ_d with on-site Hubbard repulsion U, representing the Fe d levels. We include nearest-neighbor hopping of strength w between these d levels as well as hybridization of strength t between the d levels and the SC. The model Hamiltonian

$$\mathcal{H} = \mathcal{H}_d + \mathcal{H}_s + \mathcal{H}_T \tag{3}$$

contains the BCS Hamiltonian $\mathcal{H}_s$ of the SC [40], the chain of d levels

$$\begin{aligned}\mathcal{H}_d = &\sum_{j,\sigma}(\epsilon_d - \mu)d^\dagger_{j,\sigma}d_{j,\sigma} + U\sum_j n^\dagger_{j\uparrow}n_{j\downarrow}\\ &- w\sum_{j,\sigma}[d^\dagger_{j+1,\sigma}d_{j,\sigma} + d^\dagger_{j,\sigma}d_{j+1,\sigma}],\end{aligned} \tag{4}$$

and their hybridization with the SC,

$$\mathcal{H}_T = -t\sum_{j,\sigma}[\psi^\dagger_\sigma(\mathbf{R}_j)d_{j,\sigma} + d^\dagger_{j,\sigma}\psi_\sigma(\mathbf{R}_j)]. \tag{5}$$

Here, $d_{j,\sigma}$ annihilates a spin-σ electron in the d level at site $\mathbf{R}_j = ja\hat{\mathbf{x}}$ of the chain, $n_{j,\sigma} = d^\dagger_{j,\sigma}d_{j,\sigma}$, and $\psi_\sigma(\mathbf{r})$ annihilates electrons at position $\mathbf{r}$ (taken as continuous) in the SC.

The model in Eq. (3) generalizes the Shiba chain model considered in Refs. [9,10]. It reduces to the Shiba chain in the limit of negligible spin fluctuations and weak intersite hopping w. Here, we include the hopping and the ensuing electronic dynamics of the magnetic adatoms within a mean-field treatment of the Hubbard term [41,42],

$$Un^\dagger_{j\uparrow}n_{j\downarrow} \to \frac{U}{2}\sum_\sigma[\langle n_j\rangle n_{j,\sigma} + \langle m_j\rangle\sigma n_{j,\sigma}], \tag{6}$$

where we defined the occupation $n_j = \sum_\sigma n_{j,\sigma}$ and the site polarization $m_j = n_{j,\uparrow} - n_{j,\downarrow}$. The first term merely renormalizes ϵ_d and will be absorbed in the following. The second term introduces a local exchange coupling in the adatom orbitals.

As we are predominantly interested in the localization of the Majorana modes, we do not aim at a self-consistent solution of the mean-field theory. Instead, we accept the formation of a spontaneous moment as experimental fact and explore its consequences. In the experiment, the moments order ferromagnetically along the chain. In this case, topological superconductivity requires Rashba SO coupling in the substrate SC [26,27,43,44]. For analytical tractability, we assume instead that the moments develop helical order $\mathbf{S}_j = (\sin\theta\cos\phi_j, \sin\theta\sin\phi_j, \cos\theta)$ with $\phi_j = 2k_h ja$ and $\theta = \pi/2$. We emphasize that the model with helical order can be mapped to a ferromagnetic model with SO coupling in both the adatom d band and the substrate SC. Strictly speaking, the substrate SO coupling generated by the mapping differs from conventional Rashba coupling, but it does include the specific term that allows for proximity-induced p-wave pairing. The mapping is effected by the unitary transformation $d_j \to e^{-ik_h ja\sigma_z}d_j$ and $\psi(\mathbf{r}) \to e^{-ik_h x\sigma_z}\psi(\mathbf{r})$, which rotates the spin basis along the direction of the local impurity moments [45,46].

Excitation spectrum and phase diagram.—In mean-field theory, we can describe the system equivalently by the corresponding Bogoliubov–de Gennes Hamiltonian $H = H_d + H_s + H_T$ (after the above-mentioned unitary transformation) and consider the Green function $G = (E - H)^{-1}$. In view of the local nature of the hybridization H_T, we can write a closed set of equations for the restricted Green function $g_{ij} = G(\mathbf{R}_i, \mathbf{R}_j)$ defined at the sites of the adatoms,

$$\begin{pmatrix} (g_0^{\mathrm{ss}})^{-1} & t\tau_z \\ t\tau_z & E - H_d \end{pmatrix} g = 1. \tag{7}$$

We use the Pauli matrices τ_i (σ_i) in particle-hole (spin) space. The bare Green function of the SC restricted to the adatom sites and subgap energies is readily obtained within BCS theory (see Ref. [46] for more details),

$$g^{\rm ss}_{0,ij}(E) = -\pi\nu_0 \exp(-ik_h x_{ij}\sigma_z) \times \left\{\frac{E+\Delta\tau_x}{\sqrt{\Delta^2-E^2}}\mathrm{Im}f(r_{ij}) + \tau_z\mathrm{Re}f(r_{ij})\right\}, \qquad (8)$$

where ν_0 is the normal density of state at the Fermi level, $f(r) = e^{ik_F r - r/\xi_E}/k_F r$, and $\xi_E = \hbar v_F/\sqrt{\Delta^2-E^2}$. Equation (8) is valid for $i \neq j$, but also applies to $i = j$ when dropping the $\mathrm{Re}f$ term. Here, the factor $\exp(-ik_h x_{ij}\sigma_z)$ is induced by the unitary transformation.

The subgap excitation spectrum may then be obtained from the poles of $g^{\rm ss} = g^{\rm ss}_0[1-\Sigma g^{\rm ss}_0]^{-1}$ where we define the self-energy $\Sigma = t g^{\rm dd}_0 t = t(E-H_d)^{-1}t$. As $g^{\rm ss}_0$ has no poles at subgap energies, this yields the condition $\det[1-\Sigma g^{\rm ss}_0] = 0$. In (lattice) momentum representation, the determinant involves a 4×4 matrix with [46]

$$g^{\rm ss}_0(k,E) = \pi\nu_0\left\{\frac{E+\Delta\tau_x}{\sqrt{\Delta^2-E^2}}L^{\sigma_z}_i(k,E) + \tau_z L^{\sigma_z}_r(k,E)\right\}. \qquad (9)$$

Here, $L^{\sigma_z}_r$ and $L^{\sigma_z}_i$ are real and imaginary parts of the function $L^{\sigma_z} = F(k+k_h\sigma_z) - i$, respectively, with $F(k) = (1/k_F a)\ln\{1-e^{i(k_F+k)a-a/\xi_E}\} + (k \leftrightarrow -k)$ [48]. Computing the dispersions and identifying phase boundaries by the closing of the gap, we first obtain representative phase diagrams of the adatom chain, as shown in Fig. 1.

These phase diagrams plot the topological (BDI [49]) index and make the interpolation between the band and Shiba limits explicit. The Shiba limit corresponds to weak hopping w between d levels. Here, topological superconductivity requires deep Shiba states so that the Shiba bands cross the chemical potential at the center of the host gap [10]. The band limit corresponds to weak hybridization $\Gamma = \pi\nu_0 t^2$ and thus Shiba states with energies E_s near Δ [42,46]. Then, topological superconductivity requires that one spin-polarized d band crosses the Fermi energy. The range over which this happens depends on the asymmetry of the bare exchange-split adatom states $E_{d,\sigma} = \epsilon_d - \sigma U\langle m\rangle/2$ around the chemical potential (set to $\mu = 0$). Figure 1(a) shows the symmetric case $E_{d,\uparrow} = -E_{d,\downarrow}$. There is only a narrow topological interval in w for small Γ ($E_s \simeq \Delta$) because despite the large exchange splitting of the d levels, the spin-split d bands cross μ at the same hopping strength w. As the asymmetry between $E_{d,\uparrow}$ and $E_{d,\downarrow}$ around μ increases, the d bands cross μ at different values of w, and the adatom states are perfectly spin polarized at the chemical potential over a substantial region in w; cf. Fig. 1(b).

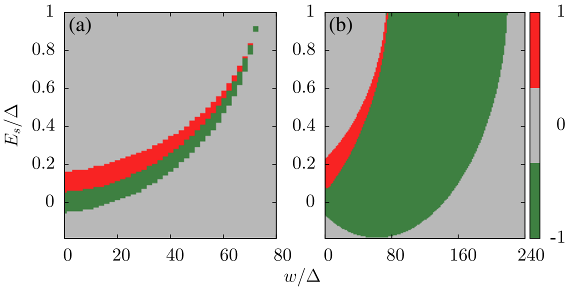

FIG. 1 (color online). Representative phase diagrams for the adatom chain as a function of the Shiba state energy E_s of an individual impurity and the hopping amplitude w between d levels. The colors indicate the topological index (grey: topologically trivial; red or green: topological phase with index ± 1). We chose $E_{d,\downarrow} = 100\Delta$, $k_F a = 4.3\pi$, $k_h a = 0.26\pi$, and $\xi_0/a = \infty$. The panels correspond to (a) symmetric adatom d bands ($E_{d,\uparrow} = -100\Delta$) and (b) asymmetric adatom d bands ($E_{d,\uparrow} = -300\Delta$). Here, $E_{d,\sigma} = \epsilon_d - \sigma U\langle m\rangle/2$.

For fully analytical results, we consider the limit of strong asymmetry with $E_{d,\uparrow} \to -\infty$ at a fixed $E_{d,\downarrow}$. In this limit, only the spin-down band $E_d = E_{d,\downarrow} - w\sum_{\pm}\cos(k \pm k_h)a$ of the d levels is relevant. A detailed but straightforward calculation [46] now shows that the condition $\det(1-\Sigma g^{\rm ss}_0) = 0$ can be reduced to the determinant of a 2×2 matrix and written in the form

$$(\Delta^2-E^2)[E_d+\Gamma L_r]^2 - E^2\left[\sqrt{\Delta^2-E^2} - \Gamma L_i\right]^2 + \Gamma^2\Delta^2(\delta L_i)^2 = 0. \qquad (10)$$

Here, we introduced the shorthand notations $L_{r/i} = (L^+_{r/i} + L^-_{r,i})/2$ and $\delta L_i = (L^+_i - L^-_i)/2$. Equation (10) is an implicit equation for the subgap excitation spectrum E_k of the adatom chain in the strongly asymmetric limit. [Note that we have suppressed all k labels in Eq. (10).]

In the limits $\Gamma \ll \Delta$ and $\Gamma \gg \Delta$, Eq. (10) gives explicit analytical expressions for the excitation spectrum throughout the entire Brillouin zone. These are obtained by keeping only the respective dominant term in the second square brackets on the left-hand side, in excellent agreement with the full Green-function solution in Figs. 2(a)–2(c). We note that there is a single subgap state for every lattice momentum k; i.e., there is one subgap state per adatom, as in the Shiba limit (small w).

Majorana wave function.—Equation (10) also encapsulates the localization of the Majorana wave functions. In the Shiba limit of small w, the Majorana localization was addressed previously [50]. Here, we focus on the band limit of large w where the spin-down d band E_d crosses the Fermi energy of the SC, as is presumably the case in the experiment [26,27]. E_d crosses $\mu = 0$ at momenta k_0, so that $E_d \simeq v_F(k-k_0)$, where v_F is the Fermi velocity of the d band at the chemical potential of the SC. Similarly, $E_d + \Gamma L_r \simeq v_F(k-k_0)$, where we simply absorb the parametrically small shifts in v_F and k_0 due to ΓL_r into their definitions.

The decay of the Majorana wave function is controlled by the behavior of the dispersion near the minimal gap at k_0. Assuming that the pitch of the spin helix (or, equivalently, the strength of SO coupling) is not too large, this topological gap will be small compared to the gap Δ of the superconducting host. Then, E is small compared to Δ in the relevant region and Eq. (10) simplifies significantly. Consider first the limit of weak hybridization $\Gamma \ll \Delta$. In this limit, Eq. (10) reduces to

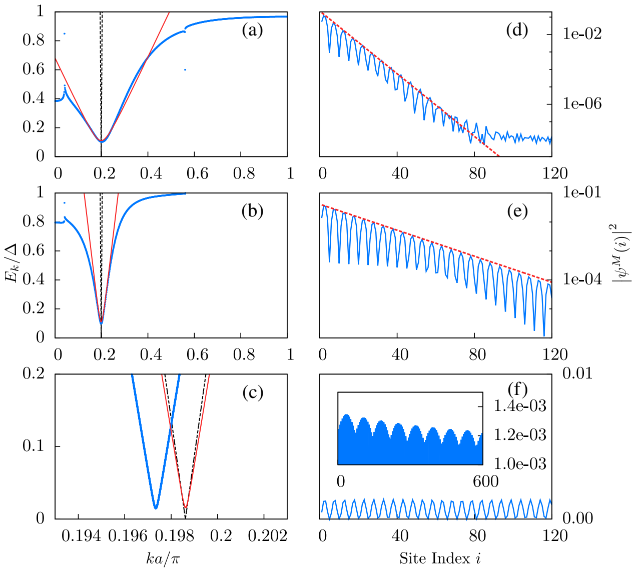

FIG. 2 (color online). Excitation spectra E_k for $ka/\pi \in [0,1]$ and (a) $\Gamma = 64\Delta$, (b) $\Gamma = 16\Delta$, and (c) $\Gamma = 0.16\Delta$. We choose $k_F a = 4.3\pi$, $k_h a = 0.26\pi$, $E_{d,\downarrow} = 100\Delta$, $E_{d,\uparrow} = -19900\Delta$, $w = 90\Delta$, and $\xi_0/a = \infty$. The dashed lines are subgap dispersions of the impurity chain without coupling to the SC. The blue curves are exact dispersions. The red curves are calculated using Eq. (12) for $\Gamma \gg \Delta$ and Eq. (11) for $\Gamma \ll \Delta$. Notice that the horizontal axis in (c) is restricted to a very narrow range and that the deviation between the red and blue curves is indeed small. Panels (d), (e), and (f) show Majorana wave functions $|\psi^M(i)|^2$ (blue lines) obtained for a finite chain of length $L = 1500a$. Only the first 120 sites i are shown. (d) and (e) are plotted on a logarithmic scale and the red dashed lines are fits using Eq. (2) for the Majorana localization length. (f) is plotted on a linear scale. (Inset) Decay over the first 600 sites.

$$E_k = \pm\sqrt{[v_F(k-k_0)]^2 + \Gamma^2(\delta L_i)^2}, \qquad (11)$$

where δL_i should be evaluated at k_0. We identify the topological gap $\Delta_{\rm top} = \Gamma(\delta L_i)_{k=k_0}$, which is small compared to Δ. The Majorana wave function is expected to decay on the characteristic length scale of this dispersion; i.e., we find the Majorana localization length $\xi_M = \hbar v_F/\Delta_{\rm top}$, consistent with the heuristic argument above for $\Gamma \ll \Delta$. For the numerical parameters of Fig. 2(c), ξ_M is larger than the length of the chain, making a direct comparison impossible.

The experiment is in the limit of the large hybridization $\Gamma \gg \Delta$, where Eq. (10) predicts a low-energy dispersion

$$E_k = \pm\sqrt{[(\Delta/\Gamma L_i)v_F(k-k_0)]^2 + [\Delta(\delta L_i/L_i)]^2}. \qquad (12)$$

In this limit, the induced gap $\Delta_{\rm top} = \Delta(\delta L_i/L_i)_{k=k_0}$ is independent of Γ and saturates to a value which is smaller than Δ by a factor measuring the effective strength of the SO coupling. The strong hybridization with the SC also induces a dramatic downward renormalization of the Fermi velocity of the excitations, $v_F \to \tilde{v}_F = (\Delta/\Gamma L_i)v_F$. These features are in excellent agreement with the numerical subgap spectra shown in Figs. 2(a) and 2(b) and vindicate our introductory heuristic arguments. Indeed, Eq. (12) predicts a Majorana localization length $\xi_M = \hbar v_F/(\Gamma\delta L_i)$, which coincides with Eq. (2) from heuristic consideration. We see that ξ_M is independent of the host gap Δ and controlled instead by the hybridization Γ. This result is in excellent agreement with numerical Majorana wave functions for $\Gamma \gg \Delta$; see Figs. 2(d) and 2(e).

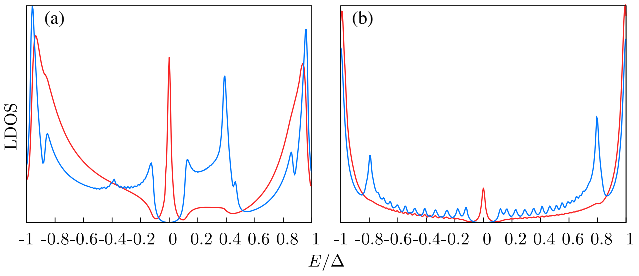

FIG. 3 (color online). Local density of states of particle excitations, computed in the center (blue lines) and at the end (red lines), for a chain of length $L = 300a$ and hybridizations (a) $\Gamma = 64\Delta$ and (b) $\Gamma = 16\Delta$. Other parameters are as in Fig. 2.

The topological gaps in Eqs. (11) and (12) are both enabled explicitly by the SO coupling in the substrate which enters via the L factors in $g_0^{\rm ss}$. In contrast, the SO coupling in the d band is fully ineffective due to the strong spin polarization. Parametrically, one finds $\delta L_i \simeq \delta L_i/L_i \simeq k_h/k_F$ in the limit $k_F a \gg 1$.

Notice that Eqs. (12) and (2) require the condition $\Gamma \ll v_F/a$. This condition ensures that the in-band propagation between adjacent sites, taking time $\tau \sim a/\tilde{v}_F$, is faster than hopping via the host SC, taking time $(\Delta L_r)^{-1}$ [10]. Then, the $k = k_0$ minimum described by Eq. (12) dominates over the additional features of the quasiparticle spectrum associated with logarithmic divergencies in L_r. They induce power-law tails in the Majorana wave functions [cf. Fig. 2(d)] which become correspondingly more pronounced as Γ increases.

Local density of states.—We have also numerically computed [46] the local density of states of the adatom chain; see Fig. 3. The zero-bias peak grows more pronounced with increasing Γ, reflecting the stronger localization of the Majorana wave function. In addition to the zero-energy Majorana peak, one discerns additional peaks at finite energies which arise from van Hove singularities in the subgap Shiba band and which approach the center of the gap as the hybridization Γ increases. The zero-energy features and their strong localization as well as the van Hove peaks are consistent with the experimental observations [26].

We thank Ali Yazdani, Andrei Bernevig, Titus Neupert, Piet Brouwer, and Allan MacDonald for the stimulating discussions. We acknowledge financial support from the Helmholtz Virtual Institute "New states of matter and their excitations," Grants No. SPP1285 and No. SPP1666 of the Deutsche Forschungsgemeinschaft, the Humboldt

Foundation, NSF DMR Grant No. 1206612, and ONR Grant No. Q00704. We are grateful to the Aspen Center for Physics, supported by NSF Grant No. PHYS-106629, for their hospitality while this line of work was initiated.

[1] J. Alicea, Rep. Prog. Phys. **75**, 076501 (2012).
[2] C. W. J. Beenakker, Annu. Rev. Condens. Matter Phys. **4**, 113 (2013).
[3] A. Kitaev, Ann. Phys. (Amsterdam) **303**, 2 (2003).
[4] L. Fu and C. L. Kane, Phys. Rev. Lett. **100**, 096407 (2008).
[5] L. Fu and C. L. Kane, Phys. Rev. B **79**, 161408(R) (2009).
[6] R. M. Lutchyn, J. D. Sau, and S. Das Sarma, Phys. Rev. Lett. **105**, 077001 (2010).
[7] Y. Oreg, G. Refael, and F. von Oppen, Phys. Rev. Lett. **105**, 177002 (2010).
[8] J. Alicea, Y. Oreg, G. Refael, F. von Oppen, and M. P. A. Fisher, Nat. Phys. **7**, 412 (2011).
[9] S. Nadj-Perge, I. K. Drozdov, B. A. Bernevig, and A. Yazdani, Phys. Rev. B **88**, 020407(R) (2013).
[10] F. Pientka, L. I. Glazman, and F. von Oppen, Phys. Rev. B **88**, 155420 (2013).
[11] Y. Kim, M. Cheng, B. Bauer, R. M. Lutchyn, and S. Das Sarma, Phys. Rev. B **90**, 060401(R) (2014).
[12] J. Klinovaja, P. Stano, A. Yazdani, and D. Loss, Phys. Rev. Lett. **111**, 186805 (2013).
[13] B. Braunecker and P. Simon, Phys. Rev. Lett. **111**, 147202 (2013).
[14] M. M. Vazifeh and M. Franz, Phys. Rev. Lett. **111**, 206802 (2013).
[15] T.-P. Choy, J. M. Edge, A. R. Akhmerov, and C. W. J. Beenakker, Phys. Rev. B **84**, 195442 (2011).
[16] M. Kjaergaard, K. Wölms, and K. Flensberg, Phys. Rev. B **85**, 020503 (2012).
[17] I. Martin and A. F. Morpurgo, Phys. Rev. B **85**, 144505 (2012).
[18] V. Mourik, K. Zuo, S. M. Frolov, S. R. Plissard, E. P. A. M. Bakkers, and L. P. Kouwenhoven, Science **336**, 1003 (2012).
[19] A. Das, Y. Ronen, Y. Most, Y. Oreg, M. Heiblum, and H. Shtrikman, Nat. Phys. **8**, 887 (2012).
[20] H. O. H. Churchill, V. Fatemi, K. Grove-Rasmussen, M. T. Deng, P. Caroff, H. Q. Xu, and C. M. Marcus, Phys. Rev. B **87**, 241401(R) (2013).
[21] L. P. Rokhinson, X. Liu, and J. K. Furdyna, Nat. Phys. **8**, 795 (2012).
[22] M. T. Deng, C. L. Yu, G. Y. Huang, M. Larsson, P. Caroff, and H. Q. Xu, Nano Lett. **12**, 6414 (2012).
[23] A. D. K. Finck, D. J. Van Harlingen, P. K. Mohseni, K. Jung, and X. Li, Phys. Rev. Lett. **110**, 126406 (2013).
[24] S. Hart, H. Ren, T. Wagner, P. Leubner, M. Mühlbauer, C. Brüne, H. Buhmann, L. W. Molenkamp, and A. Yacoby, Nat. Phys. **10**, 638 (2014).
[25] V. S. Pribiag, A. J. A. Beukman, F. Qu, M. C. Cassidy, C. Charpentier, W. Wegscheider, and L. P. Kouwenhoven, Edge-mode superconductivity in a two dimensional topological insulator, arXiv:1408.1701.
[26] S. Nadj-Perge, I. K. Drozdov, J. Li, H. Chen, S. Jeon, J. Seo, A. H. MacDonald, B. A. Bernevig, and A. Yazdani, Science **346**, 602 (2014).
[27] J. Li, H. Chen, I. K. Drozdov, A. Yazdani, B. A. Bernevig, and A. H. MacDonald, Phys. Rev. B **90**, 235433 (2014).
[28] E. Dumitrescu, B. Roberts, S. Tewari, J. D. Sau, and S. Das Sarma, Majorana fermions in chiral topological ferromagnetic nanowires, arXiv:1410.5412.
[29] P. A. Lee, commentary on Ref. [26], Journal Club for Condensed Matter Physics, http://www.condmatjournalclub.org/?m=201410.
[30] S. Nakosai, Y. Tanaka, and N. Nagaosa, Phys. Rev. B **88**, 180503(R) (2013).
[31] K. Pöyhönen, A. Westström, J. Röntynen, and T. Ojanen, Phys. Rev. B **89**, 115109 (2014).
[32] A. Heimes, P. Kotetes, and G. Schön, Phys. Rev. B **90**, 060507 (R) (2014); A. Heimes, D. Mendler, and P. Kotetes, Interplay of topological phases in magnetic adatom-chains on top of a Rashba superconducting surface, arXiv:1410.6367.
[33] P. M. R. Brydon, H. Y. Hui, and J. D. Sau, Topological Shiba chain from spin-orbit coupling, arXiv:1407.6345.
[34] L. Yu, Acta Phys. Sin. **21**, 75 (1965).
[35] H. Shiba, Prog. Theor. Phys. **40**, 435 (1968).
[36] A. I. Rusinov, Pis'ma Zh. Eksp. Teor. Fiz. **9**, 146 (1968) [JETP Lett. **9**, 85 (1969)].
[37] A. V. Balatsky, I. Vekhter, and J.-X. Zhu, Rev. Mod. Phys. **78**, 373 (2006).
[38] A. C. Potter and P. A. Lee, Phys. Rev. B **83**, 184520 (2011).
[39] A. A. Zyuzin, D. Rainis, J. Klinovaja, and D. Loss, Phys. Rev. Lett. **111**, 056802 (2013).
[40] We assume that the bulk gapΔ remains unaffected by the adatoms. While we expect that the renormalization of v_F as a single-particle quantity remains operative, studying self-consistent effects on Δ may be an interesting problem for future research [see I. Reis, D. J. J. Marchand, and M. Franz, Phys. Rev. B **90**, 085124 (2014)]; T. Meng, J. Klinovaja, S. Hoffman, P. Simon, and D. Loss, Superconducting gap renormalization around two magnetic impurities: From Shiba to Andreev bound states, arXiv:1501.07901.
[41] P. W. Anderson, Phys. Rev. **124**, 41 (1961).
[42] H. Shiba, Prog. Theor. Phys. **50**, 50 (1973).
[43] M. Duckheim and P. W. Brouwer, Phys. Rev. B **83**, 054513 (2011).
[44] S. B. Chung, H. J. Zhang, X. L. Qi, and S. C. Zhang, Phys. Rev. B **84**, 060510(R) (2011).
[45] B. Braunecker, G. I. Japaridze, J. Klinovaja, and D. Loss, Phys. Rev. B **82**, 045127 (2010).
[46] See Supplementary Material at http://link.aps.org/supplemental/10.1103/PhysRevLett.114.106801, which includes Ref. [47], for the unitary transformation of Hamiltonian of helical order, definition of the Shiba state energy, derivation of the lattice Green function, description of the numerics, derivation of Eq. (10) of main text and more discussions on the comparison with experiment.
[47] A. Fetter and D. Walecka, *Quantum Theory of Many Particle Systems* (McGraw-Hill, New York, 1971).
[48] The function L is plotted in Ref. [46]. Roughly, $L_i^{\sigma_z}$ (and hence L_i) is of order unity. $L_r^{\sigma_z}$ (and hence L_r) is of order $1/k_F a$, except at isolated values of k where it has logarithmic singularities. δL_i should be thought of as a dimensionless measure of the effective SO strength, which is also of order $1/k_F a$ for our spin-helix model.
[49] S. Ryu, A. P. Schnyder, A. Furusaki, and A. W. W. Ludwig, New J. Phys. **12**, 065010 (2010).
[50] F. Pientka, L. I. Glazman, and F. von Oppen, Phys. Rev. B **89**, 180505(R) (2014).

Supplementary material for "Strong localization of Majorana end states in chains of magnetic adatoms"

Yang Peng,[1] Falko Pientka,[1] Leonid I. Glazman,[2] and Felix von Oppen[1]
[1]*Dahlem Center for Complex Quantum Systems and Fachbereich Physik, Freie Universität Berlin, 14195 Berlin, Germany*
[2]*Department of Physics, Yale University, New Haven, CT 06520, USA*

I. UNITARY TRANSFORMATION OF HAMILTONIAN WITH HELICAL ORDER

The mean-field Hamiltonian for a chain of Anderson impurities coupled to an s-wave superconductor can be written as

$$\mathcal{H} = \mathcal{H}_s + \mathcal{H}_d + \mathcal{H}_T, \tag{1}$$

with

$$\mathcal{H}_d = \sum_{j,\sigma}(\epsilon_d - \mu)\tilde{d}^\dagger_{j,\sigma}\tilde{d}_{j,\sigma} - w\sum_{j,\sigma}\left(\tilde{d}^\dagger_{j,\sigma}\tilde{d}_{j+1,\sigma} + \tilde{d}^\dagger_{j+1,\sigma}\tilde{d}_{j,\sigma}\right) - K\sum_{j,\sigma,\sigma'}\mathbf{S}_j\tilde{d}^\dagger_{j,\sigma}\boldsymbol{\sigma}_{\sigma,\sigma'}\tilde{d}_{j,\sigma'}, \tag{2}$$

where the exchange term $K\,|\mathbf{S}_j| = U/2$ arises from a mean-field treatment of the local Hubbard interaction as described in the main text. Using the Nambu spinor notation $\tilde{d}_j = (\tilde{d}_{j\uparrow}, \tilde{d}_{j\downarrow}, \tilde{d}^\dagger_{j\downarrow}, -\tilde{d}^\dagger_{j\uparrow})^T$, we can write down its Bogoliubov-de Gennes Hamiltonian

$$\mathcal{H}_d = \frac{1}{2}\sum_{ij}\tilde{d}^\dagger_i\tilde{H}^{ij}_d\tilde{d}_j \tag{3}$$

$$\tilde{H}^{ij}_d = \left[(\epsilon_d - \mu)\tau_z - K\mathbf{S}_j\cdot\boldsymbol{\sigma}\right]\delta_{ij} - w\tau_z(\delta_{i,j-1} + \delta_{i,j+1}), \tag{4}$$

where the τ_i with $i = x, y, z$ are Pauli matrices in particle-hole space. The s-wave superconductor is modeled by the BCS Hamiltonian

$$\mathcal{H}_s = \frac{1}{2}\int d^3r\,\tilde{\psi}^\dagger(\mathbf{r})\tilde{H}_s\tilde{\psi}(\mathbf{r}) \tag{5}$$

$$\tilde{H}_s = \xi_{\mathbf{p}}\tau_z + \Delta\tau_x \tag{6}$$

$$\xi_{\mathbf{p}} = \frac{\mathbf{p}^2}{2m} - \mu, \tag{7}$$

where $\tilde{\psi}(\mathbf{r}) = (\tilde{\psi}_\uparrow(\mathbf{r}), \tilde{\psi}_\downarrow(\mathbf{r}), \tilde{\psi}^\dagger_\downarrow(\mathbf{r}), -\tilde{\psi}^\dagger_\uparrow(\mathbf{r}))^T$, and Δ is the superconducting order parameter. The hybridization between the magnetic adatoms and the superconductor in particle-hole space is given by

$$\mathcal{H}_T = -\frac{t}{2}\sum_j\left(\tilde{\psi}^\dagger(\mathbf{R}_j)\tau_z\tilde{d}_j + h.c.\right), \tag{8}$$

where $\mathbf{R}_j = ja\hat{\mathbf{x}}$ denotes the position of the jth magnetic adatom, t the hybridization strength, and a the lattice spacing along the chain (i.e., the x) direction.

We assume a spin helix configuration

$$\mathbf{S}_j = (\sin\theta_j\cos\phi_j, \sin\theta_j\sin\phi_j, \cos\theta_j) \tag{9}$$

with $\theta_j = \theta$ and $\phi_j = 2k_hja$, i.e., the spin rotates about the z-axis with wavevector $2k_h$ and opening angle θ. This is equivalent to a ferromagnetic configuration with a particular type of spin-orbit coupling via a unitary transformation. Explicitly, we transform $\psi(\mathbf{r}) = e^{ik_hx\sigma_z}\tilde{\psi}(\mathbf{r})$ and $d_j = e^{ik_hja\sigma_z}\tilde{d}_j$, which rotates the local spin quantization axis along the local direction of the magnetic moment, or equivalently, maps the system on a ferromagnetic configuration. For the superconductor, this yields

$$\mathcal{H}_s = \frac{1}{2}\int d^3r\psi^\dagger(\mathbf{r})H_s\psi(\mathbf{r}) \tag{10}$$

$$H_s = \left[\frac{(\mathbf{p} + k_h\sigma_z\hat{x})^2}{2m}\right]\tau_z + \Delta\tau_x. \tag{11}$$

The Hamiltonian for the chain of magnetic adatoms transforms into

$$\mathcal{H}_d = \frac{1}{2}\sum_{ij} d_i^\dagger H_d^{ij} d_j \tag{12}$$

$$H_d^{ij} = \left[(\epsilon_d - \mu)\delta_{ij} - W_{ij}\right]\tau_z - K\mathbf{S}\cdot\boldsymbol{\sigma}\delta_{ij} \tag{13}$$

with $W_{ij} = -we^{-ik_h a\sigma_z}$ if $i = j+1$, $W_{ij} = -we^{ik_h a\sigma_z}$ if $i = j-1$, and zero otherwise. Finally we have the hybridization term

$$\mathcal{H}_t = -\frac{t}{2}\sum_j \left(\psi^\dagger(\mathbf{R}_j)\tau_z d_j + h.c.\right), \tag{14}$$

which is invariant under this transformation.

We observe that in the transformed Hamiltonian, the helix wavevector plays the role of the strength of (a particular type of) spin-orbit coupling. There is spin-orbit coupling in both the wire and the superconductor. It can be seen from the results of the main text that it is predominantly the spin-orbit coupling in the superconductor that is operative in inducing a p-wave gap in the excitation spectrum. This is true as long as the exchange splitting of the d-bands is large compared to the effective spin-orbit strength.

The angle between the exchange splitting and the spin-orbit field depends on the opening angle θ of the spin helix. The optimal situation for topological superconductivity is when exchange splitting and spin-orbit field are orthogonal to one another. This happens for a planar spin helix $\theta = \pi/2$ which is what we consider in the main text and in the following. Explicitly, for this choice the exchange field is along the x-direction, $K\mathbf{S}\cdot\boldsymbol{\sigma} = KS\sigma_x$, with $S = |\mathbf{S}|$, while the spin-orbit field is along the z-direction.

Note that the spin-orbit coupling contains only the momentum along the chain. This is different from a conventional Rashba coupling where momenta along both directions of the surface would appear. Presumably, this has mostly quantitative consequences as it is the momentum along the chain which is essential for allowing induced p-wave pairing in the adatom band.

We finally note that one may also want to include pairing correlations $\langle d_{i\uparrow}d_{j\downarrow}\rangle$ in the mean field approximation for the Hubbard interaction on the adatom sites. We have neglected them as we assume a large exchange splitting of the d-bands which should strongly suppress any influence of these additional pairing correlations.

II. SHIBA STATE ENERGY E_s FOR AN INDIVIDUAL IMPURITY

A single Anderson impurity hybridized with a BCS superconductor induces a subgap state called Shiba state. At mean-field level (as treated in this paper) and large spin splitting, the Shiba state energy is given by [1]

$$E_s = \frac{E_{d,\uparrow}E_{d,\downarrow} - \Gamma^2}{\sqrt{(E_{d,\uparrow}E_{d,\downarrow} - \Gamma^2)^2 - \Gamma^2(E_{d,\uparrow} - E_{d,\downarrow})^2}}. \tag{15}$$

III. DERIVATION OF THE LATTICE GREEN FUNCTION

We write the Hamiltonian of the total system as

$$H = \begin{pmatrix} H_s & H_t \\ H_t^\dagger & H_d \end{pmatrix} = H_0 + H_T, \tag{16}$$

where H_s and H_d were defined in Eqs. (11) and (13), $H_0 = \mathrm{diag}(H_s, H_d)$ contains the diagonal terms, and H_T describes the hybridization on the off-diagonal

$$H_t^{\mathbf{r},j} = -t\delta(\mathbf{r} - \mathbf{R}_j)\tau_z. \tag{17}$$

Define the wavefunction of the composite system to be $\mathbf{\Psi} = (\boldsymbol{\psi}, \mathbf{d})^T$, where the two components will be referred as s and d components (which are still vectors) in the following. Then the Schrödinger equation can be written as

$$\sum_J H_{IJ}\Psi_J = E\Psi_I. \tag{18}$$

Here the indices I, J can be continuous coordinates $\mathbf{r} \in \mathbb{R}^3$ labeling the s components or be discrete $j \in \mathbb{Z}$ labeling the d components, and the summation over J combines the integration over continuous position and the summation over the discrete site index. Plugging Eq. (11), (13), (17) into the Schrödinger equation, we have

$$\left\{\left[\frac{(-i\partial_{\mathbf{r}} + k_h\sigma_z\hat{x})^2}{2m}\right]\tau_z + \Delta\tau_x\right\}\psi(\mathbf{r}) - t\sum_j \delta(\mathbf{r} - \mathbf{R}_j)\tau_z d_j = E\psi(\mathbf{r}) \tag{19}$$

$$-t\int dr^3\, \delta(\mathbf{r} - \mathbf{R}_i)\tau_z\psi(\mathbf{r}) + \sum_j \left\{\left[(\epsilon_d - \mu)\delta_{ij} - W_{ij}\right]\tau_z - K\mathbf{S}\cdot\boldsymbol{\sigma}\delta_{ij}\right\} d_j = Ed_i. \tag{20}$$

The normalization condition is given by

$$\int d^3r\, \psi(r)^\dagger\psi(r) + \sum_j d_j^\dagger d_j = 1. \tag{21}$$

Notice that the s components $\psi(r)$ have units of $[\text{volume}]^{-1/2}$ while the d components are dimensionless.

Now we turn to the Green function of the system, which reads

$$G(E) = (E - H)^{-1} = (E - H_0 - H_T)^{-1} = G_0(E) + G_0(E)H_TG_0(E) + G_0(E)H_TG_0(E)H_TG_0(E) + \cdots, \tag{22}$$

where $G_0(E) = (E - H_0)^{-1}$. Let us now define a reduced Green function g in which we restrict the position arguments of the superconductor to the discrete impurity sites. For instance, in the ss block, this reduced lattice Green function is defined as $g_{ij}^{ss} = G^{ss}(\mathbf{R}_i, \mathbf{R}_j)$ with $i, j \in \mathbb{Z}$ (as opposed to $G^{ss}(\mathbf{R}_i, \mathbf{R}_j)$ with $\mathbf{R}_i, \mathbf{R}_j \in \mathbb{R}^3$). Let's compute the separate blocks of g in (s,d) space (space formed by superconductor and d levels of Anderson impurities),

$$g_{ij}^{dd} = g_{0,ij}^{dd} + \sum_{k_1k_2} g_{0,ik_1}^{dd}(-t\tau_z)g_{0,k_1k_2}^{ss}(-t\tau_z)g_{0,k_2j}^{dd} + \cdots \tag{23}$$

$$g_{ij}^{ss} = g_{0,ij}^{ss} + \sum_{k_1k_2} g_{0,ik_1}^{ss}(-t\tau_z)g_{0,k_1k_2}^{dd}(-t\tau_z)g_{0,k_2j}^{ss} + \cdots \tag{24}$$

$$g_{ij}^{ds} = \sum_{k_1} g_{0,ik_1}^{dd}(-t\tau_z)g_{0,k_1j}^{ss} + \cdots. \tag{25}$$

with the notation

$$g_{0,ij}^{ss} = G_0^{ss}(\mathbf{R}_i, \mathbf{R}_j), \qquad g_{0,ij}^{ds} = G_0^{ds}(i, \mathbf{R}_j). \tag{26}$$

We obtain the inverse of the lattice Green function, in matrix notation,

$$g^{-1} = \begin{pmatrix} (g_0^{ss})^{-1} & t\tau_z \\ t\tau_z & E - H_d \end{pmatrix}, \tag{27}$$

leading to Eq. (5) of the main text. Here, g^{-1} is a matrix in (s,d) space, in site space, and in spin and particle-hole space. (The spin and particle-hole indices are implicitly included in the site labels.)

We first compute the Green function of the superconductor. For $i \neq j$,

$$\begin{aligned}
g_{0,ij}^{ss}(E) &= \langle\mathbf{R}_i|\,(E - H_s)^{-1}\,|\mathbf{R}_j\rangle \\
&= \langle\mathbf{R}_i|\left[E - \left(\frac{(\mathbf{p} + k_ha\sigma_z\hat{x})^2}{2m} - \mu\right)\tau_z - \Delta\tau_x\right]^{-1}|\mathbf{R}_j\rangle \\
&= \langle\mathbf{R}_i|\,e^{-ik_hx\sigma_z}\left[E - \left(\frac{(\mathbf{p} + k_ha\sigma_z\hat{x})^2}{2m} - \mu\right)\tau_z - \Delta\tau_x\right]^{-1} e^{ik_hx\sigma_z}\,|\mathbf{R}_j\rangle \\
&= e^{-ik_h(i-j)a\sigma_z}\frac{1}{V}\sum_{\mathbf{k}}\frac{e^{i\mathbf{k}\cdot(\mathbf{R}_i - \mathbf{R}_j)}}{E - \xi_k\tau_z - \Delta\tau_x} \\
&= e^{-ik_h(i-j)a\sigma_z}\left[(E + \Delta\tau_x)P_0(|i-j|\,a) + \tau_zP_1(|i-j|\,a)\right]
\end{aligned}$$

where [2]

$$P_0(r) = \frac{\nu_0}{2}\int d\xi_k \int_{-1}^{1} dx\, \frac{e^{ikrx}}{E^2-\xi_k^2-\Delta^2} = -\frac{\pi\nu_0}{\sqrt{\Delta^2-E^2}}\frac{\sin k_F r}{k_F r}e^{-r/\xi_E} \tag{28}$$

$$P_1(r) = \frac{\nu_0}{2}\lim_{\omega_D\to\infty}\int d\xi_k \int_{-1}^{1} dx\, \frac{\xi_k e^{ikrx}}{E^2-\xi_k^2-\Delta^2}\frac{\omega_D^2}{\xi_k^2+\omega_D^2} = -\pi\nu_0\frac{\cos k_F r}{k_F r}e^{-r/\xi_E} \tag{29}$$

with ν_0 the normal density of states at the Fermi energy and $\xi_E = v_F/\sqrt{\Delta^2-E^2}$. Then we obtain

$$g_{0,ij}^{ss}(E) = -\pi\nu_0 e^{-ik_h x_{ij}\sigma_z}\left\{\frac{E+\Delta\tau_x}{\sqrt{\Delta^2-E^2}}\frac{\sin k_F r_{ij}}{k_F r_{ij}}e^{-r_{ij}/\xi_E} + \tau_z\frac{\cos k_F r_{ij}}{k_F r_{ij}}e^{-r_{ij}/\xi_E}\right\} \tag{30}$$

where $x_{ij} = x_i - x_j = (i-j)a$, $r_{ij} = |x_{ij}|$. We can also rewrite it as

$$g_{0,ij}^{ss}(E) = -\pi\nu_0 e^{-ik_h x_{ij}\sigma_z}\left\{\frac{E+\Delta\tau_x}{\sqrt{\Delta^2-E^2}}\mathrm{Im}f(r_{ij}) + \tau_z\mathrm{Re}f(r_{ij})\right\} \tag{31}$$

with

$$f(r) = \frac{e^{ik_F r - r/\xi_E}}{k_F r}. \tag{32}$$

For $i=j$, we find (see Ref. [2] for details)

$$g_{0,ii}^{ss}(E) = -\pi\nu_0\frac{E+\Delta\tau_x}{\sqrt{\Delta^2-E^2}}. \tag{33}$$

IV. GREEN FUNCTION IN LATTICE MOMENTUM SPACE

We proceed by computing the Green function in lattice momentum space

$$g_0^{ss}(k) = \sum_j e^{-ikx_{ij}}g_{0,ij}^{ss} = g_{0,ii}^{ss} + 2\sum_{j=1}^{\infty}\cos((k+k_h\sigma_z)ja)\tilde{g}_{0j}^{ss}, \tag{34}$$

where

$$\tilde{g}_{ij}^{ss} = -\pi\nu_0\frac{E+\Delta\tau_x}{\sqrt{\Delta^2-E^2}}\mathrm{Im}f(r_{ij}) - \pi\nu_0\tau_z\mathrm{Re}f(r_{ij}). \tag{35}$$

For convenience, we define

$$F(k) = -2\sum_{j=1}^{\infty}\cos(k_F ja)f(ja) \tag{36}$$

$$= \frac{1}{k_F a}\left[\ln(1-e^{-a/\xi_E+i(k_F+k)a}) + \ln(1-e^{-a/\xi_E+i(k_F-k)a})\right], \tag{37}$$

which has the property $F(k) = F(-k)$, and define $L^{\sigma_z}(k) = F(k+k_h\sigma_z) - i$. We then obtain the Green function in lattice momentum space

$$g_0^{ss}(k) = \frac{\pi\nu_0(E+\Delta\tau_x)}{\sqrt{\Delta^2-E^2}}L_i^{\sigma_z}(k,E) + \pi\nu_0\tau_z L_r^{\sigma_z}(k,E) \tag{38}$$

where $L_i^{\sigma_z}$ and $L_r^{\sigma_z}$ are the imaginary and real parts of L^{σ_z}, cf. Eq. (7) of the main text.

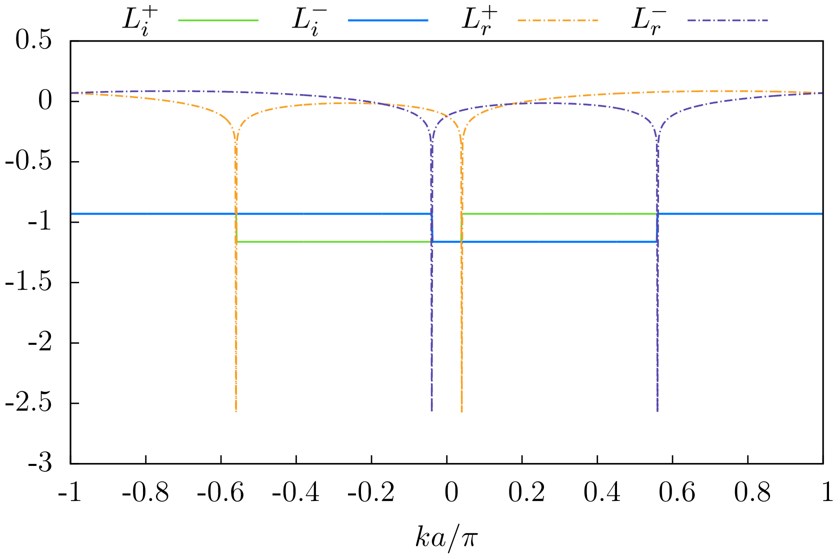

Figure 1. $L_i^{\pm}(k)$ and $L_r^{\pm}(k)$ for $k_F a = 4.3\pi$, $k_h a = 0.26\pi$ and $\xi_0/a = \infty$.

V. NUMERICAL CALCULATION OF PHYSICAL QUANTITIES

A. Excitation spectrum

The inverse Green function g^{-1} is diagonal in momentum space and we have

$$g^{-1}(k,E) = \begin{pmatrix} (g_0^{ss})^{-1}(k,E) & t\tau_z \\ t\tau_z & (g_0^{dd})^{-1}(k,E) \end{pmatrix}, \tag{39}$$

with

$$(g_0^{dd})^{-1}(k,E) = E - [\epsilon_d - 2w\cos(k + k_h\sigma_z)a]\,\tau_z + KS\sigma_x. \tag{40}$$

This is an 8×8 matrix as a function of $k \in [-\frac{\pi}{a}, \frac{\pi}{a}]$. Then the subgap band can be calculated by imposing the condition

$$\det(g^{-1}(k,E)) = 0. \tag{41}$$

B. Majorana wavefunction

Consider a finite chain of N sites. Since the Majorana state $|\psi^M\rangle \in \ker g^{-1}(E=0)$, its real space representation in terms of a column vector $\psi^M(i) = \langle i|\psi^M\rangle$, with $i = 1,\dots N$, is in the kernel of the $8N\times 8N$ matrix g_{ij}^{-1} evaluated at $E=0$. The occupation probability at site i is given by

$$\left|\psi^M(i)\right|^2 = \langle \psi^M(i), \psi^M(i)\rangle, \tag{42}$$

where $\langle\cdot,\cdot\rangle$ denotes the inner product in spin and particle-hole space. We then take either the components of the superconducting host when $\Gamma > \Delta$ or take the d components when $\Gamma < \Delta$. Note that the s and d entries have different units and cannot be added. However, the localization length of the end state is the same for both components.

C. Local density of states

The local density of states is related to the diagonal elements of

$$A^{\mu\nu}(\mathbf{r},E) = -\frac{1}{\pi}\lim_{\eta\to 0^+} \operatorname{Im}\operatorname{Tr}_\sigma G^{\mu\sigma,\nu\sigma}(E+i\eta,\mathbf{r},\mathbf{r}), \tag{43}$$

where $\mu, \nu \in \{s, d\} \times \{e, h\}$ are composite indices for (s,d) and (e,h) (particle-hole) components, and σ is the index of the spin space, within which the trace is taken. To obtain a true tunneling density of states, we would also need to use a Green function G which includes information about the spatial structure of the adatom d-states. This structure is not explicit in the Green function defined in Eq. (22). The latter treats the adatoms in tight-binding approximation and retains only the amplitudes of the atomic d-orbitals rather than the spatial structure of the corresponding wavefunctions.

In the case of $\Gamma \gg \Delta$, there is a strong transfer of the spectral weight of the subgap excitations to the superconductor. Therefore, apart from a narrow vicinity of the adatoms, the main contribution to the local density of states comes from the states of the host. In this limit, we neglect the contribution of the adatoms (i.e. the d-levels) to the local density of states. Focusing on the electron contribution, we compute $A^{\mu\nu}(\mathbf{r}, E)$ for $\mu = \nu = (s, e)$ and $\mathbf{r} = \mathbf{R}_j$ at site j. Explicitly, we are able to find the local density of states at each site j,

$$A_j(E) = A^{\mu\mu}(\mathbf{R}_j, E) = -\frac{1}{\pi} \lim_{\eta \to 0^+} \operatorname{Im} \operatorname{Tr}_\sigma g_{jj}^{\mu\sigma,\mu\sigma}(E + i\eta), \qquad \mu = (s, e), \tag{44}$$

from the lattice Green function g defined in Eq. (27). It should also be mentioned that we include a finite imaginary part in the energy $E \to E + i\eta$, with $\eta = 0.015\Delta$. This small η put in by hand introduces a finite broadening of the δ-peaks which we obtain from a finite size calculation. This results in a smooth local density of states.

VI. DERIVATION OF EQUATION (10) IN THE MAIN TEXT

The dressed Green function of the superconductor including the self-energy from hybridization with the magnetic adatoms can be written as

$$g^{ss} = g_0^{ss}(1 - \Sigma g_0^{ss}). \tag{45}$$

The self-energy takes the form

$$\begin{aligned}
\Sigma = t^2 g_0^{dd} &= \begin{pmatrix} E - \varepsilon_d^+ & KS & 0 & 0 \\ KS & E - \varepsilon_d^- & 0 & 0 \\ 0 & 0 & E + \varepsilon_d^+ & KS \\ 0 & 0 & KS & E + \varepsilon_d^- \end{pmatrix}^{-1} \\
&= \frac{t^2}{(E - \varepsilon_d^+)(E - \varepsilon_d^-) - (KS)^2} \begin{pmatrix} E - \varepsilon_d^- & -KS & 0 & 0 \\ -KS & E - \varepsilon_d^+ & 0 & 0 \\ 0 & 0 & 0 & 0 \\ 0 & 0 & 0 & 0 \end{pmatrix} + \frac{t^2}{(E + \varepsilon_d^+)(E + \varepsilon_d^-) - (KS)^2} \begin{pmatrix} 0 & 0 & 0 & 0 \\ 0 & 0 & 0 & 0 \\ 0 & 0 & E + \varepsilon_d^- & -KS \\ 0 & 0 & -KS & E + \varepsilon_d^+ \end{pmatrix}
\end{aligned} \tag{46}$$

where $\varepsilon_d^\pm(k) = \epsilon_d - 2w \cos(k \pm k_h)a$. We now assume that the spin-splitting KS is the largest energy scale in the problem and is taken to ∞. In this limit, the spin direction is frozen along the Zeeman axis. Moreover, we take the limit such that the energy of the spin-up band goes to $-\infty$ while the energy E_d of the spin-down band remains finite. To take the limit, we temporarily introduce $E_d^\pm = \varepsilon_d^\pm + KS$, and replace $\varepsilon_d^\pm = E_d^\pm - KS$ in the self-energy. Now, E and $E_d^\pm$ remain finite in the limit $KS \to \infty$, i.e., $KS \gg E, E_d$, and we can approximate

$$(E - \varepsilon_d^+)(E - \varepsilon_d^-) - (KS)^2 \simeq -KS(E_d^+ + E_d^- - 2E) \tag{47a}$$

$$(E + \varepsilon_d^+)(E + \varepsilon_d^-) - (KS)^2 \simeq -KS(E_d^+ + E_d^- + 2E) \tag{47b}$$

in the denominators and

$$E \pm \varepsilon_d^{+,-} \simeq \mp KS \tag{48}$$

in the matrix elements. Thus, for $KS \to \infty$, we find

$$\Sigma \simeq \frac{\alpha_-}{2\pi\nu_0}(1 + \tau_z)(\sigma_x - \tau_z) + \frac{\alpha_+}{2\pi\nu_0}(1 - \tau_z)(\sigma_x - \tau_z), \tag{49}$$

where

$$\alpha_\pm = \frac{\pi\nu_0 t^2}{2E_d \pm 2E}, \qquad E_d = \frac{E_d^+ + E_d^-}{2}. \tag{50}$$

Note that we can also write

$$\Sigma = e^{-i\frac{\pi}{4}\sigma_y}\left\{\frac{\alpha_-}{2\pi\nu_0}(1+\tau_z)(\sigma_z-\tau_z)+\frac{\alpha_+}{2\pi\nu_0}(1-\tau_z)(\sigma_z-\tau_z)\right\}e^{-i\frac{\pi}{4}\sigma_y} = e^{i\frac{\pi}{4}\sigma_y}\begin{pmatrix}0&0&0&0\\0&-\frac{2\alpha_-}{\pi\nu_0}&0&0\\0&0&\frac{2\alpha_+}{\pi\nu_0}&0\\0&0&0&0\end{pmatrix}e^{-i\frac{\pi}{4}\sigma_y}. \tag{51}$$

Then

$$\begin{aligned}\det(1-\Sigma g_0^{ss}) &= \det\left\{1-\begin{pmatrix}0&0&0&0\\0&-\frac{2\alpha_-}{\pi\nu_0}&0&0\\0&0&\frac{2\alpha_+}{\pi\nu_0}&0\\0&0&0&0\end{pmatrix}\begin{pmatrix}\mathcal{A}+\mathcal{B}&\mathcal{E}+\mathcal{F}&\mathcal{C}&\mathcal{D}\\\mathcal{E}+\mathcal{F}&\mathcal{A}+\mathcal{B}&\mathcal{D}&\mathcal{C}\\\mathcal{C}&\mathcal{D}&\mathcal{A}-\mathcal{B}&-\mathcal{E}+\mathcal{F}\\\mathcal{D}&\mathcal{C}&-\mathcal{E}+\mathcal{F}&\mathcal{A}-\mathcal{B}\end{pmatrix}\right\}\\ &= \det\left\{1-2\begin{pmatrix}-\alpha_-(\mathcal{A}+\mathcal{B})&-\alpha_-\mathcal{D}\\\alpha_+\mathcal{D}&\alpha_+(\mathcal{A}-\mathcal{B})\end{pmatrix}\right\}\\ &= [1+2\alpha_-(\mathcal{A}+\mathcal{B})]\,[1-2\alpha_+(\mathcal{A}-\mathcal{B})]+4\alpha_+\alpha_-\mathcal{D}^2\\ &= 1+2\mathcal{A}(\alpha_--\alpha_+)+2\mathcal{B}(\alpha_-+\alpha_+)+4\alpha_+\alpha_-(\mathcal{D}^2+\mathcal{B}^2-\mathcal{A}^2)\end{aligned} \tag{52}$$

where

$$\mathcal{A} = \frac{E}{\sqrt{\Delta^2-E^2}}L_i \qquad \mathcal{B} = L_r \qquad \mathcal{C} = \frac{\Delta}{\sqrt{\Delta^2-E^2}}L_i \tag{53}$$

$$\mathcal{D} = -\frac{\Delta}{\sqrt{\Delta^2-E^2}}(\delta L_i) \qquad \mathcal{E} = -(\delta L_r) \qquad \mathcal{F} = -\frac{E}{\sqrt{\Delta^2-E^2}}(\delta L_i) \tag{54}$$

and

$$L_{i,r} = \frac{L_{i,r}^+ + L_{i,r}^-}{2} \qquad (\delta L_{i,r}) = \frac{L_{i,r}^+ - L_{i,r}^-}{2}. \tag{55}$$

The excitation spectrum can be obtained by requiring the above determinant to be zero,

$$\begin{aligned}0 &= 1+\frac{2E}{\sqrt{\Delta^2-E^2}}L_i(\alpha_--\alpha_+)+2L_r(\alpha_-+\alpha_+)+4\alpha_+\alpha_-\left\{\frac{\Delta^2}{\Delta^2-E^2}(\delta L_i)^2-\frac{E^2}{\Delta^2-E^2}L_i^2+L_r^2\right\}\\ &= 1+\frac{2\Gamma E_d}{E_d^2-E^2}L_r+\frac{\Gamma^2}{E_d^2-E^2}L_r^2\\ &+\frac{2E^2}{\sqrt{\Delta^2-E^2}}\frac{\Gamma}{E_d^2-E^2}L_i+\frac{\Gamma^2}{E_d^2-E^2}\left\{\frac{\Delta^2}{\Delta^2-E^2}(\delta L_i)^2-\frac{E^2}{\Delta^2-E^2}L_i^2\right\}\end{aligned} \tag{56}$$

with $\Gamma = \pi\nu_0 t^2$. Multiplying by $(\Delta^2-E^2)(E_d^2-E^2)$ gives Eq. (9) of the main text,

$$(\Delta^2-E^2)[E_d+\Gamma L_r]^2-E^2[\sqrt{\Delta^2-E^2}-\Gamma L_i]^2+\Gamma^2\Delta^2(\delta L_i)^2 = 0. \tag{57}$$

VII. COMPARISON WITH EXPERIMENT

Here, we briefly discuss the Majorana localization length as given in Eq. (2) of the main text in more detail. For lead, the literature value of the coherence length ξ_0 is $\xi_0 \simeq 80$nm [4].

Given that the Fe adatoms are directly embedded into the host superconductor, the hybridization Γ is governed by physics on the atomic scale. Thus, Γ should also be of the order of atomic energies, $\Gamma \sim 1$eV (for a similar estimate of the hybridization, see Ref. [3]). According to this estimate, the adatom chains are deeply in the regime of strong hybridization, $\Gamma \gg \Delta$, with quasiparticle weight $Z \simeq \Delta/\Gamma \sim 10^{-3}$.

The value of Γ assumed in this estimate is comparable to $\hbar v_F/a$, and thus at the border of applicability of our theory.

The ratio of gaps $\alpha = \Delta_{\text{top}}/\Delta$ is controlled by the strength of spin-orbit coupling in the substrate superconductor. This is difficult to estimate from first principles. Extracting Δ_{top} from the experiment [5] is hindered by the substantial broadening of the peaks in the STM spectra. Interpreting these maxima as van-Hove singularities of the Shiba bands, one finds a topological gap of order 0.1Δ.

Inserting these numbers into Eq. (2) for the Majorana localization length ξ_M, we find that ξ_M is two orders of magnitude smaller than the coherence length ξ_0 of the substrate superconductor, i.e., of order 1nm or a few adatom spacings a ($a \simeq 0.4$nm according to Ref. [5]).

[1] H. Shiba, Prog. Theor. Phys., **50** , 50 (1973).
[2] F. Pientka, L.I. Glazman, and F. von Oppen, Phys. Rev. B **88**, 155420 (2013).
[3] J. Li, H. Chen, I.K. Drozdov, A. Yazdani, B.A. Bernevig, A.H. MacDonald, Phys. Rev. B **90**, 235433 (2014).
[4] A. Fetter and D. Walecka, *Quantum Theory of Many Particle Systems* (MacGraw-Hill, New Yorck, 1971).
[5] S. Nadj-Perge, I.K. Drozdov, J. Li, H. Chen, S. Jeon, J. Seo, A.H. MacDonald, B.A. Bernevig, A. Yazdani, Science **346**, 602 (2014).

3 Robust Majorana conductance peaks for a superconducting lead

It is a prominent prediction that tunneling into a Majorana from a metallic lead produces a quantized zero-bias conductance peak at zero temperature. However, Majorana experiments consistently show non-quantized peaks. Presumably, the failure to observe quantization is a result of temperature broadening as well as inelastic poisoning processes. I showed that using superconducting instead of normal-metal leads has two advantages. First, the conductance is not only universal but also protected against temperature effects by the superconducting gap. Second, I predicted that Majoranas are signalled by *symmetric* conductance peaks at bias voltages $eV = \pm\Delta$ (Δ is the gap of the superconducting lead). The latter prediction was already checked experimentally by the groups of K. Franke [7] and A. Yazdani [64].

Robust Majorana Conductance Peaks for a Superconducting Lead

Yang Peng,[1] Falko Pientka,[1] Yuval Vinkler-Aviv,[1] Leonid I. Glazman,[2] and Felix von Oppen[1]
[1]*Dahlem Center for Complex Quantum Systems and Fachbereich Physik, Freie Universität Berlin, 14195 Berlin, Germany*
[2]*Department of Physics, Yale University, New Haven, Connecticut 06520, USA*

(Received 29 June 2015; published 29 December 2015)

Experimental evidence for Majorana bound states largely relies on measurements of the tunneling conductance. While the conductance into a Majorana state is in principle quantized to $2e^2/h$, observation of this quantization has been elusive, presumably due to temperature broadening in the normal-metal lead. Here, we propose to use a superconducting lead instead, whose gap strongly suppresses thermal excitations. For a wide range of tunneling strengths and temperatures, a Majorana state is then signaled by symmetric conductance peaks at $eV = \pm\Delta$ of a universal height $G = (4-\pi)2e^2/h$. For a superconducting scanning tunneling microscope tip, Majorana states appear as spatial conductance plateaus while the conductance varies with the local wave function for trivial Andreev bound states. We discuss effects of nonresonant (bulk) Andreev reflections and quasiparticle poisoning.

DOI: 10.1103/PhysRevLett.115.266804 PACS numbers: 73.63.Nm, 74.20.-z, 75.70.Tj, 75.75.-c

Introduction.—Motivated by possible applications in quantum information processing [1,2], topological superconductors hosting Majorana bound states are currently under intense investigation [3–5]. Based on the superconducting proximity effect, various realistic platforms have been proposed to support Majorana states including topological insulators [6,7], semiconductor nanowires [8,9], and atomic chains [10–16]. Although these systems are available in the laboratory, the experimental observation of unique Majorana signatures remains challenging.

A widely employed diagnostic tool is the tunneling conductance of normal metal-superconductor junctions, in which Majorana bound states manifest themselves as characteristic zero-bias peaks [17,18]. Experimental signatures consistent with theoretical predictions have been observed in quantum wires [19–21] and atomic chains [22,23]. However, it is a major challenge in these experiments to uniquely distinguish Majorana bound states from conventional fermionic subgap states. Spin-polarized subgap states such as Shiba states bound to magnetic impurities [24–27] or Andreev bound states in a magnetic field can exhibit a zero-energy crossing as a function of exchange interaction or Zeeman energy [28–30]. Thus, such fermionic states may accidentally occur at zero energy and give rise to similar conductance features. As magnetic impurities or external magnetic fields are also required for the most relevant realizations of topological superconductors, such trivial conductance peaks can generally not be disregarded.

In contrast to fermionic subgap states, Majorana states exhibit a celebrated quantized zero-bias conductance of $2e^2/h$ [17,18,31]. Unfortunately, this has, so far, proved difficult to observe in experiment. The Fermi distribution in the metal lead is smooth on the scale of the temperature T, which strongly limits the experimental energy resolution. When temperature is larger than the tunnel coupling, the Majorana peak is broadened and the zero-bias conductance is reduced. Even at low temperatures (e.g., $T = 60$ mK in Ref. [19]), it may be difficult to observe the quantized peak height, as multichannel effects limit the relevant tunneling strength [32]. Quasiparticle (qp) poisoning may also lead to deviations from quantization. A fermion-parity breaking rate exceeding the tunnel coupling broadens the peak and reduces its height. This requires one to work at temperatures below the lowest fermionic excitations in the topological superconductor.

In this Letter, we show how a robust conductance signature of Majorana bound states can be obtained by employing superconducting leads. In striking contrast to normal-state contacts, effects of thermal broadening are strongly suppressed for a superconducting lead because quasiparticle excitations are exponentially suppressed $\sim\exp(-\Delta/T)$ by its superconducting gap Δ. Majorana bound states no longer appear as zero-bias anomalies but rather as two symmetric peaks in the differential conductance $G = dI/dV$ which occur when the BCS singularity of the superconducting gap lines up with the Majorana bound state, i.e., at the thresholds $eV = \pm\Delta$. These peaks have a universal height

$$G_M = (4-\pi)\frac{2e^2}{h}, \tag{1}$$

which persists over a wide range of tunnel couplings.

This yields particularly striking evidence when employing a scanning tunneling microscope (STM) with a superconducting tip which allows for spatially resolved measurements. This has previously been used to map out bound state wave functions in conventional and unconventional superconductors [22,23,33–36]. Here, we propose that such maps can clearly distinguish between Majorana bound states and trivial zero-energy bound states. Indeed, the peak conductance is uniform in the vicinity of

Majorana states and a conductance map exhibits a characteristic mesa or plateau structure. In contrast, the conductance of trivial subgap states exhibits a spatial pattern which is governed by the bound-state wave function.

In addition, STM measurements allow for systematic studies as a function of tunneling strength by varying the tip height. It was recently demonstrated [37] that this can be exploited to probe quasiparticle relaxation processes. In the present context, varying the tunneling strength may help to identify Majorana signatures despite competing effects such as nonresonant Andreev reflections or quasiparticle poisoning.

Subgap conductance for Majorana bound state.—At subgap voltages $eV < \Delta + \Delta_s$ and zero temperature, the tunneling current between superconducting tip or lead and substrate (with gap Δ_s) flows by multiple Andreev reflections. Near the threshold $e|V| = \Delta$, the differential conductance $\mathrm{d}I/\mathrm{d}V$ is dominated by single Andreev reflections from the sample. For tip locations far from the zero-energy bound state in the sample, this yields the familiar peak in $\mathrm{d}I/\mathrm{d}V$ due to the singular densities of states of incoming electrons and outgoing holes. In the vicinity of the bound state, tunneling is further enhanced by the zero-energy resonance [37–39].

Formally, the subgap current due to single Andreev reflections from the sample can be expressed as [40–42]

$$I(V) = 4e\pi^2 t^4 \int \frac{d\omega}{2\pi\hbar} \mathrm{Tr}[G_{eh}(r,\omega)G^{\dagger}_{eh}(r,\omega)] \times \rho(\omega_-)\rho(\omega_+)[n_F(\omega_-) - n_F(\omega_+)], \quad (2)$$

where t is the amplitude for tip-substrate tunneling, $\omega_\pm = \omega \pm eV$, $n_F(\omega)$ denotes the Fermi function, and the superconducting tip enters through its BCS density of states $\rho(\omega) = \nu_0\theta(|\omega| - \Delta)|\omega|/\sqrt{\omega^2 - \Delta^2}$ with ν_0 the normal density of states at the Fermi energy. Spin or subband degrees of freedom are accounted for by a possible matrix structure of the anomalous retarded Green function $G_{eh}(r,\omega)$ of the substrate at the tip position r. In terms of its Lehmann representation, $G_{eh}(r,\omega)$ has contributions from both the bound state and the above-gap continuum. In the following, we first consider the resonantly enhanced Andreev current from a Majorana bound state and subsequently discuss the contribution of the quasiparticle continuum.

For $e|V| \simeq \Delta$, we can approximate $n_F(\omega_-) - n_F(\omega_+) \simeq \mathrm{sgn}V$ in Eq. (2), up to corrections of order $\exp(-\Delta/T)$. This insensitivity to temperature is a key advantage of superconducting leads. The bound-state contribution to the substrate Green function is

$$G(r,\omega) = \frac{\langle r|\psi\rangle\langle\psi|r\rangle}{\omega + i\Gamma/2}. \quad (3)$$

Here, $\langle r|\psi\rangle = [\zeta(r), \pm\Theta\zeta(r)]^{\mathrm{T}}$ denotes the local Bogoliubov–de Gennes wave function of the Majorana bound state with Θ the time-reversal operator. The broadening $\Gamma = 2i\langle\psi|\Sigma|\psi\rangle$ of the bound state is induced by the tunnel coupling to the lead. The corresponding self energy $\Sigma = -i\pi t^2 \mathrm{diag}[\rho(\omega_-), \rho(\omega_+)]$ is diagonal as Andreev reflections in the lead can be neglected near $e|V| = \Delta$.

Inserting Eq. (3) into (2) yields (for $V > 0$) [37,43]

$$I = \frac{e}{h}\int d\omega \frac{\Gamma_e(\omega)\Gamma_h(\omega)}{\omega^2 + [\Gamma_e(\omega) + \Gamma_h(\omega)]^2/4}, \quad (4)$$

in terms of the electron and hole tunneling rates $\Gamma_{e/h}(\omega) = 2\pi t^2|\zeta|^2\rho(\omega_\mp)$. While the integrand in Eq. (4) has a resonance denominator, its behavior is peculiar due to the strong energy dependence of the tunneling rates. Specifically, the square-root singularity of the BCS density of states implies that the integrand involves a characteristic energy scale $\omega_t = [\pi t^2\nu_0|\zeta(r)|^2\sqrt{\Delta/2}]^{2/3}$ which depends on a fractional power of the tunneling rate from a normal tip $\gamma_n = 2\pi t^2\nu_0|\zeta(r)|^2$. In the weak-tunneling regime $\omega_t \ll \Delta$, we can write

$$I = \frac{4e}{h}\int_{-\eta}^{\eta} \frac{d\omega}{\sqrt{\eta^2 - \omega^2}} \frac{\omega_t^3}{\omega^2 + \omega_t^3(\frac{1}{\sqrt{\eta-\omega}} + \frac{1}{\sqrt{\eta+\omega}})^2}, \quad (5)$$

for $0 < \eta \ll \Delta$, where $\eta = eV - \Delta$ measures the voltage from the threshold Δ. In the vicinity of the threshold, $\eta \ll \omega_t$, the resonance denominator is dominated by the second term, and we obtain $I(V) = (4-\pi)(2e/h) \times (eV - \Delta)\theta(eV - \Delta)$ and, thus, Eq. (1). The entire peak line shape

$$\frac{\mathrm{d}I}{\mathrm{d}V} = (4-\pi)\frac{2e}{h}\Lambda\left(\frac{eV - \Delta}{\omega_t}\right), \quad (6)$$

involves the function $\Lambda(x)$ which vanishes for $x < 0$, jumps to $\Lambda(0^+) = 1$, and falls off with a small negative differential conductance tail at large x, cf. Fig. 1.

Thus, the differential conductance between a conventional superconductor and a Majorana state exhibits a peak which is independent of tunneling strength and Majorana wave function. While the peak height is close to the quantized Majorana peak height $2e^2/h$ for a normal-metal lead, there are several differences: (a) There are two symmetric, finite-bias Majorana peaks at $eV = \pm\Delta$ rather than a single zero-bias peak. (b) The conductance peak is strongly asymmetric with a discontinuous step at the threshold. (c) The width of the peak is set by ω_t with its sublinear dependence on junction transparency.

The threshold discontinuity in the conductance persists even when including the contributions of the quasiparticle continuum in the substrate Green function. To see this, we model the substrate superconductor by a 2×2 Nambu Green function $g(\omega, r)$. For a topological substrate, this is appropriate for perfect spin polarization (spinless p-wave superconductor). Including the tunnel coupling to the tip

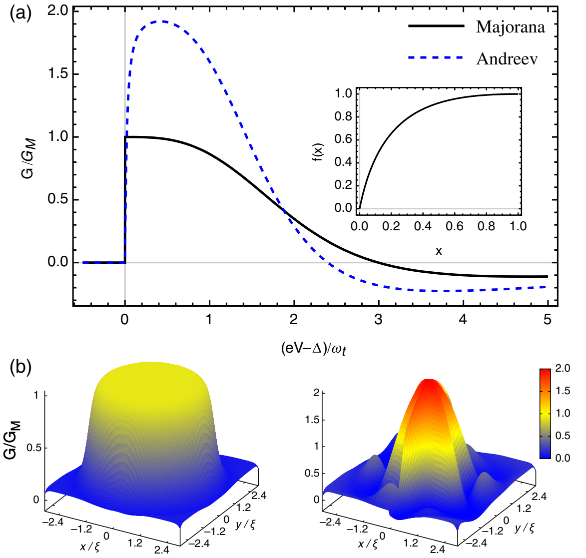

FIG. 1 (color online). (a) Differential conductance vs bias voltage near the threshold $eV = \Delta$ for Majorana states (solid line) and Andreev states with $|u| = |v|$ (dashed line). For a Majorana state, the conductance exhibits a step of height $(4-\pi)2e^2/h$ at the threshold. For an Andreev state, the conductance has a smooth onset, cf. Eq. (10). Both peaks have a negative-differential conductance dip at high voltages. Inset: Graph of $f(x)$ as defined in the main text. (b) Spatial conductance maps for Majorana states (left) and Andreev (right) states for $\omega_t(0)/\delta\Delta = 5$. The Majorana state gives rise to a conductance plateau, whereas the Andreev state exhibits a pattern reflecting the spatial dependence of the ratio $(u/v)^2$. The Majorana conductance drops far from the bound state when the broadening exceeds ω_t.

through the self energy Σ as given above, the substrate Green function becomes $G = g[1-\Sigma g]^{-1}$. We first focus on the vicinity of the bound state where the conductance is dominated by Andreev reflections from the bound state. By straightforward calculation and expansion of g in ω [40], we find

$$G(r,\omega) = \frac{\langle r|\psi\rangle\langle\psi|r\rangle}{\omega-\lambda(\omega)+i\Gamma/2}. \tag{7}$$

This differs from the pure bound-state contribution by the additional term $\lambda(\omega) = \pi^2 t^4 \omega \det g(\omega,r)\rho(\omega_-)\rho(\omega_+)$ in the denominator which involves the determinant (in particle-hole space) of the bare substrate Green function. While the determinant of the bound-state contribution to the Green function vanishes, this is no longer the case when including the quasiparticle continuum. At subgap energies away from bound states, the Green function $g(\omega,r)$ is a Hermitian 2×2 matrix, so that $\det g(\omega,r)$ and, hence, $\lambda(\omega)$ are real. Thus, we find

$$I_M(V) = \frac{4e}{h}\int_{-\eta}^{\eta}\frac{d\omega}{\sqrt{\eta^2-\omega^2}}\frac{\omega_t^3}{(\omega-\lambda)^2+\left(\frac{\omega_t^{3/2}}{\sqrt{\eta-\omega}}+\frac{\omega_t^{3/2}}{\sqrt{\eta+\omega}}\right)^2}. \tag{8}$$

For a Majorana state, the real part of the resonance denominator must vanish exactly at $\omega = 0$. Indeed, particle-hole symmetry further constrains $\det g(\omega,r)$ to be an even function of ω which can be approximated as a constant at small ω (see [40], where this conclusion is confirmed by model calculations). Then, we find $\lambda(\omega) \propto t^4\omega/\sqrt{\eta^2-\omega^2}$ near the threshold. Even with this term, the denominator in Eq. (8) remains dominated by the divergent tunnel broadenings $\sim\omega_t^{3/2}/\sqrt{\eta\pm\omega}$ and the discontinuous conductance step as well as the universal value of the threshold conductance in Eq. (1) persist.

In experiment, the square-root singularity of the BCS density of states of the tip may be broadened intrinsically due to higher-order processes or effectively due to experimental resolution. The universal threshold conductance persists as long as ω_t exceeds this broadening. This condition also determines the spatial extent of the conductance plateau, $r \lesssim 4\xi\ln[\omega_t(0)/\delta\Delta]/3$, where ξ is the Majorana localization length, $\omega_t(0)$ denotes the value of ω_t at the center of the Majorana bound state, and $\delta\Delta$ is the broadening of the tip density of state, cf. Fig. 1(b). Of course, a well-resolved Majorana peak also requires $\omega_t \ll \Delta_s$; i.e., the tunnel broadening needs to be small compared to the induced gap. If the peak is not fully resolved, it is suppressed below the universal value and its height may vary as a function of space.

For tip locations far from the bound state, the tunneling conductance is dominated by conventional ("nonresonant") Andreev reflections. These still yield a threshold peak due to the singular tip density of states in Γ_e and Γ_h but are not enhanced by a bound-state resonance. For a one-dimensional p-wave superconductor, this conductance peak has height $\simeq 1.3G_M$ and width $\sim\Delta\mathcal{T}^2$ quadratic in the junction transparency $\mathcal{T} \propto t^2$ [40]. Observing the conventional Andreev peak, thus, requires that the broadening of the tip density of states is small compared to $\sim\Delta\mathcal{T}^2$. This is a much more stringent condition than for the resonant Andreev peak as the width of the bound-state peak $\omega_t \propto t^{4/3}$ involves a lower power of t. We note that, in a typical STM experiment [37], conventional Andreev peaks can be resolved only for small tip-sample distances, while bound-state signatures persist to much weaker tunnel couplings.

Subgap conductance for Andreev bound state.—These results should be contrasted with those for trivial zero-energy Andreev bound states. For concreteness, consider an s-wave superconductor with conserved spin [44], whose Bogoliubov–de Gennes description decomposes into two independent spin sectors that interchange under particle-hole transformations. A zero-energy Andreev state corresponds to two Bogoliubov–de Gennes wave functions, $\langle r|\psi_+\rangle = [u(r), v(r)]^{\mathrm{T}}$ and $\langle r|\psi_-\rangle = [\Theta v(r), -\Theta u(r)]^{\mathrm{T}}$, one in each sector. An analogous calculation [40] yields the threshold current

$$I_A(V) = 2I_M(V)f[|u(r)|^2/|v(r)|^2]. \tag{9}$$

Reflecting the two zero-energy wave functions, the maximal threshold conductance is twice that in the Majorana case, $G_A = 2G_M$, and realized for the particle-hole symmetric case $|u| = |v|$. In general, the peak conductance depends on the ratio of electron and hole wave function at the tip position. This dependence is captured by the dimensionless function $f(x) = [2x/(4-\pi)] \int_{-1}^{1} dz \sqrt{1-z^2}/(x\sqrt{1-z}+\sqrt{1+z})^2$ which takes on values between 0 and 1 and is plotted in Fig. 1(a). The function satisfies $f(x) = f(1/x)$ as the two spin sectors contribute equally. In the limit of large particle-hole asymmetry, $G_A \sim G_M \min(|u/v|^2, |v/u|^2) \ll G_M$. The line shape of the conductance peak is similar to the Majorana peak, with a width of order ω_t upon replacing $\zeta(r)$ by $\max\{u(r), v(r)\}$.

Our results imply that the height of the conductance peak allows for a clear distinction between a conventional Andreev bound state and a Majorana state. Even when $f(u^2/v^2) \sim 1/2$ for one location of the STM tip, moving the tip to another location modifies the conductance peak height for a conventional bound state, tracking the ratio of electron and hole wave functions. In contrast, the conductance map exhibits a characteristic mesa structure for a Majorana state, see Fig. 1(b). In non-STM tunneling experiments, changes of parameters (e.g., gate voltages) which affect the Majorana wave function should leave the peak height unchanged for a Majorana bound state but not for a conventional Andreev bound state.

As there is no locking of the bound state to zero energy, the continuum contribution is also distinctly different for conventional Andreev states. The two spin sectors are described by separate 2×2 Nambu Green functions which map into one another under particle-hole transformations. This is quite unlike the Majorana Green function which maps onto itself. For each sector, $\det g(\omega, r)$ is, therefore, no longer an even function of ω and will generally have a singular contribution $\propto 1/\omega$ at the threshold so that $\lambda(\omega) \sim \mathcal{T}^2 \Delta_s \Delta / \sqrt{\eta^2 - \omega^2}$. These general arguments can be confirmed explicitly for Shiba states in s-wave superconductors [40]. Near the threshold, the resonance denominator in the expression for the current is now dominated by $\lambda(\omega)$. As illustrated in Fig. 1 by a numerical evaluation of the current, this suppresses the conductance step. Analytically, we find that just above the threshold, the conductance increases linearly,

$$G_A(V) \sim \frac{2e^2}{h} \frac{1}{\mathcal{T}^2} \frac{eV - \Delta}{\Delta} \theta(eV - \Delta), \tag{10}$$

and matches with the conductance obtained from Eq. (9) for $eV - \Delta \gg \mathcal{T}^2 \Delta$. We note that this suppression of the conductance step depends on $\mathcal{T}$ and can, thus, be probed by varying the tip-sample distance in an STM experiment. This may serve as an additional signature for distinguishing between Majorana bound states and conventional Andreev bound states.

Effects of quasiparticle poisoning.—So far, we only included bound-state broadening by the tunneling contact. At finite temperatures, the bound-state occupation also changes by inelastic transitions to other subgap states or the quasiparticle continuum in the sample [45]. We account for these processes by an additional contribution $i\Gamma_{\rm qp}/2$ to the self energy of the bound-state Green function Eq. (7). This does not affect the Andreev current at the threshold, where the denominator is dominated by the diverging tunnel coupling. However, the overall weight of the peak is reduced by a narrowing of the linewidth by a factor $(\omega_t/\Gamma_{\rm qp})^2$ once $\Gamma_{\rm qp} > \omega_t$, see Fig. 2 (inset).

In addition, quasiparticle poisoning generates a single-electron current I^s which involves tunneling of single particles followed by inelastic transitions from the zero-energy bound state to other bound states or the quasiparticle continuum [37]. For a Majorana state, we find near the threshold $eV = \Delta$ (with analogous results applying for Andreev bound states) [40]

$$I_M^s = \frac{e}{4h} \int d\omega \frac{\Gamma_{\rm qp}[\Gamma_e(\omega) + \Gamma_h(\omega)]}{\omega^2 + [\Gamma_{\rm qp} + \Gamma_e(\omega) + \Gamma_h(\omega)]^2/4}. \tag{11}$$

For weak and strong tunneling, this yields [40]

$$G_M^s \sim \frac{2e^2}{h} \begin{cases} (\omega_t/\Gamma_{\rm qp})^{3/2} & \omega_t \ll \Gamma_{\rm qp}, \\ \Gamma_{\rm qp}/\omega_t & \omega_t \gg \Gamma_{\rm qp}. \end{cases} \tag{12}$$

Figure 2 shows that this single-particle contribution assumes a maximum of $\sim 0.2 G_M$ when $\omega_t \sim \Gamma_{\rm qp}$. However, it can be easily made negligible by tuning the

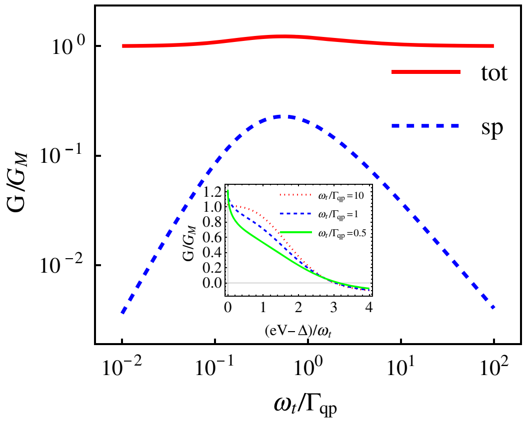

FIG. 2 (color online). Total threshold conductance for a Majorana state (tot) along with the single-particle contribution (sp) as a function of ω_t. The single-particle contribution affects the conductance only in a window of transmission values, where $\omega_t \sim \Gamma_{\rm qp}$. While the maximum is of order $0.2G_M$, the position of the maximum in tunneling strength depends sensitively on temperature (through $\Gamma_{\rm qp}$). Inset: Line shape of the total conductance as a function of voltage away from the threshold, for different ratios of $\omega_t/\Gamma_{\rm qp}$.

system away from this maximum through varying temperature or tunneling strength.

Conclusions.—We show that conductance measurements with superconducting leads constitute a promising technique for identifying Majorana states. The presence of Majorana states is signaled by conductance peaks of universal height which are largely unaffected by thermal broadening, a key obstacle in previous experiments with normal-metal contacts. We discuss strategies to systematically rule out parasitic effects such as quasiparticle poisoning or trivial subgap states. The proposed setup is readily available in the laboratory and, in fact, has already been realized in previous experiments [22,23,46,47]. (Notice, however, that temperature was comparable to the induced gap in the STM experiments performed to date, precluding observation of the universal conductance, and that the nanowire experiments focused on zero-bias peaks.) Our results also imply that quasiparticle poisoning rates can be extracted from systematic measurements as a function of tip height and temperature.

We thank P. Brouwer, K. Franke, B. Heinrich, J. Meyer, Y. Oreg, and M.-T. Rieder for stimulating discussions. We acknowledge financial support by the Helmholtz Virtual Institute "New states of matter and their excitations," Grants No. SFB 658, No. SPP1285, and No. SPP1666 of the Deutsche Forschungsgemeinschaft, the Humboldt Foundation, the Minerva Stiftung, as well as DOE Contract No. DE-FG02-08ER46482 at Yale University. We are grateful to the Aspen Center for Physics, supported by NSF Grant No. PHYS-106629, for hospitality while this line of work was initiated.

[1] A. Kitaev, Ann. Phys. (Amsterdam) **303**, 2 (2003).
[2] C. Nayak, S. H. Simon, A. Stern, M. Freedman, and S. Das Sarma, Rev. Mod. Phys. **80**, 1083 (2008).
[3] J. Alicea, Rep. Prog. Phys. **75**, 076501 (2012).
[4] C. W. J. Beenakker, Annu. Rev. Condens. Matter Phys. **4**, 113 (2013).
[5] S. R. Elliott and M. Franz, Rev. Mod. Phys. **87**, 137 (2015).
[6] L. Fu and C. L. Kane, Phys. Rev. Lett. **100**, 096407 (2008).
[7] L. Fu and C. L. Kane, Phys. Rev. B **79**, 161408(R) (2009).
[8] R. M. Lutchyn, J. D. Sau, and S. Das Sarma, Phys. Rev. Lett. **105**, 077001 (2010).
[9] Y. Oreg, G. Refael, and F. von Oppen, Phys. Rev. Lett. **105**, 177002 (2010).
[10] S. Nadj-Perge, I. K. Drozdov, B. A. Bernevig, and A. Yazdani, Phys. Rev. B **88**, 020407(R) (2013).
[11] B. Braunecker and P. Simon, Phys. Rev. Lett. **111**, 147202 (2013).
[12] M. M. Vazifeh and M. Franz, Phys. Rev. Lett. **111**, 206802 (2013).
[13] J. Klinovaja, P. Stano, A. Yazdani, and D. Loss, Phys. Rev. Lett. **111**, 186805 (2013).
[14] F. Pientka, L. I. Glazman, and F. von Oppen, Phys. Rev. B **88**, 155420 (2013).
[15] Y. Kim, M. Cheng, B. Bauer, R. M. Lutchyn, and S. Das Sarma, Phys. Rev. B **90**, 060401(R) (2014).
[16] Y. Peng, F. Pientka, L. I. Glazman, and F. von Oppen, Phys. Rev. Lett. **114**, 106801 (2015).
[17] K. T. Law, P. A. Lee, and T. K. Ng, Phys. Rev. Lett. **103**, 237001 (2009).
[18] K. Flensberg, Phys. Rev. B **82**, 180516 (2010).
[19] V. Mourik, K. Zuo, S. M. Frolov, S. R. Plissard, E. P. A. M. Bakkers, and L. P. Kouwenhoven, Science **336**, 1003 (2012).
[20] A. Das, Y. Ronen, Y. Most, Y. Oreg, M. Heiblum, and H. Shtrikman, Nat. Phys. **8**, 887 (2012).
[21] H. O. H. Churchill, V. Fatemi, K. Grove-Rasmussen, M. T. Deng, P. Caroff, H. Q. Xu, and C. M. Marcus, Phys. Rev. B **87**, 241401(R) (2013).
[22] S. Nadj-Perge, I. K. Drozdov, J. Li, H. Chen, S. Jeon, J. Seo, A. H. MacDonald, B. A. Bernevig, and A. Yazdani, Science **346**, 602 (2014).
[23] M. Ruby, F. Pientka, Y. Peng, F. von Oppen, B. W. Heinrich, and K. J. Franke, Phys. Rev. Lett. **115**, 197204 (2015).
[24] L. Yu, Acta Phys. Sin. **21**, 75 (1965).
[25] H. Shiba, Prog. Theor. Phys. **40**, 435 (1968).
[26] A. I. Rusinov, Pis'ma Zh. Eksp. Teor. Fiz. **9**, 146 (1968) [JETP Lett. **9**, 85 (1969)].
[27] A. V. Balatsky, I. Vekhter, and J.-X. Zhu, Rev. Mod. Phys. **78**, 373 (2006).
[28] K. J. Franke, G. Schulze, and J. I. Pascual, Science **332**, 940 (2011).
[29] R. S. Deacon, Y. Tanaka, A. Oiwa, R. Sakano, K. Yoshida, K. Shibata, K. Hirakawa, and S. Tarucha, Phys. Rev. Lett. **104**, 076805 (2010).
[30] E. J. H. Lee, X. Jiang, M. Houzet, R. Aguado, C. M. Lieber, and S. De Franceschi, Nat. Nanotechnol. **9**, 79 (2014).
[31] M. Wimmer, A. R. Akhmerov, J. P. Dahlhaus, and C. W. J. Beenakker, New J. Phys. **13**, 053016 (2011).
[32] F. Pientka, G. Kells, A. Romito, P. W. Brouwer, and F. von Oppen, Phys. Rev. Lett. **109**, 227006 (2012).
[33] A. Yazdani, B. A. Jones, C. P. Lutz, M. F. Crommie, and D. M. Eigler, Science **275**, 1767 (1997).
[34] A. Yazdani, C. M. Howald, C. P. Lutz, A. Kapitulnik, and D. M. Eigler, Phys. Rev. Lett. **83**, 176 (1999).
[35] E. W. Hudson, K. M. Lang, V. Madhavan, S. H. Pan, H. Eisaki, S. Uchida, and J. C. Davis, Nature (London) **411**, 920 (2001).
[36] S.-H. Ji, T. Zhang, Y.-S. Fu, X. Chen, X.-C. Ma, J. Li, W.-H. Duan, J.-F. Jia, and Q.-K. Xue, Phys. Rev. Lett. **100**, 226801 (2008).
[37] M. Ruby, F. Pientka, Y. Peng, F. von Oppen, B. W. Heinrich, and K. J. Franke, Phys. Rev. Lett. **115**, 087001 (2015).
[38] D. M. Badiane, M. Houzet, and J. S. Meyer, Phys. Rev. Lett. **107**, 177002 (2011).
[39] P. San-Jose, J. Cayao, E. Prada, and R. Aguado, New J. Phys. **15**, 075019 (2013).
[40] See Supplemental Material at http://link.aps.org/supplemental/10.1103/PhysRevLett.115.266804 for detail derivation of the Andreev and quasiparticle contribution to the current and conductance in different situations.
[41] J. C. Cuevas, A. Martín-Rodero, and A. Levy Yeyati, Phys. Rev. B **54**, 7366 (1996).
[42] I. Martin and D. Mozyrsky, Phys. Rev. B **90**, 100508 (2014).

[43] A. Levy Yeyati, J. C. Cuevas, A. López-Dávalos, and A. Martín-Rodero, Phys. Rev. B **55**, R6137(R) (1997).

[44] The conductance of Andreev states in p-wave or spin-orbit coupled superconductors is discussed in [40].

[45] The importance of quasiparticle poisoning depends strongly on temperature. Recent experiments on proximity-coupled quantum wires [A. P. Higginbotham, S. M. Albrecht, G. Kiršanskas, W. Chang, F. Kuemmeth, P. Krogstrup, T. S. Jespersen, J. Nygård, K. Flensberg, and C. M. Marcus, Nat. Phys. **11**, 1017 (2015)] find time scales as long as 10 ms.

[46] M. T. Deng, C. L. Yu, G. Y. Huang, M. Larsson, P. Caroff, and H. Q. Xu, Nano Lett. **12**, 6414 (2012).

[47] A. D. K. Finck, D. J. Van Harlingen, P. K. Mohseni, K. Jung, and X. Li, Phys. Rev. Lett. **110**, 126406 (2013).

Supplementary Material for “Robust Majorana conductance peaks for a superconducting lead”

I. GENERAL FORMULA FOR ANDREEV CURRENT INTO SUBGAP STATES

In this section, we outline the derivation of the tunneling current in Eq. (2) of the main text. This standard calculation is included to make the presentation self contained and closely follows the derivation for 2×2 Green functions presented in Ref. [1]. We describe the tunneling contact by the Hamiltonian $\hat{H} = \hat{H}_L + \hat{H}_R + \hat{H}_T$, where the three terms refer to the lead (tip), the sample, and the tunnel coupling. The superconducting tip with chemical potential μ and gap Δ is described by the BCS Hamiltonian

$$\hat{H}_L = \int \frac{d\mathbf{k}}{(2\pi)^3} \left[\sum_\sigma \xi_k \hat{c}^\dagger_{L,\mathbf{k}\sigma} \hat{c}_{L,\mathbf{k}\sigma} + (\Delta \hat{c}^\dagger_{L,\mathbf{k}\uparrow} \hat{c}^\dagger_{L,-\mathbf{k}\downarrow} + \text{h.c.}) \right], \tag{1}$$

where $\xi_k = k^2/2m - \mu$ and $c_{L,\mathbf{k}\sigma}$ ($c^\dagger_{L,\mathbf{k}\sigma}$) annihilates (creates) an electron in the tip with momentum $\mathbf{k}$ and spin σ. The sample Hamiltonian generally takes the form

$$\hat{H}_R = \int dx \sum_{\sigma,\sigma'} \hat{c}^\dagger_{R,\sigma}(x) \mathcal{H}_{R,\sigma\sigma'}(x) \hat{c}_{R,\sigma'}(x), \tag{2}$$

where $\mathcal{H}_{R,\sigma\sigma'}(x)$ is the Hamiltonian in first quantization and $\hat{c}_{R,\sigma}(x)$ annihilates an electron with spin σ at position x in the sample. We choose the superconducting order parameters in tip and sample to be real such that the superconducting phase difference $\phi(\tau)$ enters the tunneling Hamiltonian

$$\hat{H}_T(\tau) = \sum_\sigma \left[t e^{i\phi(\tau)/2} \hat{c}^\dagger_{L,\sigma}(0,\tau) \hat{c}_{R,\sigma}(x,\tau) + t e^{-i\phi(\tau)/2} \hat{c}^\dagger_{R,\sigma}(x,\tau) \hat{c}_{L,\sigma}(0,\tau) \right], \tag{3}$$

where τ the time argument, t is the hopping strength, and $\hat{c}_{L,\sigma}(0,\tau) = \int d\mathbf{k} \hat{c}_{L,\mathbf{k}\sigma}(\tau)/(2\pi)^3$ annihilates an electron in the tip at the tunneling contact, which is located at the origin. The sample is contacted at position x and we suppress the position arguments in the following for simplicity. The time-dependent phase difference between the tip and the sample, $\phi(\tau) = \phi_0 + 2eV\tau$, depends on the voltage V applied to the junction.

We evaluate the current from the Heisenberg equation of motion $\hat{I} = -e\dot{\hat{N}}_L = ie[\hat{N}_L, \hat{H}_T]$, where $\hat{N}_L$ is the electron-number operator of the tip. Taking the expectation value, we obtain

$$I(\tau) = \frac{e}{2} \operatorname{Tr} \left\{ \tau_z \left[\hat{t}(\tau) G^<_{RL}(\tau,\tau) - G^<_{LR}(\tau,\tau) \hat{t}^*(\tau) \right] \right\}, \tag{4}$$

where τ_z is a Pauli matrix acting in Nambu space, $\hat{t}(\tau) = t e^{i\tau_z \phi(\tau)/2} \tau_z$, and we have introduced the lesser Green function in Nambu and spin space with matrix elements given by $(G^<_{\alpha\beta})_{ij} = i\langle \Psi^\dagger_{\beta j} \Psi_{\alpha i} \rangle$. Here the $\Psi_{\alpha j}$ are components of the Nambu spinor $\Psi_\alpha = \left(c_{\alpha,\uparrow}, c_{\alpha,\downarrow}, c^\dagger_{\alpha,\downarrow}, -c^\dagger_{\alpha,\uparrow} \right)^T$ with $\alpha, \beta = L, R$.

We are interested in tunneling processes to lowest order in the tunneling amplitude and therefore neglect Andreev reflections in the tip, which give rise to multiple Andreev reflections. As these processes involve several single-particle tunneling events they enter only at higher orders in the tunneling amplitude. This approximation is exact when the sample is spin polarized (e.g., a proximity-coupled semiconductor nanowire in a strong magnetic field) and one of the two spin components is fully normal reflected. In this case, spin-flipping Andreev reflections in the tip do not contribute to transport.

We follow the nonequilibrium Green function approach described in Ref. [1, 2] setting the offdiagonal elements of the tip Green function in Nambu space to zero and denoting the diagonal elements by $g_L(\omega)$. We obtain the *dc* current

$$I = \frac{et^2}{2h} \int d\omega \operatorname{Tr} \left\{ G^{>,ee}_R(\omega) g^<_L(\omega - eV) - G^{<,ee}_R(\omega) g^>_L(\omega - eV) - g^>_L(\omega + eV) G^{<,hh}_R(\omega) + g^<_L(\omega + eV) G^{>,hh}_R(\omega) \right\}, \tag{5}$$

where $G_R(\omega) = \int d\tau_1 d\tau_2 \exp[i\omega(\tau_1 - \tau_2)] G_R(\tau_1, \tau_2)$ is the sample Green function in presence of the tip, (e, h) are indices in Nambu space denoting particle and hole components, and the trace is taken in spin space. This expression has been derived in Ref. [1] for the case when tip and sample are both spin-conserving s-wave superconductors.

According to the Langreth rule, the lesser Green function of the sample can be written as

$$\begin{aligned} G_R^< &= g_R^< + g_R^r \Sigma_R^r G_R^< + g_R^r \Sigma_R^< G_R^a + g_R^< \Sigma_R^a G_R^a \\ &= (1 - g_R^r \Sigma_R^r)^{-1} g_R^< (1 + \Sigma_R^a G_R^a) + G_R^r \Sigma_R^< G_R^a. \end{aligned} \tag{6}$$

Similar expressions also exist for the greater Green function. The first term involving $g_R^<$ gives rise to a single-particle current which at subgap energies requires inelastic processes in the sample. The second term leads to the current carried by Andreev reflections. The sample self energy due to the presence of the tip can be written as

$$\Sigma(\omega) = t^2 \,\mathrm{diag}(g_L(\omega_-), g_L(\omega_-), g_L(\omega_+), g_L(\omega_+)), \quad \omega_\pm = \omega \pm eV. \tag{7}$$

We now focus on the Andreev current and defer the discussion of the single-particle current to Sec. V. Thus neglecting the first term in Eq. (6) we find Eq. (2) of the main text,

$$\begin{aligned} I(V) &= \frac{et^4}{2h} \int d\omega \;\mathrm{Tr}\left\{ G_R^{r,eh}(\omega) g_L^>(\omega + eV) G_R^{a,he}(\omega) g_L^<(\omega - eV) - G_R^{r,eh}(\omega) g_L^<(\omega + eV) G_R^{a,he}(\omega) g_L^>(\omega - eV) \right\} \\ &+ \frac{et^4}{2h} \int d\omega \;\mathrm{Tr}\left\{ g_L^>(\omega + eV) G_R^{r,he}(\omega) g_L^<(\omega - eV) G_R^{a,eh}(\omega) - g_L^<(\omega + eV) G_R^{r,he}(\omega) g_L^>(\omega - eV) G_R^{a,eh}(\omega) \right\} \\ &= \frac{4\pi^2 et^4}{h} \int d\omega \, \|G_R^{eh}(\omega)\|^2 \rho(\omega + eV)\rho(\omega - eV) \left[n_F(\omega - eV) - n_F(\omega + eV) \right] \end{aligned} \tag{8}$$

where $G_R^{r,eh}$ is the electron-hole block of the (retarded) Green function of the sample and $\|G\| = \sqrt{\mathrm{Tr}\,(GG^\dagger)}$ denotes the Frobenius norm of matrix G. Here we have used the relations $g_L^<(\omega) = 2\pi i n_F(\omega)\rho(\omega)$ and $g_L^>(\omega) = -2\pi i(1 - n_F(\omega))\rho(\omega)$, where $n_F(\omega)$ is the Fermi distribution function, $\rho(\omega) = \nu_0 \, |\omega| \, \theta(\omega^2 - \Delta^2)/\sqrt{\omega^2 - \Delta^2}$ and ν_0 is the normal density of state at the Fermi energy in the tip. Due to the step functions in $\rho(\omega \pm eV)$ the integration interval is restricted to $\omega \in (-(eV - \Delta), eV - \Delta)$. Note that in this interval the self energy is purely imaginary.

II. CONDUCTANCE FOR ZERO-ENERGY BOUND STATES

In this section, we calculate the conductance for isolated Majorana or Andreev states at zero energy, cf. Eqs. (6) and (9) of the main text, neglecting the contributions of all other states in the sample. While the main text focuses on Andreev states in s-wave superconductors, we also consider more general spin structures here.

A. Topological superconductor with Majorana bound states

We first consider a topological superconductor substrate with a single zero-energy Majorana state to the tip. The Majorana wavefunction has the form $\Phi_0(x) = (u_\uparrow(x), u_\downarrow(x)^*, u_\downarrow(x), -u_\uparrow(x)^*)^T$ which maps onto itself under a particle-hole transformation. Neglecting contributions from other states, we can approximate the sample Green function by $g_M(\omega, x, x) = \Phi_0(x)\Phi_0^\dagger(x)/\omega$. Note that we suppress position arguments throughout this section. Including the coupling to the tip the full Green function can be written as

$$G = \frac{1}{\omega - \tilde{\Sigma}_M} \Phi_0 \Phi_0^\dagger, \tag{9}$$

where $\tilde{\Sigma}_M = \Phi_0^\dagger \Sigma \Phi_0$ is the self energy projected onto the Majorana bound state. We obtain

$$G_{eh}^r(\omega) = \frac{1}{\omega + i\pi t^2 \left|\zeta\right|^2 \left[\rho(\omega_+) + \rho(\omega_-)\right]} \begin{pmatrix} u_\uparrow u_\downarrow^* & -u_\uparrow^2 \\ u_\downarrow^{*2} & -u_\downarrow^* u_\uparrow. \end{pmatrix} \tag{10}$$

where we introduced $\left|\zeta\right|^2 = \left|u_\uparrow\right|^2 + \left|u_\downarrow\right|^2$. Thus we find

$$\|G_{eh}(\omega)\|^2 = \frac{\left|\zeta\right|^4}{\omega^2 + \pi^2 t^4 \left|\zeta\right|^4 \left[\rho(\omega_+) + \rho(\omega_-)\right]^2} \tag{11}$$

and using Eq. (8) we obtain the current

$$I_M(V) = \frac{e}{h}\int d\omega\, \frac{\Gamma_e^M(\omega)\Gamma_h^M(\omega)}{\omega^2 + \left(\Gamma_e^M(\omega)+\Gamma_h^M(\omega)\right)^2/4}\left[n_F(\omega - eV) - n_F(\omega + eV)\right], \tag{12}$$

with $\Gamma_{e/h}^M(\omega) = 2\pi t^2 \left|\zeta\right|^2 \rho(\omega_\mp)$.

We now evaluate the current near the threshold $eV = \Delta + \eta$, $\eta \ll \Delta$. The current at the opposite threshold $eV = -\Delta$ follows from $I(-V) = -I(V)$. At low temperatures, $T \ll \Delta$, we can set $n_F(\omega - eV) - n_F(\omega + eV) \sim 1$ and the Majorana current reads

$$I_M(V) \simeq \frac{2e}{h}\int_0^\eta d\omega\, \frac{\Gamma_e^M(\omega)\Gamma_h^M(\omega)}{\omega^2 + (\Gamma_e^M(\omega)+\Gamma_h^M(\omega))^2/4}. \tag{13}$$

To lowest order in η, one can approximate

$$\rho(\omega \pm eV) \simeq \nu_0\sqrt{\frac{\Delta}{2}}\frac{\theta(\eta \pm \omega)}{\sqrt{\eta \pm \omega}}. \tag{14}$$

This yields

$$I_M(V) \simeq \frac{2e}{h}\eta(4-\pi)\Lambda(\eta/\omega_t) \tag{15}$$

as given in Eq. (6) of the main text, where we have defined

$$\Lambda(x) = \frac{4}{4-\pi}\int_0^1 dz\, \frac{1}{\sqrt{1-z^2}}\frac{1}{z^2x^3 + \left(\frac{1}{\sqrt{1+z}} + \frac{1}{\sqrt{1-z}}\right)^2}. \tag{16}$$

At the threshold we find

$$\Lambda(0) = \frac{1}{4-\pi}\int_0^1 dz\, \frac{2\sqrt{1-z^2}}{1+\sqrt{1-z^2}} = 1 \tag{17}$$

which yields Eq. (1) of the main text. At large voltages, $\eta \gg \omega_t$, we instead find a negative differential conductance $dI/dV \propto -1/\eta^3$ in agreement with the lineshape shown in Fig. (1) of the main text.

B. Non-topological Andreev states at zero-energy

A non-topological zero-energy Andreev bound state is characterized by two Nambu spinors

$$\Phi_+ = \begin{pmatrix} \mathbf{u} \\ \mathbf{v} \end{pmatrix}, \quad \Phi_- = \begin{pmatrix} \Theta\mathbf{v} \\ -\Theta\mathbf{u} \end{pmatrix} \tag{18}$$

where $\mathbf{u} = (u_\uparrow, u_\downarrow)^{\mathrm{T}}$, $\mathbf{v} = (v_\downarrow, v_\uparrow)^{\mathrm{T}}$ are functions of space and $\Theta = -i\sigma_y\mathcal{K}$ is the time-reversal operator with $\mathcal{K}$ the complex conjugation. The Lehmann representation of the real space Green function is thus a 4×4 Matrix in Nambu and spin space

$$g(\omega) = \frac{\Phi_+\Phi_+^\dagger + \Phi_-\Phi_-^\dagger}{\omega} = \frac{1}{\omega}\left(\,\Phi_+, \Phi_-\,\right)\begin{pmatrix} \Phi_+^\dagger \\ \Phi_-^\dagger \end{pmatrix}. \tag{19}$$

When spin is a good quantum number the Green function may be reduced to a 2×2 Matrix in particle-hole space only. In the case of pure s-wave pairing, where Cooper pairs are formed from electrons with opposite spin, we can set $u_\downarrow = v_\uparrow = 0$. The spinors Φ_+ and Φ_- then belong to the orthogonal subspaces spanned by $(c_\uparrow, 0, c_\downarrow^\dagger, 0)$ and $(0, c_\downarrow, 0, -c_\uparrow^\dagger)$. The Green function decomposes into two 2×2 blocks, which are related by particle-hole symmetry and have equal contributions to the current. In the opposite case of a spin polarized p-wave superconductor we can set $u_\downarrow(x) = v_\downarrow(x) = 0$. Now Φ_+ and Φ_- belong to the same subspace spanned by $(c_\uparrow, 0, 0, -c_\uparrow^\dagger)$ and the Green function is a single 2×2 matrix.

It is therefore useful to first discuss a general 2×2 Nambu Green function

$$g = \begin{pmatrix} g_{ee} & g_{eh} \\ g_{he} & g_{hh} \end{pmatrix}. \tag{20}$$

We will return to the 4×4 case in Sec. II B 3 when discussing superconductors with spin-orbit coupling. The coupling to the tip can be included through the self-energy $\Sigma^r(\omega) = -i\pi t^2 \,\mathrm{diag}(\rho(\omega_-), \rho(\omega_+))$. The Green function of the coupled system is obtained from the Dyson equation $G = g(1-\Sigma g)^{-1}$. We find

$$G^r_{eh}(\omega) = \frac{g_{eh}(\omega)\omega}{\omega - \lambda(\omega) + i\pi\omega t^2 (g_{ee}(\omega)\rho(\omega_-) + g_{hh}(\omega)\rho(\omega_+))} \tag{21}$$

where $\lambda(\omega) = \omega\pi^2 t^4 \rho(\omega_+)\rho(\omega_-)\det g(\omega)$. Using Eq. (8), we obtain the current

$$I(V) = \frac{4\pi^2 e t^4}{h} \int_{\Delta - eV}^{eV-\Delta} d\omega \, \frac{\omega^2 \left|g_{eh}(\omega)\right|^2 \rho(\omega_-)\rho(\omega_+)}{[\omega - \lambda(\omega)]^2 + \pi^2\omega^2 t^4 \left[(g_{ee}(\omega)\rho(\omega_-) + g_{hh}(\omega)\rho(\omega_+)\right]^2}. \tag{22}$$

We now calculate the conductance for a zero-energy Andreev state in the limiting cases of pure s-wave and spinless p-wave pairing and for a general spin-structure of the order parameter in the presence of spin-orbit coupling. The result for the three cases are compared in Fig. 1.

1. *s-wave pairing*

When $u_\downarrow = v_\uparrow = 0$ the Green function in Eq. (24) is block diagonal. The 2×2 block in the basis $(c_\uparrow, c_\downarrow^\dagger)$ reads

$$g = \frac{1}{\omega}\begin{pmatrix} \left|u_\uparrow\right|^2 & u_\uparrow v_\downarrow^* \\ u_\downarrow^* v_\uparrow & \left|v_\downarrow\right|^2 \end{pmatrix}. \tag{23}$$

We find $\det g(\omega) = 0$ and thus $\lambda(\omega)$ vanishes. Using Eq. (27), we arrive at the current as given in Eq. (9) of the main text,

$$I_A(V) = \frac{2e}{h}\int_{\Delta - eV}^{eV-\Delta} d\omega \, \frac{\Gamma_e^A(\omega)\Gamma_h^A(\omega)}{\omega^2 + \left(\Gamma_e^A(\omega) + \Gamma_h^A(\omega)\right)^2/4} \tag{24}$$

where $\Gamma_e^A(\omega) = 2\pi t^2 \left|u_\uparrow\right|^2 \rho(\omega_-)$, $\Gamma_h^A(\omega) = 2\pi t^2 \left|v_\downarrow\right|^2 \rho(\omega_+)$. We have included an extra factor of two to account for the second 2×2 block of the Green function which yields an equal contribution as a consequence of particle-hole symmetry. Near the threshold when $eV = \Delta + \eta$, $\eta \ll \Delta$ we find

$$I_A(V) = 2 I_M(V) f(|u(r)|^2/|v(r)|^2), \tag{25}$$

which can be obtained by a similar analysis as for the Majorana bound state in the previous section. The dimensionless function

$$f(x) = \frac{2x}{4-\pi}\int_{-1}^{1} dz \sqrt{1-z^2}/(x\sqrt{1-z} + \sqrt{1+z})^2 \tag{26}$$

takes on values between 0 and 1. Thus, the threshold differential conductance is

$$\left.\frac{dI_A}{dV}\right|_{eV=\Delta} = \frac{4e^2}{h} f(|u(r)|^2/|v(r)|^2)(4-\pi). \tag{27}$$

2. *p-wave pairing*

In a spin-polarized p-wave superconductor Cooper pairs we can set $u_\downarrow = v_\downarrow = 0$. The Green function of an Andreev state reduces to a single 2×2 matrix

$$g = \frac{1}{\omega}\begin{pmatrix} \left|u_\uparrow\right|^2 + \left|v_\uparrow\right|^2 & 2u_\uparrow v_\uparrow^* \\ 2u_\uparrow^* v_\uparrow & \left|u_\uparrow\right|^2 + \left|v_\uparrow\right|^2 \end{pmatrix}. \tag{28}$$

We have introduced $\lambda(\omega) = \pi^2 t^4 \rho(\omega_+)\rho(\omega_-)(|u_\uparrow|^2 - |v_\uparrow|^2)^2/\omega$ and using Eq. (27) we obtain

$$I_A(V) = \frac{16\pi^2 e t^4}{h} \int_{-\eta}^{\eta} d\omega \, \frac{|u_\uparrow v_\uparrow|^2 \rho(\omega_-)\rho(\omega_+)}{\left[\omega - \frac{\rho(\omega_-)\rho(\omega_+)\pi^2|t^4|}{\omega}\left(|u_\uparrow|^2 - |v_\uparrow|^2\right)^2\right]^2 + \pi^2 t^4 (|u_\uparrow|^2 + |v_\uparrow|^2)^2 [\rho(\omega_+) + \rho(\omega_-)]^2} \tag{29}$$

with $eV = \Delta + \eta$. Close to the threshold $\eta \to 0$ the denominator is dominated by $\lambda(\omega) \propto 1/\eta^2$ and we generically find $I \propto \eta^4 \theta(\eta)$. Hence the conductance $G \propto \eta^3 \theta(\eta)$ is continuous in contrast to the case of s-wave pairing. At certain points in space it may be possible that $|u_\uparrow| = |v_\uparrow|$ in which case the conductance still jumps at the threshold. Slightly moving away from such points should restore the smooth onset of the conductance at the threshold. The conductance exhibits a peak at the characteristic scale $\eta \sim \omega_t$ with $\omega_t = (\max\{|u_\uparrow|^2, |v_\uparrow|^2\}\nu_0 t^2 \sqrt{\Delta})^{2/3}$ as shown in Fig. 1.

3. *Generic case with spin-orbit coupling*

Realistic proposals of topological superconductors typically involve a mixture of s-wave and p-wave pairing. In particular, such pairing arises in any superconductor with spin-orbit coupling. In this case all components of $\mathbf{u}$ and $\mathbf{v}$ are generically nonzero. The full sample Green function including the coupling to the tip due to the self-energy in Eq. (7) can be written in terms of Dyson series

$$G = \frac{1}{\omega} \begin{pmatrix} \Phi_+ & \Phi_- \end{pmatrix} \left[1 + \frac{1}{\omega} \begin{pmatrix} \Phi_+^\dagger \\ \Phi_-^\dagger \end{pmatrix} \Sigma \begin{pmatrix} \Phi_+ & \Phi_- \end{pmatrix} + \dots \right] \begin{pmatrix} \Phi_+^\dagger \\ \Phi_-^\dagger \end{pmatrix}. \tag{30}$$

A straightforward calculation reveals

$$G^r_{eh} = \frac{\left[(\omega - \tilde{\Sigma}^r_{--})\mathbf{u} + \tilde{\Sigma}^r_{-+}(\mathcal{C}\mathbf{v})\right]\mathbf{v}^\dagger - \left[(\omega - \tilde{\Sigma}^r_{++})\mathcal{C}\mathbf{v} + \tilde{\Sigma}^r_{+-}\mathbf{u}\right](\mathcal{C}\mathbf{u})^\dagger}{\omega^2 - \omega(\tilde{\Sigma}^r_{++} + \tilde{\Sigma}^r_{--}) + \tilde{\Sigma}^r_{++}\tilde{\Sigma}^r_{--} - \tilde{\Sigma}^r_{+-}\tilde{\Sigma}^r_{-+}} \tag{31}$$

where the projected self-energies are

$$\tilde{\Sigma}^r_{++}(\omega) = -i\pi t^2 \left[\|\mathbf{u}\|^2 \rho(\omega_-) + \|\mathbf{v}\|^2 \rho(\omega_+)\right] \tag{32a}$$

$$\tilde{\Sigma}^r_{--}(\omega) = -i\pi t^2 \left[\|\mathbf{v}\|^2 \rho(\omega_-) + \|\mathbf{u}\|^2 \rho(\omega_+)\right] \tag{32b}$$

$$\tilde{\Sigma}^r_{+-}(\omega) = -i\pi t^2 \langle \mathbf{u}, \Theta\mathbf{v}\rangle \left[\rho(\omega_-) + \rho(\omega_+)\right] \tag{32c}$$

$$\tilde{\Sigma}^r_{-+}(\omega) = -i\pi t^2 \langle \Theta\mathbf{v}, \mathbf{u}\rangle \left[\rho(\omega_-) + \rho(\omega_+)\right] = -\tilde{\Sigma}^r_{+-}(\omega)^*, \tag{32d}$$

and $\langle \cdot, \cdot \rangle$ is the inner product. In the above derivations, we have used the anti-unitarity of the time-reversal operator and that $\Theta^2 = -1$, namely $\langle \mathbf{u}, \Theta\mathbf{v}\rangle = \langle \mathbf{v}, \Theta^\dagger \mathbf{u}\rangle = -\langle \mathbf{v}, \Theta\mathbf{u}\rangle$. Then the norm can be written as

$$\|G_{eh}\|^2 = W \frac{2\omega^2 + W\pi^2 t^4 Y \left\{[\rho(\omega_+)^2 + \rho(\omega_-)^2] Z + 4\rho(\omega_+)\rho(\omega_-) Y\right\}}{\left\{\omega^2 - W\pi^2 t^4 \left[(\rho(\omega_+)^2 + \rho(\omega_-)^2) Y + Z\rho(\omega_+)\rho(\omega_-)\right]\right\}^2 + W\omega^2\pi^2 t^4 (Z+2)[\rho(\omega_-) + \rho(\omega_+)]^2} \tag{33}$$

where

$$W = \|\mathbf{u}\|^2 \|\mathbf{v}\|^2 + |\langle \mathbf{u}, \Theta\mathbf{v}\rangle|^2 \tag{34a}$$

$$Y = \left(\|\mathbf{u}\|^2 \|\mathbf{v}\|^2 - |\langle \mathbf{u}, \Theta\mathbf{v}\rangle|^2\right)/W \tag{34b}$$

$$Z = \left(\|\mathbf{u}\|^4 + \|\mathbf{v}\|^4 - 2\,|\langle \mathbf{u}, \Theta\mathbf{v}\rangle|^2\right)/W. \tag{34c}$$

The differential conductance is then a function of Y, Z and $\eta/\tilde{\omega}_t$, where $\tilde{\omega}_t^3 = \Delta\nu_0^2\pi^2 t^4 W$. The parameter Y interpolates between s-wave pairing ($Y = 1$, Sec. II B 1), where the threshold conductance is maximal, p-wave pairing ($Y = 0$, Sec. II B 2), where the threshold conductance is zero. In Fig. 1 we show the conductance for different values of this parameter.

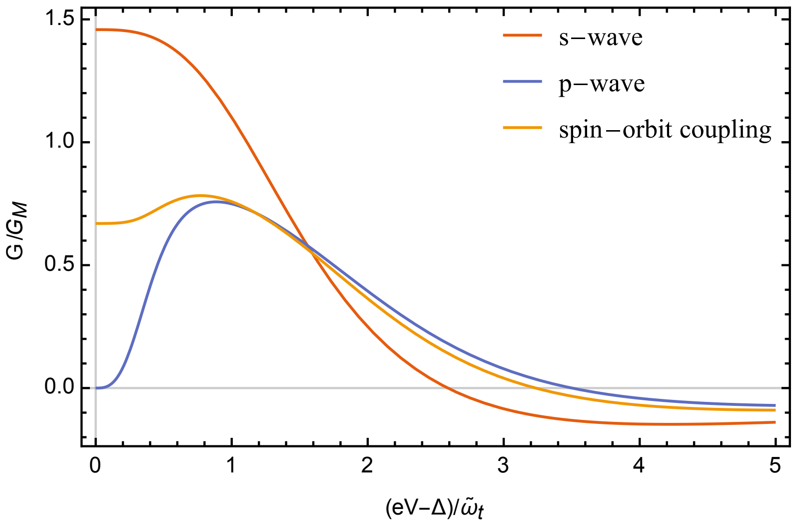

FIG. 1. Conductance near the threshold. The parameters for the s-wave pairing case are $Y = 1$, $Z = 4.25$. For the p-wave pairing case, $Y = 0$, $Z = 1.13$. And in the case with spin-orbit coupling, $Y = 0.05$, $Z = 0.74$.

III. CONTINUUM CONTRIBUTION TO THE CONDUCTANCE

In this section, we provide details on evaluating the contribution of the quasiparticle continuum to the conductance near the threshold. We identify two different effects of the continuum states, namely, (a) a possible smoothening of the step in the bound-state conductance [see Fig. 1(a) and Eq. (10) of the main text] due to interference between resonant and nonresonant Andreev reflections and (b) additonal contributions to the conductance from nonresonant Andreev reflections. The latter effect becomes important when probing the conductance away from the bound state, where resonant and nonresonant Andreev reflections compete as discussed in the main text.

A. Continuum effect on resonant Andreev reflections

1. General considerations

As follows from Sec. II, the lineshape of a zero-energy Andreev state in an s-wave superconductor closely resembles that of a Majorana state. In particular, the conductance exhibits a step at the threshold $eV = \Delta$ in both cases. We now revisit these two cases and discuss whether this step is robust when the quasiparticle continuum is taken into account. As discussed in the main text, we find a suppression of the conductance for the Andreev state close to the threshold, while the step remains robust for the Majorana. This behavior is reminiscent of tunneling from a normal metal tip, where Majorana states appear as a robust zero-bias conductance peaks while zero-energy Andreev states generically exhibit zero conductivity.

For simplicity, we focus our analysis on samples in which spin is a good quantum number and that can be described in 2×2 Nambu space. An example of a more general model is discussed in Sec. IV. In particular, we consider an s-wave superconductor with a zero-energy Andreev state and a spinless p-wave superconductor with a Majorana state. In these cases the Lehmann representation of the Green function reads

$$g(\omega) = \frac{\Phi_0(x)\Phi_0^\dagger(x)}{\omega} + \sum_n \int_{|E|\geq\Delta_s} dE \frac{\Phi_{E,n}(x)\Phi_{E,n}^\dagger(x)}{\omega - E}, \tag{35}$$

where the spinor Φ_0 describes a single zero-energy bound state and $\Phi_{E,n}$ are continuum states above the gap Δ_s with energy E and index n labeling the degeneracy. Using this expression in the Green function in the presence of a tunnel coupling in Eq. (26) and expanding to lowest order in energy, we obtain

$$G^r_{eh}(\omega) = \frac{\Phi_0(r)\Phi_0^\dagger(r)}{\omega - \lambda(\omega) + i(\Gamma_e + \Gamma_h)/2}. \tag{36}$$

To determine the effect of the extra term $\lambda(\omega) \propto \det g(\omega)$ we analyze the energy dependence of $\det g(\omega)$ in more detail. The function $g(\omega)$ has a simple pole at $\omega = 0$ and branch cuts on the real axis for $|\omega| > \Delta_s$ but is analytic elsewhere. The residue of $g(\omega)$ at $\omega = 0$ is $\Phi_0(x)\Phi_0^\dagger(x)$ which has zero determinant and we can thus write

$$\lim_{\omega\to 0} \omega^2 \det g(\omega) = 0 \tag{37}$$

and expand $\det g(\omega)$ as a Laurent series around $\omega = 0$

$$\det g(\omega) = \sum_{n=-1}^{\infty} c_n \omega^n. \tag{38}$$

Furthermore $g(\omega)$ is hermitian at nonzero subgap energies and thus its determinant is real. We now determine the lowest-order cotribution to $\det g$ for Majorana and Andreev states.

2. Majorana states

The Green function of a topological superconductor satisfies particle-hole symmetry $U_{\mathcal{C}} g(\omega) U_{\mathcal{C}}^\dagger = -g^*(-\omega)$ with a unitary operator $U_{\mathcal{C}}$. This yields $\det g(\omega) = -\det g^*(-\omega)$ and reality further requires $\det g(\omega)$ to be an even function of ω. Hence, we obtain $c_{-1} = 0$ and $\lambda(\omega) \sim \omega t^4 \rho(\omega_+)\rho(\omega_-)$, which approaches a constant in the limit $\eta = eV - \Delta \to 0^+$ with $|\omega| < \eta$. The Majorana contribution to the current reads

$$I_M(V) \simeq \frac{2e}{h} \int_0^\eta d\omega \, \frac{\Gamma_e^M(\omega)\Gamma_h^M(\omega)}{(\omega-\lambda)^2 + (\Gamma_e^M(\omega) + \Gamma_h^M(\omega))^2/4}. \tag{39}$$

The rates $\Gamma_{e/h}^M$ diverge at the threshold and the continuum term $\lambda(\omega)$ becomes negligible. The threshold conductance of Majorana states thus remains unaffected by the continuum states.

3. Zero-energy Shiba state

In contrast to Majoranas, the 2×2 Green function describing zero-energy Andreev states generically does not satisfy particle-hole symmetry and thus $c_{-1} \neq 0$. As an example of a system with trivial zero-energy Andreev state, we consider a magnetic impurity in an s-wave superconductor, which induces a bound state localized at the impurity, known as a Shiba state. The Hamiltonian describing a Shiba state localized at the origin due to a magnetic impurity can be written in first quantization as

$$\mathcal{H}_S(\mathbf{x}) = \mathcal{H}_{BCS}(\mathbf{x}) + (V\tau_z - JS\sigma_z)\delta(\mathbf{x}), \tag{40}$$

where τ_i and σ_i are Pauli matrices in Nambu and spin space, where V and JS are the potential scattering and exchange coupling strength. Since $\mathcal{H}_S$ is block diagonal in spin space, we only need to deal with one of the blocks, say $\sigma_z = 1$. The other block related to the first by particle-hole symmetry contributes a second (equivalent) zero-energy state as mentioned above. The sample Green function g_S at the impurity position has the form [1]

$$g_S(\omega) = \frac{\pi\nu_s}{2\omega\alpha - (1-\alpha^2+\beta^2)\sqrt{\Delta_s^2-\omega^2}} \begin{pmatrix} \omega + (\alpha+\beta)\sqrt{\Delta_s^2-\omega^2} & \Delta_s \\ \Delta_s & \omega + (\alpha-\beta)\sqrt{\Delta_s^2-\omega^2} \end{pmatrix}, \tag{41}$$

where ν_s and Δ_s are the normal density of states and gap of the sample and we introduced the dimensionless parameters $\alpha = \pi\nu_0 JS$ and $\beta = \pi\nu_0 V$. The Shiba bound state energy is given by

$$\epsilon_0 = \Delta_s \frac{1-\alpha^2+\beta^2}{\sqrt{(1-\alpha^2+\beta^2)^2 + 4\alpha^2}}. \tag{42}$$

Thus, since we focus on zero-energy bound states we set $\alpha^2 = 1 + \beta^2$. After a straightforward calculation, we obtain

$$\omega \det g(\omega) \simeq \frac{\pi^2\nu_s^2\Delta_s}{2\alpha} \tag{43}$$

for small ω. From the Green function we also obtain (for $V > 0$)

$$|u|^2 = \pi\nu_s\Delta_s(\alpha + \sqrt{\alpha^2 - 1}), \tag{44}$$

$$|v|^2 = \pi\nu_s\Delta_s(\alpha - \sqrt{\alpha^2 - 1}). \tag{45}$$

Near the threshold, for small $\eta = eV - \Delta$, the term $\propto \lambda(\omega)$ in the denominator of Eq. (27) dominates and we find

$$I_A(V) = \frac{2e}{h}\frac{16\eta^2\alpha^2}{\nu_0^2\nu_s^2\pi^3 t^4\Delta}. \tag{46}$$

Thus the conductance $dI_A/d\eta$ is zero at $eV = \Delta$ and then rises linearly as described by Eq. (10) of the main text. This originates from the interference between resonant and nonresonant Andreev reflection, which suppresses the differential conductance at $eV = \Delta$. In order to estimate the width of this suppression we determine the value of η when the term λ in the denominator of Eq. (27) becomes of the same order of magnitude as the tunneling broadening $\sim \omega t^2[g_{ee}\rho(\omega_-) + g_{hh}\rho(\omega_+)]$, i.e.,

$$\frac{\nu_0^2\Delta t^4\omega \det g(\omega)}{\eta} \sim \nu_0|t|^2\left(|u|^2 + |v|^2\right)\sqrt{\frac{\Delta}{\eta}}, \tag{47}$$

which yields

$$\eta \sim \frac{\nu_0^2\nu_s^2 t^4\Delta}{\alpha^4} \sim \frac{\mathcal{T}^2\Delta}{\alpha^4}. \tag{48}$$

B. Nonresonant Andreev reflection

We now determine the conductance due to nonresonant Andreev reflections from the quasiparticle continuum in the substrate. To evaluate the conductance contributions from the continuum, we focus on a specific model of a Dirac Hamiltonian with a domain wall, where the mass changes sign. We first calculate the real space Green function and then evaluate the conductance as a function of separation from the impurity.

1. *Topological superconductor Green function*

As an example of a topological superconductor hosting a Majorana state we calculate the Green function of a Dirac Hamiltonian with a domain wall

$$H_{\text{Dirac}} = -iv_F\partial_x\tau_x - m[\theta(x) - \theta(-x)]\tau_z \tag{49}$$

in the spinless Nambu basis $(\psi, \psi^\dagger)$. Here v_F is the velocity of the Dirac fermion and m is the effective mass. The system satisfies particle-hole symmetry $\{\mathcal{C}, H_{\text{Dirac}}\} = 0$ with the charge conjugation operator $\mathcal{C} = \tau_x\mathcal{K}$, where $\mathcal{K}$ is the complex conjugation. This is a generic model for the low-energy behavior of a topological superconductor close to the phase transition. Specifically, a spinless p-wave superconductor with a chemical potential close to the bottom of the band can be approximated by Eq. (54). To compute the eigenstates of this Hamiltonian it is convenient to solve for the rotated Hamiltonian $e^{i\pi\tau_y/4}H_{\text{Dirac}}e^{-i\pi\tau_y/4}$. Notice that the charge conjugation operator is now given by $\tau_z\mathcal{K}$.

One readily shows that the domain wall supports a single Majorana state at zero energy with the wavefunction

$$\psi_0(x) = \sqrt{\frac{m}{2v_F}}e^{-m|x|/v_F}\begin{pmatrix} i \\ 1 \end{pmatrix}. \tag{50}$$

All other states in the system are extended with energies above the gap m. The wavefunctions of the continuum states can be determined using the ansatz

$$\psi_{\pm\epsilon}(x) = \begin{pmatrix} m\text{sgn}\{x\} \\ -(v_F p \mp \epsilon) \end{pmatrix} e^{ipx}\left[A\theta(-x) + B\theta(x)\right] + \begin{pmatrix} m\text{sgn}\{x\} \\ (v_F p \pm \epsilon) \end{pmatrix} e^{-ipx}\left[C\theta(-x) + D\theta(x)\right], \tag{51}$$

where $v_F p = \sqrt{\epsilon^2 - m^2}$ and ϵ is the positive eigenvalue. The matching condition at $x = 0$ leads to

$$A + B + C + D = 0, \qquad v_F p(A - B - C + D) \mp \epsilon(A - B + C - D) = 0. \tag{52}$$

For positive-energy solutions, we get

$$\frac{A + D}{A + C} = \frac{\epsilon}{v_F p} = \sqrt{1 + \left(\frac{m}{v_F p}\right)^2}. \tag{53}$$

For incoming waves from $x = -\infty$ we require $D = 0$ and obtain

$$C^{in} = \frac{v_F p - \epsilon}{\epsilon} A^{in}, \qquad B^{in} = -\frac{v_F p}{\epsilon} A^{in}. \tag{54}$$

Similarly, for outgoing waves to $x = -\infty$ we have $A = 0$ and thus

$$C^{out} = \frac{v_F p}{\epsilon} D^{out}, \qquad B^{out} = -\frac{\epsilon + v_F p}{\epsilon} D^{out}. \tag{55}$$

This yields the scattering states

$$\begin{aligned}
\psi_\epsilon^{in}(x) &= A\left\{\begin{pmatrix} -m\theta(-x) - m\frac{v_F p}{\epsilon}\theta(x) \\ (\epsilon - v_F p)\theta(-x) - \frac{v_F p}{\epsilon}(\epsilon - v_F p)\theta(x) \end{pmatrix} e^{ipx} + \frac{v_F p - \epsilon}{\epsilon}\begin{pmatrix} -m \\ v_F p + \epsilon \end{pmatrix}\theta(-x)e^{-ipx}\right\}, \\
\psi_\epsilon^{out}(x) &= D\left\{\frac{\epsilon + v_F p}{\epsilon}\begin{pmatrix} -m \\ v_F p - \epsilon \end{pmatrix}\theta(x)e^{ipx} + \begin{pmatrix} m\theta(x) - m\frac{v_F p}{\epsilon}\theta(-x) \\ (v_F p + \epsilon)\theta(x) + v_F p\frac{v_F p + \epsilon}{\epsilon}\theta(-x) \end{pmatrix} e^{-ipx}\right\}.
\end{aligned} \tag{56}$$

One can easily check that incoming and outgoing states are orthogonal $\langle\psi_\epsilon^{out}|\psi_\epsilon^{in}\rangle = 0$. From the normalization conditions $\|\psi_\epsilon^{in}\| = \|\psi_\epsilon^{out}\| = 1$ we obtain the coefficients $A = [2L\epsilon(\epsilon - v_F p)]^{-1/2}$ and $D = [2L\epsilon(\epsilon + v_F p)]^{-1/2}$ for a system of size L. The Green function can now be obtained from its spectral decomposition

$$\tilde{g}(x, x'; \omega) = \frac{\psi_0(x)\psi_0(x')^\dagger}{\omega} + \sum_{\substack{\epsilon>0, \\ \alpha=in,out}} \left[\frac{\psi_\epsilon^\alpha(x)\psi_\epsilon^\alpha(x')^\dagger}{\omega - \epsilon} + \frac{(\mathcal{C}\psi_\epsilon^\alpha(x))\,(\mathcal{C}\psi_\epsilon^\alpha(x'))^\dagger}{\omega + \epsilon}\right] \tag{57}$$

where we have used the charge conjugation operator $\mathcal{C}$ to relate the negative solution to the positive ones. Focusing on $x = x' = 0$ for simplicity we find the wavefunctions of the continuum states

$$\psi_\epsilon^{in}(0) = -\frac{1}{\sqrt{2L\epsilon(\epsilon - v_F p)}}\frac{v_F p}{\epsilon}\begin{pmatrix} m \\ \epsilon - v_F p \end{pmatrix}, \qquad \psi_\epsilon^{out}(0) = \frac{1}{\sqrt{2L\epsilon(\epsilon + v_F p)}}\frac{v_F p}{\epsilon}\begin{pmatrix} -m \\ \epsilon + v_F p \end{pmatrix}. \tag{58}$$

Using Eq. (62), we obtain the Green function

$$\tilde{g}(0, 0; \omega) = \frac{m}{2v_F\omega}\begin{pmatrix} 1 & i \\ -i & 1 \end{pmatrix} + \frac{1}{L}\sum_{\epsilon>0}\frac{\epsilon^2 - m^2}{\epsilon^2}\frac{2\omega}{\omega^2 - \epsilon^2}\begin{pmatrix} 1 & 0 \\ 0 & 1 \end{pmatrix} = \frac{1}{2v_F}\frac{m}{\omega}\begin{pmatrix} \sqrt{1 - (\omega/m)^2} & \dfrac{i}{\sqrt{1 - (\omega/m)^2}} \\ -i & \end{pmatrix}. \tag{59}$$

Here we have used

$$\frac{1}{L}\sum_{\epsilon>0} = \int\frac{dp}{2\pi} = \frac{1}{2\pi v_F}\int_m^\infty d\epsilon\frac{\epsilon}{\sqrt{\epsilon^2 - m^2}}. \tag{60}$$

Notice that the matrix commutes with τ_y, and thus commutes with the rotation operation introduced at the beginning. We find the Green function for the original Hamiltonian H_{Dirac}

$$g(0, 0; \omega) = \pi\nu_s\frac{m}{\omega}\begin{pmatrix} \sqrt{1 - (\omega/m)^2} & \dfrac{i}{\sqrt{1 - (\omega/m)^2}} \\ -i & \end{pmatrix}, \tag{61}$$

where $\nu_s = (2\pi v_F)^{-1}$ is the normal density of states.

Away from the mass domain wall, the sample Green function at $x \geq 0$ can be computed similarly from Eq. (61) and (62), which yields

$$\begin{aligned}
g_{ee}(x) = g_{hh}(x) &= \frac{\pi\nu_s}{\sqrt{1 - (\omega/m)^2}}\left(\frac{m}{\omega}e^{-2x/\xi} - \frac{\omega}{m}\right) \\
g_{eh}(x) = g_{he}(x)^* &= \pi\nu_s\left(i\frac{m}{\omega}e^{-2x/\xi} - \frac{1 - e^{-2x/\xi}}{\sqrt{1 - (\omega/m)^2}}\right).
\end{aligned} \tag{62}$$

where $\xi = [2\pi\nu_s m\sqrt{1 - (\omega/m)^2}]^{-1} = v_F/m\sqrt{1 - (\omega/m)^2}$ is the coherence length that characterizes the exponential decay of the Majorana wavefunction.

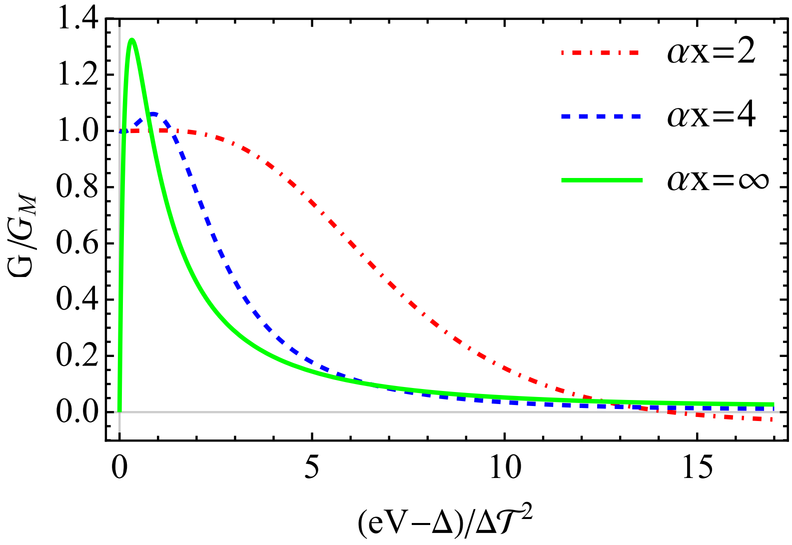

FIG. 2. Differential conductance of the topological superconductor with a mass domain wall. The three curves correspond different tip locations measured from the domain wall. For all curves we have set $\Delta\mathcal{T}^2/m = 0.016$.

2. Differential conductance away from the Majorana state

The Green function has a pole at zero energy whose amplitude decays exponentially away from the domain wall reflecting the probability density of the Majorana bound state. This singular part fully determines the threshold conductance and yields the quantized value G_M. Notice that $\lim_{\omega\to 0}\omega \det g = 0$ guarantees the robustness of this quantization consistent with the general argument based on particle-hole symmetry given in Sec. III A 2. The conductance at voltages above the threshold depends on the competition between the singular part and a nonsingular contribution which originates from the quasiparticle continuum. The continuum contribution can be readily evaluated for $x \to \infty$, where the Green function describes a homogeneous p-wave superconductor,

$$g(\omega) = -\frac{\pi\nu_s}{\sqrt{m^2-\omega^2}}\begin{pmatrix} \omega & m \\ m & \omega \end{pmatrix}. \tag{63}$$

Using this expression in the current formula in Eq. (27) we find

$$\begin{aligned} I &= \frac{4\pi^2 e\,|t|^4}{h}\int_\eta^\eta d\omega \frac{\rho_+\rho_-\pi^2\nu_s^2 m^2}{(m^2-\omega^2)\,(1+\pi^4\nu_s^2 t^4\rho_+\rho_-)^2+\pi^4\nu_s^2 t^4\omega^2(\rho_++\rho_-)^2} \\ &\simeq \frac{8e}{h}\Delta\mathcal{T}^2\int_{-1}^{1} dz \frac{\sqrt{1-z^2}}{\left(2\sqrt{1-z^2}+\Delta\mathcal{T}^2/\eta\right)^2}, \end{aligned} \tag{64}$$

where we introduced the transmission probability of the junction $\mathcal{T} = \pi^2\nu_s\nu_0 t^2$ and assumed $\Delta\mathcal{T}^2 \ll m$. This yields the conductance

$$G(V) = \frac{8G_M}{4-\pi}\int_0^1 dz\,\frac{(2\eta/\Delta\mathcal{T}^2)\sqrt{1-z^2}}{(1+(2\eta/\Delta\mathcal{T}^2)\sqrt{1-z^2})^3}. \tag{65}$$

The conductance has a maximum at $\eta \sim \Delta\mathcal{T}^2$ with a magnitude $\sim 1.3G_M$ and a peak width $\sim \Delta\mathcal{T}^2$. In Fig. 2 we show the differential conductance *vs* voltage for different separations between tip and domain wall. As the tip is moved away from the domain wall, nonresonant Andreev reflections become more important and the conductance peak becomes narrower and slightly higher.

IV. DOMAIN WALL AT THE QSHI EDGE

While the quantized conductance step for the Majorana state derived in the main text is model independent, its robustness to continuum effects was only shown for spinless models described by a 2×2 Hamiltonian. As an example of a more realistic model, we consider the edge of a quantum spin Hall insulator (QSHI). We calculate the threshold conductance including the continuum contribution for the case when the sample is contacted at the domain wall. We find the universal step at the threshold to be robust in line with the results for the spinless case. This suggests that the conductance step at the threshold may be robust even for more general models of topological superconductors.

The edge of a QSHI, with a domain wall at the origin, can be described by the first quantized Hamiltonian

$$\begin{aligned}\mathcal{H}(x) &= -iv_F\partial_x\sigma_z\tau_z + \Delta(x)\tau_x + B(x)\sigma_x,\\ \Delta(x) &= M - \frac{m(x)}{2},\\ B(x) &= M + \frac{m(x)}{2},\end{aligned}$$

where

$$m(x) = m\left[\theta(x) - \theta(-x)\right]. \tag{66}$$

Applying the unitary transformation $U = e^{\frac{i\pi}{4}\sigma_y}e^{i\frac{\pi}{4}\tau_y}$, we have

$$\mathcal{H} \to \tilde{\mathcal{H}} = U\mathcal{H}U^\dagger = \begin{pmatrix} M & 0 & 0 & -iv_F\partial_x \\ 0 & -m(x) & -iv_F\partial_x & 0 \\ 0 & -iv_F\partial_x & m(x) & 0 \\ -iv_F\partial_x & 0 & 0 & -M \end{pmatrix}.$$

Let $M \gg m$, and focus on the inner block, which decribes a Dirac field with a domain wall created by a mass jump, as discussed in Sec. III B 1. According to Eq. (66), the Green function at the domain wall is

$$\tilde{g}(0,\omega) = \pi\nu_s\frac{m}{\omega}\begin{pmatrix} 0 & 0 & 0 & 0 \\ 0 & \sqrt{1-\frac{\omega^2}{m^2}} & i & 0 \\ 0 & -i & \sqrt{1-\frac{\omega^2}{m^2}} & 0 \\ 0 & 0 & 0 & 0 \end{pmatrix}. \tag{67}$$

We rotate it back to the original basis $g(0,\omega) = U\tilde{g}(0,\omega)U^\dagger$ and obtain the full Green function

$$G(0,\omega) = g(0,\omega)(1-\Sigma(\omega)g(0,\omega))^{-1}, \tag{68}$$

where the self energy is given by

$$\Sigma(\omega) = t^2\,\mathrm{diag}(g(\omega_-), g(\omega_-), g(\omega_+), g(\omega_+)). \tag{69}$$

Calculation reveals

$$\begin{aligned} G^{r,eh}(0,\omega) = {} & \frac{\pi\nu_s m}{\omega\left[1 + t^4\pi^4\nu_s^2(\rho(\omega_-)+\rho(\omega_+))^2\right] + 2i\pi^2\nu_s m t^2\sqrt{1-\frac{\omega^2}{m^2}}\left[\rho(\omega_-)+\rho(\omega_+)\right]} \\ & \times \begin{pmatrix} i & \sqrt{1-\frac{\omega^2}{m^2}} - i\pi\left(\frac{\pi\nu_s\omega}{m}\right)t^2(\rho(\omega_-)+\rho(\omega_+)) \\ \sqrt{1-\frac{\omega^2}{m^2}} - i\pi\left(\frac{\pi\nu_s\omega}{m}\right)t^2(\rho(\omega_-)+\rho(\omega_+)) & -i \end{pmatrix}. \end{aligned}$$

Denoting $\Gamma_{e/h} = 4\pi^2\nu_s m t^2\rho(\omega_\mp)$ we find

$$\|G^{eh}(0,\omega)\|^2 = \frac{2(\pi\nu_s)^2\left[2m^2 - \omega^2(1-(\Gamma_e+\Gamma_h)^2/16m^2)\right]}{\omega^2\left[1-(\Gamma_e+\Gamma_h)^2/16m^2\right]^2 + (\Gamma_e+\Gamma_h)^2/4}. \tag{70}$$

We readily verify that the denominator is dominated by the second term at the threshold. In particular, we see the continuum contribution in the denominator appears proportional to ω^2 as for the spinless case. Hence, the conductance quantization at $eV = \Delta$ is unaffected by the continuum contribution in this model.

V. SINGLE-PARTICLE CURRENT CONTRIBUTION TO THE CONDUCTANCE

In this section we analyze the single-particle tunneling current that can flow in addition to the Andreev current discussed above. A single-particle current is possible if the quasiparticle occupying the bound state can relax to the quasiparticle continuum. Such relaxation can occur, e.g., due to inelastic transitions assisted by phonons or photons. We concentrate on the Majorana state, although a similar analysis is possible for a trivial Andreev state. We neglect the quasiparticle continuum and include relaxation as a phenomenological parameter, without specifying its microscopic origin. We first derive the single-particle current [given in Eq. (11) of the main text], from which we then calculate the threshold conductance from single-particle tunneling [Eq. (12)].

A. Self energy due to relaxation processes

Let us assume that the local environment of the Majorana state introduces relaxation processes, induced by phonons or photons, via the self-energy Σ_{ph}. The substrate Green function can be determined from the Dyson series

$$g_R = g + g\Sigma_{\mathrm{ph}}g + g\Sigma_{\mathrm{ph}}g\Sigma_{\mathrm{ph}}g + \ldots, \tag{71}$$

where g is the Green function without relaxation processes. We approximate the bare substrate Green function g by the Majorana contribution,

$$g(\omega) = |\psi_M\rangle \frac{1}{\omega} \langle\psi_M|, \tag{72}$$

and project the self-energy onto the Majorana subspace introducing

$$\Gamma_{\mathrm{qp}} = 2\mathrm{Im}\langle\psi_M|\Sigma_{\mathrm{ph}}(0)|\psi_M\rangle, \tag{73}$$

where we approximate the self-energy by its value at zero energy. The invariance of the Majorana state under particle-hole transformation guarantees that the expectation value $\langle\psi_M|\Sigma_{\mathrm{ph}}(0)|\psi_M\rangle$ is purely imaginary. Thus, the retarded and advanced Green functions of the Majorana state read

$$g_R^{r,a}(\omega) = \frac{|\psi_M\rangle\langle\psi_M|}{\omega \pm i\Gamma_{qp}/2}. \tag{74}$$

In quasi-equilibrium, we can express the greater and lesser Green function in terms of the retarded and advanced Green functions,

$$g_R^<(\omega) = f(\omega)(g_R^a(\omega) - g_R^r(\omega)) = \frac{\Sigma_{\mathrm{ph}}^<(0)}{\omega^2 + \Gamma_{\mathrm{qp}}^2/4}|\psi_M\rangle\langle\psi_M|, \tag{75}$$

$$g_R^>(\omega) = -(1 - f(\omega))(g_R^a(\omega) - g_R^r(\omega)) = \frac{\Sigma_{\mathrm{ph}}^>(0)}{\omega^2 + \Gamma_{\mathrm{qp}}^2/4}|\psi_M\rangle\langle\psi_M|, \tag{76}$$

where $f(\omega)$ is the quasi-equilibrium distribution function and we used the relations

$$-i\Sigma_{\mathrm{ph}}^<(0) = \Gamma_{\mathrm{qp}} f\,, \qquad i\Sigma_{\mathrm{ph}}^>(0) = \Gamma_{\mathrm{qp}}(1 - f). \tag{77}$$

These terms are the rates for emptying and filling of the delocalized fermion formed by the Majorana at the contact and a second one far away. Note that local transitions can change the occupation of this state. Since this fermion has zero energy the two rates are equal $i\Sigma_{ph}^>(0) = -i\Sigma_{ph}^<(0) = \Gamma_{\mathrm{qp}}/2$ according to detailed balance.

B. Expressions for the single-particle current

We can now evaluate the current in Eq. (5). Besides the Andreev current in Eq. (8), we find the single-particle current from the first term in Eq. (6)

$$I_M^s(V) = \frac{e}{4h}\int d\omega \frac{\Gamma_{\mathrm{qp}}[\Gamma_e(\omega)n_F(\omega_-) - \Gamma_h(\omega)n_F(\omega_+)] - \Gamma_{\mathrm{qp}}[\Gamma_e(\omega)(1 - n_F(\omega_-)) - \Gamma_h(\omega)(1 - n_F(\omega_+))]}{\omega^2 + (\Gamma_e(\omega) + \Gamma_h(\omega) + \Gamma_{\mathrm{qp}})^2/4}, \tag{78}$$

which gives Eq. (11) in the main text if we take $n_F(\omega_-) \simeq 1$ and $n_F(\omega_+) \simeq 0$ assuming $T \ll \Delta$.

C. Analysis of current

We compute the single-particle current near the threshold at $eV = \Delta + \eta$ with $\eta \ll \Delta$

$$\begin{aligned}
I_M^s(V) \simeq & \frac{e}{2h}\int_{-\Delta-\eta}^{\Delta+\eta} d\omega \frac{\omega_t^{3/2}\Gamma_{\rm qp}\left(\frac{\theta(\eta-\omega)}{\sqrt{\eta-\omega}}+\frac{\theta(\eta+\omega)}{\sqrt{\eta+\omega}}\right)}{\omega^2+\left(\frac{\omega_t^{3/2}\theta(\eta+\omega)}{\sqrt{\eta+\omega}}+\frac{\omega_t^{3/2}\theta(\eta-\omega)}{\sqrt{\eta-\omega}}+\frac{\Gamma_{\rm qp}}{2}\right)^2} \\
= & \frac{e\omega_t^{3/2}\Gamma_{\rm qp}}{h}\int_0^{\Delta}\frac{d\omega}{\sqrt{\omega}}\frac{1}{(\omega-\eta)^2+\left(\frac{\omega_t^{3/2}}{\sqrt{\omega}}+\frac{\Gamma}{2}\right)^2}, \qquad (79)
\end{aligned}$$

to lowest order in η. We thus obtain the differential conductance

$$G_M^s(x) \simeq \frac{2e^2\Gamma_{\rm qp}}{h\omega_t}\int_0^{\infty}\frac{d\omega}{\sqrt{\omega}}\frac{\omega - x}{\left[(\omega-x)^2+\left(\omega^{-1/2}+\Gamma_{\rm qp}/(2\omega_t)\right)^2\right]^2}, \qquad x = \frac{eV-\Delta}{\omega_t}. \qquad (80)$$

Now we focus on the conductance at the threshold, namely $x = 0$. For weak tip-substrate tunneling, $\omega_t \ll \Gamma_{\rm qp}$, we find

$$\begin{aligned}
G_M^s \simeq & \frac{2e^2\Gamma_{\rm qp}}{h\omega_t}\int_0^{\infty} d\omega \frac{\sqrt{\omega}}{\left[\omega^2+\left(\Gamma_{\rm qp}/(2\omega_t)\right)^2\right]^2} \\
= & \frac{2\pi e^2}{h}\frac{\omega_t^{3/2}}{\Gamma_{\rm qp}^{3/2}}, \qquad (81)
\end{aligned}$$

where the x-integration is elementary. In the opposite limit of strong tip-substrate tunneling, $\omega_t \gg \Gamma_{\rm qp}$, we can neglect the contribution of $\Gamma_{\rm qp}$ in the denominator. In this limit, we find the peak conductance

$$\begin{aligned}
G_M^s(\Delta) \simeq & \frac{2e^2\Gamma_{\rm qp}}{h\omega_t}\int_0^{\infty} d\omega \frac{\sqrt{\omega}}{\left[\omega^2+1/\omega\right]^2} \\
= & \frac{2\pi e^2}{9h}\frac{\Gamma_{\rm qp}}{\omega_t}. \qquad (82)
\end{aligned}$$

The parametric dependence of G_M^s is summarized in Eq. (12) of the main text.

---

[1] M. Ruby, F. Pientka, Y. Peng, F. von Oppen, B. W. Heinrich, K. J. Franke, arXiv:1502.05048 (2015)
[2] J.C. Cuevas, A. Martín Rodero, and A. Levy Yeyati, Phys. Rev. B, **54**, 7366 (1996).

4 Signatures of topological Josephson junctions

A fractional 4π Josephson effect is predicted to be one of the strongest indications of topological superconductivity. However, this effect is presumably difficult to observe due to quasiparticle poisoning processes and diabatic transitions. Rather than measuring the current-phase relation directly, I proposed to perform a much simpler switching probability measurement, which provides robust signatures of topological Josephson junctions even in the presence of quasiparticle poisoning. Given that this type of measurements has already been performed for conventional Josephson junctions (e.g., by the Quantronics group in Paris), measurements on topological Josephson junctions are likely to be performed in the near future.

PHYSICAL REVIEW B **94**, 085409 (2016)

Signatures of topological Josephson junctions

Yang Peng,[1] Falko Pientka,[1,2] Erez Berg,[3] Yuval Oreg,[3] and Felix von Oppen[1]
[1]*Dahlem Center for Complex Quantum Systems and Fachbereich Physik, Freie Universität Berlin, 14195 Berlin, Germany*
[2]*Department of Physics, Harvard University, Cambridge, Massachusetts 02138, USA*
[3]*Department of Condensed Matter Physics, Weizmann Institute of Science, Rehovot, Israel*

(Received 3 May 2016; revised manuscript received 22 July 2016; published 11 August 2016)

Quasiparticle poisoning and diabatic transitions may significantly narrow the window for the experimental observation of the 4π-periodic dc Josephson effect predicted for topological Josephson junctions. Here, we show that switching-current measurements provide accessible and robust signatures for topological superconductivity which persist in the presence of quasiparticle poisoning processes. Such measurements provide access to the phase-dependent subgap spectrum and Josephson currents of the topological junction when incorporating it into an asymmetric SQUID together with a conventional Josephson junction with large critical current. We also argue that pump-probe experiments with multiple current pulses can be used to measure the quasiparticle poisoning rates of the topological junction. The proposed signatures are particularly robust, even in the presence of Zeeman fields and spin-orbit coupling, when focusing on short Josephson junctions. Finally, we also consider microwave excitations of short topological Josephson junctions which may complement switching-current measurements.

DOI: 10.1103/PhysRevB.94.085409

I. INTRODUCTION

Topological superconductors with p-wave pairing and Majorana bound states [1] are currently attracting much interest, motivated in part by possible applications to topological quantum information processing [2]. Several solid-state platforms have been proposed [3–12] and are vigorously pursued experimentally [13–24]. A key question of current research is to develop appropriate detection schemes which allow one to identify topological superconducting phases and Majorana bound states.

A particularly striking signature of topological superconductivity is provided by Josephson junctions formed by a weak link between two topological superconductors hosting unpaired Majorana bound states at their ends [1,4]. While for conventional superconductors, the Josephson current is 2π periodic in the applied phase difference, the Josephson current across a junction made from topological superconductors is predicted to be 4π periodic [1]. This period doubling of the Josephson current in a topological Josephson junction [3,4,25–33] is protected by fermion number parity and as such quite sensitive to quasiparticle poisoning which changes the occupation of subgap states by inelastic processes involving the quasiparticle continuum. If the temporal variation of the superconducting phase difference across the junction is too slow, quasiparticle poisoning restores the 2π periodicity [4]. If the phase difference is varied too fast, the periodicity is restored by diabatic transitions into the quasiparticle continuum [25].

Here, we explore an alternative approach to probe the phase-dependent subgap spectrum of a topological Josephson junction, which is inspired by a recent series of remarkable experiments on conventional Josephson junctions [34–37]. These experiments consider Josephson junctions based on atomic weak links which host localized subgap Andreev states. The experiments explore the phase-dependent subgap spectrum by switching-current measurements as well as microwave spectroscopy. Here, we establish that analogous experiments provide a promising technique to distinguish between conventional and topological Josephson junctions. We find that this is particularly true in the short-junction limit, i.e., for junctions which are short compared to the coherence length of the adjacent (topological) superconductors. An important advantage of such measurements is that they can be performed in the presence of quasiparticle poisoning and in fact explicitly exploit processes that break fermion parity.

Ideally, Josephson junctions carry a dissipationless supercurrent (or Josephson current) as long as the applied current remains below the critical current and switch to a resistive state once the current exceeds the critical current [38]. In practice, the switching current fluctuates about the critical current due to thermal fluctuations. This has characteristic consequences in switching- current measurements based on applying short current pulses. Indeed, the switching probability as a function of the height of the applied current pulse does not increase abruptly from zero to one at the critical current, but rather exhibits a smooth step when accounting for fluctuations arising from the electromagnetic environment. When the junction hosts subgap states, their occupations also fluctuate due to quasiparticle poisoning processes. The current-phase relation and hence the critical current depend on the occupation of the subgap states, so that poisoning processes lead to fluctuations in the switching current.

The effect of poisoning processes is particularly simple when the current pulses are short compared to typical poisoning processes. In this case, the poisoning dynamics determines the occupation probability of the various subgap states prior to applying the current pulse but does not modify the state during the pulse duration. The switching probability becomes a superposition of step functions corresponding to the various subgap occupations. When the broadening of the steps is small compared to the shifts in the switching current between different occupation states, the measured switching probability exhibits a sequence of steps, one for each occupation of the subgap states, with intermediate plateaus. The heights of the plateaus reflect the occupation probabilities of the various junction states at the beginning of the current pulse. As a consequence, the switching probability encodes information

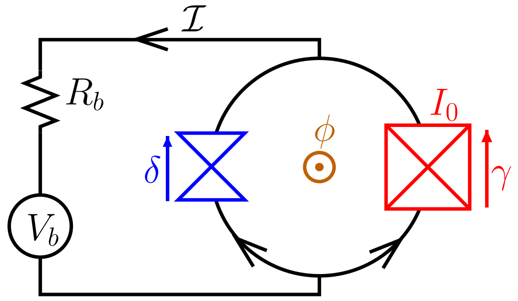

FIG. 1. Basic setup of the asymmetric SQUID, involving a weak conventional/topological Josephson junction (blue triangles) and a strong auxiliary Josephson junction (red checked box) with critical current I_0. The phase δ across the weak junction is linked to the phase γ across the auxiliary junction and the phase drop $\phi = 2e\varphi/\hbar$ induced by the magnetic flux φ threading the SQUID loop, $\delta = \phi + \gamma$. The applied voltage V_b drives a current $\mathcal{I}$ through the resistance R_b and the SQUID.

on the current-phase relations for the various occupation states of the Josephson junction.

Switching-current measurements on a single Josephson junction do not provide access to the phase dependence of the Josephson current, but merely to the maximal Josephson current and its dependence on the junction occupation. Phase-dependent information can be obtained by incorporating the junction of interest into an asymmetric SQUID where the second auxiliary junction in the SQUID loop has a much larger critical current and no subgap states [34]. This setup is illustrated in Fig. 1. The switching current of the SQUID is shifted away from the switching current of the large junction by the phase-dependent Josephson current of the weak one, so that switching current measurements as a function of flux can provide access to the entire current-phase relation of the various states of the weak junction of interest.

This makes switching-current measurements suitable to probe a unique distinction between topological and conventional Josephson junctions. As a function of the phase difference δ across the junction, the difference in Josephson currents between different junction states must vanish an even number of times within a 2π period in a trivial junction, and an odd number of times in a topological junction.

In this scheme, the initial occupation probability of the various junction states is assumed thermal. When driving the system out of equilibrium, switching-current measurements also provide access to the poisoning dynamics [35]. Imagine that the system is taken out of equilibrium at some initial time $t = 0$ so that the occupation probability of the various subgap states is no longer thermal. Poisoning processes will subsequently induce relaxation to equilibrium, and the rate of this relaxation can be probed by switching-current measurements after a time delay t. This pump-probe scheme can either be implemented by a sequence of two current pulses with time delay t, or by applying an appropriate microwave pulse at time $t = 0$ prior to the switching current measurements at time t.

Microwave irradiation also provides an alternative spectroscopic way of measuring the subgap spectrum as it induces transitions between different occupation states of the Josephson junction by microwave radiation [37,39–42]. Thus, evidence for topological superconductivity can be further strengthened by performing switching-current measurements in conjunction with microwave spectroscopy. This motivates us to calculate the admittance of a topological Josephson junction in the short-junction limit, complementing the results of Ref. [42] for the long-junction limit.

Such measurements provide various opportunities to distinguish topological from nontopological Josephson junctions. We find that the signatures are particularly distinctive for short junctions as their subgap spectrum contains only few Andreev states. Such short topological junctions support only a single subgap state at energy E_M (and its particle-hole conjugate at $-E_M$), originating from the hybridization of the two Majorana bound states. In contrast, a short conventional junction frequently (but not necessarily) supports additional Andreev states associated with the spin degree of freedom. In this case, topological and nontopological junctions can be distinguished by the number of plateaus in the switching probability as a function of applied current. Only junctions with a single plateau are suspects for being topological [see Fig. 4(a)]. Among these suspects, the subgap spectrum exhibits a fermion-parity protected level crossing at a phase difference of $\delta = \pi$ for topological junctions, and an anticrossing for nontopological junctions. Thus, the Josephson current at a phase difference of π is maximal for topological junctions and vanishes for conventional ones. This leads to characteristic differences in the flux dependence of the plateau width [see Fig. 4(b)]. Finally, even if the anticrossing of a nontopological junction happens to be too weak to be resolved, its poisoning dynamics should be characteristically different. Poisoning dynamics necessarily involves the quasiparticle continuum for topological junctions while poisoning processes involving only subgap states can exist for conventional junctions. These signatures based on switching current measurements can be further corroborated by microwave spectroscopy.

The paper is organized as follows. In Sec. II, we review basic considerations on the differences between the topological and conventional Josephson junctions. Section III contains the central results of this paper. After introducing the asymmetric SQUID setup, we discuss the characteristic distinctions between topological and conventional Josephson junctions in switching-current measurements, including the effects of thermal fluctuations in the context of the resistively and capacitively shunted junction (RCSJ) model. We end this section with a discussion of pump-probe experiments with multiple current pulses which provide access to the quasiparticle poisoning rates. Microwave absorption is discussed for short topological junctions based on two-dimensional (2D) topological insulators in Sec. IV. While we discuss nontopological junctions in the absence of Zeeman fields or spin-orbit coupling in the earlier sections, these couplings are typically present in experiments searching for possible topological superconductivity. We show in Sec. V that the signatures distinguishing topological from nontopological junctions remain robust in the presence of these effects when focusing on the short-junction limit. Finally, we conclude in Sec. VI.

II. BASIC CONSIDERATIONS

A. Conventional Josephson junction

To set the stage, we first review the case of a conventional Josephson junction. As realized in experiment [34–36], we consider a short junction (i.e., shorter than the superconducting coherence length) in the single-channel limit. If this channel has transmission D, the junction binds a single, spin-degenerate Andreev bound state at subgap energy [43]

$$E_A(\delta) = \Delta\sqrt{1 - D\sin^2\frac{\delta}{2}}. \tag{1}$$

Here, δ denotes the phase difference across the junction and Δ the superconducting gap. Figure 2(a) shows this particle-hole symmetric pair $E = \pm E_A(\delta)$ of Bogoliubov–de Gennes states as a function of the phase difference δ.

In the absence of above-gap excitations, these single-particle subgap states give rise to four many-body states associated with the Josephson junction. In the ground state, denoted by $|0\rangle$, the positive-energy Andreev bound state is empty. In addition, there are two degenerate excited states in which either the spin-up or the spin-down Andreev level is occupied. We denote these states by $|1\uparrow\rangle = \gamma_\uparrow^\dagger|0\rangle$ and $|1\downarrow\rangle = \gamma_\downarrow^\dagger|0\rangle$, where $\gamma_\uparrow$ and $\gamma_\downarrow$ are the Bogoliubov operators associated with the Andreev state. Finally, the Andreev state can be doubly occupied, $|2\rangle = \gamma_\uparrow^\dagger\gamma_\downarrow^\dagger|0\rangle$. Note that the states $|0\rangle$ and $|2\rangle$ are even states in terms of fermion parity, while $|1\uparrow\rangle$ and $|1\downarrow\rangle$ are odd.

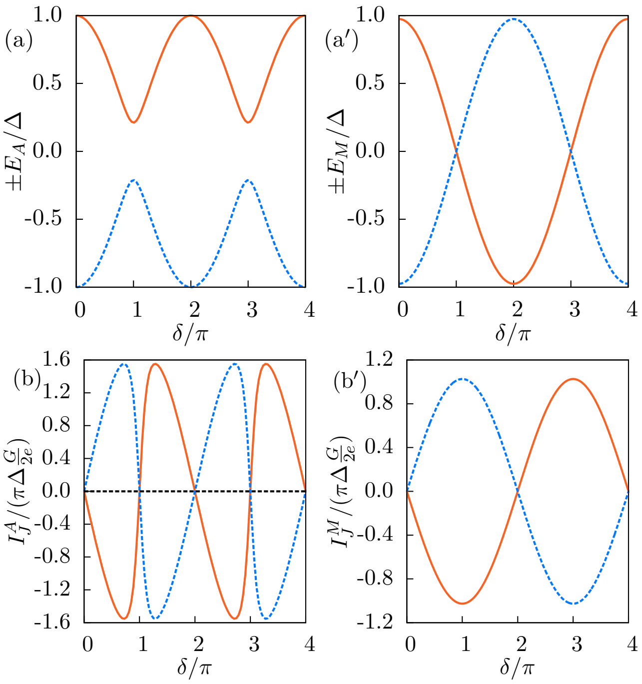

FIG. 2. Upper panels: single-particle energies of the subgap state as a function of the phase difference across the junction for (a) conventional and (a′) topological Josephson junctions. Lower panels: supercurrent as a function of phase difference for the various possible states of (b) conventional and (b′) topological Josephson junctions ($G = e^2D/\pi$, $D = 0.95$). The blue, black, and red curves in (b) display the currents for the states $|0\rangle$, $|1,\sigma\rangle$, and $|2\rangle$, respectively. The blue and red curves in (b′) display the currents for the states $|0\rangle$ and $|1\rangle$.

In equilibrium, the Josephson current is governed by the many-body energy $\mathcal{E}(\delta)$ of the junction. In the ground state $|0\rangle$, the (phase-dependent) junction energy is given by $-E_A(\delta)$. Correspondingly, the two odd states $|1\uparrow\rangle$ and $|1\downarrow\rangle$ have zero energy, while the doubly occupied state $|2\rangle$ has energy $+E_A(\delta)$. This is summarized as

$$\mathcal{E}_n(\delta) = (n-1)E_A(\delta), \tag{2}$$

where $n = 0,1,2$ denotes the occupancy of the Andreev bound state. The Josephson current in state $|n\rangle$ can be obtained from the energy as

$$\mathcal{I}_n(\delta) = 2e\frac{\partial\mathcal{E}_n(\delta)}{\partial\delta} = 2(n-1)e\frac{\partial E_A(\delta)}{\partial\delta}. \tag{3}$$

Thus, the Josephson currents of the two states $|0\rangle$ and $|2\rangle$ have the same magnitude, but flow in opposite directions, while the Josephson current vanishes in the odd states $|1\uparrow\rangle$ and $|1\downarrow\rangle$. The 2π-periodic supercurrents for these states are shown in Fig. 2(b).

B. Topological Josephson junction

The corresponding results for topological Josephson junctions differ in several essential ways. Here, we focus attention on junctions made of topological superconductors which break time-reversal symmetry and are hence characterized by unpaired Majorana bound states at their ends. The simplest realization of such a topological superconducting phase occurs in spinless p-wave superconductors [1,44,45]. These phases can for instance be realized experimentally based on two-dimensional topological insulators proximity coupled to conventional s-wave superconductors [4] or semiconductor quantum wires [5,6]. When tuned to the right parameter regime, these systems realize phases which are adiabatically connected to the topological phase of spinless p-wave superconductors and are thus promising venues for realizing the topological Josephson junction setup which we propose. Indeed, several experiments have already investigated such Josephson junctions with the goal of identifying signatures of topological superconductivity [16,19,20,23].

In the following, we assume that any ungapped normal part of the junction region is short compared to the coherence length ξ of the adjacent topological superconducting phase. Then, the subgap spectrum emerges from two overlapping Majorana bound states localized at the ends of the two topological superconductors [4–7]. This yields one nondegenerate Andreev level $E_M(\delta)$. While $E_M(\delta)$ is 4π periodic, the overall particle-hole-symmetric subgap spectrum $\pm E_M(\delta)$ is 2π periodic. Moreover, the level crossings between $E_M(\delta)$ and $-E_M(\delta)$ at δ equal to odd multiples of π are protected by conservation of fermion parity. This single-particle spectrum is shown in Fig. 2(a′).

As the topological Josephson junction has a single nondegenerate Andreev state, there are only two rather than four many-body states in the absence of above-gap quasiparticle excitations. We denote the state in which the Andreev level $E_M(\delta)$ is empty (occupied) as $|0\rangle$ ($|1\rangle$). The two states satisfy

$|1\rangle = \gamma^\dagger |0\rangle$, where γ is the Bogoliubov operator associated with the subgap state $E_M(\delta)$. We will also refer to $|0\rangle$ as having even fermion parity or the even state and to $|1\rangle$ as the odd state. (In the presence of above-gap quasiparticles, both occupations are however accessible for any parity of the electron number. Such processes are known as quasiparticle poisoning.)

The phase-dependent many-body energy of the junction is equal to $-E_M(\delta)/2$ for the even state $|0\rangle$ and $+E_M(\delta)/2$ for the odd state $|1\rangle$, or

$$\mathcal{E}_n(\delta) = (2n-1)\frac{E_M(\delta)}{2} \tag{4}$$

for state $|n\rangle$ with $n = 0,1$ denoting the occupation of the Andreev state. Just as the Bogoliubov–de Gennes states, the two many-body states $|n\rangle$ become degenerate for δ equal to odd multiples of π. Notice that the odd state can have lower energy than the even state as $E_M(\delta)$ becomes negative, which cannot happen in a conventional Josephson junction.

The Josephson current follows from the many-body energy in the usual way, so that

$$\mathcal{I}_n(\delta) = 2e\frac{\partial \mathcal{E}_n(\delta)}{\partial \delta} = e(2n-1)\frac{\partial E_M(\delta)}{\partial \delta}. \tag{5}$$

For fixed fermion parity n, the Josephson current is 4π periodic, as illustrated in Fig. 2(b′). The two states carry supercurrents of the same magnitude but of opposite sign.

This implies that there are distinct differences in the supercurrent carried by conventional and topological Josephson junctions. Unlike a conventional Josephson junction, a topological Josephson junction does not have states with zero Josephson current. Moreover, conventional Josephson junctions can assume three different current states, while topological junctions are limited to two states. We will explore experimental consequences of these differences in Sec. III.

C. Excitation spectra

The differences in subgap structures are also reflected in the excitation spectrum of the junction under microwave irradiation. Continuing to focus on short junctions, the many-body energy of a conventional junction can assume three different values. Correspondingly, the subgap states lead to three resonances in the differential absorption of microwave irradiation, as shown in Fig. 3(a) [39]. In the absence of subgap states, the only excitation process that breaks up a Cooper pair excites both electrons into the quasiparticle continuum [see process (1) in Fig. 3], which has a threshold energy of 2Δ. The existence of subgap states allows for the following additional processes. In process (2), a Cooper pair in the condensate is split, with one of the quasiparticles excited into the bound state at energy E_A and the second into the quasiparticle continuum above the gap Δ. This process has threshold energy $E_A + \Delta$. Process (3) corresponds to a quasiparticle in the bound state being excited into the continuum. This process has threshold energy $\Delta - E_A$. Finally, process (4) splits a Cooper pair, with both quasiparticles getting excited into the bound state. This process requires a threshold energy of $2E_A$. The thresholds of processes (2)–(4) are sketched in Fig. 3(b) as a function of the phase δ across the junction. We note in passing that these considerations are valid for zero magnetic field. The more general case will be considered in Sec. V.

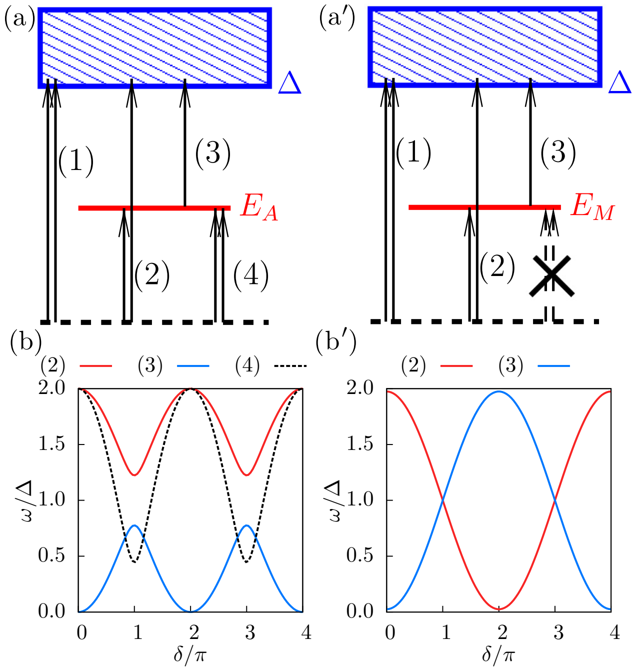

FIG. 3. Upper panels: possible quasiparticle processes numbered by (1)–(4) in (a) conventional and (a′) topological Josephson junctions. The black dashed lines indicate the many-body ground state and the upper blue boxes the quasiparticle continuum above the energy gap Δ. The red lines indicate the bound state at energies E_A or E_M for conventional and topological junctions, respectively. Lower panels: excitation energies (or energy thresholds) involving the bound state corresponding to the various processes in panels (a) and (a′).

A topological Josephson junction allows fewer microwave-induced transitions involving subgap states as it can only assume two possible junction energies [42]. When the junction is in the even-parity state, a Cooper pair can be split, with one electron occupying the subgap level and the second getting excited into the quasiparticle continuum. This process requires a threshold photon energy of $\Delta + E_M$ and is labeled as process (2) in Fig. 3(a′). When the junction is in the odd-parity state, the quasiparticle occupying the Andreev state $E_M(\delta)$ can be excited to the quasiparticle continuum. This process, labeled as (3) in Fig. 3(a′), requires a threshold energy of $\Delta - E_M$. While these two processes are similar to corresponding processes in conventional Josephson junctions, there is no analog of process (4). Indeed, there is only a single, nondegenerate Andreev level in topological Josephson junctions and it is impossible to split a Cooper pair exciting both electrons into a subgap state. A more complete theory of the microwave absorption is presented in Sec. IV.

III. SWITCHING PROBABILITY OF TOPOLOGICAL JOSEPHSON JUNCTIONS

In this section, we explore the consequences of the qualitative differences between the subgap spectra of conventional and topological superconductors for switching-current

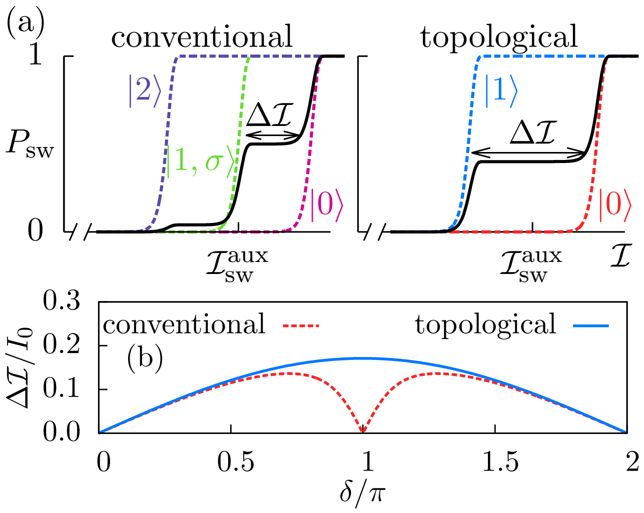

FIG. 4. (a) Probability $P_{\rm sw}$ of switching to the resistive state as a function of current for conventional (left) and topological (right) Josephson junctions for $\delta = 0.9\pi$ and $D = 0.95$. The dashed lines are the switching probabilities for the junction assuming a fixed occupation state [cf. Eq. (12)]. The black solid curves display the switching probability $P_{\rm sw}$ in the presence of quasiparticle poisoning, and can be obtained from a weighted average over the switching probabilities of the various occupation states [cf. Eq. (13)]. For the conventional Josephson junction, we choose the weight factors $c_0 = 0.5$, $c_{1,\uparrow} = c_{1,\downarrow} = 0.23$, and $c_2 = 0.04$. For the topological Josephson junction, we choose the weight factors $c_0 = 0.6$ and $c_1 = 0.4$. (b) Width of the plateau $\Delta\mathcal{I}/I_0$ as a function of $\delta = \gamma + \phi$ for the case of conventional (red dashed) and topological Josephson junctions (blue solid) (for $E_J^{\rm aux}/\Delta = 5.7$, where $E_J^{\rm aux} = \hbar I_0/2e$ is the Josephson energy of the auxiliary junction and Δ the gap of the weak junction).

measurements of asymmetric SQUIDs. We first present a heuristic approach in Sec. III A. As illustrated in Fig. 4, we find that there are characteristic differences between short topological and conventional junctions both in the number and the width of the plateaus in the switching probability. These schematic results are further corroborated by detailed numerical results in Sec. III C, based on the RCSJ theory developed in Sec. III B, with the central results shown in Fig. 6. Finally, in Sec. III D, we propose pump-probe approaches to the switching probability to explore the poisoning dynamics and show that this encodes further characteristic differences between topological and nontopological Josephson junctions.

A. Plateaus in the switching probability

Consider the SQUID device shown in Fig. 1, consisting of a large auxiliary Josephson junction and the weak junction of interest which can be either conventional or topological. The auxiliary Josephson junction is assumed to have a large critical current I_0 and no internal dynamics. The weak junction of interest has a much smaller critical current and internal dynamics associated with the bound-state occupation, as discussed in the previous section. The phase differences across the large junction (denoted by γ) and the weak junction (denoted by δ) are related through

$$\delta = \phi + \gamma, \tag{6}$$

where $\phi = 2e\varphi/\hbar$ is the phase drop induced by the magnetic flux φ threading the SQUID loop. (This relation assumes that the geometric inductance of the SQUID loop can be neglected as in recent experiments [35].)

The total applied current $\mathcal{I}$ flowing through the SQUID splits between the auxiliary junction with current

$$\mathcal{I}_{\rm aux}(\gamma) = I_0 \sin\gamma, \tag{7}$$

and the weak junction of interest with current $\mathcal{I}_n(\delta)$,

$$\mathcal{I} = \mathcal{I}_{\rm aux}(\gamma) + \mathcal{I}_n(\phi+\gamma). \tag{8}$$

Here, we have used the relation (6) between the phase differences. For zero applied current $\mathcal{I} = 0$, the current circulates around the SQUID loop and both junctions carry the same current, albeit with opposite signs. As the auxiliary junction has a much larger critical current, its phase difference γ is small and the phase drop ϕ due to the flux is applied almost entirely to the weak junction, i.e., $\delta \simeq \phi$.

When a current bias $\mathcal{I}$ is applied to the junction, the auxiliary junction carries most of this current and we can first focus on its behavior. Then, the phase difference across this junction is approximately

$$\gamma \simeq \arcsin\frac{\mathcal{I}}{I_0}, \tag{9}$$

and the junction becomes resistive when the current exceeds the critical current $\mathcal{I}_{\rm sw}^{\rm aux} = I_0$ of the junction. Ideally, this occurs when γ reaches $\gamma_{\rm sw} = \pi/2$.

In the presence of the weak junction, switching occurs for the value of $\gamma = \gamma_{\rm sw}$ for which the right-hand side of Eq. (8) has its maximum. Expanding to linear order in the small current $\mathcal{I}_n$, we have

$$\gamma_{\rm sw} \simeq \frac{\pi}{2} + \frac{1}{I_0}\left.\frac{d\mathcal{I}_n(\phi+\gamma)}{d\gamma}\right|_{\gamma=\pi/2} \tag{10}$$

and

$$\mathcal{I}_{\rm sw} \simeq \mathcal{I}_0 + \mathcal{I}_n(\phi+\pi/2) \tag{11}$$

for the switching current. This relation implies that the switching current of the SQUID reflects the current-phase relation of the weak junction. A measurement of the switching current of the asymmetric SQUID as a function of flux ϕ can therefore be used to measure this current-phase relation.

As shown in Ref. [35] for a nontopological Josephson junction based on an atomic contact, this can be used to resolve the current-phase relation of the various many-body states of the junction. Indeed, if the switching-current measurement is performed sufficiently fast compared to quasiparticle poisoning processes in the weak junction, the switching current of the SQUID depends on the occupancy n of the Andreev state. In practice [34–37], this measurement can be performed by applying short current pulses and measuring the probability that the SQUID switches into the resistive state as a function of applied current $\mathcal{I}$. In the simple approximation given here, this probability has the steplike form

$$P_{\rm sw}^n(\mathcal{I},\phi) = \theta[\mathcal{I} - I_0 - \mathcal{I}_n(\phi+\pi/2)] \tag{12}$$

when the weak junction is in state n. The switching probabilities, for fixed n and ϕ, are illustrated by the dashed lines in Fig. 4(a), which includes plots for both conventional and topological Josephson junctions. (The steps in the switching probability as a function of current are smoothed in this figure, anticipating the more elaborate model discussed in Sec. III B.) The critical current $\mathcal{I}_{\rm sw}^{\rm aux} = I_0$ of the auxiliary junction by itself is marked on the x axis. According to Eq. (12), the shifts of the steps away from this value can be interpreted as the supercurrent flowing through the weak junction of interest.

The dashed lines in Fig. 4(a) assume that the junction of interest is in a specific state n in the beginning of the current pulse (and that this charge state does not get modified during the pulse duration). In practice, the state of the junction changes statistically due to quasiparticle poisoning processes and is in general uncontrolled in experiment. Thus, the junction has probability c_n to be in state n at the beginning of the current pulse. If we keep assuming that the junction does not switch between states over the duration of the current pulse, the experimentally measured switching probability

$$P_{\rm sw}(\mathcal{I},\phi) = \sum_n c_n P_{\rm sw}^n(\mathcal{I},\phi) \tag{13}$$

is a weighted average over the states n of the junction. Such weighted averages are illustrated by black full lines in Fig. 4(a).

In the simplest approximation, the probabilities c_n can be assumed as thermal. More generally, they can be obtained from rate equations which describe the relevant poisoning processes [46,47]. Remarkably, one does not need detailed information about this poisoning kinetics for establishing robust signatures of topological superconductivity. Indeed, as illustrated in Fig. 4(a), the weighted average exhibits plateaus as a function of current. The number of plateaus increases with the number of current states of the junction. A conventional Josephson junction can have three different current states, and will then exhibit *two* plateaus in a plot of the switching probability versus current. In contrast, a short topological junction has only two current states and thus merely a *single* plateau. Thus, if all junction states are occupied with an appreciable probability c_n, topological and nontopological junctions frequently differ in the number of plateaus.

However, the number of plateaus may also be the same for topological and nontopological junctions. This happens when one of the c_n is so small (presumably for the $|2\rangle$ state) for a conventional junction that only a single plateau can be resolved, or because the nontopological junction also has only a single subgap state, as can be the case in the presence of Zeeman splitting (see Sec. V below for explicit model calculations). Even in this case, however, there remains a clear-cut difference between topological and conventional junctions when considering the width of the plateau as a function of the flux applied to the SQUID. The width of the plateau measures the difference in the supercurrents between the two contributing junction states.

At the flux ϕ such that the phase across the weak junction δ is equal to π, the difference in supercurrent is maximal for a topological junction, but vanishes for conventional junctions. Correspondingly, the width of the plateau should be maximal near $\delta = \pi$ for a topological junction, but vanishes for a conventional junction. This central result of this paper is illustrated in Fig. 4(b). Note that the experimental control parameter is ϕ rather than δ. However, these are simply related by $\delta = \phi + \gamma_{\rm sw} \simeq \phi + \pi/2$ at the position of the steps. It is useful to mention that the plateau width in the topological case is linear in the transmission amplitude $\sqrt{D}$. Thus, the lower the transmission, the narrower the plateau, making it more difficult to detect and characterize it experimentally.

In the more detailed considerations presented in Sec. III C, we show that the height and the location of the plateau provide additional criteria for distinguishing topological and conventional junctions.

B. RCSJ model

A more accurate description of the asymmetric SQUID is provided by the RCSJ model [38,48–52], which takes into account its shunting resistance R_S and capacitance C. Starting from this model and assuming that the weak junction remains in a particular state n, current conservation and the Josephson relation imply that the dynamics of the phase γ across the auxiliary junction is described by

$$\frac{\hbar C}{2e}\ddot{\gamma} = \mathcal{I} - I_0 \sin\gamma - \mathcal{I}_n(\phi+\gamma) - \frac{\hbar}{2eR_S}\dot{\gamma} + \tilde{\zeta}(t). \tag{14}$$

The term $\tilde{\zeta}(t)$ accounts for the thermal fluctuations associated with the resistance R_S and satisfies $\langle\tilde{\zeta}(t)\tilde{\zeta}(t')\rangle = (2T/R_S)\delta(t-t')$ at temperature T. Note that Eq. (14) reduces to Eq. (8), when neglecting the thermal fluctuations and searching for a solution with time-independent γ. It is convenient to introduce new parameters through

$$m = \left(\frac{\hbar}{2e}\right)^2 C, \quad \eta = \frac{1}{R_S C}, \quad \zeta(t) = \frac{\hbar}{2e}\tilde{\zeta}(t)$$

as well as the effective potential

$$U(\gamma) = -E_J^{\rm aux}\cos\gamma + \mathcal{E}_n(\phi+\gamma) - \frac{\hbar\mathcal{I}\gamma}{2e}, \tag{15}$$

where $E_J^{\rm aux} = \hbar I_0/2e$. Then, the equation for the phase γ takes the form of a Langevin equation

$$m\ddot{\gamma} = -U'(\gamma) - m\eta\dot{\gamma} + \zeta(t) \tag{16}$$

for a "particle" moving in the "tilted washboard" potential $U(\gamma)$ with friction coefficient η and the correlator

$$\langle\zeta(t)\zeta(t')\rangle = 2Tm\eta\delta(t-t') \tag{17}$$

of the Langevin force.

At zero bias current $\mathcal{I} = 0$, $U(\gamma) \simeq -E_J^{\rm aux}\cos\gamma$ and the "particle" will most likely remain near the potential minimum $\gamma \simeq 0$ (modulo 2π). With increasing bias current, the potential $U(\gamma)$ is tilted and the particle eventually escapes from the minimum (see Fig. 5), with the SQUID developing a voltage according to the Josephson relation $V = \hbar\dot{\gamma}/2e$.

The probability $P_{\rm sw}$ that a current pulse of duration t_p switches the junction to a finite-voltage state can be expressed in terms of the escape rate Γ from the minimum [34–36]

$$P_{\rm sw} = 1 - \exp(-\Gamma t_p). \tag{18}$$

To determine Γ, we consider the overdamped limit of the Langevin equation

$$\dot{\gamma} = -(m\eta)^{-1}U'(\gamma) + (m\eta)^{-1}\zeta(t). \tag{19}$$

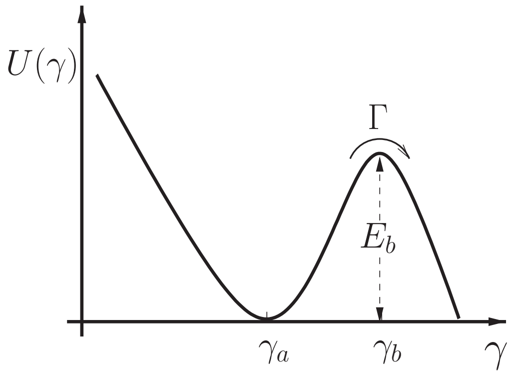

FIG. 5. Sketch of the "tilted washboard" potential governing the dynamics of the Josephson junction near one minimum.

In this limit, the probability density $\mathcal{P}(\gamma,t)$ of the auxiliary junction's phase difference γ is governed by the Smoluchowski equation [53]

$$\frac{\partial \mathcal{P}(\gamma,t)}{\partial t} = \frac{1}{m\eta}\frac{\partial}{\partial \gamma}\left[U'(\gamma)\mathcal{P}(\gamma,t) + T\frac{\partial \mathcal{P}(\gamma,t)}{\partial \gamma}\right] \tag{20}$$

and the escape rate can be computed by Kramers rate theory [53,54].

Consider the minimum of $U(\gamma)$ at γ_a and the neighboring maximum at γ_b (see Fig. 5). The rate Γ can be obtained by solving the stationary Smoluchowski equation at a constant probability current

$$j = \frac{1}{m\eta}\left[U'(\gamma)\mathcal{P}(\gamma,t) + T\frac{\partial \mathcal{P}(\gamma,t)}{\partial \gamma}\right] \tag{21}$$

with absorbing boundary condition at $\gamma = \gamma_+$, $\mathcal{P}(\gamma_+) = 0$. The position γ_+ has to be sufficiently far to the right of γ_b, i.e., $\gamma_+ > \gamma_b$, but is otherwise arbitrary. Then, the probability current j, normalized to the occupation n_a of the minimum at γ_a, describes the rate Γ at which transitions occur out of the minimum γ_a.

Note that the Smoluchowski equation implies that j is independent of γ for stationary solutions, so that we find

$$\mathcal{P}(\gamma) = \frac{m\eta j}{T}\exp\left[-U(\gamma)/T\right]\int_{\gamma}^{\gamma_+} dy \, \exp\left[U(y)/T\right] \tag{22}$$

by solving Eq. (21). For γ near γ_a, we can perform the integral by saddle-point integration and obtain

$$\mathcal{P}(\gamma) \simeq \frac{m\eta j}{\omega_b T}\sqrt{\frac{2\pi T}{m}}\exp\left(\frac{U(\gamma_b)}{T}\right)\exp\left[-U(\gamma)/T\right]. \tag{23}$$

Here, we approximate $U(\gamma) \simeq U(\gamma_b) - \frac{1}{2}m\omega_b^2(\gamma - \gamma_b)^2$ around γ_b. The population n_a in the potential well around γ_a is

$$n_a \simeq \int_{-\infty}^{\infty} d\gamma' \, \mathcal{P}(\gamma') = \frac{2\pi\eta j}{\omega_a\omega_b}\exp\left(E_b/T\right), \tag{24}$$

where the integral should be evaluated with the expression in Eq. (23). We used the expansion $U(\gamma) \simeq U(\gamma_a) + \frac{1}{2}m\omega_a^2(\gamma - \gamma_a)^2$ for γ near γ_a and introduced the barrier height $E_b = U(\gamma_b) - U(\gamma_a)$. Finally, one obtains the Arrhenius-type expression

$$\Gamma = \frac{j}{n_a} = \frac{\omega_a\omega_b}{2\pi\eta}\exp\left(-E_b/T\right) \tag{25}$$

for the escape rate Γ.

The two points γ_a and γ_b satisfy the condition $\partial U(\gamma)/\partial\gamma = 0$, which yields

$$I_0 \sin\gamma + \mathcal{I}_n(\gamma + \phi) = \mathcal{I}. \tag{26}$$

First neglecting the contribution of the weak junction, one has

$$\gamma_a \simeq \arcsin\frac{\mathcal{I}}{I_0}; \quad \gamma_b \simeq \pi - \arcsin\frac{\mathcal{I}}{I_0} \tag{27}$$

as well as

$$\omega_a\omega_b \simeq \frac{E_J^{\mathrm{aux}}}{m}|\cos\gamma_a\cos\gamma_b|^{1/2} \tag{28}$$

and

$$E_b \simeq E_J^{\mathrm{aux}}(\cos\gamma_a - \cos\gamma_b) - \frac{\hbar\mathcal{I}}{2e}(\gamma_b - \gamma_a). \tag{29}$$

Then, Eq. (25) yields the phase escape rate

$$\Gamma^{\mathrm{aux}}(\mathcal{I}) = \frac{eI_0R_S}{\pi\hbar}\sqrt{1 - (\mathcal{I}/I_0)^2} \times e^{-\frac{\hbar}{2eT}\{\mathcal{I}[2\arcsin(\mathcal{I}/I_0) - \pi] + 2I_0\sqrt{1-(\mathcal{I}/I_0)^2}\}} \tag{30}$$

by Eq. (18), the switching probability of the auxiliary junction is

$$P_{\mathrm{sw}}^{\mathrm{aux}}(\mathcal{I}) = 1 - e^{-\Gamma^{\mathrm{aux}}(\mathcal{I})t_p}. \tag{31}$$

$P_{\mathrm{sw}}^{\mathrm{aux}}$ has a steplike shape as shown in Fig. 4, with the steps occurring near $\mathcal{I}_{\mathrm{sw}}^{\mathrm{aux}}$ which is generally smaller than I_0 due to the thermal fluctuations.

Now, the weak junction can be readily included to first order. We first need to solve Eq. (26) for γ_a and γ_b. In doing so, we can replace γ in the argument of $\mathcal{I}_n$ by the results in Eq. (27) for γ_a and γ_b to zeroth order. At sufficiently low temperatures, the junction switches only once the barrier becomes small and hence when γ_a and γ_b are close together (and thus close to $\pi/2$). In computing the switching probability to first order in $\mathcal{I}_n$, it is sufficient to set $\gamma \simeq \pi/2$ in the argument of $\mathcal{I}_n$ in Eq. (26). Then, we can account for the weak junction simply by shifting $\mathcal{I} \to \mathcal{I} - \mathcal{I}_n(\phi + \pi/2)$ in the above considerations. This yields

$$P_{\mathrm{sw}}^{n}(\mathcal{I}) \simeq P_{\mathrm{sw}}^{\mathrm{aux}}\left[\mathcal{I} - \mathcal{I}_n\left(\phi + \frac{\pi}{2}\right)\right] \tag{32}$$

for the switching probability of the asymmetric SQUID.

C. Signatures of topological Josephson junctions

The differences between topological and trivial junctions are most pronounced in the switching probability P_{sw} as a function of the flux and the height of the current pulse. We can use the RCSJ approach developed in the previous section to calculate P_{sw} in Eq. (13) numerically [see Eq. (32)]. This leads to Fig. 6 which contains a central result of this paper and highlights the qualitative difference between topological and trivial junctions. Figure 6(a) shows a color plot of the switching probability for a nontopological junction as a function of the

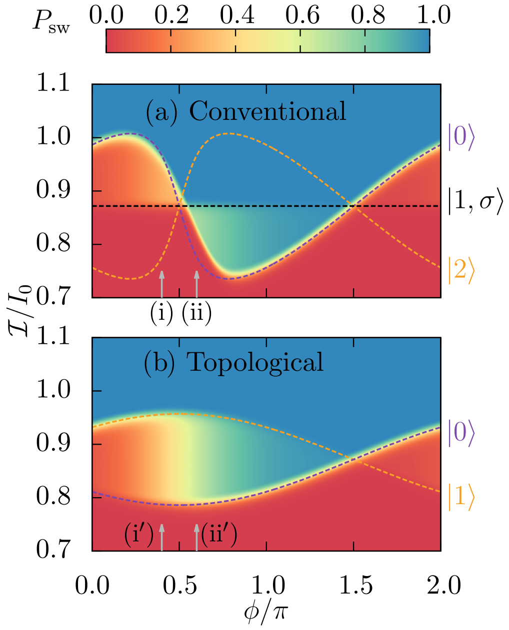

FIG. 6. Color plot of the switching probability $P_{\rm sw}$ of asymmetric SQUIDs as a function of flux ϕ and height $\mathcal{I}$ of the current pulse for (a) a conventional and (b) a topological Josephson junction. The occupation probabilities of the various junction states prior to the current pulse are taken to be thermal, with effective temperature $T_{\rm eff}$. In (a), parameters are such that the occupation probability of the doubly occupied Andreev state is negligible. The dashed lines indicate the switching currents based on the Josephson currents associated with the various junction states as indicated in the figure, with the phase difference across the weak junction taken as $\delta = \phi + \pi/2$. In (a), the purple line corresponds to the ground state, the black line to the singly occupied Andreev state, and the orange one to the doubly occupied state. In (b), the purple and orange lines correspond to the two states of the topological junction. The parameters were chosen as $R_s = 550\ \Omega$, $I_0 = 553.7$ nA, $T = 100$ mK, $E_{\rm J}^{\rm aux}/\Delta = 5.7$, $t_p = 1\ \mu$s, and $D = 0.95$, according to the parameters used in Ref. [35]. The effective temperature $T_{\rm eff}$ is chosen as such that $E_J^{\rm aux}/T_{\rm eff} = 10$. The gray arrows with labels (i), (ii) indicate values of ϕ for which line cuts are shown in Fig. 7.

height $\mathcal{I}$ of the current pulse and the flux threading the SQUID. The dashed lines indicate the switching currents for the various junction states as obtained on the basis of the current-phase relation of the weak junction and discussed in Sec. III A. The purple line corresponds to the ground state of the junction, the black line to the odd states, and the orange line to the doubly occupied Andreev level.

For the parameters chosen, double occupation of the Andreev level can be neglected so that the switching probability effectively exhibits only a single plateau as a function of current. In Fig. 6, this plateau is well resolved for $0 \lesssim \phi \lesssim \pi$, corresponding to a phase difference of $\pi/2 \lesssim \delta \lesssim 3\pi/2$ across the weak junction. Outside this region, the energy of the odd states becomes too high, and their thermal occupation too low, so that the corresponding step in the switching probability is no longer resolved. Obviously, the range over which the plateau can be resolved depends on the junction parameters and temperature.

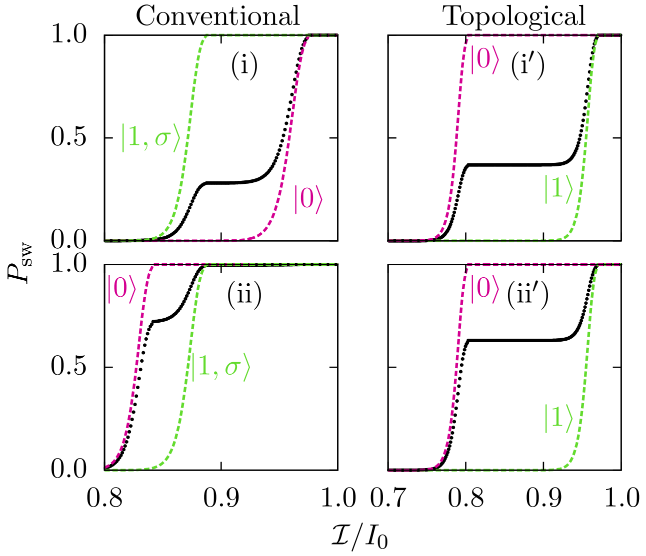

FIG. 7. Switching probability of a conventional (topological) junction as a function of the applied current for fixed ϕ. The black symbols represent $P_{\rm sw}$ along the fixed-ϕ cuts indicated by gray arrows in Fig. 6 for conventional junctions: (i) switching probability for $\phi = 0.4\pi$; (ii) for $\phi = 0.6\pi$. (i′) and (ii′) show the corresponding plots along the same ϕ cuts for the topological junction. The dashed curves denote the switching probability when the weak junction is in the fixed occupation state as specified in the figure, similar to those in Fig. 4. Note that for conventional junction, the state with the lower switching current inverts between (i) and (ii). It is this inversion which explains the sudden change in the plateau height for (i) $\phi < \pi/2$ and (ii) $\phi > \pi/2$, as discussed in the text. In contrast, there are no such inversions in the topological case.

The height of the intermediate plateau changes quite abruptly at $\phi \simeq \pi/2$, corresponding to a phase difference of $\delta = \pi$ across the weak junction. This is seen in Fig. 6 and further illustrated in the line cuts presented in Fig. 7. At $\delta = \pi$, there is a change in sign of the Josephson current flowing through the weak junction. Consequently, the low-current step in the switching probability is due to the odd states (ground state) to the left (right) of $\phi = \pi/2$, and the step heights therefore controlled by the low (high) thermal occupations of these states. Note that this change in the plateau height occurs at a flux where the width of the plateau goes through zero.

Corresponding results for a topological junction are shown in Fig. 6(b). The two dashed lines correspond to the expected switching currents based on the even and odd states of the topological junction. The plateau in the switching probability occurs between these two lines. Unlike for the conventional junction, the width of the plateau is now maximal for $\phi = \pi/2$, corresponding to a phase difference of $\delta = \pi$ across the topological junction. This qualitative difference between topological and conventional junctions was already highlighted in Fig. 4. Note also that there is now a rather abrupt change in the height of the plateau at this point of maximal plateau width, rather than the point of minimal plateau width as for conventional junctions.

Finally, there are characteristic differences between conventional and topological junctions based on the flux dependence

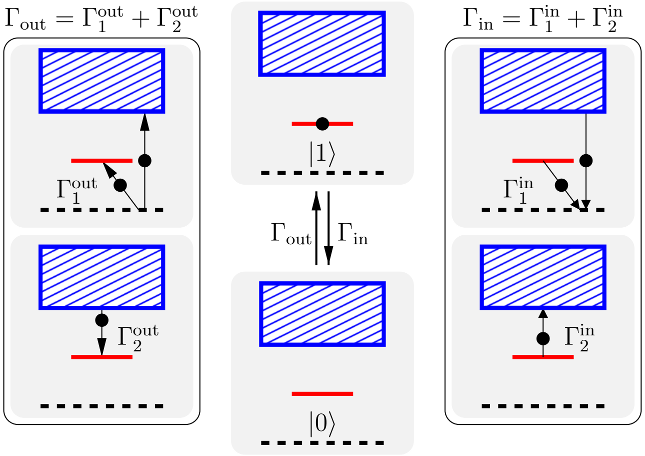

FIG. 8. Center: parity switching between states $|1\rangle$ and $|0\rangle$, with rates Γ_{in} and Γ_{out}. Left: quasiparticle processes that contribute to Γ_{out}. The top panel shows the breaking of a Cooper pair, with one electron excited into the subgap state (red line) and the second electron excited to the continuum (blue box). The bottom panel shows the transition of a quasiparticle from the continuum into the subgap state. Right: quasiparticle processes that contribute to Γ_{in}. The top panel shows the recombination of quasiparticle excitations from the continuum and the subgap state into a Cooper pair. The bottom panel shows the excitation of an excitation from the subgap state into the quasiparticle continuum.

of the Josephson current. In a conventional junction, one of the steps of the switching probability as a function of current is due to the odd state which carries zero Josephson current for all phase differences. Thus, the position of one of the steps should be rather insensitive to the flux ϕ. Conversely, both occupation states of a topological junction generally carry Josephson currents, with their currents being equal in magnitude but opposite in sign. Thus, both steps should depend on flux in a symmetric manner. This difference is clearly seen in Fig. 6.

D. Poisoning dynamics

According to Eq. (13), the measured switching probability is sensitive to the probabilities c_n for the various occupation states n of the junction. As shown experimentally in Ref. [35], this can be used to extract the poisoning dynamics of the weak Josephson junction by a "pump-probe" technique. This technique can be readily extended to topological Josephson junctions.

The basic idea of the technique [35] is to drive the occupation probabilities c_n out of equilibrium, e.g., by a short initial current pulse, and to probe the switching current by a second current pulse at a later time t. With increasing time delay Δt between the current pulses, the junction occupations relax back towards equilibrium, and this is reflected in the switching probability P_{sw}, due to its dependence on the c_n.

This can be used to extract the dependence of the c_n's on the time delay Δt and hence the poisoning rates by comparison with a simple rate equation. The dominant poisoning processes in a short topological junction are shown in Fig. 8. Note that in short junctions, the presence of above-gap quasiparticles leaves the Josephson current unchanged. Denoting the occupations of the states $|0\rangle$ and $|1\rangle$ by p and $1-p$, respectively, the rate equation takes the form

$$\frac{dp}{dt} = -\Gamma_{\text{out}}\, p + \Gamma_{\text{in}}(1-p). \tag{33}$$

In equilibrium, this is solved by $p = p_\infty = \Gamma_{\text{in}}/(\Gamma_{\text{in}} + \Gamma_{\text{out}})$, and this equilibrium is approached with rate $\Gamma = \Gamma_{\text{in}} + \Gamma_{\text{out}}$. Both Γ and p_∞ can be measured, yielding the poisoning rates Γ_{in} and Γ_{out}.

While quasiparticle poisoning frequently suppresses Majorana signatures such as the 4π-periodic Josephson effect or the $2e^2/h$ conductance quantization of a Majorana tunnel junction, measurements of the poisoning dynamics may actually be helpful in distinguishing between topological and nontopological junctions. This is related to the fact that a nontopological junction typically has additional channels of poisoning dynamics which are absent in a short topological junction. Specifically, a nontopological junction can have two pairs of subgap states while a topological junction has only one. As a result, we can have poisoning processes in a nontopological junction in which a Cooper pair is split up between (or recombined from) the two positive-energy subgap states. No such process exists in a short topological junction where all poisoning processes necessarily involve the quasiparticle continuum, as shown in Fig. 8.

This difference becomes particularly dramatic and helpful at $\delta = \pi$ when the nontopological junction has only weakly anticrossing Andreev levels. Such a situation is shown in Fig. 13 in Sec. V. Then, it may be challenging to resolve the weak splitting in switching-current measurements. However, the poisoning dynamics of the two settings remains distinctly different. The fastest rate for the topological junction has an activated temperature dependence with an activation energy of the order of the topological superconducting gap. In contrast, the fastest rate of a nontopological junction should involve a considerably smaller activation energy which equals the sum of the energies of the spin-up and -down Andreev levels.

IV. MICROWAVE ABSORPTION

In addition to the switching current, topological and nontopological Josephson junctions also differ in their microwave absorption. Microwave absorption was studied for nontopological junctions by Kos *et al.* [39] and for long topological junctions by Väyrynen *et al.* [42]. Here, we present corresponding results for short topological Josephson junctions. (Related results were also obtained very recently in Ref. [55].) For definiteness, we consider a model Hamiltonian of a short topological Josephson junction which is appropriate for a topological Josephson junction based on a proximity-coupled topological-insulator edge [4]. This model allows us to explicitly compute the Josephson current and the transition rates for the various microwave-induced quasiparticle processes. Related calculations of admittance of topological wires have been done in Refs. [56,57].

A. Bound states and Josephson current

Consider the Fu-Kane model of a topological Josephson junction [4]. The banks, consisting of a topological insulator edge proximity coupled to a conventional superconductor, are separated by a section in which the edge state is gapped out by a Zeeman field or proximity coupling to a ferromagnetic insulator. The banks are considered to be long enough that the Majorana bound states at the junction are decoupled from other Majoranas far from the junction. We also require the edge state to be well separated so that we can focus on an individual edge mode.

To model a short junction for which the length L of the junction is small compared to the superconducting coherence length, we take the limit $L \to 0$ while keeping $R = ML/v_F$ fixed, where M is the strength of the magnetic gap in the junction, i.e., we treat the Zeeman field as a δ-function perturbation. In the Nambu basis $\Psi = (\psi_\uparrow, \psi_\downarrow, \psi_\downarrow^\dagger, -\psi_\uparrow^\dagger)^T$, the Hamiltonian takes the form $H = \frac{1}{2}\Psi^\dagger \mathcal{H} \Psi$ with

$$\mathcal{H} = v_F p \sigma_z \tau_z + \Delta(x)\tau_x + M(x)\sigma_x, \tag{34}$$

where x (p) denotes the coordinate (momentum) along the topological-insulator edge, v_F is the edge-mode velocity, and σ_j and τ_j are Pauli matrices in spin and Nambu (particle-hole) space, respectively. The proximity-induced superconducting gap

$$\begin{aligned}\Delta(x) &= \Delta[\theta(-x - L/2) + e^{i\phi\tau_z}\theta(x - L/2)] \\ &\to \Delta e^{i\phi(x)\tau_z}\end{aligned} \tag{35}$$

has strength Δ and a phase difference of ϕ across the junction located at $x = 0$, so that $\phi(x) = \phi\theta(x)$. (In this section, we use ϕ instead of δ to avoid confusion with the δ function.) Similarly, the magnetic gap takes the form

$$M(x) = M\theta(x + L/2)\theta(-x + L/2) \to v_F R\delta(x) \tag{36}$$

in the short-junction limit.

Thus, we can also write the Hamiltonian as

$$\mathcal{H} = v_F p \sigma_z \tau_z + \Delta e^{i\phi(x)\tau_z}\tau_x + v_F R \delta(x)\sigma_x. \tag{37}$$

The spatial dependence of the superconducting phase can be eliminated by a local gauge transformation $U = e^{i\phi(x)\tau_z/2}$. This transforms the Hamiltonian into

$$U^\dagger \mathcal{H} U = v_F p \sigma_z \tau_z + \Delta \tau_x + v_F\left[\frac{\phi}{2}\sigma_z + R\sigma_x\right]\delta(x), \tag{38}$$

which we will denote as $\mathcal{H}$ in the following.

The connection formula across the δ function can be readily derived by rearranging the Bogoliubov–de Gennes equation $\mathcal{H}\psi = E\psi$ as

$$i\frac{\partial \psi}{\partial x} = -\frac{1}{v_F}\sigma_z\tau_z\left[E - \Delta\tau_x - v_F\left(\frac{\phi}{2}\sigma_z + R\sigma_x\right)\delta(x)\right]\psi. \tag{39}$$

By writing the solution as $\psi(x) = U(x,x_0)\psi(x_0)$ in terms of the state at some reference point x_0, we find

$$\begin{aligned}U(x,x_0) = \mathcal{P}\exp\bigg\{\frac{i}{v_F}\sigma_z\tau_z\int_{x_0}^{x} dx'\bigg[E - \Delta\tau_x \\ - v_F\left(\frac{\phi}{2}\sigma_z + R\sigma_x\right)\delta(x')\bigg]\bigg\},\end{aligned} \tag{40}$$

where $\mathcal{P}$ is an ordering operator which moves larger x to the left. Specifically, we can now compute

$$U(0^+,0^-) = e^{-i\phi\tau_z/2}[\cosh R + \sigma_y \tau_z \sinh R], \tag{41}$$

which connects the states on the two sides of the δ function $\psi(0^+) = U(0^+,0^-)\psi(0^-)$.

We can use this connection formula to obtain the bound states localized at the junction. To do so, we match the properly decaying solutions of the Bogoliubov–de Gennes equation on the left and right sides of the δ function by means of the connection formula (41) and obtain one pair of localized Andreev bound states $\pm E_M(\phi)$ with

$$E_M(\phi) = \frac{\Delta}{\cosh R}\cos\frac{\phi}{2} = \sqrt{D}\Delta\cos\frac{\phi}{2}. \tag{42}$$

Here, we have defined the junction transmission $D = 1/\cosh^2 R$. This pair of Andreev bound states emerges from the pair of coupled Majorana bound states adjacent to the topological Josephson junction. For completeness, we include details of this calculation in Appendix A 1.

Combining Eqs. (5) and (42), we can obtain the Josephson current as

$$\mathcal{I}_n = \frac{e\Delta}{2\cosh R}\sin\frac{\phi}{2}(1 - 2n) = \frac{\pi G}{2}\frac{\Delta^2 \sin\phi}{2eE_M(\phi)}(1 - 2n), \tag{43}$$

where $n = 0,1$ denotes the occupancy of the bound state and we defined $G = e^2 D/\pi$. For a given junction occupation n, the Josephson current is 4π periodic in ϕ and the two states of the junction carry exactly opposite supercurrents, as shown in Fig. 2(b′).

B. Linear response to microwave radiation

We model the microwave radiation as an applied time-dependent bias $V(t)$ which modifies the phase difference across the junction according to $\phi \to \phi - 2\phi_1(t)$, where $\dot\phi_1(t) = eV(t)$. We assume that the microwave radiation of frequency ω is weak, $\phi_1 \sim |eV/\omega| \ll 1$, so that we can treat the perturbation

$$\begin{aligned}H'(t') &= v_F[\psi_+^\dagger(0)\psi_+(0) - \psi_-^\dagger(0)\psi_-(0)]\phi_1(t') \\ &= \frac{1}{e}I(t')\phi_1(t'),\end{aligned} \tag{44}$$

in linear response. We note in passing that we neglect the shift in chemical potential by $eV(t)$. This term yields a purely real response function and is thus irrelevant for microwave absorption [39].

Using the Kubo formula, the current response to the microwave radiation can be expressed as

$$\begin{aligned}\delta\langle I(t)\rangle &= -i\int_{-\infty}^{t}\langle[I(t),H'(t')]\rangle\, dt' \\ &= -\frac{i}{e}\int_{-\infty}^{t}\langle[I(t),I(t')]\rangle\,\phi_1(t')dt',\end{aligned} \tag{45}$$

and described by the response function

$$\chi(t) = -\frac{i}{e}\theta(t)\langle[I(t),I(0)]\rangle. \tag{46}$$

The admittance $Y(\omega)$ of the junction can be written as $Y(\omega) = \frac{ie}{\omega}\chi(\omega)$, where $\chi(\omega)$ denotes the Fourier transform of $\chi(t)$. The linear absorption rate W of the microwave radiation becomes [39]

$$W = \frac{\phi_1^2}{2e^2}\omega\,\mathrm{Re}Y(\omega), \quad \omega > 0. \tag{47}$$

This quantity is a measure of the microwave-induced rate of change of the weight factors c_n in P_{sw} as given in Eq. (13).

The admittance can be computed by using the current operator

$$I = ev_F[\psi_+^\dagger(0)\psi_+(0) - \psi_-^\dagger(0)\psi_-(0)], \tag{48}$$

where $\psi_\pm(0)$ is the annihilation operator for the left/right moving electron at position $x = 0$ of the junction. We need to choose either $x = 0^+$ or 0^- for the wave functions to be well defined. The electron operators can be expressed in terms of the Bogoliubov quasiparticle operators γ_ν [25]:

$$\psi_+(0) = \sum_\nu u_{+\nu}(0)\gamma_\nu - v_{-\nu}^*(0)\gamma_\nu^\dagger,$$

$$\psi_-(0) = \sum_\nu u_{-\nu}(0)\gamma_\nu + v_{+\nu}^*(0)\gamma_\nu^\dagger. \tag{49}$$

Here, we introduced the spinor wave functions $\Psi_\nu = (u_{+\nu},u_{-\nu},v_{+\nu},v_{-\nu})$. The Andreev bound state is labeled by $\nu = 0$ and the continuum states by $\nu = (E,\eta,\chi)$, with $\eta = e,h$ and $\chi = l,r$ corresponding to the state generated by incoming electron/hole states from the left/right. The ± label refers to the two spin components which are locked to the propagation directions of the edge channel.

By using the explicit expressions for the wave functions of both bound and continuum states, as calculated in Appendix A, we can first recover the Josephson current given in Eq. (43). The corresponding derivation is given in Appendix B. Extending the calculation to the current-current correlation function (46), we can then obtain microscopic results for the admittance of short Josephson junctions, as shown in Appendix C. We neglect above-gap excitations, as they are suppressed by the superconducting gap. Then, the real part of the admittance can be written as a sum of three terms

$$\mathrm{Re}Y = \mathrm{Re}Y_1 + (1-n)\mathrm{Re}Y_2 + n\,\mathrm{Re}Y_3. \tag{50}$$

The three terms correspond to three different quasiparticle processes shown in Fig. 3(a′). Explicitly, $\mathrm{Re}Y_1(\omega) \propto \theta(\omega - 2\Delta)$ corresponds to the process (1) in which a Cooper pair is excited into the continuum as two quasiparticles. This process requires a threshold energy of 2Δ. $\mathrm{Re}Y_2(\omega) \propto \theta(\omega - \Delta - E_M)$ describes the process (2), in which a Cooper pair is split between the Andreev level and the quasiparticle continuum. This process requires a threshold energy $\Delta + E_M$ and an initially empty Andreev level. Finally, $\mathrm{Re}Y_3(\omega) \propto \theta(\omega - \Delta + E_M)$ corresponds to the process (3), in which a quasiparticle is excited from the Andreev level into the continuum. This requires a threshold energy of $\Delta - E_M$ and an occupied Andreev level. Unlike for conventional Josephson junctions as discussed in Ref. [39], there is no process with absorption energy $2E_M$ as the Andreev level is nondegenerate for a topological Josephson junction.

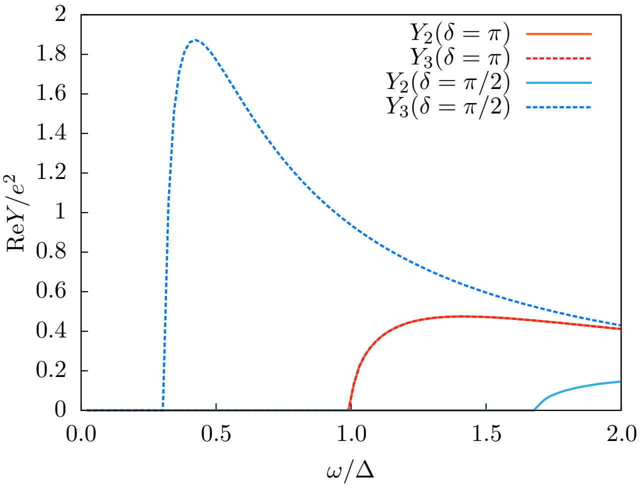

FIG. 9. Various contributions to the real part of the admittance for the Fu-Kane model, based on Eq. (C39), for $D = 0.95$ and phase differences $\phi = \pi$ as well as $\phi = \pi/2$. For $\phi = \pi$, $E_A = 0$, so that $\mathrm{Re}Y_2$ and $\mathrm{Re}Y_3$ coincide. At phase differences ϕ away from π, the two curves differ.

Detailed expressions for these functions are included in Eq. (C39) in Appendix C. The explicit expressions show that the thresholds at $\Delta + E_M$ and $\Delta - E_M$ are sharp in the sense that their derivatives with respect to ω have square-root singularities at the threshold. This is shown in Fig. 9, which plots $\mathrm{Re}Y_2$ and $\mathrm{Re}Y_3$ for various phase differences ϕ across the junction. These results also allow one to compute the absorption rate $dW/d\omega$ according to Eq. (47). A corresponding color plot as a function of both ϕ and ω which emphasizes the threshold energies is shown in Fig. 10. Here, we assume that both parity states are equally populated, independently of the applied flux.

V. TOPOLOGICAL VS NONTOPOLOGICAL JUNCTIONS: EFFECTS OF ZEEMAN FIELD AND SPIN-ORBIT COUPLING

Potential realizations of topological Josephson junctions require systems which involve spin-orbit coupling and/or Zeeman fields. When searching for topological superconductivity, one is thus dealing with Josephson junctions which are subject to both of these. Strictly speaking, our considerations for nontopological junctions in the previous sections did not include these effects. One may thus worry that their inclusion makes the proposed experimental distinctions between topological and nontopological junctions less clear cut. This question is addressed in the present section. Our principal conclusion is that the signatures remain essentially robust as long as one considers short Josephson junctions.

Important realizations of topological Josephson junctions rely on 2D topological insulators [4] or semiconductor quantum wires [5,6]. In Sec. IV A, we presented microscopic results for short junctions made of 2D topological insulator edges, subject to a Zeeman field in the junction region. These junctions are topological, and their subgap spectrum agrees with the generic subgap spectrum of short topological

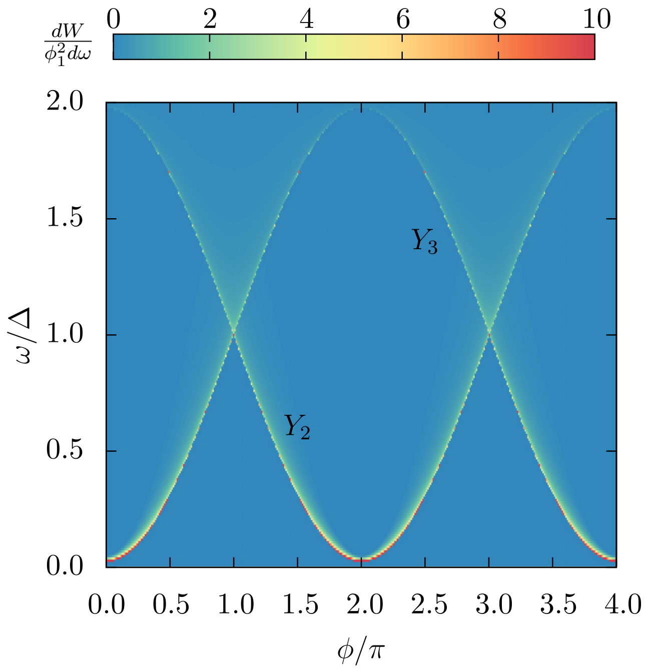

FIG. 10. Derivative of the linear absorption rate with respect to the microwave frequency $dW/d\omega$ [see Eq. (47)]. For optimal visibility of the thresholds, we assume an occupation of $n = \frac{1}{2}$ in Eq. (50) independently of flux. While the figure displays the sum of contributions from Y_2 and Y_3, the bright curves result predominantly from Y_2 and Y_3 as labeled in the figure.

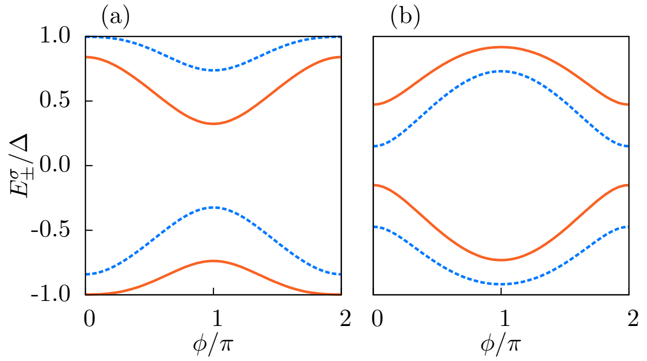

FIG. 11. Subgap energies of a short conventional Josephson junction as a function of the phase difference, in the presence of Zeeman field applied in the junction region. The orange solid curves are the spectra for spin up with Nambu spinor $(\psi_\uparrow, \psi_\downarrow^\dagger)^T$. The blue dashed lines are the corresponding spectra for spin down following from particle-hole symmetry. The panels illustrate the two types of typical behaviors, with parameters chosen as (a) $\tilde{\eta} = 0.5$ and (b) $\tilde{\eta} = 2.8$, with $D = 0.6$ and $R\cos\tilde{\gamma} = 0.2$ in both panels.

junctions which underlies the considerations of this paper. At the same time, there is experimental evidence that there can be edge-state transport even in the trivial regime [58]. For this reason, in Sec. V A, we study short nontopological junctions which are one dimensional and subject to a strong Zeeman field inside the junction region. In Sec. V B, we explore Josephson junctions based on proximity-coupled semiconductor quantum wires with Zeeman and spin-orbit coupling. This model can be explicitly tuned between the topological and the nontopological phase.

A. Nontopological Josephson junctions with strong Zeeman field in the junction region

Consider a Josephson junction made from a nontopological (i.e., nonhelical) one-dimensional channel. In the short-junction limit, the splitting of Andreev levels due to spin-orbit coupling is of order $\Delta^2\tau_{\mathrm{dw}}/\hbar$ [59–61]. Here, τ_{dw} denotes the dwell time in the junction which approaches zero in the short-junction regime. Hence, we can neglect spin-orbit coupling and focus on the Zeeman field. The subgap states and Josephson current of such junction can quite generally be obtained by scattering theory [43] (see Appendix D for a detailed calculation). Figure 11 shows two typical subgap spectra as a function of the phase difference across the junction in the case of a short nontopological junction with Zeeman field inside the junction region.

We observe that in short junctions, the main consequence of Zeeman and spin-orbit coupling in the junction region is that the odd-parity state spin splits. This implies that the odd-parity states carry nonzero supercurrent, leading to an additional plateau in the switching probability. This actually enhances the contrast with the short topological junctions which exhibit a single plateau. Even if this additional plateau is not resolved, however, we find that the supercurrent still vanishes when ϕ is an odd multiple of π. Thus, the behavior of the plateau width with phase difference remains as discussed in Sec. III.

The spin splitting of the odd-parity states also modifies the behavior in microwave absorption. Let us denote the two positive-energy Andreev levels as $E_\pm$. Then, transitions appear when the microwave frequency equals (i) $E_+ + E_-$, generalizing the line at $2E_A$ in the absence of the Zeeman field, (ii) $\Delta \pm E_+$ or $\Delta \pm E_-$, generalizing the lines at $\Delta \pm E_A$ to the spin-split case, and (iii) $E_+ - E_-$. The latter is visible only due to spin-orbit coupling and should therefore be weak. Thus, the magnetic field and spin-orbit coupling introduce additional absorption lines in microwave absorption, while short topological Josephson junctions have only two absorption lines.

B. Josephson junctions based on proximitized Rashba nanowires

Nontopological junctions based on proximity-coupled Rashba nanowires include both Zeeman and spin-orbit coupling also in the superconducting leads. Here, we explore the corresponding modifications for short junctions and show that both switching-current and ac-absorption measurements continue to provide clear-cut distinctions between topological and nontopological junctions.

The explicit Hamiltonian and the bulk dispersions for this system are given by Eq. (E1). We compute the spectrum of the Hamiltonian (E1) numerically by discretizing the model into a finite-difference representation. The results are shown in Figs. 12 and 13. In Fig. 12, we fix the chemical potential to $\mu = 0$. Results for a short junction are shown in panels (a)–(c), with the Zeeman field increasing from (a) to (c). Far on the nontopological side of the topological phase

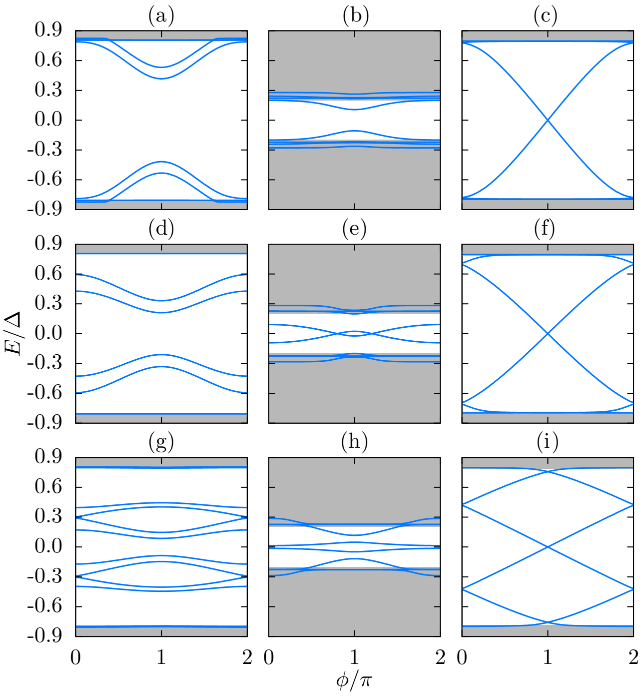

FIG. 12. Low-energy spectra of Hamiltonian (E1) as a function of phase difference φ, for various Zeeman fields and junction lengths. The results are obtained numerically for finite-length samples, showing all levels which become subgap states at least for some range of phase differences. Energies corresponding to the quasiparticle continuum of infinite wires are shown in gray. We choose a chemical potential $\mu = 0$, spin-orbit interaction $m\alpha^2 = \Delta$, and a total length 60ξ of the system, with $\xi = 2\alpha/\Delta$ the bulk coherence length of the superconductor when $B = 0$. Results for a short junction with $L = 0.05\xi$ are shown in (a)–(c) for increasing Zeeman field: (a) nontopological junction, $B = 0.2\Delta$; (b) nontopological junction, $B = 0.8\Delta$; (c) topological junction, $B = 2.0\Delta$. The subgap spectrum behaves in a qualitatively similar manner in intermediate length junctions with $L = 0.5\xi$. Results for junctions of this length are shown in (d)–(f), with the other parameters equal to those of panels (a)–(c). Additional subgap states emerge only in long junctions, as shown in panels (g) and (h) for $L = 2\xi$, and other parameters again as in (a)–(c). The numerical results are obtained by discretizing the Hamiltonian (E1) with a minimal spacing of 0.025ξ and an eighth-order approximation to the Laplacian.

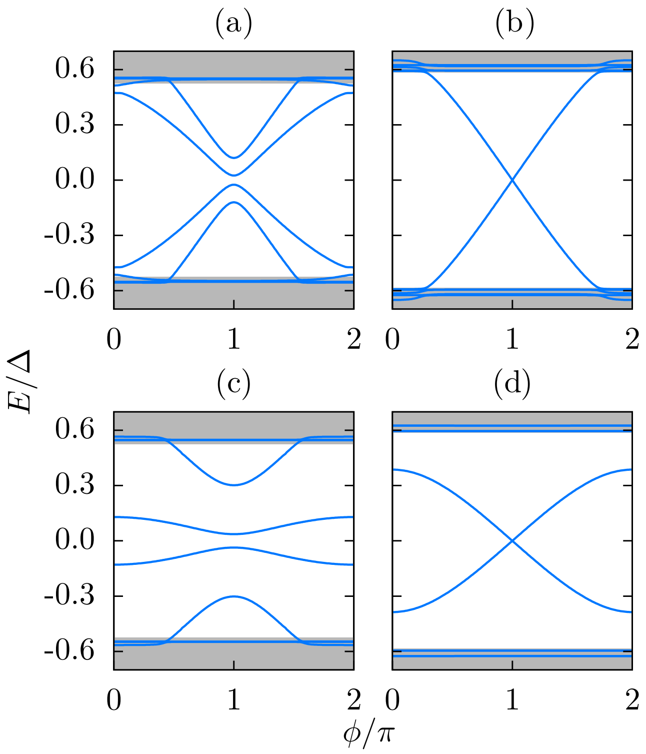

FIG. 13. Low-energy spectra of Hamiltonian (E1) as a function of phase difference φ, for fixed Zeeman fields $B = 2.0\Delta$ and junction length $L = 0.5\xi$. The results are obtained numerically for finite-length samples, showing all levels which become subgap states at least for some range of phase differences. Energies corresponding to the quasiparticle continuum of infinite wires are shown in gray. We choose a spin-orbit interaction of $m\alpha^2 = \Delta$ and a total length of 60ξ of the system, with $\xi = 2\alpha/\Delta$ the bulk coherence length of the superconductor when $B = 0$. (a) Nontopological junction with $\mu = 3.0\Delta$. (b) Topological junction with $\mu = 1.0\Delta$. Panels (c) and (d) are for parameters as in (a) and (b), respectively, but with an additional potential barrier of height 3Δ in the junction region, which reduces the junction transmission. The numerical results are obtained by discretizing the Hamiltonian (E1) with a minimal spacing of 0.025ξ and an eighth-order approximation to the Laplacian.

transition [Fig. 12(a)], the results differ from those for the simplified model of a nontopological junction in that the subgap states are spin split, leading to four subgap states. As argued in Sec. V A, this leads to additional plateaus in the switching probability and additional lines in microwave absorption, which enhances the central distinctions between short topological and nontopological junctions.

When approaching the topological phase transition by increasing the Zeeman field, the bulk gap $\Delta - B$ becomes smaller and two of the subgap states merge with the continuum. This is shown in Fig. 12(b). Thus, the switching probability is expected to exhibit only a single plateau, as in the topological phase. However, the plateau width remains distinctly different as the Josephson current vanishes at $\phi = \pi$ where it becomes maximal in a topological junction. The latter can be seen from Fig. 12(c) which shows the subgap spectrum in the topological phase.

The results in Figs. 12(a)–12(c) were obtained for a very short junction with a length of $L = 0.05\xi$, where ξ is the superconducting coherence length for $B = 0$ and $\mu = 0$. Qualitatively the same results are found for intermediate length junctions with $L = 0.5\xi$, as shown in Figs. 12(d)–12(f). Additional subgap states appear only for even longer junctions of length $L = 2\xi$, as shown in Figs. 12(g)–12(i).

We can also tune the junction across the topological phase transition by varying the chemical potentials μ. Corresponding results are shown in Fig. 13 for a junction of moderate length, $L = 0.5\xi$. Figure 13(a) corresponds to a nontopological junction with spin-split subgap states and vanishing supercurrent for $\phi = \pi$. Figure 13(b) corresponds to a topological junction with maximal supercurrent at $\phi = \pi$. Potential scattering in the junction region reduces the junction transmission which opens a gap between subgap states and quasiparticle continuum in the topological case while leaving the behavior near $\phi = \pi$ qualitatively unchanged. Corresponding numerical subgap spectra are shown in Figs. 13(c) and 13(d).

VI. CONCLUSION

The most immediate detection of a topological Josephson junction relies on the 4π-periodic Josephson effect. Its observation is, however, complicated by quasiparticle poisoning and diabatic effects. In this paper, we showed that topological Josepshon junctions can be identified even in the presence of quasiparticle poisoning. The proposed technique relies on switching-current measurements. While such measurements may be interesting even for the Josephson junction by itself, they provide much more information when including the junction into an asymmetric SQUID, together with an auxiliary junction with much larger critical current. Most importantly, incorporation into an asymmetric SQUID allows for phase-resolved measurements of the Josephson junction of interest.

Rather than measuring the 4π periodicity of individual subgap levels, the proposed switching-current measurements probe the existence of a protected level crossing at a certain phase difference δ. While in a topological junction, this level crossing is protected by fermion parity, there is no corresponding protection in nontopological junctions. For a particular junction state, the Josephson current is correspondingly maximal in magnitude at the protected crossing of a topological junction, but vanishes in a nontopological junction. We showed that this has striking manifestations in the switching probability of the junction as a function of the height of the applied current pulse, as illustrated in Figs. 4 and 6.

Specifically, our considerations focused on short Josephson junctions for which the number of subgap states is limited and the differences between topological and nontopological junctions are most pronounced. Especially, near degeneracies of subgap levels are quite unlikely in short nontopological junctions, as we show by explicitly calculating the subgap spectra for specific models based on topological-insulator edge modes or semiconductor quantum wires.

The proposed measurements are not only tolerant of (and in fact exploit) quasiparticle poisoning, but also provide access to the poisoning dynamics. The poisoning rates can be extracted by means of a pump-probe technique with multiple current pulses offset in time. As we showed, this is particularly useful to identify nontopological junctions with anomalously weak anticrossings of the Andreev levels. Microwave irradiation may be another useful technique in probing the poisoning dynamics as it also drives the system out of equilibrium. Moreover, microwave absorption provides access to the subgap spectrum of Josephson junctions, providing additional signatures which differentiate topological from nontopological junctions.

Throughout our discussion, we focused on the Majoranas which are localized at the junction and did not consider additional Majoranas located far from the junction. This is justified when the overlap between these additional outer Majoranas and the junction Majoranas can be neglected. Then, the subgap states resulting from the outer Majoranas are independent of the phase difference across the junction and the Josephson currents remain unaffected. Similarly, the transition matrix elements vanish for microwave processes involving both these and the junction Majoranas.

It is interesting to consider how our results become modified when there is substantial overlap between the junction and outer Majoranas. A topological junction would now have a "counterpart" of process (4) in Fig. 3, yielding an absorption line at the energy E_M plus the small splitting of the outer Majoranas (as opposed to $2E_A$ for a nontopological junction). In addition, there should also be an absorption feature with a threshold near Δ, which distinguishes this case from conventional Andreev states. Both additional features should be much dimmer than other features as they require overlap of the outer and junction Majoranas. In switching current measurements, the signature in Fig. 4(b) weakens a bit: In an exponentially narrow window around $\phi = \pi$, the plateau width would go to zero even in the topological phase. The signature in Figs. 6(a) and 6(b) would only be weakly affected. In particular, the fact that in Fig. 6(b) the plateau in $P_{\rm sw}$ is centered around the same current should be quite robust.

Thus, we conclude that the proposed signatures remain quite useful in the presence of weak coupling to the outer Majoranas. An exception is the discussion at the end of Sec. III D concerning poisoning processes. With coupling to outer Majoranas, the activation energy of the poisoning rates of topological junctions would no longer be necessarily larger than the gap, and a measurement without this overlap has clear benefits.

Combined switching-current and microwave absorption measurements on the same Josephson junction should thus be a powerful combination to identify topological Josephson junctions. In view of the fact that corresponding measurements have already been carried out successfully on nontopological junctions based on atomic point contacts [34–37], we hope that the proposed measurements can be readily implemented for topological junctions.

ACKNOWLEDGMENTS

We acknowledge discussions with L. Glazman and T. Karzig, and thank H. Pothier, D. van Woerkom, and R. Egger for comments on the manuscript. This work was supported in part by Priority Programs No. 1666 and No. 1285 as well as CRC 183 of the Deutsche Forschungsgemeinschaft (DFG), by the STC Center for Integrated Quantum Materials under NSF Grant No. DMR-1231319, by the Israeli Science Foundation (ISF), Minerva grants, a Career Integration Grant (CIG), a Minerva ARCHES prize, and an ERC Grant No. 340210 (FP7/2007-2013).

APPENDIX A: CALCULATION OF WAVE FUNCTIONS

In this appendix, we derive the wave functions for the bound states (Appendix A 1) and continuum states (Appendix A 2) of the Fu-Kane model in the short-junction limit. The Hamiltonian is given in Eq. (38).

1. Andreev bound state with $|E| < \Delta$

For $E < \Delta$, we write the left ($x < 0$) and right ($x > 0$) wave functions which are solutions to the Hamiltonian $\mathcal{H}$ without the δ-function term,

$$\begin{aligned}\Psi_L(x) &= e^{\kappa x}(aA_0,B_0,A_0,aB_0)^T, \quad x<0\\ \Psi_R(x) &= e^{-\kappa x}(C_0,aD_0,aC_0,D_0)^T, \quad x>0\end{aligned} \tag{A1}$$

where $\kappa(E)=\sqrt{\Delta^2-E^2}/v_F$ and $a(E)=E/\Delta - i\sqrt{1-E^2/\Delta^2}$. The connection condition in Eq. (41) leads to

$$\begin{aligned}e^{i\phi/2}C_0 &= aA_0\cosh R - i\sinh RB_0,\\ e^{-i\phi/2}C_0 &= a^{-1}A_0\cosh R + i\sinh RB_0,\\ e^{i\phi/2}D_0 &= i\sinh RA_0 + a^{-1}\cosh RB_0,\\ e^{-i\phi/2}D_0 &= -i\sinh RA_0 + a\cosh RB_0,\end{aligned} \tag{A2}$$

which can be further simplified to become

$$\begin{aligned}C_0 &= \frac{E}{\Delta}A_0\frac{\cosh R}{\cos\phi/2} = A_0,\\ D_0 &= \frac{E}{\Delta}B_0\frac{\cosh R}{\cos\phi/2} = B_0,\\ C_0 &= -\frac{\sqrt{D}\sinh RB_0}{\sqrt{1-D\cos^2\frac{\phi}{2}}+\sqrt{D}\sin\frac{\phi}{2}}.\end{aligned} \tag{A3}$$

These equations are a set of homogeneous linear equations for the coefficients A_0, B_0, C_0, and D_0. The condition to have nonzero solutions leads to the Andreev bound-state energy

$$E_M(\phi) = \Delta\cos\left(\frac{\phi}{2}\right)\Big/\cosh R = \sqrt{D}\Delta\cos\left(\frac{\phi}{2}\right) \tag{A4}$$

given in Eq. (42).

To obtain the bound-state wave function, we note that the coefficients fulfill $A_0=C_0$ and

$$B_0 = D_0 = \left(\frac{\sqrt{1-D\cos^2\frac{\phi}{2}}+\sqrt{D}\sin\frac{\phi}{2}}{\sqrt{1-D\cos^2\frac{\phi}{2}}-\sqrt{D}\sin\frac{\phi}{2}}\right)^{1/2} A_0. \tag{A5}$$

Imposing the normalization condition

$$\int dx\,\Psi^\dagger(x)\Psi(x) = \frac{2}{\kappa}\left(|A_0|^2+|B_0^2|\right)=1, \tag{A6}$$

and using

$$|A_0|^2+|B_0|^2 = \frac{2\sqrt{1-D\cos^2\frac{\phi}{2}}}{\sqrt{1-D\cos^2\frac{\phi}{2}}-\sqrt{D}\sin\frac{\phi}{2}}|A_0|^2 \tag{A7}$$

as well as

$$\kappa(E_M) = \frac{\Delta}{v_F}\sqrt{1-D\cos^2\frac{\phi}{2}}, \tag{A8}$$

we obtain

$$\begin{aligned}|A_0|^2 &= \frac{\Delta}{4v_F}\left(\sqrt{1-D\cos^2\frac{\phi}{2}}-\sqrt{D}\sin\frac{\phi}{2}\right),\\ |B_0|^2 &= \frac{\Delta}{4v_F}\left(\sqrt{1-D\cos^2\frac{\phi}{2}}+\sqrt{D}\sin\frac{\phi}{2}\right).\end{aligned} \tag{A9}$$

2. Continuum state with $|E|\geqslant\Delta$

For $E\geqslant\Delta$, we have four kinds of wave functions $\Psi_E^{(\eta,\chi)}$:

$$\begin{aligned}\Psi_E^{(e,l)} =\ & J(E)[e^{ipx}(1,0,a,0)+e^{-ipx}(aA^{(e,l)},0,A^{(e,l)},0)^T+e^{-ipx}(0,B^{(e,l)},0,aB^{(e,l)})^T]\theta(-x)\\ &+J(E)[e^{ipx}(C^{(e,l)},0,aC^{(e,l)},0)+e^{ipx}(0,aD^{(e,l)},0,D^{(e,l)})]\theta(x),\end{aligned} \tag{A10a}$$

$$\begin{aligned}\Psi_E^{(h,l)} =\ & J(E)[e^{ipx}(0,a,0,1)+e^{-ipx}(aA^{(h,l)},0,A^{(h,l)},0)^T+e^{-ipx}(0,B^{(h,l)},0,aB^{(h,l)})^T]\theta(-x)\\ &+J(E)[e^{ipx}(C^{(h,l)},0,aC^{(h,l)},0)+e^{ipx}(0,aD^{(h,l)},0,D^{(h,l)})]\theta(x),\end{aligned} \tag{A10b}$$

$$\begin{aligned}\Psi_E^{(e,r)} =\ & J(E)[e^{-ipx}(aA^{(e,r)},0,A^{(e,r)},0)^T+e^{-ipx}(0,B^{(e,r)},0,aB^{(e,r)})^T]\theta(-x)\\ &+J(E)[e^{-ipx}(0,1,0,a)^T+e^{ipx}(C^{(e,r)},0,aC^{(e,r)},0)+e^{ipx}(0,aD^{(e,r)},0,D^{(e,r)})]\theta(x),\end{aligned} \tag{A10c}$$

$$\begin{aligned}\Psi_E^{(h,r)} =\ & J(E)[e^{-ipx}(aA^{(h,r)},0,A^{(h,r)},0)^T+e^{-ipx}(0,B^{(h,r)},0,aB^{(h,r)})^T]\theta(-x)\\ &+J(E)[e^{-ipx}(a,0,1,0)^T+e^{ipx}(C^{(h,r)},0,aC^{(h,r)},0)+e^{ipx}(0,aD^{(h,r)},0,D^{(h,r)})]\theta(x),\end{aligned} \tag{A10d}$$

where $\eta=e,h$ denote electron or hole source, $\chi=l,r$ denote the source field coming from left or right,

$$p(E)=\frac{\sqrt{E^2-\Delta^2}}{v_F},\quad a(E)=\frac{E}{\Delta}-\sqrt{\frac{E^2}{\Delta^2}-1}, \tag{A11}$$

and $J(E)=[2\pi v_F(1-|a|^2)]^{-1/2}$ is the normalization constant. These coefficients for the continuum wave functions can be obtained by using the connection condition in Eq. (41), which will be shown in the following.

a. Electron source from left

For electron source from left, the wave function fulfills

$$\begin{pmatrix} C^{(e,l)} \\ aD^{(e,l)} \\ aC^{(e,l)} \\ D^{(e,l)} \end{pmatrix} = \begin{pmatrix} e^{-i\phi/2}\cosh R & -e^{-i\phi/2}i\sinh R & 0 & 0 \\ e^{-i\phi/2}i\sinh R & e^{-i\phi/2}\cosh R & 0 & 0 \\ 0 & 0 & e^{i\phi/2}\cosh R & e^{i\phi/2}i\sinh R \\ 0 & 0 & -e^{i\phi/2}i\sinh R & e^{i\phi/2}\cosh R \end{pmatrix} \begin{pmatrix} 1 + aA^{(e,l)} \\ B^{(e,l)} \\ a + A^{(e,l)} \\ aB^{(e,l)} \end{pmatrix}, \tag{A12}$$

$$A^{(e,l)} = \mathcal{A} = \frac{E\left(E_M^2 - \Delta^2\right) - iE_M\sqrt{E^2-\Delta^2}\Delta\sqrt{D}\sin\frac{\phi}{2}}{\Delta(E^2 - E_M^2)},$$

$$B^{(e,l)} = \mathcal{B} = \frac{-iE\sqrt{E^2-\Delta^2}\tanh R}{E^2 - E_M^2}. \tag{A13}$$

b. Hole source from left

For hole source from left, the wave function fulfills

$$\begin{pmatrix} C^{(h,l)} \\ aD^{(h,l)} \\ aC^{(h,l)} \\ D^{(h,l)} \end{pmatrix} = \begin{pmatrix} e^{-i\phi/2}\cosh R & -e^{-i\phi/2}i\sinh R & 0 & 0 \\ e^{-i\phi/2}i\sinh R & e^{-i\phi/2}\cosh R & 0 & 0 \\ 0 & 0 & e^{i\phi/2}\cosh R & e^{i\phi/2}i\sinh R \\ 0 & 0 & -e^{i\phi/2}i\sinh R & e^{i\phi/2}\cosh R \end{pmatrix} \begin{pmatrix} aA^{(h,l)} \\ a + B^{(h,l)} \\ A^{(h,l)} \\ 1 + aB^{(h,l)} \end{pmatrix}, \tag{A14}$$

$$A^{(h,l)} = \mathcal{B}, \quad B^{(h,l)} = \mathcal{A}^*. \tag{A15}$$

c. Electron source from right

For electron source from right, the wave function fulfills

$$\begin{pmatrix} C^{(e,r)} \\ 1 + aD^{(e,r)} \\ aC^{(e,r)} \\ a + D^{(e,r)} \end{pmatrix} = \begin{pmatrix} e^{-i\phi/2}\cosh R & -e^{-i\phi/2}i\sinh R & 0 & 0 \\ e^{-i\phi/2}i\sinh R & e^{-i\phi/2}\cosh R & 0 & 0 \\ 0 & 0 & e^{i\phi/2}\cosh R & e^{i\phi/2}i\sinh R \\ 0 & 0 & -e^{i\phi/2}i\sinh R & e^{i\phi/2}\cosh R \end{pmatrix} \begin{pmatrix} aA^{(e,r)} \\ B^{(e,r)} \\ A^{(e,r)} \\ aB^{(e,r)} \end{pmatrix}, \tag{A16}$$

$$A^{(e,r)} = \mathcal{C} = -\frac{iE_M\sqrt{E^2-\Delta^2}\tanh R}{E^2 - E_M^2},$$

$$B^{(e,r)} = \mathcal{D}^* = \frac{(E^2-\Delta^2)E_M + iE\sqrt{E^2-\Delta^2}\Delta\sqrt{D}\sin\frac{\phi}{2}}{\Delta(E^2 - E_M^2)}. \tag{A17}$$

d. Hole source from right

For hole source from right, the wave function fulfills

$$\begin{pmatrix} a + C^{(h,r)} \\ aD^{(h,r)} \\ 1 + aC^{(h,r)} \\ D^{(h,r)} \end{pmatrix} = \begin{pmatrix} e^{-i\phi/2}\cosh R & -e^{-i\phi/2}i\sinh R & 0 & 0 \\ e^{-i\phi/2}i\sinh R & e^{-i\phi/2}\cosh R & 0 & 0 \\ 0 & 0 & e^{i\phi/2}\cosh R & e^{i\phi/2}i\sinh R \\ 0 & 0 & -e^{i\phi/2}i\sinh R & e^{i\phi/2}\cosh R \end{pmatrix} \begin{pmatrix} aA^{(h,r)} \\ B^{(h,r)} \\ A^{(h,r)} \\ aB^{(h,r)} \end{pmatrix}, \tag{A18}$$

$$A^{(h,r)} = \mathcal{D}, \quad B^{(h,r)} = \mathcal{C}. \tag{A19}$$

APPENDIX B: DERIVATION OF JOSEPHSON CURRENT

In this appendix, we derive the Josephson current formula in Eq. (43) in Sec. IV A. By using Eq. (49), we can write the field operators for left/right moving electrons in terms Bogoliubov quasiparticle operators, in terms of coefficients of wave functions derived in the previous section:

$$\begin{aligned} \psi_+(0^-) = \int dE\, J(E)[&(1 + a\mathcal{A})\gamma_{(E,e,l)} + a\mathcal{B}\gamma_{(E,h,l)} + a\mathcal{C}\gamma_{(E,e,r)} + a\mathcal{D}\gamma_{(E,h,r)} \\ &- a\mathcal{B}^*\gamma^\dagger_{(E,e,l)} - (1 + a\mathcal{A})\gamma^\dagger_{(E,h,l)} - a\mathcal{D}\gamma^\dagger_{(E,e,r)} - a\mathcal{C}^*\gamma^\dagger_{(E,h,r)}] + a(E_M)A_0\gamma_0 - a(E_M)^*B_0^*\gamma_0^\dagger, \end{aligned} \tag{B1}$$

$$\begin{aligned} \psi_-(0^-) = \int dE\, J(E)[&\mathcal{B}\gamma_{(E,e,l)} + (a + \mathcal{A}^*)\gamma_{(E,h,l)} + \mathcal{D}^*\gamma_{(E,e,r)} + \mathcal{C}\gamma_{(E,h,r)} \\ &+ (a + \mathcal{A}^*)\gamma^\dagger_{(E,e,l)} + \mathcal{B}^*\gamma^\dagger_{(E,h,l)} + \mathcal{C}^*\gamma^\dagger_{(E,e,r)} + \mathcal{D}^*\gamma^\dagger_{(E,h,r)}] + B_0\gamma_0 + A_0^*\gamma_0^\dagger. \end{aligned} \tag{B2}$$

At zero temperature, all continuum states with negative eigenvalues of the Bogoliubov–de Gennes Hamiltonian are occupied, and all continuum states with positive eigenvalues are empty. The occupation of the Andreev bound state is $n = 0,1$, depending on the fermion parity of the system. This leads to the Josephson current, by using Eq. (48),

$$\begin{aligned}\langle I\rangle &= ev_F\big[|A_0|^2 - \big|B_0^2\big|\big](2n-1)\\ &= \frac{e\Delta}{2}\sqrt{D}\sin\frac{\phi}{2}(1-2n)\\ &= \frac{\pi G}{2}\frac{\Delta^2\sin\phi}{2eE_M(\phi)}(1-2n),\quad G = e^2D/\pi.\end{aligned} \tag{B3}$$

To obtain the above equation, we have used the identity

$$|\mathcal{A}|^2 + |\mathcal{B}|^2 + |\mathcal{C}|^2 + |\mathcal{D}|^2 = 1. \tag{B4}$$

APPENDIX C: DERIVATION OF Re$Y(\omega)$

In this appendix, we apply linear response theory to derive the real part of the admittance via the response function given in Eq. (46) of Sec. IV B. The response function $\chi(t)$ can be written as

$$\begin{aligned}\chi(t) = &-i\theta(t)ev_F^2\{\langle[\psi_+^\dagger(t)\psi_+(t),\psi_+^\dagger\psi_+]\rangle_0 + \langle[\psi_-^\dagger(t)\psi_-(t),\psi_-^\dagger\psi_-]\rangle_0\}\\ &+ i\theta(t)ev_F^2\{\langle[\psi_+^\dagger(t)\psi_+(t),\psi_-^\dagger\psi_-]\rangle_0 + \langle[\psi_-^\dagger(t)\psi_-(t),\psi_+^\dagger\psi_+]\rangle_0\}.\end{aligned} \tag{C1}$$

As a function of Matsubara frequency, it can be written as

$$\chi(i\Omega_n) = ev_F^2[\mathcal{G}_1(i\Omega_n) + \mathcal{G}_2(i\Omega_n) - \mathcal{G}_3(i\Omega_n) - \mathcal{G}_4(i\Omega_n)] \tag{C2}$$

and the frequency-dependent response function follows from it by analytical continuation.

1. $\mathcal{G}_1(i\Omega_n)$

For $\tau \geqslant 0$,

$$\mathcal{G}_1(\tau) = -\langle\mathcal{T}\psi_+^\dagger(\tau)\psi_+(\tau)\psi_+^\dagger\psi_+\rangle_0 = -\langle\psi_+^\dagger(\tau)\psi_+\rangle_0\langle\psi_+(\tau)\psi_+^\dagger\rangle_0 + \langle\psi_+^\dagger(\tau)\psi_+^\dagger\rangle_0\langle\psi_+(\tau)\psi_+\rangle_0. \tag{C3}$$

By using the relation between electron operators and Bogoliubov quasiparticle operators in Eq. (49), at $T = 0$, we have

$$\langle\psi_+^\dagger(\tau)\psi_+\rangle_0 = \int dE\, P(E)e^{-E\tau} + |B_0|^2e^{-E_M\tau}(1-n) + |A_0|^2e^{E_M\tau}n, \tag{C4}$$

$$\langle\psi_+(\tau)\psi_+^\dagger\rangle_0 = \int dE\, P(E)e^{-E\tau} + |A_0|^2e^{-E_M\tau}(1-n) + |B_0|^2e^{E_M\tau}n, \tag{C5}$$

$$\langle\psi_+^\dagger(\tau)\psi_+^\dagger\rangle_0 = -B_0A_0^*[e^{-E_M\tau}(1-n) + e^{E_M\tau}n], \tag{C6}$$

$$\langle\psi_+(\tau)\psi_+\rangle_0 = -A_0B_0^*[e^{-E_M\tau}(1-n) + e^{E_M\tau}n], \tag{C7}$$

with

$$P(E) = \frac{1}{2\pi v_F}\frac{E\sqrt{E^2-\Delta^2}}{E^2-E_M^2}. \tag{C8}$$

Hence,

$$\begin{aligned}\mathcal{G}_1(\tau) &= -\langle\mathcal{T}\psi_+^\dagger(\tau)\psi_+(\tau)\psi_+^\dagger\psi_+\rangle_0\\ &= -\int dE_1dE_2\, P(E_1)P(E_2)e^{-(E_1+E_2)\tau} - (|A_0|^2 + |B_0|^2)\bigg[\int dE\,(1-n)P(E)e^{-(E+E_M)\tau} + \int dE\, nP(E)e^{-(E-E_M)\tau}\bigg].\end{aligned} \tag{C9}$$

Finally, we obtain

$$\mathcal{G}_1(i\Omega_n) = \int dE_1dE_2\frac{P(E_1)P(E_2)}{i\Omega_n - E_1 - E_2} + (|A_0|^2 + |B_0|^2)\int dE\, P(E)\bigg[\frac{(1-n)}{i\Omega_n - E - E_M} + \frac{n}{i\Omega_n - E + E_M}\bigg]. \tag{C10}$$

2. $\mathcal{G}_2(i\Omega_n)$

For $\tau \geqslant 0$,

$$\mathcal{G}_2(\tau) = -\langle\mathcal{T}\psi_-^\dagger(\tau)\psi_-(\tau)\psi_-^\dagger\psi_-\rangle_0 = -\langle\psi_-^\dagger(\tau)\psi_-\rangle_0\langle\psi_-(\tau)\psi_-^\dagger\rangle_0 + \langle\psi_-^\dagger(\tau)\psi_-^\dagger\rangle_0\langle\psi_-(\tau)\psi_-\rangle_0. \tag{C11}$$

Consider $T = 0$,

$$\langle\psi_-^\dagger(\tau)\psi_-\rangle_0 = \int dE\, P(E)e^{-E\tau} + |A_0|^2 e^{-E_M\tau}(1-n) + |B_0|^2 e^{E_M\tau} n, \tag{C12}$$

$$\langle\psi_-(\tau)\psi_-^\dagger\rangle_0 = \int dE\, P(E)e^{-E\tau} + |B_0|^2 e^{-E_M\tau}(1-n) + |A_0|^2 e^{E_M\tau} n, \tag{C13}$$

$$\langle\psi_-^\dagger(\tau)\psi_-^\dagger\rangle_0 = A_0 B_0^*[e^{-E_M\tau}(1-n) + e^{E_M\tau} n], \tag{C14}$$

$$\langle\psi_-(\tau)\psi_-\rangle_0 = A_0^* B_0[e^{-E_M\tau}(1-n) + e^{E_M\tau} n]. \tag{C15}$$

Thus, we have

$$\mathcal{G}_2(i\Omega_n) = \mathcal{G}_1(i\Omega_n) = \int dE_1 dE_2\, \frac{P(E_1)P(E_2)}{i\Omega_n - E_1 - E_2} + (|A_0|^2 + |B_0|^2)\int dE\, P(E)\left[\frac{(1-n)}{i\Omega_n - E - E_M} + \frac{n}{i\Omega_n - E + E_M}\right]. \tag{C16}$$

3. $\mathcal{G}_3(i\Omega_n)$

For $\tau \geqslant 0$,

$$\mathcal{G}_3(\tau) = -\langle\mathcal{T}\psi_+^\dagger(\tau)\psi_+(\tau)\psi_-^\dagger\psi_-\rangle_0 = -\langle\psi_+^\dagger(\tau)\psi_-\rangle_0\langle\psi_+(\tau)\psi_-^\dagger\rangle_0 + \langle\psi_+^\dagger(\tau)\psi_-^\dagger\rangle_0\langle\psi_+(\tau)\psi_-\rangle_0. \tag{C17}$$

Consider $T = 0$, we have

$$\langle\psi_+^\dagger(\tau)\psi_-\rangle_0 = -\int dE\, M(E)e^{-E\tau} - a(E_M)A_0^* B_0 e^{-E_M\tau}(1-n) + a(E_M)^* A_0^* B_0 e^{E_M\tau} n, \tag{C18}$$

$$\langle\psi_+(\tau)\psi_-^\dagger\rangle_0 = \int dE\, M(E)e^{-E\tau} + a(E_M)A_0 B_0^* e^{-E_M\tau}(1-n) - a(E_M)^* B_0^* A_0 e^{E_M\tau} n, \tag{C19}$$

$$\langle\psi_+^\dagger(\tau)\psi_-^\dagger\rangle_0 = -\int dE\, Q(E)^* e^{-E\tau} - a(E_M)|B_0|^2 e^{-E_M\tau}(1-n) + a(E_M)^*|A_0|^2 e^{E_M\tau} n, \tag{C20}$$

$$\langle\psi_+(\tau)\psi_-\rangle_0 = \int dE\, Q(E)e^{-E\tau} + a(E_M)|A_0|^2 e^{-E_M\tau}(1-n) - a(E_M)^*|B_0|^2 e^{E_M\tau} n, \tag{C21}$$

where

$$M(E) = \frac{1}{2\pi v_F}\frac{iE\sqrt{E^2-\Delta^2}\tanh R}{E^2 - E_M^2},$$
$$Q(E) = \frac{1}{2\pi v_F}\frac{E_M\sqrt{E^2-\Delta^2}}{E^2 - E_M^2}. \tag{C22}$$

Hence,

$$\begin{aligned}\mathcal{G}_3(\tau) = {}& \int dE_1 dE_2\, e^{-(E_1+E_2)\tau}[M(E_1)M(E_2) - Q^*(E_1)Q(E_2)]\\ &+ (1-n)a(E_M)\int dE\, e^{-(E+E_M)\tau}[M(E)(A_0^*B_0 + A_0B_0^*) - Q(E)|B_0|^2 - Q(E)^*|A_0|^2]\\ &+ na(E_M)^*\int dE\, e^{-(E-E_M)\tau}[Q(E)|A_0|^2 + Q(E)^*|B_0|^2 - M(E)(A_0^*B_0 + A_0B_0^*)],\end{aligned} \tag{C23}$$

$$\begin{aligned}\mathcal{G}_3(i\Omega_n) = {}& \int dE_1 dE_2\, \frac{Q^*(E_1)Q(E_2) - M(E_1)M(E_2)}{i\Omega_n - E_1 - E_2}\\ &+ (1-n)a(E_M)\int dE\, \frac{Q(E)|B_0|^2 + Q(E)^*|A_0|^2 - M(E)(A_0^*B_0 + A_0B_0^*)}{i\Omega_n - E - E_M}\\ &+ na(E_M)^*\int dE\, \frac{M(E)(A_0^*B_0 + A_0B_0^*) - Q(E)|A_0|^2 - Q(E)^*|B_0|^2}{i\Omega_n - E + E_M}.\end{aligned} \tag{C24}$$

4. $\mathcal{G}_4(i\Omega_n)$

For $\tau \geqslant 0$,

$$\mathcal{G}_4(\tau) = -\langle\mathcal{T}\psi_-^\dagger(\tau)\psi_-(\tau)\psi_+^\dagger\psi_+\rangle_0 = -\langle\psi_-^\dagger(\tau)\psi_+\rangle_0\langle\psi_-(\tau)\psi_+^\dagger\rangle_0 + \langle\psi_-^\dagger(\tau)\psi_+^\dagger\rangle_0\langle\psi_-(\tau)\psi_+\rangle_0. \tag{C25}$$

By using the zero-temperature averages of electron operators

$$\langle\psi_-^\dagger(\tau)\psi_+\rangle_0 = \int dE\, M(E)e^{-E\tau} - a^*(E_M)A_0B_0^*e^{-E_M\tau}(1-n) + a(E_M)A_0B_0^*e^{E_M\tau}n, \tag{C26}$$

$$\langle\psi_-(\tau)\psi_+^\dagger\rangle_0 = -\int dE\, M(E)e^{-E\tau} + a^*(E_M)A_0^*B_0e^{-E_M\tau}(1-n) - a(E_M)A_0^*B_0e^{E_M\tau}n, \tag{C27}$$

$$\langle\psi_-^\dagger(\tau)\psi_+^\dagger\rangle_0 = \int dE\, Q(E)^*e^{-E\tau} + a^*(E_M)|A_0|^2e^{-E_M\tau}(1-n) - a(E_M)|B_0|^2e^{E_M\tau}n, \tag{C28}$$

$$\langle\psi_-(\tau)\psi_+\rangle_0 = -\int dE\, Q(E)e^{-E\tau} - a^*(E_M)|B_0|^2e^{-E_M\tau}(1-n) + a(E_M)|A_0|^2e^{E_M\tau}n, \tag{C29}$$

we obtain

$$\begin{aligned}\mathcal{G}_4(\tau) = &\int dE_1dE_2\, e^{-(E_1+E_2)\tau}[M(E_1)M(E_2) - Q^*(E_1)Q(E_2)]\\ &-(1-n)a(E_M)^*\int dE\, e^{-(E+E_M)\tau}[M(E)(A_0^*B_0 + A_0B_0^*) + Q(E)|A_0|^2 + Q(E)^*|B_0|^2]\\ &+na(E_M)\int dE\, e^{-(E-E_M)\tau}[Q(E)^*|A_0|^2 + Q(E)|B_0|^2 + M(E)(A_0^*B_0 + A_0B_0^*)],\end{aligned} \tag{C30}$$

$$\begin{aligned}\mathcal{G}_4(i\Omega_n) = &\int dE_1dE_2\, \frac{Q^*(E_1)Q(E_2) - M(E_1)M(E_2)}{i\Omega_n - E_1 - E_2}\\ &+(1-n)a(E_M)^*\int dE\, \frac{M(E)(A_0^*B_0 + A_0B_0^*) + Q(E)|A_0|^2 + Q(E)^*|B_0|^2}{i\Omega_n - E - E_M}\\ &-na(E_M)\int dE\, \frac{Q(E)^*|A_0|^2 + Q(E)|B_0|^2 + M(E)(A_0^*B_0 + A_0B_0^*)}{i\Omega_n - E + E_M}.\end{aligned} \tag{C31}$$

5. Re$Y(\omega)$

Plug the expressions for $\mathcal{G}_1$, $\mathcal{G}_2$, $\mathcal{G}_3$, and $\mathcal{G}_4$ into Eq. (C2), and make analytical continuation $i\Omega_n \to \omega + i\eta$, where $\eta \to 0^+$, we obtain the retarded response function

$$\chi(\omega + i\eta) = \chi_1(\omega + i\eta) + (1-n)\chi_2(\omega + i\eta) + n\chi_3(\omega + i\eta) \tag{C32}$$

with

$$\begin{aligned}\chi_1(\omega + i\eta) &= 2ev_F^2\int dE_1dE_2\, \frac{P(E_1)P(E_2) + M(E_1)M(E_2) - Q^*(E_1)Q(E_2)}{\omega + i\eta - E_1 - E_2}\\ &= \frac{eD}{2\pi^2}\int_\Delta^\infty dE_1dE_2\, \frac{(E_1E_2 - E_M)\sqrt{E_1^2 - \Delta^2}\sqrt{E_2^2 - \Delta^2}}{(\omega + i\eta - E_1 - E_2)(E_1^2 - E_M^2)(E_2^2 - E_M^2)},\end{aligned} \tag{C33}$$

$$\begin{aligned}\chi_2(\omega + i\eta) &= 2ev_F^2\int dE\, \frac{(|A_0|^2 + |B_0|^2)P(E) + \mathrm{Re}\{a(E_M)[M(E)(A_0^*B_0 + A_0B_0^*) - Q(E)|B_0|^2 - Q(E)^*|A_0|^2]\}}{\omega + i\eta - E - E_M}\\ &= \frac{eD}{\pi}\int_\Delta^\infty dE\, \frac{\sqrt{E^2 - \Delta^2}\sqrt{\Delta^2 - E_M^2}}{(\omega + i\eta - E - E_M)(E + E_M)},\end{aligned} \tag{C34}$$

$$\begin{aligned}\chi_3(\omega + i\eta) &= 2ev_F^2\int dE\, \frac{(|A_0|^2 + |B_0|^2)P(E) + \mathrm{Re}\{a(E_M)[Q(E)|B_0|^2 + Q(E)^*|A_0|^2 + M(E)(A_0^*B_0 + A_0B_0^*)]\}}{\omega + i\eta - E + E_M}\\ &= \frac{eD}{\pi}\int_\Delta^\infty dE\, \frac{\sqrt{E^2 - \Delta^2}\sqrt{\Delta^2 - E_M^2}}{(\omega + i\eta - E + E_M)(E - E_M)}.\end{aligned} \tag{C35}$$

To obtain the above expressions, we have used

$$2\,\mathrm{Re}[M(E)(A_0^* B_0 + A_0 B_0^*)] = \frac{-E\sqrt{E^2-\Delta^2}\sqrt{\Delta^2-E_M^2}(1-D)}{2\pi v_F^2\Delta\left(E^2-E_M^2\right)}, \tag{C36}$$

$$2\,\mathrm{Re}[Q(E)|B_0|^2 + Q(E)^*|A_0|^2] = Q(E)|B_0|^2 + Q(E)^*|A_0|^2 = \frac{E_M\sqrt{E^2-\Delta^2}\sqrt{\Delta^2-E_M^2}D}{2\pi v_F^2\Delta\left(E^2-E_M^2\right)}, \tag{C37}$$

$$2P(E)(|A_0|^2 + |B_0|^2) = \frac{E\sqrt{E^2-\Delta^2}\sqrt{\Delta^2-E_M^2}}{2\pi v_F^2\Delta\left(E^2-E_M^2\right)}. \tag{C38}$$

By using the relation $\mathrm{Re}Y = -(e/\omega)\mathrm{Im}\chi$, we obtain the real part of the admittance:

$$\mathrm{Re}Y_1 = \frac{e^2 D}{2\pi\omega}\theta(\omega-2\Delta)\int_\Delta^{\omega-\Delta} dE\,\frac{\left[E(\omega-E)-E_M^2\right]\sqrt{E^2-\Delta^2}\sqrt{(\omega-E)^2-\Delta^2}}{\left(E^2-E_M^2\right)\left[(\omega-E)^2-E_M^2\right]}, \tag{C39a}$$

$$\mathrm{Re}Y_2 = e^2 D\theta(\omega-E_M-\Delta)\frac{\sqrt{(\omega-E_M)^2-\Delta^2}\sqrt{\Delta^2-E_M^2}}{\omega^2}, \tag{C39b}$$

$$\mathrm{Re}Y_3 = e^2 D\theta(\omega+E_M-\Delta)\frac{\sqrt{(\omega+E_M)^2-\Delta^2}\sqrt{\Delta^2-E_M^2}}{\omega^2}. \tag{C39c}$$

APPENDIX D: ZEEMAN FIELD INSIDE A NONTOPOLOGICAL JUNCTION

In this appendix, we provide some technical details underlying the results presented in Sec. V A. As long as we can neglect spin-orbit and Zeeman coupling in the superconducting leads (but not in the junction region), the subgap spectrum of a nontopological junction can be obtained from the condition [43]

$$\det\left(1-\alpha_A^2 r_A^* S_e r_A S_h\right) = 0. \tag{D1}$$

Here, Andreev reflection from the superconductors is described by

$$\alpha_A = \frac{E}{\Delta} - i\frac{\sqrt{\Delta^2-E^2}}{\Delta}, \quad r_A = e^{i\phi\rho_z/2}, \tag{D2}$$

with ϕ the phase difference between the two superconductors and ρ_j Pauli matrices in left/right space. The normal section of the junction is characterized by the electron and hole scattering matrices S_e and S_h. In the presence of Zeeman and spin-orbit coupling, the electron and hole scattering matrices S_e and S_h are 4×4 matrices describing the normal section coupled to normal-metal leads and relating outgoing to ingoing channels, with the four components corresponding to left and right channels of either spin. The hole scattering matrix S_h is related to the electron scattering matrix through

$$S_h = \sigma_y(S_e)^*\sigma_y, \tag{D3}$$

which follows by particle-hole symmetry. (This uses the same Nambu basis as in Sec. IV A.)

In the short-junction limit, S_e and S_h can be evaluated at zero energy. In this limit, spin-orbit coupling leaves the spin degeneracy of the Andreev levels unchanged [59–61]. Choosing the spin quantization axis along $\mathbf{B}$, the scattering matrices S_e and S_h are diagonal in the spin indices, with the diagonal entries labeled by S_e^σ and S_h^σ (with $\sigma = \uparrow,\downarrow$). Then, Eq. (D1) breaks up into two separate determinant equations for the spin components.

For a single spin channel with transmission $D_\sigma = 1 - R_\sigma$, the scattering matrices can be parametrized as

$$S_e^\sigma = e^{i\eta_\sigma}\left(\sqrt{R_\sigma}\rho_z e^{i\rho_z\gamma_\sigma} + \sqrt{D_\sigma}\rho_x\right). \tag{D4}$$

Exploiting unitarity and Eq. (D3), we obtain

$$\det\left(S_e^{\bar\sigma} - \alpha^2 r_A^* S_e^\sigma r_A\right) = 0 \tag{D5}$$

with $\bar\sigma = -\sigma$. Focusing on $\sigma = \uparrow$ and the Nambu spinor $(\psi_\uparrow,\psi_\downarrow^\dagger)^T$, the determinant condition becomes

$$\cos(2\tilde\alpha + \tilde\eta) = R\cos\tilde\gamma + D\cos\phi, \tag{D6}$$

where $\tilde\eta = \eta_\uparrow - \eta_\downarrow$, $\tilde\gamma = \gamma_\uparrow - \gamma_\downarrow$, $D = \sqrt{D_\uparrow D_\downarrow}$, $R = \sqrt{R_\uparrow R_\downarrow}$, and $\alpha = \exp(i\tilde\alpha)$. This equation was derived in Ref. [59]. The corresponding results for $\sigma = \downarrow$ with Nambu spinor $(\psi_\downarrow, -\psi_\uparrow^\dagger)^T$ follow by particle-hole symmetry. If we denote the subgap eigenstates for spin σ by $E_n^\sigma(\phi)$, we have $E_n^\downarrow(\phi) = -E_n^\uparrow(\phi)$.

For spin-independent scattering matrices, one has $\tilde\eta = 0$ and $R + D = 1$, and recovers the Andreev bound state given in Eq. (1). When the two spin channels are subject to different scattering potentials, we have $R + D < 1$ and the energies of the Andreev bound states can be written as

$$E_\pm(\phi) = \Delta\,\mathrm{Sgn}\left[\sin\left(\frac{\tilde\eta}{2} \pm \chi\right)\right]\cos\left(\frac{\tilde\eta}{2} \pm \chi\right), \tag{D7}$$

where

$$\chi = \tfrac{1}{2}\arccos\left(R\cos\tilde\gamma + D\cos\phi\right). \tag{D8}$$

APPENDIX E: JUNCTION BASED ON PROXIMITIZED RASHBA NANOWIRES

In this appendix, we provide some technical details underlying Sec. V B. Consider a Josephson junction formed by two semiconductor nanowires with Rashba spin-orbit coupling, proximity coupled to s-wave superconductors and subject to a Zeeman field B. For a phase difference of ϕ, the corresponding Hamiltonian takes the form [5]

$$H = \left(-\frac{\partial_x^2}{2m} + i\alpha\sigma_y\partial_x - \mu\right)\tau_z + B\sigma_x + \Delta\theta\left(x - \frac{L}{2}\right)\tau_x + \Delta\theta\left(-x - \frac{L}{2}\right)(\cos\phi\tau_x + \sin\phi\tau_y), \quad \text{(E1)}$$

where α denotes the strength of the Rashba spin-orbit coupling, μ the chemical potential, m the effective mass, L the length of the junction, and Δ the induced pairing strength. We also introduced the Pauli matrices σ_j and τ_j in spin and Nambu space, respectively.

The bulk dispersion of the model is

$$E_\pm(p)^2 = B^2 + \Delta^2 + \xi_p^2 + (\alpha p)^2 \pm 2\sqrt{B^2\Delta^2 + B^2\xi_p^2 + (\alpha p)^2\xi_p^2}, \quad \text{(E2)}$$

where $\xi_p = \frac{p^2}{2m} - \mu$. For finite B and Δ, gaps open at $p = 0$ and $p = \pm k_F$, where

$$k_F = \sqrt{2m(m\alpha^2 + \sqrt{m^2\alpha^4 + B^2})}. \quad \text{(E3)}$$

The gap

$$E_{\text{gap}}(p = 0) = |B - \sqrt{\Delta^2 + \mu^2}| \quad \text{(E4)}$$

at $p = 0$ closes for $B = \sqrt{\Delta^2 + \mu^2}$ indicating the topological phase transition, with the topological (nontopological) phase corresponding to $B > \sqrt{\Delta^2 + \mu^2}$ ($B < \sqrt{\Delta^2 + \mu^2}$). The gap

$$E_{\text{gap}}(p = \pm k_F) = \sqrt{\Delta^2 + 2\xi_{k_F}^2 - 2\sqrt{B^2\Delta^2 + \xi_{k_F}^4}} \quad \text{(E5)}$$

at $\pm k_F$ remains finite throughout.

[1] A. Y. Kitaev, Phys.-Usp. **44**, 131 (2001).
[2] A. Y. Kitaev, Ann. Phys. (NY) **303**, 2 (2003).
[3] L. Fu and C. L. Kane, Phys. Rev. Lett. **100**, 096407 (2008).
[4] L. Fu and C. L. Kane, Phys. Rev. B **79**, 161408 (2009).
[5] R. M. Lutchyn, J. D. Sau, and S. Das Sarma, Phys. Rev. Lett. **105**, 077001 (2010).
[6] Y. Oreg, G. Refael, and F. von Oppen, Phys. Rev. Lett. **105**, 177002 (2010).
[7] J. Alicea, Y. Oreg, G. Refael, F. von Oppen, and M. P. A. Fisher, Nat. Phys. **7**, 412 (2011).
[8] T.-P. Choy, J. M. Edge, A. R. Akhmerov, and C. W. J. Beenakker, Phys. Rev. B **84**, 195442 (2011).
[9] M. Kjaergaard, K. Wölms, and K. Flensberg, Phys. Rev. B **85**, 020503 (2012).
[10] I. Martin and A. F. Morpurgo, Phys. Rev. B **85**, 144505 (2012).
[11] S. Nadj-Perge, I. K. Drozdov, B. A. Bernevig, and A. Yazdani, Phys. Rev. B **88**, 020407 (2013).
[12] F. Pientka, L. I. Glazman, and F. von Oppen, Phys. Rev. B **88**, 155420 (2013).
[13] V. Mourik, K. Zuo, S. M. Frolov, S. R. Plissard, E. P. A. M. Bakkers, and L. P. Kouwenhoven, Science **336**, 1003 (2012).
[14] A. Das, Y. Ronen, Y. Most, Y. Oreg, M. Heiblum, and H. Shtrikman, Nat. Phys. **8**, 887 (2012).
[15] H. O. H. Churchill, V. Fatemi, K. Grove-Rasmussen, M. T. Deng, P. Caroff, H. Q. Xu, and C. M. Marcus, Phys. Rev. B **87**, 241401 (2013).
[16] L. P. Rokhinson, X. Liu, and J. K. Furdyna, Nat. Phys. **8**, 795 (2012).
[17] M. T. Deng, C. L. Yu, G. Y. Huang, M. Larsson, P. Caroff, and H. Q. Xu, Nano Lett. **12**, 6414 (2012).
[18] A. D. K. Finck, D. J. Van Harlingen, P. K. Mohseni, K. Jung, and X. Li, Phys. Rev. Lett. **110**, 126406 (2013).
[19] S. Hart, H. Ren, T. Wagner, P. Leubner, M. Muehlbauer, C. Bruene, H. Buhmann, L. Molenkamp, and A. Yacoby, Nat. Phys. **10**, 638 (2014).
[20] V. S. Pribiag, A. J. Beukman, F. Qu, M. C. Cassidy, C. Charpentier, W. Wegscheider, and L. P. Kouwenhoven, Nat. Nanotechnol. **10**, 593 (2015).
[21] S. Nadj-Perge, I. K. Drozdov, J. Li, H. Chen, S. Jeon, J. Seo, A. H. MacDonald, B. A. Bernevig, and A. Yazdani, Science **346**, 602 (2014).
[22] M. Ruby, F. Pientka, Y. Peng, F. von Oppen, B. W. Heinrich, and K. J. Franke, Phys. Rev. Lett. **115**, 197204 (2015).
[23] J. Wiedenmann, E. Bocquillon, R. S. Deacon, S. Hartinger, O. Herrmann, T. M. Klapwijk, L. Maier, C. Ames, C. Bruene, C. Gould, A. Oiwa, K. Ishibashi, S. Tarucha, H. Buhmann, and L. W. Molenkamp, Nat. Commun. **7**, 10303 (2016).
[24] J. Paajaste, E. Strambini, M. Amado, S. Roddaro, P. San-Jose, R. Aguado, F. S. Bergeret, D. Ercolani, L. Sorba, and F. Giazotto, arXiv:1601.02955.
[25] D. M. Badiane, M. Houzet, and J. S. Meyer, Phys. Rev. Lett. **107**, 177002 (2011).
[26] L. Jiang, D. Pekker, J. Alicea, G. Refael, Y. Oreg, and F. von Oppen, Phys. Rev. Lett. **107**, 236401 (2011).
[27] P. San-Jose, E. Prada, and R. Aguado, Phys. Rev. Lett. **108**, 257001 (2012).
[28] D. I. Pikulin and Y. V. Nazarov, Phys. Rev. B **86**, 140504 (2012).
[29] C. W. J. Beenakker, D. I. Pikulin, T. Hyart, H. Schomerus, and J. P. Dahlhaus, Phys. Rev. Lett. **110**, 017003 (2013).
[30] P. San-Jose, J. Cayao, E. Prada, and R. Aguado, New J. Phys. **15**, 075019 (2013).
[31] F. Zhang and C. L. Kane, Phys. Rev. Lett. **113**, 036401 (2014).
[32] S.-P. Lee, K. Michaeli, J. Alicea, and A. Yacoby, Phys. Rev. Lett. **113**, 197001 (2014).
[33] P. Marra, R. Citro, and A. Braggio, Phys. Rev. B **93**, 220507(R) (2016).
[34] M. L. Della Rocca, M. Chauvin, B. Huard, H. Pothier, D. Esteve, and C. Urbina, Phys. Rev. Lett. **99**, 127005 (2007).
[35] M. Zgirski, L. Bretheau, Q. Le Masne, H. Pothier, D. Esteve, and C. Urbina, Phys. Rev. Lett. **106**, 257003 (2011).

[36] L. Bretheau, C. O. Girit, C. Urbina, D. Esteve, and H. Pothier, Phys. Rev. X **3**, 041034 (2013).
[37] L. Bretheau, C. O. Girit, H. Pothier, D. Esteve, and C. Urbina, Nature (London) **499**, 312 (2013).
[38] M. Tinkham, *Introduction to Superconductivity: Second Edition*, Dover Books on Physics (Dover, New York, 2004).
[39] F. Kos, S. E. Nigg, and L. I. Glazman, Phys. Rev. B **87**, 174521 (2013).
[40] P. Virtanen and P. Recher, Phys. Rev. B **88**, 144507 (2013).
[41] L. Bretheau, C. O. Girit, M. Houzet, H. Pothier, D. Esteve, and C. Urbina, Phys. Rev. B **90**, 134506 (2014).
[42] J. I. Väyrynen, G. Rastelli, W. Belzig, and L. I. Glazman, Phys. Rev. B **92**, 134508 (2015).
[43] C. W. J. Beenakker, Phys. Rev. Lett. **67**, 3836 (1991).
[44] J. Alicea, Rep. Prog. Phys. **75**, 076501 (2012).
[45] C. W. J. Beenakker, Annu. Rev. Condens. Matter Phys. **4**, 113 (2013).
[46] D. G. Olivares, A. L. Yeyati, L. Bretheau, C. O. Girit, H. Pothier, and C. Urbina, Phys. Rev. B **89**, 104504 (2014).
[47] A. Zazunov, A. Brunetti, A. L. Yeyati, and R. Egger, Phys. Rev. B **90**, 104508 (2014).
[48] D. E. McCumber, J. Appl. Phys. **39**, 3113 (1968).
[49] W. C. Stewart, Appl. Phys. Lett. **12**, 277 (1968).
[50] V. Ambegaokar and B. I. Halperin, Phys. Rev. Lett. **22**, 1364 (1969).
[51] J. Kurkijärvi, Phys. Rev. B **6**, 832 (1972).
[52] T. A. Fulton and L. N. Dunkleberger, Phys. Rev. B **9**, 4760 (1974).
[53] P. Hänggi, P. Talkner, and M. Borkovec, Rev. Mod. Phys. **62**, 251 (1990).
[54] H. Kramers, Physica (Amsterdam) **7**, 284 (1940).
[55] A. Zazunov, R. Egger, and A. Levy Yeyati, Phys. Rev. B **94**, 014502 (2016).
[56] O. Dmytruk, M. Trif, and P. Simon, Phys. Rev. B **92**, 245432 (2015).
[57] O. Dmytruk, M. Trif, and P. Simon, arXiv:1604.06780.
[58] F. Nichele, H. J. Suominen, M. Kjaergaard, C. M. Marcus, E. Sajadi, J. A. Folk, F. Qu, A. J. A. Beukman, F. K. de Vries, J. van Veen, S. Nadj-Perge, L. P. Kouwenhoven, B.-M. Nguyen, A. A. Kiselev, W. Yi, M. Sokolich, M. J. Manfra, E. M. Spanton, and K. A. Moler, New J. Phys. **18**, 083005 (2016).
[59] J. Michelsen, V. S. Shumeiko, and G. Wendin, Phys. Rev. B **77**, 184506 (2008).
[60] N. M. Chtchelkatchev and Y. V. Nazarov, Phys. Rev. Lett. **90**, 226806 (2003).
[61] B. Béri, J. H. Bardarson, and C. W. J. Beenakker, Phys. Rev. B **77**, 045311 (2008).

5 Parity Anomaly and Spin Transmutation in Quantum Spin Hall Josephson Junctions

Superconductor/quantum spin Hall/superconductor junctions in the presence of a Zeeman field are a prototypical setup for creating topological Josephson junctions. When the Zeeman field is absent and electron-electron interactions are neglected, the junction is expected to exhibit a 2π-periodic dissipative Josephson effect. It thus came as a surprise when Molenkamp's group probed Shapiro steps and Josephson radiation in such junctions and found evidence for 4π-periodic currents [68, 69]. Motivated by this puzzle, I considered realistic junctions in which there are charge puddles which act as magnetic impurities coupled to the helical edge. I showed that as long as the coupling is time-reversal symmetric, the Josephson effect generically becomes 8π-periodic, which can be thought as boiling down to coupling of $\mathbb{Z}_4$ parafermions. This 8π Josephson effect is a result of the fermion parity anomaly and a remarkable spin transmutation. To connect to the experimental observations, I provided scenarios how this effect may appear as having period 4π. It will be interesting to see whether future experiments can distinguish this explanation as a parafermion effect from a more elementary explanation in terms of inelastic relaxation of two quasiparticles into a Cooper pair which applies even to pristine junctions.

Parity Anomaly and Spin Transmutation in Quantum Spin Hall Josephson Junctions

Yang Peng,[1] Yuval Vinkler-Aviv,[1] Piet W. Brouwer,[1] Leonid I. Glazman,[2] and Felix von Oppen[1]
[1]*Dahlem Center for Complex Quantum Systems and Fachbereich Physik, Freie Universität Berlin, 14195 Berlin, Germany*
[2]*Department of Physics, Yale University, New Haven, Connecticut 06520, USA*

(Received 13 September 2016; revised manuscript received 1 November 2016; published 23 December 2016)

We study the Josephson effect in a quantum spin Hall system coupled to a localized magnetic impurity. As a consequence of the fermion parity anomaly, the spin of the combined system of impurity and spin-Hall edge alternates between half-integer and integer values when the superconducting phase difference across the junction advances by 2π. This leads to characteristic differences in the splittings of the spin multiplets by exchange coupling and single-ion anisotropy at phase differences, for which time-reversal symmetry is preserved. We discuss the resulting 8π-periodic (or $\mathbb{Z}_4$) fractional Josephson effect in the context of recent experiments.

DOI: 10.1103/PhysRevLett.117.267001

Introduction.—The fractional Josephson effect [1–3] constitutes one of the most striking effects heralding topological superconductivity [4,5]. In Josephson junctions of conventional superconductors, the Josephson current is carried by Cooper pairs and is 2π periodic in the phase difference applied to the junction. When the junction connects topological superconductors [6–9], the coupling of Majorana bound states across the junction allows a Josephson current to flow by coherent transfer of single electrons, resulting in 4π periodicity in the phase difference. Robust 4π periodicity requires that time-reversal symmetry be broken through proximity coupling to a magnetic insulator or an applied magnetic field [6]. A fractional Josephson effect can occur in time-reversal-symmetric junctions as a consequence of electron-electron interactions [10,11]. In the limit of strong interactions, this 8π-periodic effect can be understood in terms of domain walls carrying $\mathbb{Z}_4$ parafermions, enabling tunneling of $e/2$ quasiparticles between the superconductors.

Recent experiments on superconductor—quantum spin Hall—superconductor junctions show intriguing evidence for 4π-periodic Josephson currents. One experiment probes Shapiro steps and shows that the first Shapiro step is absent [12]. A second experiment reports that the Josephson radiation emitted by a biased junction is also consistent with 4π periodicity [13]. These results are surprising as both experiments were performed without explicitly breaking time-reversal symmetry so that basic theory would predict a dissipative 2π-periodic behavior when neglecting electron-electron interactions, or an 8π-periodic behavior when taking interactions into account.

These expectations are based on considering pristine quantum spin Hall Josephson junctions with a fully gapped bulk and a single helical channel propagating along its edges. Density modulations in actual quantum spin Hall samples are widely believed to induce puddles of electrons in addition to the helical edge channels [14]. When these puddles host an odd number of electrons, charging effects turn them into magnetic impurities that are exchange coupled to the helical edge channels. In this Letter, we discuss the fractional Josephson effect in realistic quantum spin Hall Josephson junctions that include such magnetic impurities.

The effects of magnetic impurities on quantum spin Hall edge channels have been intensively studied in the absence of superconductivity [15–18]. In the high-temperature limit, a magnetic impurity induces backscattering between the Kramers pair of helical edge channels and thus deviations from a quantized conductance in a two-terminal measurement. As the temperature is lowered, the impurity spin is increasingly Kondo screened by the helical edge channel and perfect conductance quantization is recovered when the temperature is low compared to the Kondo temperature T_K. In the presence of superconductivity, the Kondo effect is quenched by the superconducting gap Δ so that one may expect that magnetic impurities field more prominent consequences [19]. Here, we assume that $T_K \ll \Delta$ so that we can safely neglect the effects of Kondo screening.

We find that magnetic impurities alter the behavior of quantum spin Hall Josephson junctions qualitatively. The Josephson current becomes 8π periodic, replacing the dissipative 2π-periodic effect in pristine junctions. This can be viewed as a variant of the $\mathbb{Z}_4$ Josephson effect. Indeed, unlike its classical counterpart, coupling to a quantum spin preserves time-reversal symmetry and interactions are effectively included through the local-moment formation. This is quite reminiscent of the ingredients of the $\mathbb{Z}_4$ fractional Josephson effect. Thus, our results show that this remarkable effect is considerably more generic than one might have previously thought.

Moreover, the present setting emphasizes a remarkable mechanism for producing an 8π-periodic fractional Josephson effect. As a result of the fermion parity anomaly

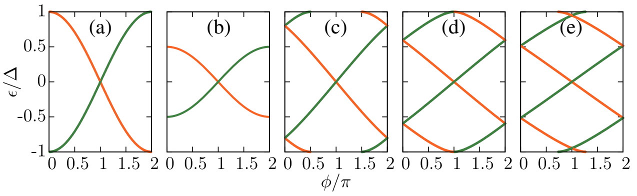

FIG. 1. Andreev spectrum of quantum spin Hall Josephson junctions of different lengths. (a) $L = 0$. (b) $L = 0$ in the presence of backscattering due to a Zeeman field. (c) $L = 0.8\hbar v/\Delta$. (d) $L = (\pi/2)\hbar v/\Delta$. (e) $L = 2\hbar v/\Delta$. The green curves correspond to Andreev states consisting of a superposition of an up-spin electron and an Andreev-reflected hole. The orange curves are for the particle-hole conjugated states.

[3], the spin of the helical edge effectively changes by $\hbar/2$ when the superconducting phase difference is advanced by 2π. This adiabatically transmutes the combined spin of helical edge and magnetic impurity between half-integer and integer values, with their characteristically different behavior in the presence of time-reversal symmetry as described by the Kramers theorem.

Quantum spin Hall Josephson junctions.—We first review the Andreev spectrum of pristine quantum spin Hall Josephson junctions [3]. Consider a quantum spin Hall edge with edge modes counterpropagating at velocity v, placed in between two superconductors at a distance L whose phases differ by ϕ. This junction is described by the Bogoliubov–de Gennes Hamiltonian

$$\mathcal{H} = vp\sigma_z\tau_z + \Delta(x)\tau_+ + \Delta^*(x)\tau_-, \qquad (1)$$

where σ_j and τ_j are Pauli matrices in spin and Nambu (particle-hole) space, respectively. The subgap spectrum as a function of ϕ is shown in Fig. 1.

For short junctions ($L \to 0$), the subgap spectrum contains a particle-hole symmetric pair of Andreev states [see Fig. 1(a)]. Both Andreev levels emanate from and merge into the quasiparticle continuum. An applied bias voltage V advances the phase difference at a rate $\dot{\phi} = 2eV/\hbar$ and leads to the generation of continuum quasiparticles above the superconducting gap. These can diffuse away from the junction, which causes dissipation. Thus, the junction exhibits an ac Josephson effect with conventional frequency and energy dissipation rate $(2\Delta)(\dot{\phi}/2\pi)$.

The dissipative nature of the Josephson effect is closely related to the absence of backscattering. When introducing backscattering into the junction by breaking time-reversal symmetry through an applied magnetic field or proximity coupling to a magnetic insulator, the Andreev levels no longer merge with the quasiparticle continuum [see Fig. 1(b)]. Now, the quasiparticles generated by the advancing phase difference remain at subgap energies and localized at the junction, which quenches dissipation in the small-voltage limit [6]. Moreover, the ac Josephson effect occurs at half the conventional frequency, i.e., at $eV/\hbar$, as fermion number parity is conserved. Indeed, the level crossing at $\phi = \pi$ is protected by fermion number parity so that the individual Andreev levels are 4π periodic in the phase difference ϕ. This can be viewed as a consequence of the fermion parity anomaly (see Ref. [20] for more details): as a result of the quantum spin Hall effect, the parity of the fermion number of the edge changes when the superconducting phase difference is advanced by 2π, requiring a phase change of 4π for a full period.

Additional subgap levels appear for longer junctions, see Figs. 1(c) and 1(d). The level crossings in these spectra are not only controlled by fermion number parity, but also by time-reversal symmetry. While time reversal is broken by the phase difference across the junction (causing a nonzero Josephson current to flow), it remains unbroken when ϕ is an integer multiple of π.

Coupling to magnetic impurity.—We now consider the coupling of the edge channel to a magnetic impurity with spin S. Generically, disorder in conjunction with the strong spin-orbit coupling will remove any symmetry other than time reversal, which we assume to be broken only by the applied superconducting phase difference. Thus, we focus on the general Hamiltonian

$$H_S = \sum_{\alpha,\beta} J_{\alpha\beta}\hat{S}^\alpha\hat{\sigma}^\beta(0) + \sum_\alpha D_\alpha(\hat{S}^\alpha)^2 \qquad (2)$$

for the impurity spin $\hat{\mathbf{S}}$. The first term describes the exchange coupling between the impurity spin and the helical edge, with $\hat{\sigma}^\alpha(0) = \sum_{i,j}\psi_i^\dagger(0)(\sigma^\alpha)_{ij}\psi_j(0)$ denoting the local spin density of the edge at the position $x = 0$ of the impurity. The operator $\psi_i(x)$ annihilates an electron with spin projection i at position x. The second term describes a single-ion anisotropy of the impurity spin with strengths D_α. Time reversal implies that the exchange couplings are real, but otherwise arbitrary.

Josephson effect.—Analyzing the Josephson effect of the quantum spin Hall edge channel coupled to the magnetic impurity is greatly simplified by the discrete nature of the subgap spectrum. For definiteness, consider an intermediate-length junction whose subgap spectrum has exactly two positive-energy subgap states $\epsilon_n(\phi)$ ($n = 1, 2$) at all values of the phase difference as in Fig. 1(d). (This convenient choice is used in our numerical illustrations but is not essential for our results.) Then, we can analyze the low-energy (many-body) spectrum of the junction in the finite-dimensional space of low-energy states spanned by the product of occupation states of the two subgap Bogoliubov quasiparticles (yielding four basis states) and the $2S + 1$ spin states of the spin-S impurity. The low-energy many-body spectrum effectively decouples from the quasiparticle continuum when the Kondo temperature is small compared to the superconducting gap [21]. The corresponding Hamiltonian is readily derived by retaining only the contributions of the two positive-energy subgap Bogoliubov operators γ_n to the edge-state electron

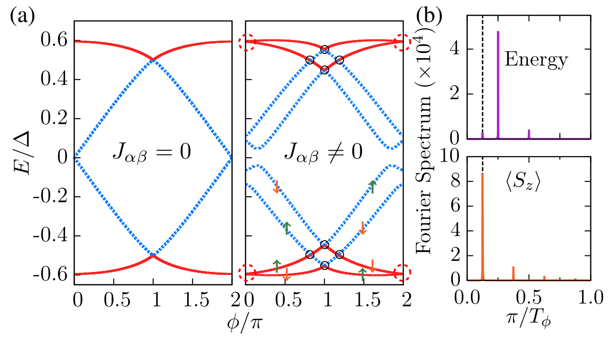

FIG. 2. (a) Generic many-body spectrum for the quantum spin Hall Josephson junction [$L=(\pi/2)\hbar v/\Delta$] without (left) and with coupling to the impurity spin (right) (for parameters see Ref. [20]). The red solid and blue dashed curves indicate even and odd fermion number parity, respectively. The discontinuity in fermion number parity at $\phi=\pi$ originates from the merging of Andreev levels with the continuum, see Fig. 1(d). The crossings at and near $\phi=\pi$ (black circles) are between states of opposite fermion number parity. The crossings between states with even fermion number parity at $\phi=0$ and 2π (red dashed circles) are protected by time reversal. The arrows indicate the impurity-spin polarization along the z axis. (b) Fourier transforms of the many-body ground state energy (equivalently, Josephson current) (upper panel) and of the expectation value of the impurity spin $\langle S_z\rangle$ (lower panel) as a function of the phase difference ϕ. The 8π-periodic harmonics are indicated by the vertical dashed lines.

operators (see Ref. [20] for details). In this limit, the total Hamiltonian can be approximated as $H=H_e+H_S$ with

$$H_e=\sum_n \epsilon_n(\phi)\left(\gamma_n^\dagger\gamma_n-\frac{1}{2}\right) \tag{3}$$

the Hamiltonian of the bare edge.

Consider coupling the quantum spin Hall edge states to a spin-$1/2$ impurity. Figure 2(a) shows the many-body spectrum of H_e in Eq. (3), i.e., of the bare edge (left panel), and of $H=H_e+H_S$ for a generic choice of exchange couplings $J_{\alpha\beta}$ (right panel). The spectrum of the coupled edge is best understood by analyzing the nature of the degeneracies at phase differences equal to integer multiples of π. The degeneracies at and near $\phi=\pi$ are protected by fermion number parity. Here, level crossings occur between states with even and odd occupations of the Bogoliubov quasiparticles of the edge. In contrast, the level crossings at $\phi=0$ and $\phi=2\pi$ occur between states of the same fermion number parity and are Kramers degeneracies reflecting time-reversal symmetry.

In the present system, a Kramers degeneracy appears when the Bogoliubov quasiparticles γ_n of the edge are either both empty or both occupied, leading to a half-integer spin of the combined system of edge and impurity. Specifically, the lower (higher) energy crossing in Fig. 2(a) corresponds to states in which the quasiparticle states are both empty (occupied). Away from $\phi=0$ and 2π, time reversal is broken and the Kramers degeneracies are lifted. This interpretation is corroborated by further restricting the Hamiltonian H for small ϕ to the low-energy subspace of empty quasiparticle states. In this limit, the spin density $\hat{\sigma}^\alpha(0)$ of the edge only has a nonzero z component $\hat{\sigma}^z(0)=-\epsilon\phi/[2\hbar v(1+\kappa L)^2]$ and the Hamiltonian simplifies to

$$H\simeq -\sum_\alpha B^\alpha S^\alpha+\text{const} \tag{4}$$

with the effective Zeeman field $\mathbf{B}=[\epsilon\phi/2\hbar v(1+\kappa L)^2]\sum_\alpha J_{\alpha z}\hat{\mathbf{e}}_\alpha$. Here, we use the subgap energy $\epsilon=\Delta\cos[\epsilon L/(\hbar v)]$ and $\kappa=\sqrt{\Delta^2-\epsilon^2}/(\hbar v)$.

The four nondegenerate states at intermediate energies for $\phi=0$ [see Fig. 2(a)] have overall single occupation of the quasiparticle states, leading to a combined edge-impurity system with integer spin. Unlike in the odd-integer spin case, time reversal does not enforce a degeneracy of the many-body spectrum in this case. Writing the Hamiltonian for small ϕ in this subspace using the basis $|\Uparrow\rangle=\gamma_1^\dagger|\text{gs}\rangle$ and $|\Downarrow\rangle=\gamma_2^\dagger|\text{gs}\rangle$ (with the junction ground state $|\text{gs}\rangle$ such that $\gamma_1|\text{gs}\rangle=\gamma_2|\text{gs}\rangle=0$) for the states of the edge (with corresponding Pauli matrices ρ_α), we find the effective Hamiltonian

$$H\simeq\frac{\kappa}{2(1+\kappa L)}\left(\sum_\alpha J_\alpha+S^\alpha\rho_+ +\text{H.c.}\right). \tag{5}$$

Generically, this Hamiltonian has no degeneracies.

With this understanding, the many-body spectrum in Fig. 2(a) reveals a remarkable fact: adiabatically advancing the superconducting phase difference by 2π connects the low-energy Kramers doublet at $\phi=0$ to states of the totally lifted spin quartet at $\phi=2\pi$. Thus, adiabatic quantum dynamics changes the total spin of the edge-impurity system between half-integer and integer values. This spin transmutation is a direct consequence of the fermion parity anomaly (see also Ref. [20]): as the phase difference changes by 2π, the fermion number parity of the edge changes by virtue of the quantum spin Hall effect. Consequently, also the spin of the edge changes by $\hbar/2$. This change in spin has important consequences for the periodicity of the Josephson effect. Indeed, adiabatically following the energy levels in Fig. 2(a), we find that they are 8π periodic, corresponding to an ac Josephson frequency of $eV/2\hbar$. Because of the spin transmutation, the system passes through successive Kramers degeneracies only after advancing the superconducting phase difference by 4π, requiring a phase change of 8π for completing a full period. Note that starting with the ground state at $\phi=0$, the many-body state remains well below the quasiparticle continuum for all ϕ, so that the ac Josephson effect is nondissipative at a sufficiently small bias.

The polarization of the impurity spin varies with the superconducting phase difference in an 8π-periodic

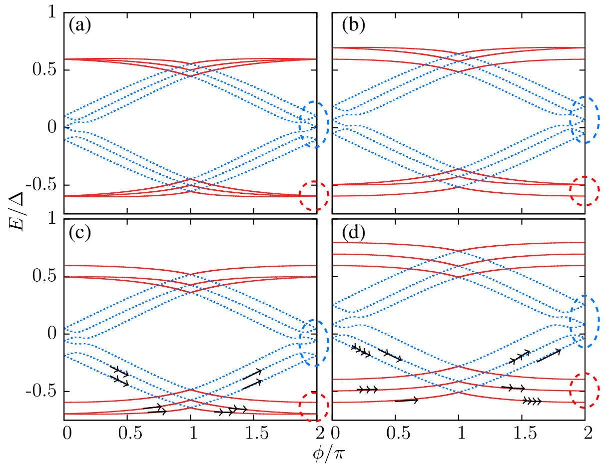

FIG. 3. Many-body spectrum for a quantum spin Hall edge coupled to an $S = 1$ impurity (for explicit parameters, see Ref. [20]). The red solid and blue dashed curves correspond to many-body states with even and odd fermion number parity, respectively. Spectra correspond to (a) vanishing single-ion anisotropy, (b) easy-plane anisotropy $D_z > 0$, (c) easy-axis anisotropy $D_z < 0$, and (d) generic single-ion anisotropy with D_x, D_y, $D_z \neq 0$. The degeneracies at $\phi = 2\pi$ (blue dashed circles) and their partners at $\phi = 0$ are Kramers degeneracies. Red circles highlight degeneracies that are lifted by generic single-ion anisotropy. The number of arrows indicates subsequent 2π periods when adiabatically advancing ϕ.

manner. When adiabatically varying ϕ, the spin orientation remains unchanged at the Kramers crossings and flips in the vicinity of the avoided crossings where the edge-impurity system is in an integer-spin state. This variation of the spin with ϕ is illustrated in Fig. 2(a).

These results for $S = 1/2$ impurities persist for higher-spin impurities. Results for an $S = 1$ impurity are shown in Fig. 3. Figure 3(d) shows results for generic values of $J_{\alpha\beta}$ and D_α. Unlike in the $S = 1/2$ case, the low-energy states now have integer spin and are nondegenerate, while the intermediate-energy states have half-integer spin and are Kramers degenerate at $\phi = 0$ and 2π. Nevertheless, the 8π periodicity remains intact.

Different periodicities occur for nongeneric D_α. Without single-ion anisotropy [see Fig. 3(a)], the spectrum does not decouple from the quasiparticle continuum and the Josephson effect becomes dissipative and 2π periodic. The same results occur for easy-plane anisotropy, with one of the single-ion anisotropies being positive and the others equal to zero, see Fig. 3(b). Finally, easy-axis anisotropy makes the junction nondissipative and 4π periodic as shown in Fig. 3(c).

Discussion.—We find that, generically, coupling to a magnetic impurity makes the Josephson effect in quantum spin Hall systems 8π periodic, corresponding to a frequency $eV/2\hbar$ of the ac Josephson effect. The 8π periodicity relies only on time-reversal symmetry, the parity anomaly, and the absence of fine tuning such as the absence of interactions or the presence of spin conservation. It can be thought of as resulting from the coupling of $\mathbb{Z}_4$ parafermions across the junction.

This general conclusion requires two comments. First, the 8π-periodic Josephson current may not be the dominant Fourier component in experiment. Indeed, as is evident from Fig. 2, the 8π-periodic cycle consists of two rather similar 4π sections. The splitting between the two sections is controlled by the exchange coupling. When the exchange splitting is small compared to the superconducting gap, the dominant Fourier component of the Josephson current is 4π periodic. This is shown in Fig. 2(b), together with the Fourier components of the impurity spin polarization that has a dominant 8π-periodic harmonic. It is interesting to note that this result for the Josephson current is different from the realization of the $\mathbb{Z}_4$ Josephson effect discussed by Zhang and Kane [10], which has a dominant 8π-periodic Fourier component.

Second, our results so far consider only the electronic system. Coupling to other degrees of freedom such as phonons or the electromagnetic environment introduces inelastic relaxation processes that may crucially affect the experimentally observed periodicity. While relaxation between states of opposite fermion number parity may be slow, parity-conserving relaxation processes should be considerably more efficient. Observation of the 8π periodicity requires that the latter relaxation processes be slow compared to the time in which the 8π cycle is traversed. Indeed, the two 4π sections of the 8π cycle involve states of the same fermion number parity. Thus, the system always remains in the lower-energy state if the cycle is traversed slowly on the time scale of parity-conserving relaxation processes. This makes the observed Josephson effect 4π rather than 8π periodic.

It is interesting to compare these results to the recent experiments on quantum spin Hall junctions, which observe Shapiro steps and Josephson radiation consistent with 4π periodicity [12,13]. Our results provide an intriguing scenario that is consistent with these observations. However, this is not the only explanation of a 4π-periodic Josephson effect in this system. An alternative scenario considers relaxation processes in a pristine quantum spin Hall junction. Consider an intermediate-length junction with at least two positive-energy Andreev states for any phase difference. When both of these Andreev states are occupied, the two quasiparticles can relax inelastically by recombining into a Cooper pair. Two positive-energy quasiparticles are created every time the phase difference advances by 4π. Thus, if recombination into a Cooper pair is an efficient process, one would also observe a 4π-periodic Josephson effect. It is an interesting problem to devise experiments that distinguish between these alternative scenarios. Such efforts may benefit from the considerable recent progress in directly probing the subgap

TABLE I. Generic Josephson periodicities of a quantum-spin-Hall-based junction coupled to a spin-S impurity or quantum dot, with or without a Zeeman field B. The dc periodicities assume full equilibration including fermion number parity. The ac results assume that fermion number parity is conserved on the relevant time scale. Note that the 8π-periodic ac current may have a large 4π-periodic component, while the periodicity of the dot spin is robustly 8π, see Figs. 2(b) and 2(c).

Josephson effect	$S = 0$, $B = 0$	Any S, $B \neq 0$	$S \neq 0$, $B = 0$
dc	2π	2π	2π
ac	Dissipative, 2π	Nondissipative, 4π	Nondissipative, 8π

spectrum of Josephson junctions by microwave spectroscopy and switching current measurements [22–27].

Finally, our results suggest probing the Josephson effect of a quantum spin Hall edge that is intentionally coupled to a quantum dot. Such a setup would allow one to tune the quantum dot in and out of the local moment regime and to control the exchange coupling between dot and edge. In addition to the Josephson periodicity, such a setup might provide access to the 8π periodicity of the impurity spin (see Table I) and would be a promising setup for detecting $\mathbb{Z}_4$ parafermions.

We acknowledge financial support by the Deutsche Forschungsgemeinschaft (CRC 183 as well as Priority Program 1666), the Minerva Foundation, the Alexander-von-Humboldt Foundation, and NSF Grant No. DMR-1603243. Part of this work was performed at the Aspen Center for Physics, which is supported by National Science Foundation Grant No. PHY-1066293.

[1] A. Y. Kitaev, Phys. Usp. **44**, 131 (2001).
[2] H.-J. Kwon, K. Sengupta, and V. M. Yakovenko, Eur. Phys. J. B **37**, 349 (2003).
[3] L. Fu and C. L. Kane, Phys. Rev. B **79**, 161408 (2009).
[4] J. Alicea, Rep. Prog. Phys. **75** (2012).
[5] C. W. J. Beenakker, Annu. Rev. Condens. Mattter Phys. **4**, 113 (2013).
[6] L. Fu and C. L. Kane, Phys. Rev. Lett. **100**, 096407 (2008).
[7] R. M. Lutchyn, J. D. Sau, and S. Das Sarma, Phys. Rev. Lett. **105**, 077001 (2010).
[8] Y. Oreg, G. Refael, and F. von Oppen, Phys. Rev. Lett. **105**, 177002 (2010).
[9] J. Alicea, Y. Oreg, G. Refael, F. von Oppen, and M. P. A. Fisher, Nat. Phys. **7**, 412 (2011).
[10] F. Zhang and C. L. Kane, Phys. Rev. Lett. **113**, 036401 (2014).
[11] C. P. Orth, R. P. Tiwari, T. Meng, and T. L. Schmidt, Phys. Rev. B **91**, 081406(R) (2015).
[12] E. Bocquillon, R. S. Deacon, J. Wiedenmann, P. Leubner, T. M. Klapwijk, C. Brüne, K. Ishibashi, H. Buhmann, and L. W. Molenkamp, Nat. Nanotechnol. **159** (2016).
[13] R. S. Deacon, J. Wiedenmann, E. Bocquillon, T. M. Klapwijk, P. Leubner, C. Brüne, S. Tarucha, K. Ishibashi, H. Buhmann, and L. W. Molenkamp, arXiv:1603.09611.
[14] J. I. Väyrynen, M. Goldstein, and L. I. Glazman, Phys. Rev. Lett. **110**, 216402 (2013).
[15] J. Maciejko, C. Liu, Y. Oreg, X.-L. Qi, C. Wu, and S.-C. Zhang, Phys. Rev. Lett. **102**, 256803 (2009).
[16] Y. Tanaka, A. Furusaki, and K. A. Matveev, Phys. Rev. Lett. **106**, 236402 (2011).
[17] V. Cheianov and L. I. Glazman, Phys. Rev. Lett. **110**, 206803 (2013).
[18] B. L. Altshuler, I. L. Aleiner, and V. I. Yudson, Phys. Rev. Lett. **111**, 086401 (2013).
[19] A. V. Balatsky, I. Vekhter, and Jian-Xin Zhu, Rev. Mod. Phys. **78**, 373 (2006).
[20] See Supplemental Material at http://link.aps.org/supplemental/10.1103/PhysRevLett.117.267001 for a brief introduction of fermion parity anomaly, the derivation of Andreev bound states' wavefunctions, and the effective Hamiltonian describing the coupling between the bound states and the magnetic impurity.
[21] Strictly speaking, the quasiparticle continuum also contributes to the Josephson effect. However, this contribution is necessarily 2π periodic so that any fractional Josephson effect originates from the subgap spectrum.
[22] L. Bretheau, C. O. Girit, C. Urbina, D. Esteve, and H. Pothier, Phys. Rev. X **3**, 041034 (2013).
[23] L. Bretheau, C. O. Girit, H. Pothier, D. Esteve, and C. Urbina, Nature (London) **499**, 312 (2013).
[24] J. I. Vayrynen, G. Rastelli, W. Belzig, and L. I. Glazman, Phys. Rev. B **92**, 134508 (2015).
[25] Y. Peng, F. Pientka, E. Berg, Y. Oreg, and F. von Oppen, Phys. Rev. B **94**, 085409 (2016).
[26] D. J. van Woerkom, A. Proutski, B. van Heck, D. Bouman, J. I. Vayrynen, L. I. Glazman, P. Krogstrup, J. Nygard, L. P. Kouwenhoven, and A. Geresdi, arXiv:1609.00333.
[27] M. Zgirski, L. Bretheau, Q. Le Masne, H. Pothier, D. Esteve, and C. Urbina, Phys. Rev. Lett. **106**, 257003 (2011).

Supplemental Material
Parity anomaly and spin transmutation in quantum spin Hall Josephson junctions

Yang Peng,[1] Yuval Vinkler-Aviv,[1] Piet W. Brouwer,[1] Leonid I. Glazman,[2] and Felix von Oppen[1]

[1] *Dahlem Center for Complex Quantum Systems and Fachbereich Physik, Freie Universität Berlin, 14195 Berlin, Germany*
[2] *Department of Physics, Yale University, New Haven, Connecticut 06520, USA*

FERMION NUMBER PARITY

For the benefit of general readers, we include a brief review of the concept of fermion number parity and its application to topological Josephson junctions. Pairing Hamiltonians (i.e., Hamiltonians describing superconductors within mean-field theory) include terms which change the number of particles of the system by two. This can be thought of as describing the addition or removal of Cooper pairs from the system. As a result, these Hamiltonians break particle number conservation but preserve particle number modulo two. Consequently, systems with even and odd numbers of electrons decouple and fermion number parity is a good quantum number. One refers to systems with even (odd) electron number as having even (odd) fermion number parity.

The Hamiltonian of a Josephson junction based on a quantum spin Hall edge also conserves fermion number parity. We can label the many body eigenstates of the system by fermion number parity and states with different fermion number parity cannot anticross, but must exhibit a true level crossing. This explains the level crossings in the many-body spectra near a phase difference of π, see Fig. 2(a) of the main text.

While the spectrum behaves as if fermion number parity is a good quantum number, it is not conserved in the quantum dynamics. This is referred to as an anomaly (or more specifically the fermion parity anomaly): While the fermion number parity is conserved classically, it is not in the quantum dynamics. In the absence of an anomaly, the fermion number parity has to remain unchanged when changing any parameter in the (fermion-parity-conserving) Hamiltonian. As a corollary, this also implies that the spin has to remain integer or half-integer at all times, and transmutation between integer and half-integer spin is forbidden.

Nevertheless, in the present case, the system transmutes between integer and half-integer spin (and even and odd fermion parity) when the superconducting phase difference is advanced by 2π. When the phase difference advances adiabatically, the system follows a specific eigenstate. Due to the crossings near $\phi = \pi$ protected by fermion parity, the system passes, say, from a half-integer Kramers doublet at zero phase difference to a state which is part of a completely lifted integer-spin quartet at $\phi = 2\pi$, see Fig. 2(b) of the main text. Thus, the adiabatic quantum dynamics does indeed violate fermion parity conservation.

Physically, the fermion parity anomaly can be understood as follows. In a Corbino geometry, changes in the superconducting phase difference can be effected by changing the magnetic flux piercing the hole of the Corbino disk. Changes in flux induce an azimuthal electric field circulating around the Corbino disk. By virtue of the quantum spin Hall effect, this azimuthal electric field drives a radial spin Hall current. It is a simple exercise to compute the total spin change of the inner and outer edges of the Corbino disk when the superconducting phase is advanced by 2π and one finds that it is exactly $\hbar/2$. It is by this mechanism that the spin of the edge states transmutes between integer and half integer spins.

ANDREEV BOUND STATES

The Hamiltonian for the quantum spin Hall Josephson junction takes the form $H = \frac{1}{2}\Psi^\dagger \mathcal{H}\Psi$ with Nambu spinor $\Psi = (\psi_\uparrow, \psi_\downarrow, \psi_\downarrow^\dagger, -\psi_\uparrow^\dagger)^T$ in terms of electron operators and the Bogoliubov-de Gennes Hamiltonian

$$\mathcal{H} = vp\sigma_z\tau_z + \Delta(x)\tau_x, \tag{S1}$$

where x (p) denotes the coordinate (momentum) along the quantum spin Hall insulator edge, v is the edge-mode velocity, and σ_j and τ_j are Pauli matrices in spin and Nambu (particle-hole) space, respectively. The proximity-induced superconducting gap

$$\begin{aligned}\Delta(x) =& \Delta\left[\theta(-x-L/2) + e^{i\phi\tau_z}\theta(x-L/2)\right]\\ =& \Delta\theta(|x| - \frac{L}{2})e^{i\varphi(x)\tau_z}\end{aligned} \tag{S2}$$

has strength $\Delta > 0$ and a phase difference ϕ across the junction region of length L. We have introduced a spatially dependent phase

$$\varphi(x) = \frac{\phi}{L}(x + \frac{L}{2})\theta(\frac{L}{2} - |x|) + \theta(x - \frac{L}{2})\phi. \tag{S3}$$

for convenience. We set $\hbar = 1$ in this supplemental material.

We introduce a local gauge transformation $U = e^{i\varphi(x)\tau_z/2}$ to eliminate the spatial dependence of the superconducting phase, and obtain the transformed Hamiltonian

$$U^\dagger \mathcal{H} U = -iv\partial_x \sigma_z \tau_z + \frac{v\varphi'(x)\sigma_z}{2} + \Delta\theta(|x| - \frac{L}{2})\tau_x, \tag{S4}$$

where the prime denotes a derivative with respect to x. We will denote $U^\dagger \mathcal{H} U$ as $\mathcal{H}$ in the following.

To solve for the Andreev bound states, we follow the approach detailed in Ref. [1] to rearrange the Bogoliubov-de Gennes equation $\mathcal{H}\psi = \epsilon\psi$ as

$$i\frac{\partial\psi}{\partial x} = -\frac{1}{v}\sigma_z\tau_z \left[\epsilon - \Delta\theta(|x| - \frac{L}{2})\tau_x - \frac{v\varphi'(x)}{2}\sigma_z\right]\psi. \tag{S5}$$

The solution can be written as $\psi(x) = U(x, x_0)\psi(x_0)$ in terms of the state at some reference point x_0. In particular, we have

$$U(\frac{L}{2}, -\frac{L}{2}) = \exp\left\{\frac{i}{v}\sigma_z\tau_z \int_{-\frac{L}{2}}^{\frac{L}{2}} dx' \left[\epsilon - \frac{v\varphi'(x')}{2}\sigma_z\right] = \exp\left(\frac{iEL}{v}\sigma_z\tau_z - \frac{\phi}{2}\tau_z\right)\right\} \tag{S6}$$

which connects the states $\psi(L/2) = U(L/2, -L/2)\psi(-L/2)$. We match the properly decaying solutions of the Bogoliubov de-Gennes equation on the left and right of the junction, and obtain the bound state wave functions in the two spin sectors:

$$\Psi_\uparrow(x) = \begin{pmatrix} a_\uparrow A_\uparrow \\ 0 \\ A_\uparrow \\ 0 \end{pmatrix} e^{\kappa_\uparrow(x+\frac{L}{2})}\theta(-x-\frac{L}{2}) + \begin{pmatrix} a_\uparrow A_\uparrow e^{-i(\frac{\phi}{2}-\frac{\epsilon}{v}L)} \\ 0 \\ A_\uparrow e^{i(\frac{\phi}{2}-\frac{\epsilon}{v}L)} \\ 0 \end{pmatrix} e^{-\kappa_\uparrow(x-\frac{L}{2})}\theta(x-\frac{L}{2}) + \begin{pmatrix} a_\uparrow A_\uparrow e^{-i(\frac{\phi}{2L}-\frac{\epsilon}{v})(x+\frac{L}{2})} \\ 0 \\ A_\uparrow e^{i(\frac{\phi}{2L}-\frac{\epsilon}{v})(x+\frac{L}{2})} \\ 0 \end{pmatrix} \theta(\frac{L}{2}-|x|) \tag{S7}$$

and

$$\Psi_\downarrow(x) = \begin{pmatrix} 0 \\ A_\downarrow \\ 0 \\ a_\downarrow A_\downarrow \end{pmatrix} e^{\kappa_\downarrow(x+\frac{L}{2})}\theta(-x-\frac{L}{2}) + \begin{pmatrix} 0 \\ A_\downarrow e^{-i(\frac{\phi}{2}+\frac{\epsilon}{v}L)} \\ 0 \\ a_\downarrow A_\downarrow e^{i(\frac{\phi}{2}+\frac{\epsilon}{v}L)} \end{pmatrix} e^{-\kappa_\downarrow(x-\frac{L}{2})}\theta(x-\frac{L}{2}) + \begin{pmatrix} 0 \\ A_\downarrow e^{-i(\frac{\phi}{2L}+\frac{\epsilon}{v})(x+\frac{L}{2})} \\ 0 \\ a_\downarrow A_\downarrow e^{i(\frac{\phi}{2L}+\frac{\epsilon}{v})(x+\frac{L}{2})} \end{pmatrix} \theta(\frac{L}{2}-|x|) \tag{S8}$$

where

$$a_\sigma = \frac{\epsilon}{\Delta} - i\frac{\sqrt{\Delta^2 - \epsilon_\sigma^2}}{\Delta}, \qquad |A_\sigma|^2 = \frac{\kappa_\sigma}{2(1 + L\kappa_\sigma)}, \qquad \kappa_\sigma = \frac{\sqrt{\Delta^2 - \epsilon_\sigma^2}}{v} \tag{S9}$$

with $\sigma = \uparrow, \downarrow$, and ϵ_σ is the positive eigenvalue in each spin sector given by the relation

$$\epsilon_\uparrow/\Delta = \begin{cases} \cos(\frac{\phi}{2} - \frac{\epsilon_\uparrow}{v}L) & \sin(\frac{\phi}{2} - \frac{\epsilon_\uparrow}{v}L) < 0 \\ -\cos(\frac{\phi}{2} - \frac{\epsilon_\uparrow}{v}L) & \sin(\frac{\phi}{2} - \frac{\epsilon_\uparrow}{v}L) > 0 \end{cases} \tag{S10}$$

and

$$\epsilon_\downarrow/\Delta = \begin{cases} \cos(\frac{\phi}{2} + \frac{\epsilon_\downarrow}{v}L) & \sin(\frac{\phi}{2} + \frac{\epsilon_\downarrow}{v}L) > 0 \\ -\cos(\frac{\phi}{2} + \frac{\epsilon_\downarrow}{v}L) & \sin(\frac{\phi}{2} + \frac{\epsilon_\downarrow}{v}L) < 0 \end{cases}. \tag{S11}$$

For ϕ around $2n\pi, n \in \mathbb{Z}$, solutions in both spin sectors can exist simultaneously for $L > 0$. We will consider the situation when at most one solution in each spin sector exists, and write the subgap effective Hamiltonian as

$$H_e = \sum_\sigma \epsilon_\sigma(\phi)(\gamma_\sigma^\dagger\gamma_\sigma - \frac{1}{2}), \tag{S12}$$

where γ_σ is the Bogoliubov quasiparticle annihilation operator for the Andreev bound state with spin σ. When projected onto the subspace spanned by the subgap Andreev bound states, the electron annihilation operators for both spins can be written approximately as

$$\begin{aligned} \psi_\uparrow &= a_\uparrow A_\uparrow e^{-ik_\uparrow L/2}\gamma_\uparrow - a_\downarrow^* A_\downarrow^* e^{-ik_\downarrow L/2}\gamma_\downarrow^\dagger \\ \psi_\downarrow &= A_\downarrow e^{-ik_\downarrow L/2}\gamma_\downarrow + A_\uparrow^* e^{-ik_\uparrow L/2}\gamma_\uparrow^\dagger \\ k_{\uparrow,\downarrow} &= \frac{\varphi}{2L} \mp \frac{\epsilon_\sigma}{v}. \end{aligned} \tag{S13}$$

COUPLING OF AN EDGE CHANNEL TO A MAGNETIC IMURITY

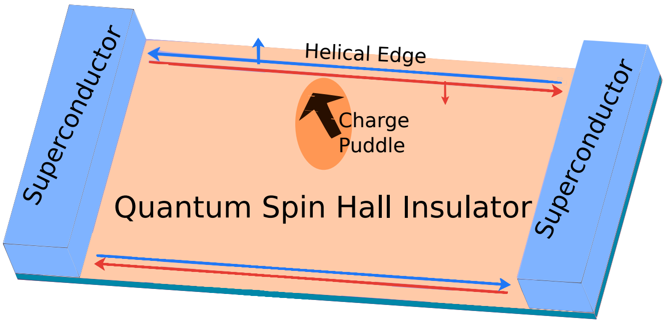

Figure S1. Setup for the quantum spin Hall Josephson junction in which the helical edge state is coupled to a charge puddle formed by a potential variation in the bulk. Due to charging effects, the charge puddle may effectively act as a magnetic impurity as indicated by the black arrow in the figure. The left/right moving electrons of the helical edges with opposite spins are depicted in different colors.

Consider the Hamiltonian describing the coupling of the edge channel to a magnetic impurity with spin S (see setup in Fig. S1)

$$H_S = \sum_{\alpha,\beta} J_{\alpha\beta} \hat{S}^\alpha \hat{\sigma}^\beta(0) + \sum_\alpha D_\alpha (\hat{S}^\alpha)^2, \tag{S14}$$

in which the spin density of the helical edge can be written in term of the Bogoliubov operators

$$\begin{aligned} \hat{\sigma}^+ &= \psi_\uparrow^\dagger \psi_\downarrow = \left(a_\uparrow^* e^{i\Delta kL/2} + a_\downarrow e^{-i\Delta kL/2}\right) A_\uparrow^* A_\downarrow \gamma_\uparrow^\dagger \gamma_\downarrow \\ \hat{\sigma}^- &= \psi_\downarrow^\dagger \psi_\uparrow = \left(a_\uparrow e^{-i\Delta kL/2} + a_\downarrow^* e^{i\Delta kL/2}\right) A_\uparrow A_\downarrow^* \gamma_\downarrow^\dagger \gamma_\uparrow \\ \hat{\sigma}^x &= \left(\hat{\sigma}^+ + \hat{\sigma}^-\right)/2, \quad \hat{\sigma}^y = \left(\hat{\sigma}^+ + \hat{\sigma}^-\right)/2i \\ \hat{\sigma}^z &= \psi_\uparrow^\dagger \psi_\uparrow - \psi_\downarrow^\dagger \psi_\downarrow = \left(\left|A_\uparrow\right|^2 \left(2\gamma_\uparrow^\dagger \gamma_\uparrow - 1\right) - \left|A_\downarrow\right|^2 \left(2\gamma_\downarrow^\dagger \gamma_\downarrow - 1\right)\right) + (a_\uparrow^* a_\downarrow^* e^{i\Delta kL/2} - e^{-i\Delta kL/2}) A_\uparrow^* A_\downarrow^* \gamma_\downarrow^\dagger \gamma_\uparrow^\dagger \\ &\quad + (a_\uparrow a_\downarrow e^{-i\Delta kL/2} - e^{i\Delta kL/2}) A_\uparrow A_\downarrow \gamma_\uparrow \gamma_\downarrow, \end{aligned} \tag{S15}$$

where

$$\Delta k = k_\uparrow - k_\downarrow = -\frac{\epsilon_\uparrow + \epsilon_\downarrow}{v}. \tag{S16}$$

Note that we can also write

$$a_\uparrow = \mathrm{Sgn}\sin\left(\frac{\epsilon_\uparrow L}{v} - \frac{\phi}{2}\right) e^{-i\frac{\epsilon_\uparrow L}{v}} e^{i\phi/2}, \quad a_\downarrow = \mathrm{Sgn}\sin\left(\frac{\epsilon_\downarrow L}{v} + \frac{\phi}{2}\right) e^{-i\frac{\epsilon_\downarrow L}{v}} e^{-i\phi/2}, \tag{S17}$$

then we have

$$\hat{\sigma}^+ = \left(\mathrm{Sgn}\sin(\frac{\epsilon_\uparrow L}{v} - \frac{\phi}{2}) + \mathrm{Sgn}\sin(\frac{\epsilon_\downarrow L}{v} + \frac{\phi}{2})\right) e^{i\frac{(\epsilon_\uparrow - \epsilon_\downarrow)L}{2v}} e^{-i\phi/2} A_\uparrow^* A_\downarrow \gamma_\uparrow^\dagger \gamma_\downarrow \tag{S18}$$

$$\hat{\sigma}^- = \left(\mathrm{Sgn}\sin(\frac{\epsilon_\uparrow L}{v} - \frac{\phi}{2}) + \mathrm{Sgn}\sin(\frac{\epsilon_\downarrow L}{v} + \frac{\phi}{2})\right) e^{-i\frac{(\epsilon_\uparrow - \epsilon_\downarrow)L}{2v}} e^{i\phi/2} A_\uparrow A_\downarrow^* \gamma_\downarrow^\dagger \gamma_\uparrow \tag{S19}$$

$$\begin{aligned}\hat{\sigma}^z = &\left(|A_\uparrow|^2 (2\gamma_\uparrow^\dagger\gamma_\uparrow - 1) - |A_\downarrow|^2 (2\gamma_\downarrow^\dagger\gamma_\downarrow - 1)\right) \\ &+ \left[\mathrm{Sgn}\sin(\frac{\epsilon_\uparrow L}{v} - \frac{\phi}{2})\,\mathrm{Sgn}\sin(\frac{\epsilon_\downarrow L}{v} + \frac{\phi}{2}) - 1\right] \left(e^{i\frac{(\epsilon_\uparrow + \epsilon_\downarrow)L}{2v}} A_\uparrow^* A_\downarrow^* \gamma_\downarrow^\dagger \gamma_\uparrow^\dagger + e^{-i\frac{(\epsilon_\uparrow + \epsilon_\downarrow)L}{2v}} A_\uparrow A_\downarrow \gamma_\downarrow^\dagger \gamma_\uparrow^\dagger\right).\end{aligned} \tag{S20}$$

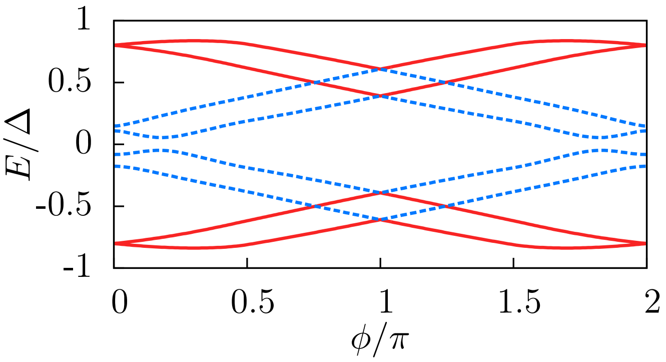

Figure S2. Generic many body spectrum for the quantum spin Hall Josephson junction coupled to a spin-1/2 impurity with $\Delta L/v = 0.8$. The red solid and blue dashed curves indicate that the corresponding many-body states have even and odd fermion parity, respectively. The coupling between the impurity and the edge and the single-ion anisotropy are chosen to be the same as in Fig. 2 of the main text, see Eq. (S21).

PARAMETERS FOR THE COUPLING MATRIX USED IN FIGS. 2 AND 3 OF THE MAIN TEXT

In Fig. 2 of the main text, the coupling matrix between edge and spin-1/2 impurity was chosen as

$$\frac{J^{S=1/2}}{2\pi v} = \begin{pmatrix} 0.2041 & 0.124268 & 0.33448 \\ 0.197511 & -0.185256 & 0.0733386 \\ 0.394004 & 0.0849569 & 0.288134 \end{pmatrix} \tag{S21}$$

The single-ion anisotropy was set to zero since it is only a constant shift in energy for spin-1/2 impurities. A similar figure for a shorter junction with the same parameters is shown in Fig. S2.

In Fig. 3 of the main text, the coupling matrix between edge and spin-1 impurity was chosen as $J^{S=1} = J^{S=1/2}/2$. In Fig. 3(b), $D_z = 0.1\Delta$. In Fig. 3(c), $D_z = -0.1\Delta$. In Fig. 3(d), $D_x = 0.3, D_y = 0.2, D_z = 0.1$.

ANALYSIS AROUND $\phi = 0$

In the case $\Delta L/v \in [0, \pi/2]$, and for ϕ close to 0 we have

$$\mathrm{Sgn}\sin(\frac{\epsilon_\downarrow L}{v} - \frac{\phi}{2}) = \mathrm{Sgn}\sin(\frac{\epsilon_\uparrow L}{v} + \frac{\phi}{2}) = 1. \tag{S22}$$

Let us first focus on the case when $\phi = 0$, we have

$$\epsilon_\uparrow = \epsilon_\downarrow = \Delta\cos\left(\frac{\epsilon_{\uparrow,\downarrow} L}{v}\right). \tag{S23}$$

Let us denote the common solution as ϵ.

Now we consider $\phi \ll 1$ and denote $\delta\epsilon = \epsilon_\uparrow - \epsilon_\downarrow$. By Eq. (S10) and (S11) and condition (S22), we have

$$\begin{aligned}\delta\epsilon &= \Delta\left[\cos(\frac{\epsilon_\uparrow}{v}L - \frac{\phi}{2}) - \cos(\frac{\epsilon_\downarrow L}{v} + \frac{\phi}{2})\right] \\ &= \Delta\cos\frac{\phi}{2}\left(\cos\frac{\epsilon_\uparrow L}{v} - \cos\frac{\epsilon_\downarrow L}{v}\right) + \Delta\sin\frac{\phi}{2}\left(\sin\frac{\epsilon_\uparrow L}{v} + \sin\frac{\epsilon_\downarrow L}{v}\right) \\ &\simeq \Delta\sin(\frac{\epsilon L}{v})\phi = \kappa v\phi, \end{aligned} \tag{S24}$$

where

$$\kappa = \frac{\sqrt{\Delta^2 - \epsilon^2}}{v}. \tag{S25}$$

This is valid up to first order in ϕ.

In this situation, the operators $\hat\sigma^+$, $\hat\sigma^-$ and $\hat\sigma^z$ get simplified as

$$\hat\sigma^+ = 2\exp\left[i\left(\kappa L - 1\right)\frac{\phi}{2}\right] A_\uparrow^* A_\downarrow \gamma_\uparrow^\dagger \gamma_\downarrow \tag{S26}$$

$$\hat\sigma^- = 2\exp\left[-i\left(\kappa L - 1\right)\frac{\phi}{2}\right] A_\uparrow A_\downarrow^* \gamma_\uparrow^\dagger \gamma_\downarrow \tag{S27}$$

$$\hat\sigma^z = \left|A_\uparrow\right|^2\left(2\gamma_\uparrow^\dagger\gamma_\uparrow - 1\right) - \left|A_\downarrow\right|^2\left(2\gamma_\downarrow^\dagger\gamma_\downarrow - 1\right). \tag{S28}$$

Because of this, the total occupation number $N = \gamma_\uparrow^\dagger\gamma_\uparrow + \gamma_\downarrow^\dagger\gamma_\downarrow$ becomes a good quantum number, namely $[N, H] = 0$ where $H = H_e + H_S$. The many body Hilbert space is spanned by the states $|N\alpha\rangle = |N\rangle \otimes |\alpha\rangle$ with $N = 0, 1, 2$ labeling the occupation number of the Andreev bound state and $\alpha = +, -$ labeling the eigenstates of S_z of the impurity spin.

The subspace for $N = 0$ is spanned by $|0+\rangle$, and $|0-\rangle$. The Hamiltonian H in this subspace is represented by a 2 by 2 matrix

$$H^{N=0} = -\epsilon - \frac{\left|A_\uparrow\right|^2 - \left|A_\downarrow\right|^2}{2}\left(J_{zz}\tau_z + J_{+z}\tau_+ + J_{+z}^*\tau_-\right) \tag{S29}$$

where $\tau_\pm = (\tau_x \pm i\tau_y)/2$ with $\tau_{x,y,z}$ are Pauli matrices in this two dimensional subspaces.

By using Eq. (S9), we have

$$\left|A_\uparrow\right|^2 - \left|A_\downarrow^2\right| \simeq -\frac{\epsilon}{2v(1 + L\kappa)^2}\phi. \tag{S30}$$

The subspace with $N = 1$ is spanned by $|\uparrow +\rangle$, $|\downarrow +\rangle$, $|\uparrow -\rangle$, $|\downarrow -\rangle$. The Hamiltonian in this case can be written as

$$H^{N=1} = 2\exp\left[i\left(\kappa L - 1\right)\frac{\phi}{2}\right] A_\uparrow^* A_\downarrow (J_{z+}\tau_z + J_{++}\tau_+ + J_{-+}\tau_-)\rho_+ + h.c. \tag{S31}$$

where $\rho_\pm = (\rho_x \pm i\rho_y)/2$ and $\rho_{x,y,z}$ are Pauli matrices in $\left|\uparrow\right\rangle, \left|\downarrow\right\rangle$ space, and we have neglected terms linear in $\phi \simeq 0$.

An unitary transformation $U = e^{-i\eta\rho_z/2}$ for some $\eta \in [0, \pi/2]$ can always be chosen such that

$$UH^{N=1}U^\dagger = \frac{\kappa}{2(1 + \kappa L)}\left[(J_{z+}\tau_z + J_{++}\tau_+ + J_{-+}\tau_-)\rho_z + h.c.\right] \tag{S32}$$

which has the same spectrum as $H^{N=1}$. The four eigenvalues are generically nondegenerate.

[1] Y. Peng, F. Pientka, E. Berg, Y. Oreg, and F. von Oppen, Phys. Rev. B **94**, 085409 (2016).

6 Conclusions

Given their highly interesting physical properties and potential application to quantum computation, engineering topological superconductors hosting Majoranas in the laboratory is an important research objective. Although more and more experiments based on theoretical proposals have claimed to find evidence for Majoranas, these results consistently raised puzzles and consequently doubts regarding the interpretation of the experiments.

This thesis contributes to this field in two aspects. On the one hand (Chapter 2 and 5), it unravels puzzles originating from discrepancies between simplified theoretical models and the physics of realistic materials, and hence improves our understanding of Majorana physics under experimental conditions. On the other hand (Chapter 3 and 4), it proposes various signatures of topological superconductivity, which can be observed using current experimental techniques. Moreover, some predictions have been already tested in several laboratories. In the following, we summarize the four projects that are pursued in this thesis.

In Chapter 2, we solved the puzzle posed by the recent STM experiment from Yazdani's group [57], providing evidence for Majoranas in chains of magnetic adatoms on superconductors. We looked into the proximity effect more carefully, which was largely treated phenomenologically in previous theoretical works on topological superconductors. We found that for strong coupling between normal and superconducting system, the coherence length of the proximity-induced superconductivity can differ dramatically from the coherence length of the proximity-providing superconductor, as reflected in a strong velocity renormalization [1]. The physics of strong localization of the Majoranas may actually be significant for realizing quantum computation, since braiding should be performed when Majoranas are well separated. Thus, it is very desirable to have an interface which makes the most of the superconducting proximity effect and strongly localizes the Majoranas.

In Chapter 3, we suggested to use superconducting rather than normal-metal leads to probe Majoranas. This has two important advantages: (i) The conductance is not only universal but also protected against temperature effects by the superconducting gap. This may make observation of the predicted universal conductance more accessible. (ii) Majoranas are signaled by *symmetric* conductance peaks at bias voltages $eV = \pm\Delta$. (Δ is the gap of the superconducting lead.) [2] The latter prediction has already motivated experimental checks by the groups of K. Franke [7] and A. Yazdani [64]. Nevertheless, while there are encouraging signatures, the experimental situation is still unclear and further work is needed.

In parallel to the above two projects, there are several related works done in collaboration with the experimentalists in the group of K. Franke, which are also part of the PhD research. In Ref. [5], we studied the tunneling processes from a superconducting STM tip into subgap states in superconductors. In Ref. [7], we investigated the end states in a magnetic adatom chain made of Fe on a Pb superconductor. In Ref. [10], we looked at the subgap states created by a magnetic adatom on a superconductor and analyzed its spatial pattern.

In Chapter 4, we explored topological Josephson junctions. The prominent 4π-periodic fractional Josephson effect, predicted for topological Josephson junctions, is presumably difficult to observe due to quasiparticle poisoning processes. We propose to perform a simple switching probability measurement, which provides robust signatures of topological Josephson junctions even in the presence of quasiparticle poisoning [3].

In Chapter 5, we looked at the recent experiments [68, 69] on superconductor/quantum spin Hall/superconductor junctions in Molenkamp's group, which showed evidence for a 4π-periodic rather than the expected 2π-dissipative Josephson effect. These experiments motivated us to consider realistic junctions in which the helical edge states are coupled to charge puddles which act as magnetic impurities. We showed that this makes the Josephson effect generically 8π-periodic. This 8π Josephson effect is the result of the fermion parity anomaly and a remarkable spin transmutation, and can be thought of as emerging from coupling $\mathbb{Z}_4$ parafermions which enable the transfer of $e/2$ charges. To connect to the experimental observations, we provided scenarios how this effect may appear in experiment as having period 4π. It will be interesting to see whether future experiments can distinguish this explanation as a parafermion effect from a more elementary explanation in terms of inelastic relaxation of quasiparticles into Cooper pairs which applies even to pristine junctions [4].

Finally, although in this thesis we only discuss Majorana zero modes that appear as excitations in topological superconductors, it is worth mentioning that Majoranas together with their exotic nonabelian statistics were first introduced as quasiparticles in the fractional quantum Hall state known as the *Moore-Read Pfaffian state* [70], at Landau level filling factor 5/2. It was shown later [35] that there is an intimate connection between the the Moore-Read Pfaffian states and the topological spinless 2D $p + ip$ superconductor (See Sec. 1.3.4 in Chapter 1), which implies that some universal properties of the former (such as non-abelian statistics) must also be shared by the latter [71].

Since fractional quantum Hall quasiparticles are anyons, one may make use of this to construct platforms which host nonabelian anyons beyond Majoranas. One possibility is based on fractional quantum Hall/superconductor hybrid systems. Indeed, there are already theoretical proposals for realizing parafermions [72, 73] and even Fibonacci anyons [74], which are able to provide universal quantum computation via braiding, in this type of system. To realize this, it turns out that graphene is an attractive platform, since it allows for high tunability by gate voltages and can be interfaced with a variety of superconductors with strong spin-orbit coupling such as Pb. Recently, fractional quantum Hall states with helical edge states have been realized [75] and superconducting correlations have been observed in graphene-based quantum Hall/superconductor hybrid systems [76]. Because of the rapid experimental progress, this direction seems to be very promising for future research.

Acknowledgements

First, I want to express my gratitude to my supervisor Felix von Oppen for his guidance and support during my PhD over the past three and a half year. I benefited from and very much enjoyed discussing with him on various topics. Moreover, I am grateful to him for providing me chances to collaborate with many great physicists and to attend various scientific events.

I appreciate numerous enlightening discussions with all collaborators who contributed to my work on this topic: Leonid I. Glazman, Falko Pientka, Yuval Vinkler-Aviv, Piet W. Brouwer, Erez Berg, Yuval Oreg, Michael Ruby, Benjamin W. Heinrich, and Katharina J. Franke.

I want to thank all members in the Dahlem Center for Quantum Complex Systems, especially my officemate Anton Bruch for creating a dynamic and inspiring research atmosphere. I am indebted to Brigitte Odeh for her administrative support.

I would like to acknowledge financial support by the German Research foundation (DFG) through CRC 183.

Finally, I am indebted to my parents for supporting me throughout my life and I am deeply grateful to my wife Ningning for her love, understanding, and support which carried me through this work.

Bibliography

[1] Yang Peng, Falko Pientka, Leonid I. Glazman, and Felix von Oppen. Strong localization of majorana end states in chains of magnetic adatoms. *Phys. Rev. Lett.*, 114:106801, Mar 2015.

[2] Yang Peng, Falko Pientka, Yuval Vinkler-Aviv, Leonid I. Glazman, and Felix von Oppen. Robust majorana conductance peaks for a superconducting lead. *Phys. Rev. Lett.*, 115:266804, Dec 2015.

[3] Yang Peng, Falko Pientka, Erez Berg, Yuval Oreg, and Felix von Oppen. Signatures of topological josephson junctions. *Phys. Rev. B*, 94:085409, Aug 2016.

[4] Yang Peng, Yuval Vinkler-Aviv, Piet W. Brouwer, Leonid I. Glazman, and Felix von Oppen. Parity anomaly and spin transmutation in quantum spin hall josephson junctions. *Phys. Rev. Lett.*, 117:267001, Dec 2016.

[5] Michael Ruby, Falko Pientka, Yang Peng, Felix von Oppen, Benjamin W. Heinrich, and Katharina J. Franke. Tunneling processes into localized subgap states in superconductors. *Phys. Rev. Lett.*, 115:087001, Aug 2015.

[6] Falko Pientka, Yang Peng, Leonid Glazman, and Felix von Oppen. Topological superconducting phase and majorana bound states in shiba chains. *Phys. Scr.*, 2015(T164):014008, 2015.

[7] Michael Ruby, Falko Pientka, Yang Peng, Felix von Oppen, Benjamin W. Heinrich, and Katharina J. Franke. End states and subgap structure in proximity-coupled chains of magnetic adatoms. *Phys. Rev. Lett.*, 115:197204, Nov 2015.

[8] Niko Sakkinen, Yang Peng, Heiko Appel, and Robert van Leeuwen. Many-body green's function theory for electron-phonon interactions: Ground state properties of the holstein dimer. *J. Chem. phys.*, 143(23):234101, 2015.

[9] Niko Säkkinen, Yang Peng, Heiko Appel, and Robert van Leeuwen. Many-body green's function theory for electron-phonon interactions: The kadanoff-baym approach to spectral properties of the holstein dimer. *The Journal of chemical physics*, 143(23):234102, 2015.

[10] Michael Ruby, Yang Peng, Felix von Oppen, Benjamin W. Heinrich, and Katharina J. Franke. Orbital picture of yu-shiba-rusinov multiplets. *Phys. Rev. Lett.*, 117:186801, Oct 2016.

[11] Felix von Oppen, Yang Peng, and Falko Pientka. Topological superconducting phases in one dimension. In Claudio Chamon, Mark O. Goerbig, Roderich Moessner, and Leticia F. Cugliandolo, editors, *Lecture Notes of the Les Houches Summer School:*

Topological Aspects of Condensed Matter Physics, chapter 9, pages 387–447. Oxford University Press, Oxford, 2017.

[12] Yang Peng, Yimu Bao, and Felix von Oppen. Boundary green functions of topological insulators and superconductors. *Phys. Rev. B*, 95:235143, Jun 2017.

[13] Michael Ruby, Benjamin W. Heinrich, Yang Peng, Felix von Oppen, and Katharina J. Franke. Exploring a proximity-coupled co chain on pb(110) as a possible majorana platform. *Nano Letters*, 17(7):4473–4477, 2017.

[14] Benedikt Friess, Yang Peng, Bernd Rosenow, Felix von Oppen, Vladimir Umansky, Klaus von Klitzing, and Jurgen H Smet. Negative permittivity in bubble and stripe phases. *Nature Physics*, 2017.

[15] K. v. Klitzing, G. Dorda, and M. Pepper. New method for high-accuracy determination of the fine-structure constant based on quantized hall resistance. *Phys. Rev. Lett.*, 45:494–497, Aug 1980.

[16] R. B. Laughlin. Quantized hall conductivity in two dimensions. *Phys. Rev. B*, 23:5632–5633, May 1981.

[17] B. I. Halperin. Quantized hall conductance, current-carrying edge states, and the existence of extended states in a two-dimensional disordered potential. *Phys. Rev. B*, 25:2185–2190, Feb 1982.

[18] D. J. Thouless, M. Kohmoto, M. P. Nightingale, and M. den Nijs. Quantized hall conductance in a two-dimensional periodic potential. *Phys. Rev. Lett.*, 49:405–408, Aug 1982.

[19] F. D. M. Haldane. Model for a quantum hall effect without landau levels: Condensed-matter realization of the "parity anomaly". *Phys. Rev. Lett.*, 61:2015–2018, Oct 1988.

[20] Chao-Xing Liu, Shou-Cheng Zhang, and Xiao-Liang Qi. The quantum anomalous hall effect: Theory and experiment. *Annu. Rev. Condens. Matter Phys.*, 7:301–321, 2016.

[21] Gregor Jotzu, Michael Messer, Rémi Desbuquois, Martin Lebrat, Thomas Uehlinger, Daniel Greif, and Tilman Esslinger. Experimental realization of the topological haldane model with ultracold fermions. *Nature*, 515(7526):237–240, 2014.

[22] Cui-Zu Chang, Jinsong Zhang, Xiao Feng, Jie Shen, Zuocheng Zhang, Minghua Guo, Kang Li, Yunbo Ou, Pang Wei, Li-Li Wang, Zhong-Qing Ji, Yang Feng, Shuaihua Ji, Xi Chen, Jinfeng Jia, Xi Dai, Zhong Fang, Shou-Cheng Zhang, Ke He, Yayu Wang, Li Lu, Xu-Cun Ma, and Qi-Kun Xue. Experimental observation of the quantum anomalous hall effect in a magnetic topological insulator. *Science*, 340(6129):167–170, 2013.

[23] C. L. Kane and E. J. Mele. Z_2 topological order and the quantum spin hall effect. *Phys. Rev. Lett.*, 95:146802, Sep 2005.

[24] C. L. Kane and E. J. Mele. Quantum spin hall effect in graphene. *Phys. Rev. Lett.*, 95:226801, Nov 2005.

[25] B. Andrei Bernevig and Shou-Cheng Zhang. Quantum spin hall effect. *Phys. Rev. Lett.*, 96:106802, Mar 2006.

[26] Markus König, Steffen Wiedmann, Christoph Brüne, Andreas Roth, Hartmut Buhmann, Laurens W Molenkamp, Xiao-Liang Qi, and Shou-Cheng Zhang. Quantum spin hall insulator state in hgte quantum wells. *Science*, 318(5851):766–770, 2007.

[27] M. Z. Hasan and C. L. Kane. *Colloquium* : Topological insulators. *Rev. Mod. Phys.*, 82:3045–3067, Nov 2010.

[28] Xiao-Liang Qi and Shou-Cheng Zhang. Topological insulators and superconductors. *Rev. Mod. Phys.*, 83:1057–1110, Oct 2011.

[29] M. Tinkham. *Introduction to Superconductivity: Second Edition.* Dover Books on Physics. Dover Publications, 2004.

[30] P.G. de Gennes. *Superconductivity Of Metals And Alloys.* Advanced Books Classics. Westview Press, 1999.

[31] Yoichiro Nambu. Quasi-particles and gauge invariance in the theory of superconductivity. *Phys. Rev.*, 117:648–663, Feb 1960.

[32] Andreas P. Schnyder, Shinsei Ryu, Akira Furusaki, and Andreas W. W. Ludwig. Classification of topological insulators and superconductors in three spatial dimensions. *Phys. Rev. B*, 78:195125, Nov 2008.

[33] Jeffrey C. Y. Teo and C. L. Kane. Topological defects and gapless modes in insulators and superconductors. *Phys. Rev. B*, 82:115120, Sep 2010.

[34] Ching-Kai Chiu, Jeffrey C. Y. Teo, Andreas P. Schnyder, and Shinsei Ryu. Classification of topological quantum matter with symmetries. *Rev. Mod. Phys.*, 88:035005, Aug 2016.

[35] N. Read and Dmitry Green. Paired states of fermions in two dimensions with breaking of parity and time-reversal symmetries and the fractional quantum hall effect. *Phys. Rev. B*, 61:10267–10297, Apr 2000.

[36] Shinsei Ryu, Andreas P Schnyder, Akira Furusaki, and Andreas WW Ludwig. Topological insulators and superconductors: tenfold way and dimensional hierarchy. *New Journal of Physics*, 12(6):065010, 2010.

[37] Alexander Altland and Martin R. Zirnbauer. Nonstandard symmetry classes in mesoscopic normal-superconducting hybrid structures. *Phys. Rev. B*, 55:1142–1161, Jan 1997.

[38] Alexei Kitaev. Periodic table for topological insulators and superconductors. *AIP Conf. Proc.*, 1134:22, 2009.

[39] T. Senthil. Symmetry-Protected Topological Phases of Quantum Matter. *Annu. Rev. Condens. Matter Phys.*, 6:299, 2015.

[40] Raoul Bott. The stable homotopy of the classical groups. *Annals. Math.*, pages 313–337, 1959.

[41] Michael F Atiyah, Raoul Bott, and Arnold Shapiro. Clifford modules. *Topology*, 3:3–38, 1964.

[42] D. A. Ivanov. Non-abelian statistics of half-quantum vortices in p-wave superconductors. *Phys. Rev. Lett.*, 86:268–271, Jan 2001.

[43] A. Y. Kitaev. Unpaired majorana fermions in quantum wires. *Phys.-Usp.*, 44(10S):131, 2001.

[44] A. Y. Kitaev. Fault-tolerant quantum computation by anyons. *Ann. Phys.*, 303(1):2–30, 2003.

[45] Chetan Nayak, Steven H. Simon, Ady Stern, Michael Freedman, and Sankar Das Sarma. Non-abelian anyons and topological quantum computation. *Rev. Mod. Phys.*, 80:1083–1159, Sep 2008.

[46] Andrei Bernevig and Titus Neupert. Topological superconductors and category theory. In Claudio Chamon, Mark O. Goerbig, Roderich Moessner, and Leticia F. Cugliandolo, editors, *Lecture Notes of the Les Houches Summer School: Topological Aspects of Condensed Matter Physics*, pages 63–121. Oxford University Press, Oxford, 2017.

[47] R. Jackiw and C. Rebbi. Solitons with fermion number 1/2. *Phys. Rev. D*, 13:3398–3409, Jun 1976.

[48] Eric Rowell, Richard Stong, and Zhenghan Wang. On classification of modular tensor categories. *Comm. Math. Phys.*, 292(2):343–389, 2009.

[49] Sankar Das Sarma, Michael Freedman, and Chetan Nayak. Topologically protected qubits from a possible non-abelian fractional quantum hall state. *Phys. Rev. Lett.*, 94:166802, Apr 2005.

[50] Sergey Bravyi. Universal quantum computation with the $\nu = 5/2$ fractional quantum hall state. *Phys. Rev. A*, 73:042313, Apr 2006.

[51] Liang Fu and C. L. Kane. Superconducting proximity effect and majorana fermions at the surface of a topological insulator. *Phys. Rev. Lett.*, 100:096407, Mar 2008.

[52] Liang Fu and C. L. Kane. Josephson current and noise at a superconductor/quantum-spin-hall-insulator/superconductor junction. *Phys. Rev. B*, 79:161408, Apr 2009.

[53] Roman M. Lutchyn, Jay D. Sau, and S. Das Sarma. Majorana fermions and a topological phase transition in semiconductor-superconductor heterostructures. *Phys. Rev. Lett.*, 105:077001, Aug 2010.

[54] Yuval Oreg, Gil Refael, and Felix von Oppen. Helical liquids and majorana bound states in quantum wires. *Phys. Rev. Lett.*, 105:177002, Oct 2010.

[55] S. Nadj-Perge, I. K. Drozdov, B. A. Bernevig, and Ali Yazdani. Proposal for realizing majorana fermions in chains of magnetic atoms on a superconductor. *Phys. Rev. B*, 88:020407, Jul 2013.

[56] Falko Pientka, Leonid I. Glazman, and Felix von Oppen. Topological superconducting phase in helical shiba chains. *Phys. Rev. B*, 88:155420, Oct 2013.

[57] Stevan Nadj-Perge, Ilya K. Drozdov, Jian Li, Hua Chen, Sangjun Jeon, Jungpil Seo, Allan H. MacDonald, B. Andrei Bernevig, and Ali Yazdani. Observation of majorana fermions in ferromagnetic atomic chains on a superconductor. *Science*, 2014.

[58] Hiroyuki Shiba. Classical spins in superconductors. *Prog. Theor. Phys.*, 40(3):435–451, 1968.

[59] Hiroyuki Shiba. A hartree-fock theory of transition-metal impurities in a superconductor. *Prog. Theor. Phys.*, 50(1):50–73, 1973.

[60] Vincent Mourik, Kun Zuo, Sergey M Frolov, SR Plissard, EPAM Bakkers, and LP Kouwenhoven. Signatures of majorana fermions in hybrid superconductor-semiconductor nanowire devices. *Science*, 336(6084):1003–1007, 2012.

[61] Anindya Das, Yuval Ronen, Yonatan Most, Yuval Oreg, Moty Heiblum, and Hadas Shtrikman. Zero-bias peaks and splitting in an al-inas nanowire topological superconductor as a signature of majorana fermions. *Nature Physics*, 8(12):887–895, 2012.

[62] H. O. H. Churchill, V. Fatemi, K. Grove-Rasmussen, M. T. Deng, P. Caroff, H. Q. Xu, and C. M. Marcus. Superconductor-nanowire devices from tunneling to the multichannel regime: Zero-bias oscillations and magnetoconductance crossover. *Phys. Rev. B*, 87:241401, Jun 2013.

[63] Sven Marian Albrecht, AP Higginbotham, Morten Madsen, Ferdinand Kuemmeth, Thomas Sand Jespersen, Jesper Nygård, Peter Krogstrup, and CM Marcus. Exponential protection of zero modes in majorana islands. *Nature*, 531(7593):206–209, 2016.

[64] Benjamin E Feldman, Mallika T Randeria, Jian Li, Sangjun Jeon, Yonglong Xie, Zhijun Wang, Ilya K Drozdov, B Andrei Bernevig, and Ali Yazdani. High-resolution studies of the majorana atomic chain platform. *Nature Physics*, 2016.

[65] Rémy Pawlak, Marcin Kisiel, Jelena Klinovaja, Tobias Meier, Shigeki Kawai, Thilo Glatzel, Daniel Loss, and Ernst Meyer. Probing atomic structure and majorana wavefunctions in mono-atomic fe-chains on superconducting pb-surface. *npj Quantum Information*, 2:16035, 2016.

[66] K. T. Law, Patrick A. Lee, and T. K. Ng. Majorana fermion induced resonant andreev reflection. *Phys. Rev. Lett.*, 103:237001, Dec 2009.

[67] Karsten Flensberg. Tunneling characteristics of a chain of majorana bound states. *Phys. Rev. B*, 82:180516, Nov 2010.

[68] J. Wiedenmann, E. Bocquillon, R. S. Deacon, S. Hartinger, O. Herrmann, T. M. Klapwijk, L. Maier, C. Ames, C. Bruene, C. Gould, A. Oiwa, K. Ishibashi, S. Tarucha, H. Buhmann, and L. W. Molenkamp. 4π-periodic Josephson supercurrent in HgTe-based topological Josephson junctions. *Nature Communications*, 7:10303, 2016.

[69] Russell S Deacon, Jonas Wiedenmann, Erwann Bocquillon, Teun M Klapwijk, Philipp Leubner, Christoph Brüne, Seigo Tarucha, Koji Ishibashi, Hartmut Buhmann, and Laurens W Molenkamp. Josephson radiation from gapless andreev bound states in hgte-based topological junctions. *arXiv preprint arXiv:1603.09611*, 2016.

[70] Gregory Moore and Nicholas Read. Nonabelions in the fractional quantum hall effect. *Nuclear Physics B*, 360(2-3):362–396, 1991.

[71] Jason Alicea. New directions in the pursuit of majorana fermions in solid state systems. *Rep. Prog. Phys.*, 75(7), 2012.

[72] Abolhassan Vaezi. Superconducting analogue of the parafermion fractional quantum hall states. *Phys. Rev. X*, 4:031009, Jul 2014.

[73] David J Clarke, Jason Alicea, and Kirill Shtengel. Exotic circuit elements from zero-modes in hybrid superconductor-quantum-hall systems. *Nature Physics*, 10(11):877–882, 2014.

[74] Roger S. K. Mong, David J. Clarke, Jason Alicea, Netanel H. Lindner, Paul Fendley, Chetan Nayak, Yuval Oreg, Ady Stern, Erez Berg, Kirill Shtengel, and Matthew P. A. Fisher. Universal topological quantum computation from a superconductor-abelian quantum hall heterostructure. *Phys. Rev. X*, 4:011036, Mar 2014.

[75] Javier D Sanchez-Yamagishi, Jason Y Luo, Andrea F Young, Benjamin M Hunt, Kenji Watanabe, Takashi Taniguchi, Raymond C Ashoori, and Pablo Jarillo-Herrero. Helical edge states and fractional quantum hall effect in a graphene electron–hole bilayer. *Nature Nanotechnology*, 2016.

[76] Gil-Ho Lee, Ko-Fan Huang, Dmitri K Efetov, Di S Wei, Sean Hart, Takashi Taniguchi, Kenji Watanabe, Amir Yacoby, and Philip Kim. Inducing superconducting correlation in quantum hall edge states. *arXiv preprint arXiv:1609.08104*, 2016.